Doped Beam Very Low Energy Particle Induced X-Ray Emission

By Daniel Totonjian

Thesis submitted in fulfilment of the
requirements for the degree of

Doctor of Philosophy

Under the supervision of Milos Toth
and John A. Scott

University of Technology Sydney
Faculty of Science
July 2022

Certificate of original authorship

I, Daniel Totonjian declare that this thesis, is submitted in fulfilment of the requirements for the award of Doctor of Philosophy, in the Faculty of Science at the University of Technology Sydney.

This thesis is wholly my own work unless otherwise referenced or acknowledged. In addition, I certify that all information sources and literature used are indicated in the thesis.

This document has not been submitted for qualifications at any other academic institution.

This research is supported by an Australian Research Council Linkage Grant and the Australian Government Research Training Program.

Signature of Student:

Production Note:
Signature removed prior to publication.

Date: February 2022

Acknowledgements

I would first like to thank my supervisors for patiently supporting me throughout my PhD, providing lengthy intellectual discussions, and expert guidance to shape my future work and studies. In particular I would like to thank Milos Toth who has supported me from the very beginning of my undergraduate studies to the end of my PhD, and John Scott who has helped shaped me into the scientist I am today. I would also like to thank Igor Aharonovich for providing support and guidance throughout my studies.

I would like to thank the members of my research group who have nurtured me over the years, teaching me new skills, methods, and techniques, and for creating a welcoming environment in which to thrive.

I would also like to thank my collaborators at Thermo Fisher Scientific and ETP by Adaptas for funding my research and providing exciting new projects and opportunities throughout my PhD.

I would finally like to thank my family for providing me love and support over the years and my Bungalow family for keeping me grounded and sane throughout my studies.

Contents

Glossary

PIXE Particle Induced X-Ray Emission

VLE-PIXE Very Low Energy PIXE

SEM Scanning Electron Microscope

EDS Energy Dispersive Spectroscopy

FIB Focused Ion Beam

IBA Ion Beam Analysis

BSI Backscattered Ions

PFIB Plasma Focused Ion Beam

LMIS Liquid Metal Ion Source

GFIS Gaseous Field Ionisation Source

ICP Inductively Coupled Plasma

PWBA Plane Wave Born Approximation

eECusPSShsR **e**xact, **E**nergy corrected, **C**oulomb corrected, **u**nited-**s**eparated, **P**erturbed **S**tationary **S**tate, **h**artree-**s**later, **R**elativistic correction

XRPCS X-Ray Production Cross Section

MO Molecular Orbital

SDD Silicon Drift Detector

LOD Limit of Detection

SNR Signal To Noise Ratio

RF Radio Frequency

amu Atomic Mass Unit or Dalton

TMP Turbo Molecular Pump

IGP Ion Getter Pump

SRM Standard Reference Material

C-K Coster-Kronig

LEIS Low Energy Ion Scattering

QCM Quartz Crystal Monitor

AFM Atomic Force Microscope

List of Figures

List of Tables

Abstract

Particle Induced X-Ray Emission (PIXE) is a spectroscopic technique where characteristic X-Rays are generated from a sample by the impact of high energy particles. PIXE is typically performed with protons in a particle accelerator at energies in excess of 1MeV and is used for the detection of trace elements due to the lower background compared to complementary techniques such as Scanning Electron Microscope (SEM) Energy Dispersive Spectroscopy (EDS). PIXE performed at energies of less than 1MeV is sometimes used to enhance sensitivity to light elements, however very low energy PIXE (VLE-PIXE) performed at energies available to a commercial focused ion beam microscope of $\leq$30keV was considered impossible due to the extremely low X-Ray production at these energies.

In this research, VLE-PIXE was made possible by doping a hydrogen focused ion beam with a small proportion of a heavier ion species such as Ar or Xe. The characteristic X-Ray signal was shown to increase dramatically, allowing trace element analysis in the low parts per million range, offering performance comparable to proton only PIXE performed at much higher energies. This thesis outlines the implementation, characterisation, and application of the doped beam VLE-PIXE technique in a commercial focused ion beam microscope utilising available hardware and little to no modification to the instrument.

An investigation into the beam doping technique led to an interpretive model which considers various physical mechanisms which may be responsible for the increased performance which includes: the formation of quasi-molecules between the heavy projectile ion and the target atom, the suppression of non-radiative transitions, and vacancy lifetime modification due to multiple ionisation. These mechanisms may arise from the coincident impact of protons and a heavy ion species upon the same region of the sample.

The ions backscattering from the surface during VLE-PIXE analysis were also analysed to provide additional information regarding the sample thickness and composition. This leads to the possibility of several new techniques such as simultaneous doped beam VLE-PIXE and backscattered ion spectroscopy for real-time tomography, or endpointing during Focused Ion Beam (FIB) milling.

Chapter 1

Introduction and Background

1.1 Introduction

Focused Ion Beam (FIB) instruments, are a staple of sample preparation, nanofabrication, and materials analysis. They are typically found in the form of dual or triple beam microscopes in combination with a scanning electron microscope (SEM) and more recently, femtosecond laser ablation systems [3]. FIB instruments dominate applications in the middle ground between small scale electron beam processing and large scale bulk processing, where the focused beam allows the mask-free processing of small feature sizes inaccessible to bulk processing such as reactive ion etching (RIE), with a throughput significantly higher than that offered by processing using an electron beam such as electron beam lithography and focused electron beam induced processing (FEBIP) [4, 5]. For this reason, FIB instruments typically find use in industrial applications such as semiconductor failure analysis where cross sectioning, tomography or Transmission Electron Microscope (TEM) lamella preparation is required on a relatively small scale, and high throughput is fundamental for cost reasons. FIBs also find their place in research and development, with such applications as the preparation of biological samples for cryo-TEM analysis, preparation of samples for atom probe tomography, or fabrication of optical components such as solid immersion lenses. As such, the FIB instrument is ubiquitous and can be found in a large number of factories and labs across the world [6, 7, 8, 4].

A FIB can also be considered a small, relatively low energy particle accelerator, given that the primary purpose of both a FIB and a particle accelerator is to generate and accelerate ions for the purpose of imaging, processing and ion beam analysis. With the advent of the ion microprobe, a module fitted to par-

ticle accelerator beamlines to produce a focused beam capable of micrometer level resolution, the line between a FIB and a particle accelerator is even further blurred [9]. In comparison to FIB instruments however, particle accelerators are somewhat rarer with only over 30,000 accelerators in operation as of 2014, ranging from small tabletop particle accelerators to the large hadron collider, which vary significantly in their intended use and application and can reach costs of several billions of dollars [10, 11].

One of the primary functions of many particle accelerator facilities is Ion Beam Analysis (IBA), a suite of techniques which involve the interaction of high energy particles with a sample and the analysis of signals generated as a result of these interactions. These techniques include: [12]

- Rutherford backscattering spectroscopy (RBS), the analysis of kinetically scattered primary ions from a sample
- Ion beam induced charge (IBIC), which involves the production of electron-hole pairs by a primary ion beam and the subsequent analysis of charge transport within the sample
- Nuclear reaction analysis (NRA), the analysis of charged particles emitted as a result of nuclear reactions following the interaction of a primary ion and the target nucleus
- Particle induced Gamma ray emission (PIGE), the analysis of Gamma rays emitted following the interaction of a primary ion and the target nucleus
- Particle induced X-Ray emission (PIXE), the analysis of characteristic X-Rays emitted as a result of ionisation of the target atom by a primary ion

Of particular interest to this thesis is the technique of particle induced X-Ray emission (PIXE). This technique is ideal for trace-element analysis, where a sample composition can be determined with a sensitivity at or below 1 part per million [13, 14]. The PIXE technique is often compared to a similar X-Ray spectroscopic technique; energy dispersive spectroscopy performed in a scanning electron microscope (SEM-EDS). EDS can offer better spatial resolution than PIXE due to a smaller electron probe size, allowing the potential for atomic resolution compositional mapping [15], and higher throughput at lower energies due to the increased X-Ray production cross section of electrons (see section 1.3.4.3, however sensitivity of EDS is typically between 100-500 ppm [16], several orders of magnitude worse than what can be achieved by PIXE.

PIXE is typically performed at energies of several MeV, predominantly due to the

significantly increased X-Ray production cross sections at higher energies [17] as well as the reduced damage caused by incident ions [18]. These high primary ion energies however restrict this technique to particle accelerator facilities, which as discussed previously are limited in terms of availability, cost and the large size of these facilities. The result is that the PIXE technique can be somewhat inaccessible to general lab users and specialised facilities must be accessed in order to perform PIXE. Similarly, techniques such as Scanning Transmission X-Ray Microscopy (STXM) whereby an X-Ray beam is focused onto a sample for the purpose of trace element analysis, also suffers from similar accessibility issues due to the need to perform this technique in a synchrotron facility [19].

Low energy PIXE (LE-PIXE), is carried out at energies $<$1MeV and offers several advantages over PIXE such as increased sensitivity to light elements and reduced background, particularly in the low energy X-Ray region. This technique however is still typically carried out using decelerated accelerator beamlines or modified ion implanters and as such, carries many of the same issues as PIXE in terms of cost and availability [20, 21]. The ability to perform PIXE on a FIB instrument would signify a large step in the progression of this technique, opening the availability of PIXE to a range of additional facilities and providing a complementary technique to SEM-EDS, affording significantly improved sensitivity to trace elements.

In this thesis, the term **Very Low Energy PIXE (VLE-PIXE)** is introduced which describes PIXE performed in the energy range available to a standard commercial FIB instrument of $\leq$ 30keV. Performing PIXE at such low energy range comes at the expense of significantly reduced X-Ray production due to the mechanism responsible for ionisation of the target atoms. PIXE performed at such low energies with protons alone was deemed to be impossible, [22] which warranted the introduction of a method for enhancement of X-Ray production at low energies. This came in the form of the beam doping mechanism discussed throughout this thesis, where the addition of a small amount of a heavy ion species such as Ar or Xe to a hydrogen beam demonstrated a drastic enhancement in X-Ray production in the energy range $\leq$30keV.

This thesis will focus on the implementation, characterisation, and application of doped beam VLE-PIXE in a FIB instrument, demonstrating performance approaching PIXE performed at energies of 1MeV.

1.2 Description of Chapters

Chapter 1 includes an introduction to the thesis and background information required to understand the doped beam VLE-PIXE technique. A comparison between the various FIB types is presented, introducing the multi species plasma FIB, and its importance to the implementation of doped beam VLE-PIXE. A brief outline of ion-solid interactions are given, with an emphasis on the ionisation of a target atom by the impact of protons and heavier ions. Practical aspects of the PIXE technique are outlined, as well as some complementary techniques such as EDS, backscattering spectroscopy, and secondary ion mass spectroscopy.

Chapter 2 describes the implementation and characterisation of an H_2 and doped H_2 FIB source on the Thermo Scientific Helios Hydra FIB microscope, a key step for the implementation of doped beam VLE-PIXE. This chapter outlines some of the challenges faced during the characterisation of the H_2 source and their potential influence on the doped beam VLE-PIXE technique.

Chapter 3 outlines the validity and viability of implementing doped beam VLE-PIXE on a FIB instrument. Additional signal contributions such as charging related effects, neutral molecules, and electrons are characterised. Methods to eliminate these contributions are discussed and a range of optimal operating parameters for the VLE-PIXE technique are outlined.

Chapter 4 describes application of the doped beam VLE-PIXE technique for trace element analysis of a number of standard samples. A comparison between doped beam VLE-PIXE and a complementary technique, SEM-EDS is carried out. The performance of these techniques in terms of the signal to noise ratio and limits of detection are compared. The X-Ray production cross sections for the doped beam VLE-PIXE technique are determined and compared to theoretical values for proton only cross sections at similar energies.

Chapter 5 describes an investigation into the performance of the beam doping mechanism. The influence of dopant species, proportion of dopant and accelerating voltage are determined and optimal beam doping conditions are outlined.

Chapter 6 outlines an interpretive physical model for the increase in X-Ray production through the introduction of beam dopants, based on the concept of the quasi-molecular interactions between the slow, heavy projectile and the target atom, and the suppression of non-radiative transitions. Kinetic calculations and Monte-Carlo simulation of the projectile-target system are performed.

Chapter 7 demonstrates the analysis of Backscattered Ions (BSI) produced during VLE-PIXE measurements. These BSIs can be used to provide additional information about the sample surface composition. This technique is used to measure the thickness of a number of Cu films deposited on an Si substrate with an accuracy of less than 1nm over an area of several micrometres, in good agreement with simulated values.

Chapter 8 provides a summary of the thesis and the conclusions drawn from the research. This chapter includes possible future experiments to continue this line of investigation and potential industrial applications of this technique.

1.3 Background Information

In this section, the recent technological advancements in FIB source technology are discussed which has allowed the implementation of the VLE-PIXE technique on a dual-beam FIB/SEM platform. The background knowledge required to understand the VLE-PIXE technique is outlined, starting from the interaction of a incident ions with a sample and the resulting processes culminating in the emission of characteristic X-Rays from the sample. Some practical aspects of the VLE-PIXE technique are then discussed such as detector instrumentation, and interpretation of results as well as a brief description of some other complementary IBA techniques.

1.3.1 Ion Sources

The primary distinguishing factor between focused ion beam (FIB) microscope types is the source of ions. This underpins the form and function of the microscope and its intended use in processing and analysis. In this section the most common ion sources are briefly discussed, and their use cases in FIB microscopy are outlined with an emphasis on the Plasma Focused Ion Beam (PFIB) used in the VLE-PIXE experiments.

1.3.1.1 Field Ionisation Sources

Field ionisation is a quantum phenomenon which occurs when a very high electrical potential is applied to a sharp tip in a vacuum. When the electric field is sufficient, the potential barrier for the removal of an electron from a surface atom

to the bulk is reduced such that the electron is able to tunnel into the bulk. When the surface atom has been ionised, the resultant positive ion is driven away from the surface by the large negative potential and the ion is emitted into vacuum [23]. An example potential diagram outlining this procedure is shown in figure 1.1

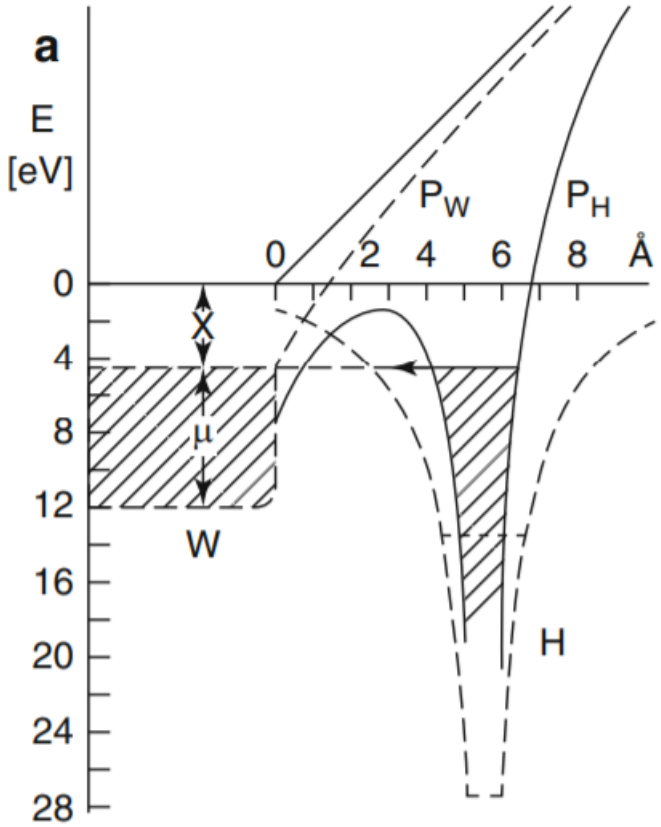

Figure 1.1: Potential diagram of a Hydrogen (H) atom adsorbed to a tungsten surface (W). Solid lines: potential at field strength of 2VÅ^{-1}, Dashed lines: zero field potential. P_W and P_H, image potential of W and H distorted by the field respectively. X denotes the work function, and μ denotes the Fermi level. (From [23]).

Liquid Metal Ion Sources:

The most common ion source type in focused ion beam microscopes is a Liquid Metal Ion Source (LMIS) which utilises the field ionisation technique described above. The most commonly used metal for these applications is Gallium (Ga), primarily due to its low melting point (T_{mp} = 29.8 °C), and high mass and therefore sputter yield [5]. A typical LMIS needle with and without the Ga metal is shown in figure 1.2.

When a large negative potential is then applied between the needle tip and an extraction electrode, the extraction bias is balanced by the surface tension of the Ga liquid, pinching the liquid to a fine point known as a Taylor cone, with a cusp

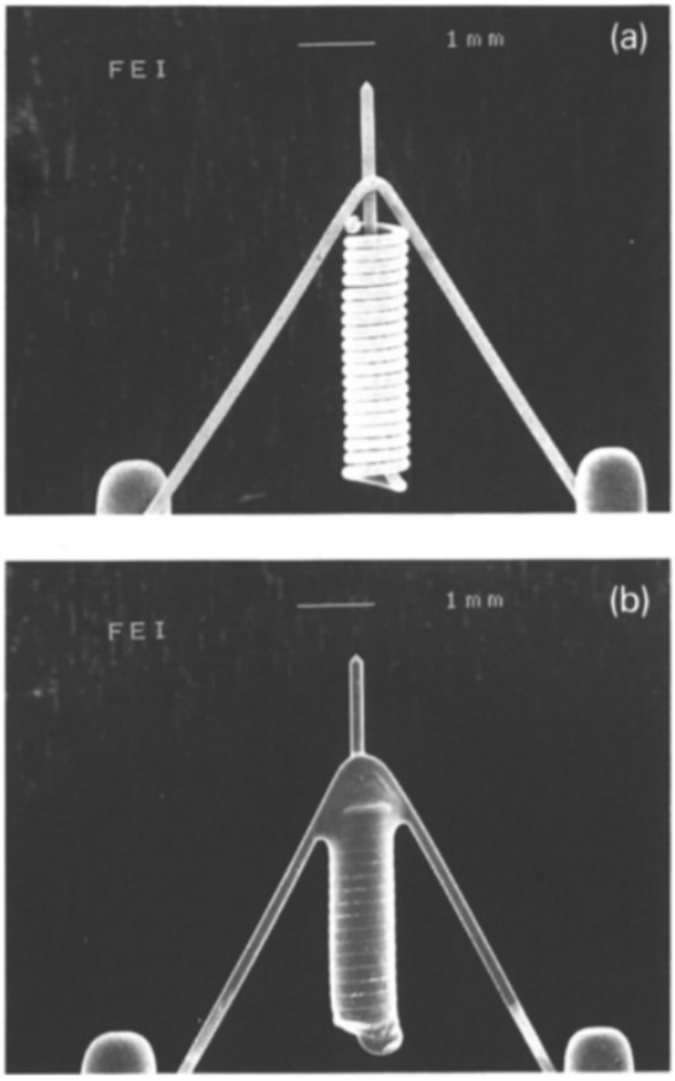

Figure 1.2: Image of a typical wetted needle type LMIS which can hold up to 15 mg of Ga (a) before loading the reservoir, (b) after loading the reservoir with Ga (From [24]).

forming at the tip of the Taylor cone a tip radius of approximately 5 nm [6]. In a high vacuum, this potential is sufficient to generate field emission of Ga^+ ions from the cusp [25, 26, 23]. Modern LMIS based FIB instruments have a beam spot size on the order of $\approx$10nm [8].

Issues with the extraction of Ga ions begin to arise at high extraction biases and currents where instability at the cusp increases the probability of emitting charged clusters, droplets, singly or doubly charged monomer ions, and neutral atoms. These effects limit the emission current of an LMIS to several tens of nA [5]. Most importantly, as an LMIS can only be operated with a liquid metal source, the LMIS is incapable of producing light ions such as protons which are required for generating X-Rays through the VLE-PIXE technique.

Gaseous Field Ionisation Sources:
The Gaseous Field Ionisation Source (GFIS) utilises a metallic needle with a final radius of just 3 atoms [27]. A very low partial pressure of gas is introduced to the needle where the gas molecules will rapidly adsorb to the tip surface. A strong electric field is then applied to the tip, such that field emission will only occur from the three gas atoms adsorbed to the final radius of the tip [28]. A cartoon of the atomically sharp tip and a source image of the GFIS is shown in figure 1.3.

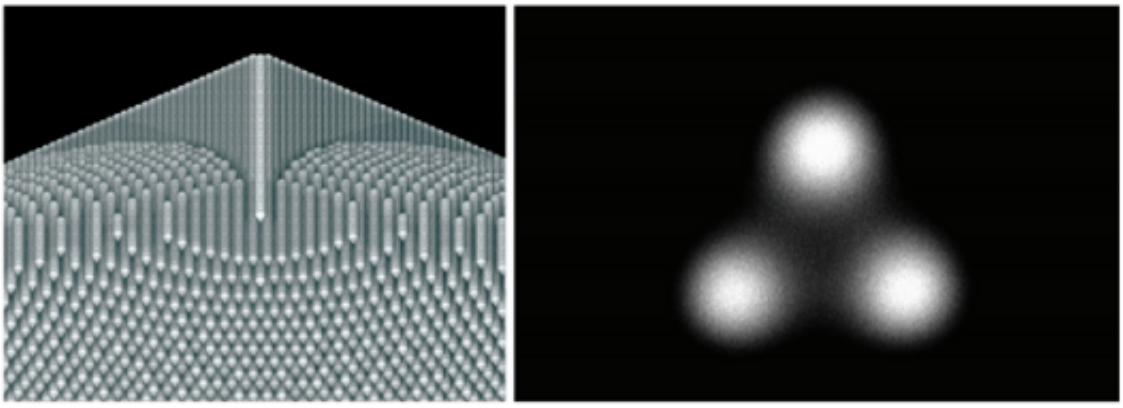

Figure 1.3: The atomically sharp pyramidal tip of the helium GFIS source and a source image of the helium ion emission from the tip (From [27]).

While typically operated with Helium gas, these sources are also capable of producing heavier ions such as Neon with a higher sputter yield for faster FIB processing [28]. As for lighter ions such as protons, Moritani et. al. and Matsubara et al. demonstrated the production of H^+ ions in a GFIS source, however in very small percentages relative to H_2^+, and H_3^+ ions [29, 30, 31].

Where a typical FIB operates with a fixed current and alters the size of the apertures to modify the beam current, the current of the GFIS source is altered by changing the pressure of the gas surrounding the tip. A greater pressure allows faster replenishment of the gas atoms on the tip, resulting in a faster extraction rate and a higher current. As the gas pressure increases however, the potential barrier for field ionisation also increases which results in a maximum working current of approximately 100pA [32, 33]. The small number of protons produced by this source, combined with the very small currents available to the GFIS makes this source unsuitable for VLE-PIXE analysis. Additionally, the GFIS is only capable of hosting one source species at a time, making it incapable of being utilised for doped beam VLE-PIXE.

1.3.1.2 Plasma Ion Sources

A plasma is defined as a fully or partially ionised gas consisting of electrons and ions and has been identified as a readily available source of ions for use in a FIB system. Plasmas come in one of several types and are named for the technique used to generate the plasma. One major benefit of plasma ion sources is that they are capable of hosting multiple ion species, a requirement for doped beam VLE-PIXE.

Plasma Types:
DC discharges are formed when a sufficiently high voltage bias between two parallel plates is placed across across a body of gas. When a primary electron is emitted from the cathode and is accelerated in the electric field, a collision with a gas molecule provides sufficient energy to ionise the gas molecule creating an ion and one or more free electrons. These electrons are then accelerated towards more gas molecules and the process continues, forming a cascade of ionisation events. When ions collide with the cathode, secondary electrons are emitted from the surface and the process continues. This self sustaining discharge is known as a Townsend cascade and is shown in figure 1.4. DC discharges are not typically used in plasma processing or ion source production due to their low current density [34].

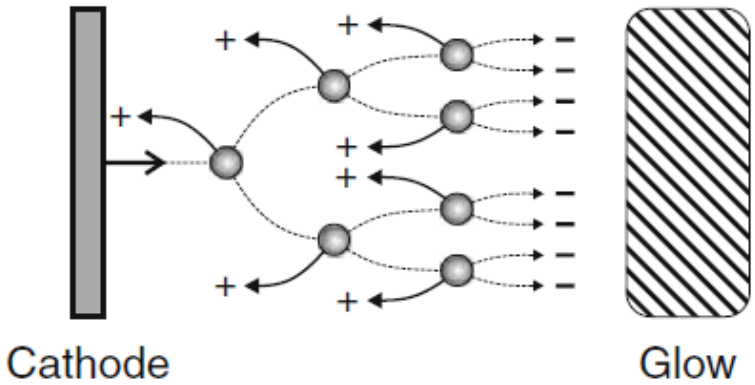

Figure 1.4: Operating principle of a Townsend DC discharge plasma (From [34]).

Capacitatively coupled plasmas are formed when an Radio Frequency (RF) wave is driven between two parallel plates with a body of gas contained between. The RF field is also accompanied by a potential difference between the power supply and the ground which is sufficient to ionise the gas molecules, similar to that of a DC discharge.

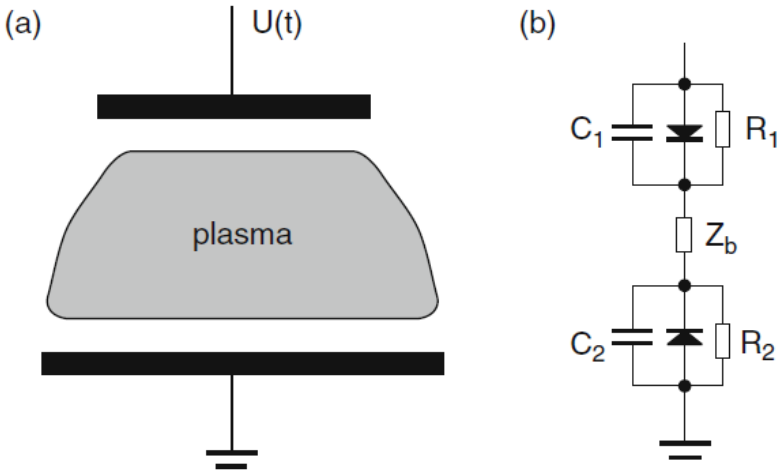

Figure 1.5: Operating principle of a capacitatively coupled plasma (a) schematic of the electrode configuration (b) the equivalent electronic circuit of the sheath regions and the bulk plasma. R_1 and R_2 denote a resistor representing the ion current in the upper and lower sheath respectively and C_1 and C_2 denote the upper and lower sheath capacity respectively. Z_b denotes the impedence of the bulk plasma. (From [34]).

Due to the significant difference in mobility between the electrons and ions in the plasma, the electrons are free to follow the instantaneous RF field, however the ions are not and can be considered almost stationary. This higher mobility allows the electrons to collide with surfaces and rapidly build up a negative charge. This in turn attracts the positive ions which creates a region of high positive ion density known as a plasma ”sheath”. A schematic of the electrode configuration and the equivalent electronic circuit of the CCP is shown in figure 1.5. CCPs are favoured for plasma processing due to greater homogeneity of the plasma, however are typically not used for plasma ion sources due to a relatively low ion density and low efficiency. [34] Additionally, the possibility of beam contamination due to sputtering of the electrode materials may be of some concern.

An Inductively Coupled Plasma (ICP) is unique compared to DC and CCP plasmas in that the plasma can be generated by use of an antenna which is external to the plasma chamber. The primary benefit of this is that the plasma itself does not come into contact with the antenna, significantly increasing the lifetime of the antenna and expanding the range of possible plasmas to those which include oxidising gases. An ICP is formed by applying an RF wave to a helical or coiled conductive antenna, separated from the gas by use of a dielectric insulator, typically high quality quartz which has low dielectric losses and good resistance to high coil temperatures.

At relatively low RF power, the RF field from the antenna penetrates through the

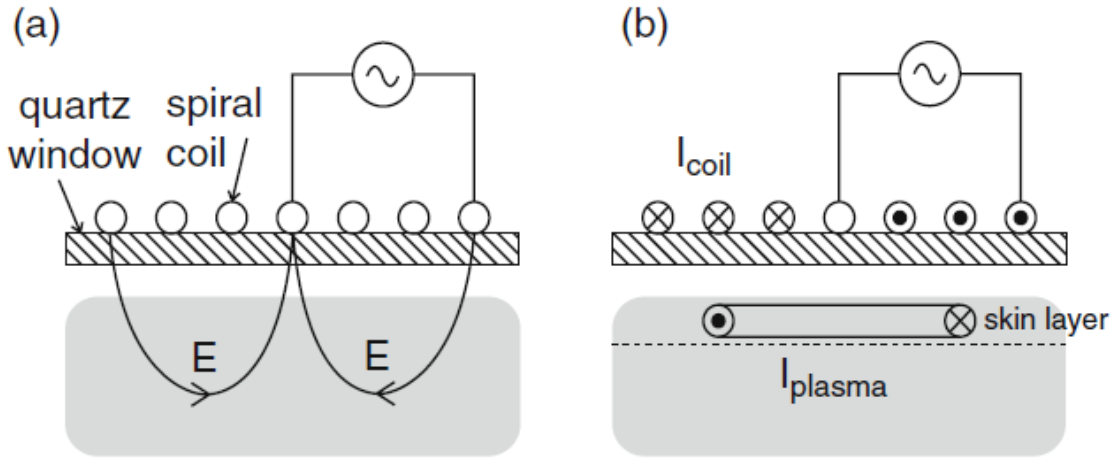

Figure 1.6: Operating principle of inductively coupled plasma (a) operating in low power E mode (b) operating in high power H mode. (From [34]).

dielectric providing an electric field which is sufficient to ionise the gas. This is known as E mode due to the primary excitation mechanism being the electric field of the RF coil, similar to that of a DC discharge. At higher RF power, the energy is sufficient to accelerate the electrons in the sheath near the edge of the dielectric, also known as the skin layer. This is known as H mode, as a true inductive coupling is formed between the antenna and the plasma generating a very high density plasma. An ideal ICP acts like a transformer with the primary winding being the antenna, and the induction field in the plasma forming a single-turn secondary coil. The E and H mode ICP operation is shown schematically in figure 1.6 [34]. ICP is used in applications where a very high density plasma is required, making it suitable for use as a high brightness ion source, and ideal for use as an ion source for VLE-PIXE.

ICP Ion Sources:

ICP Ion sources take advantage of the benefits of an ICP plasma such as the high plasma density, efficient and contact-free operation to create a high-brightness, source with essentially infinite lifetime [35]. Another benefit of the ICP ion source is the ability to rapidly switch between source types. This is achieved by simply pumping out the previous source gas and introducing a new gas [36]. Xe is typically used ion in ICP ion sources due its high mass and therefore high sputter yield however Ar, O_2 and N_2 are also commonly available. In this study, a hydrogen gas source was introduced to generate the protons required for VLE-PIXE. This hydrogen beam is also doped with a number of heavier ion species which is possible due to the multi source implementation of the FIB instrument.

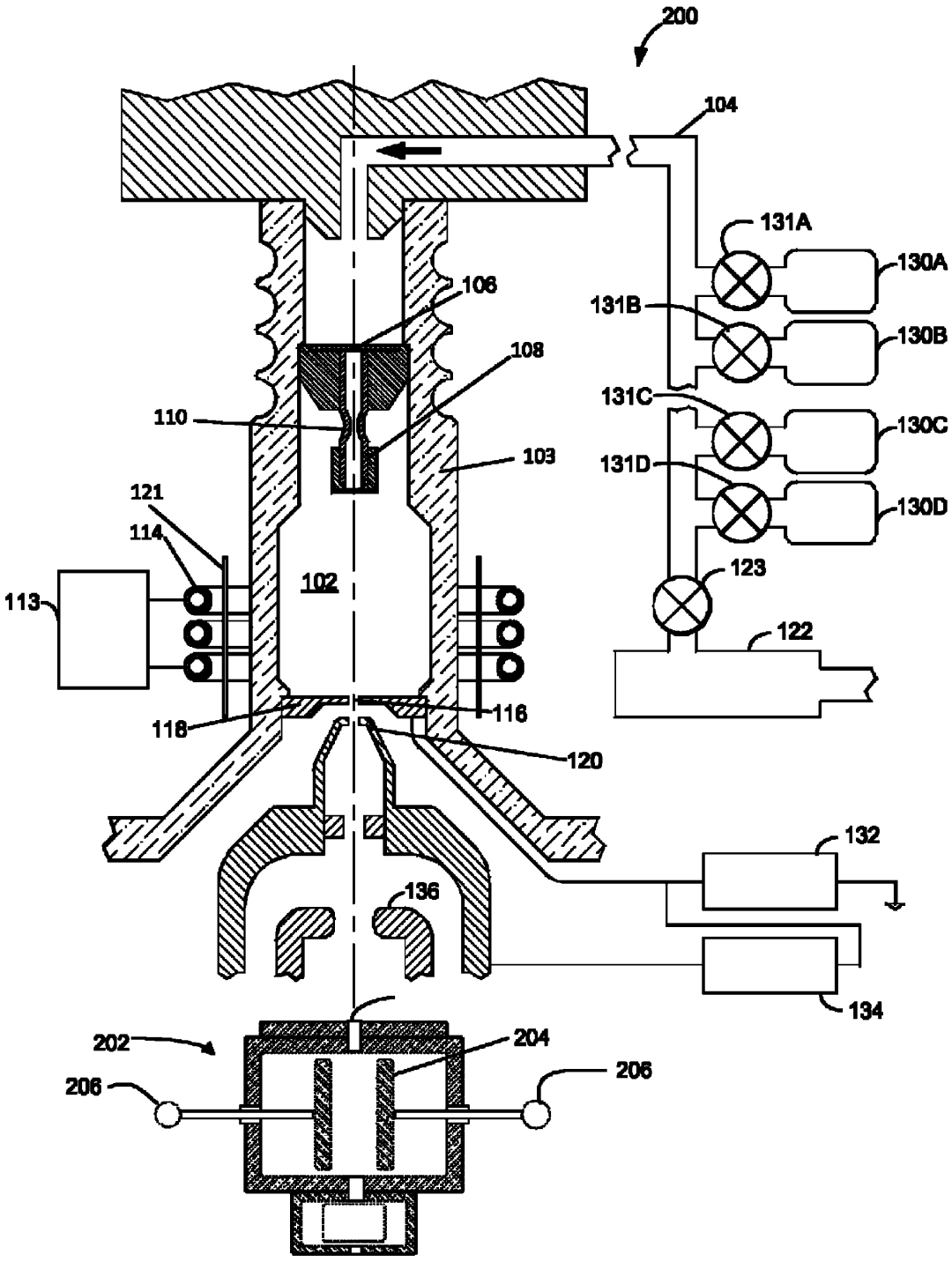

Figure 1.7: Schematic of a typical ICP source. (From [37]).

The ICP ion source used for the applications in this thesis is shown in figure 1.7 and is described as such: the desired gaseous species is fed into a quartz source tube (item 102), from an external gas supply system. The plasma is then generated using an RF coil-type antenna (item 114) wrapped around the quartz source tube. The RF wave is provided by a high-power RF supply (item 113). Once the plasma ions have been generated, they are then extracted from the

source chamber by an extraction electrode (item 120) through a source electrode aperture (item 116) and through a first lens where the beam is collimated (item 136). The collimated beam then encounters an optional mass filter such as the one pictured in figure 1.7, item 202 before it is directed towards the sample [37].

Alternative Plasma Ion Sources:
While ICP ion sources are ideal as high brightness sources, they lack the flexibility often required for particle accelerators which may need to fit a number of use-cases. Particularly, ICP ion sources are limited to gaseous plasmas and are very inefficient at producing negative ions [38, 39] which may be required for some experiments. For this reason, ICP plasma sources are not commonly used in particle accelerators [40]. Some alternative plasma sources which are typically used for PIXE in particle accelerator systems are discussed.

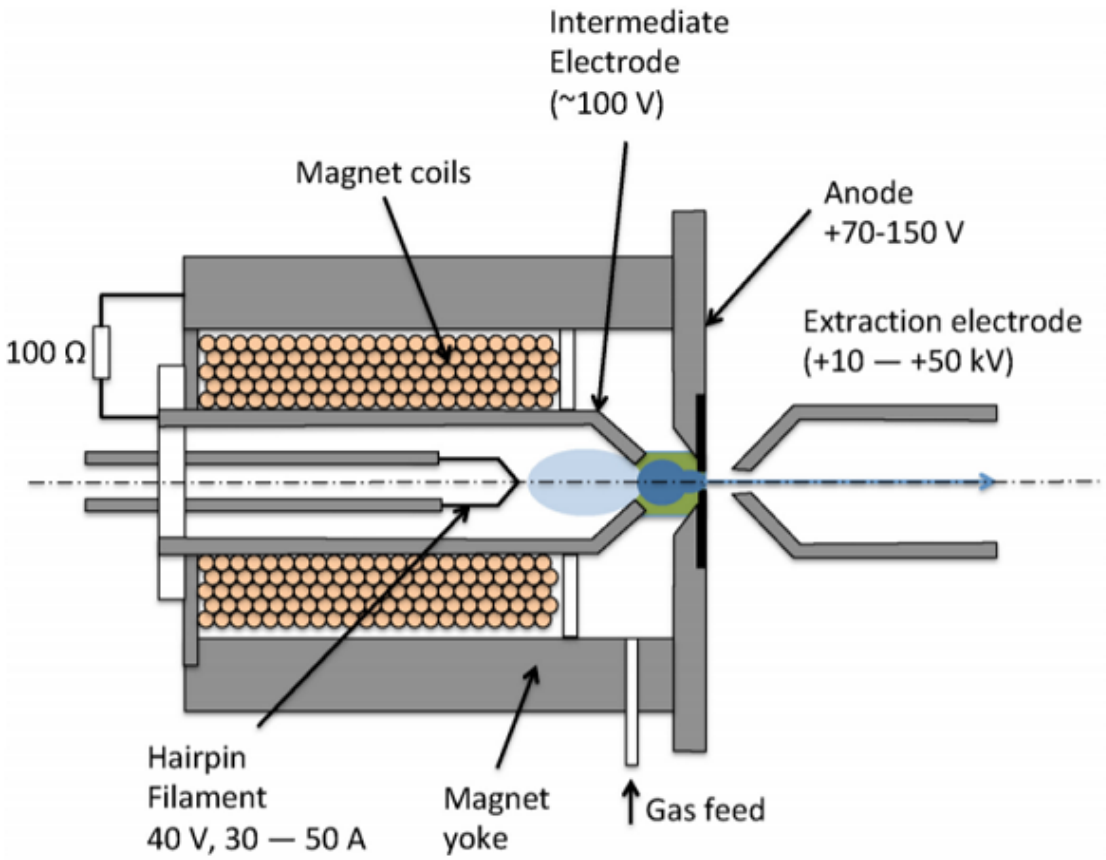

Figure 1.8: Schematic of a Duoplasmatron ion source. (From [41]).

Some alternative ion sources utilise a technique known as electron impact ionisation, where a cathode filament is heated and following extraction by an intermediate electrode, emits electrons into a small partial pressure of gas. The electrons are accelerated by the intermediate electrode such that their energy is sufficient

to ionise the gas molecules. The ions are then extracted and can be focused to form a beam. A benefit of electron impact ionisation is that sources are also capable of forming negative ion beams via electron capture [41].

One of the more popular electron impact sources is the Duoplasmatron, which utilises a series of electromagnets to focus the electron beam into a tight spot, also condensing the plasma and significantly increasing the density of the plasma formed [42, 43]. A variation on the duoplasmatron is a Freeman ion source which also incorporates an oven, extending the range of possible ion sources from gases, to vapours of solid precursors [44]. A schematic of a Duoplasmatron source is shown in figure 1.8.

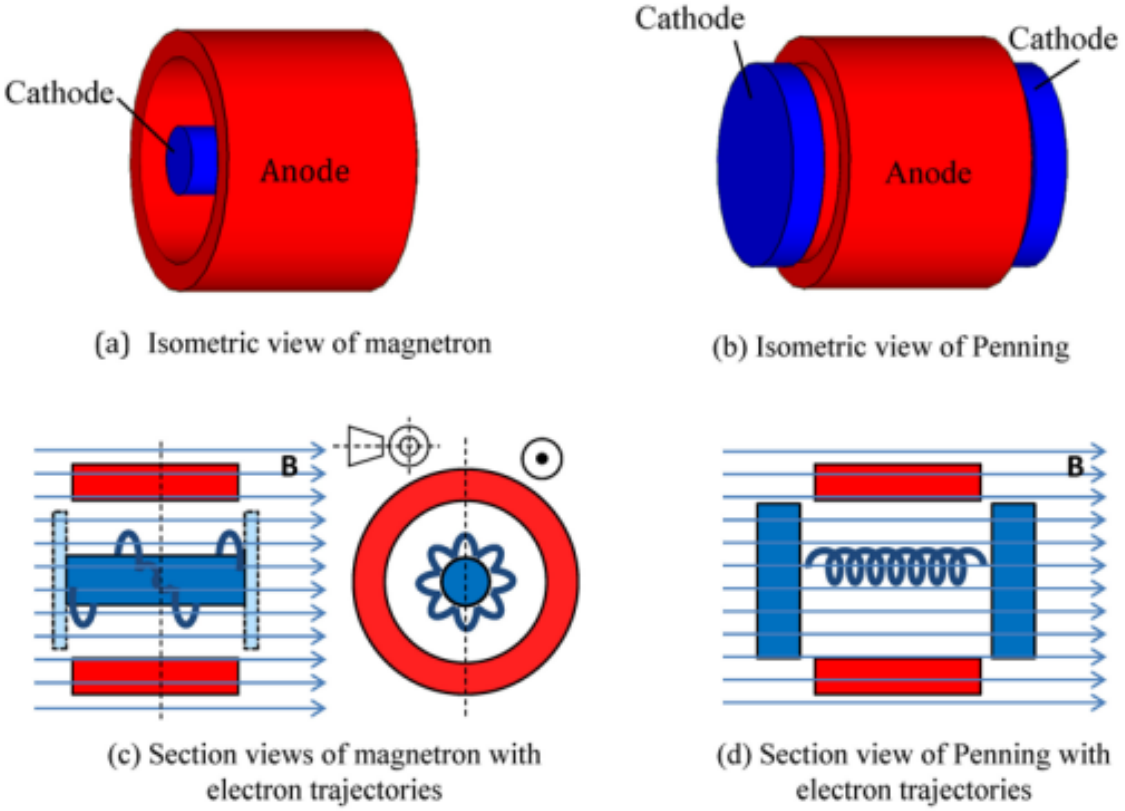

(a) Isometric view of magnetron

(b) Isometric view of Penning

(c) Section views of magnetron with electron trajectories

(d) Section view of Penning with electron trajectories

Figure 1.9: Schematic of (a) magnetron and (b) Penning ion sources. (From [45]).

The Penning and Magnetron ion sources are similar to a Duoplasmatron source in that they use a magnetic field to direct and confine the electrons generated as a result of a DC discharge of gas within the source. In the case of the magnetron, this causes the electrons to circulate around the cathode and in the penning, the electrons will bounce between the two cathodes. This significantly increases the mean free path of the electrons and results in a much higher plasma density. At low pressures, the gas itself can be used as the ion source and extracted through a hollow cathode. At higher pressures however, sputtering of the cathode

becomes significant and the cathode material itself can be used as a source of ions. Due to the destructive nature of the sputtering process however, the lifetime of the penning and magnetron sources are limited and require frequent maintenance, making them suitable for research environments however unsuitable for commercial applications where instrument down-time can result in significant loss of income [45, 46]. A schematic of these two sources is shown in figure 1.9.

Electron impact sources are used extensively in a wide range of applications such as mass spectrometry, ion implantation and accelerator physics due to their relatively low cost, simplicity, wide range of available gas sources, and high brightness [41, 43, 42, 47]. These sources however have several disadvantages such as high energy consumption [41], wide ion energy spread due to a thermionic electron source [48] and the consumable nature of the filament, whose lifetime is further reduced by operation in reactive gases [49].

Laser plasma ion sources (LPIS) utilise the plasma generated by a very high power pulsed laser directed towards a solid target. The energy deposited into the target material by the laser is sufficient to both athermally ablate and ionise the target surface atoms, generating a localised plasma plume. The electrons ejected from the surface are again heated by the intense laser radiation, reaching energies of several hundred electron volts. These electrons are in turn free to ionise any neutral atoms or molecules ejected from the surface or create secondary ionisation of ions ejected from the surface. They do so by a process known as the inverse Bremsstrahlung mechanism where kinetic energy from the electrons is absorbed by the atoms and ions.

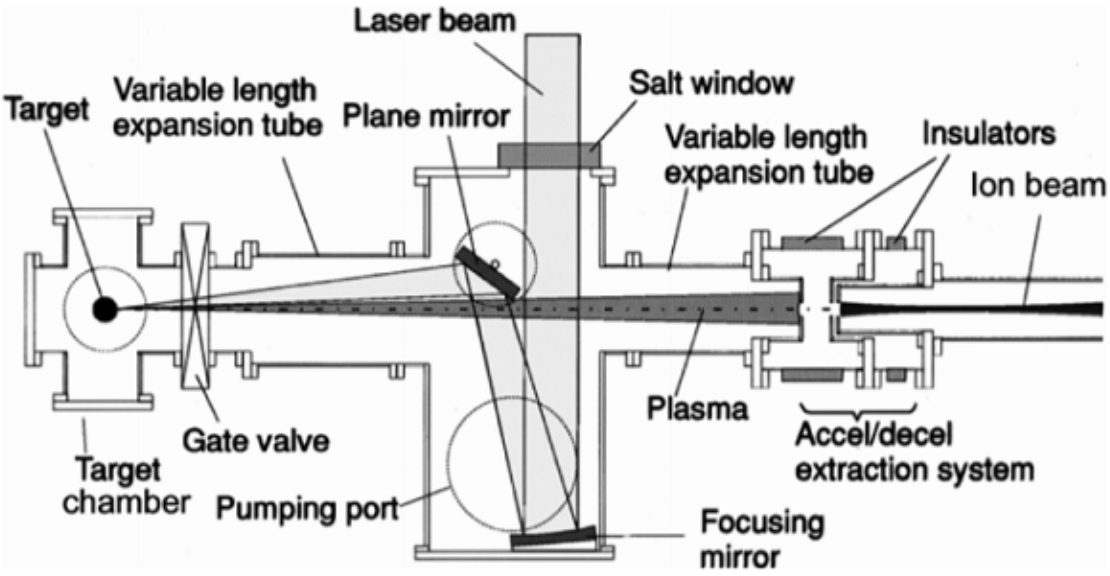

Figure 1.10: Schematic of a laser plasma ion source instrument. (From [41]).

The ions generated in by the laser plasma can then be extracted by a voltage bias and directed towards a series of optics to form an ion beam [50, 51]. A Schematic of a LPIS system is shown in figure 1.10. LPIS systems are used in accelerator facilities where very intense beams of multiply charged (up to 50+) ions of heavy elements may be desirable [51].

1.3.2 Ion Beam Characterisation

Once the ions have been generated at the source, a beam is formed by a series of electrostatic potentials, apertures, and lenses. The ability to form a focused beam is what distinguishes FIBs and ion microprobes from other more diffuse ion sources such as those typically found in particle accelerators or ion implanters which require the use of hard masks in order to direct ions towards specific regions on a sample. The focused beam also allows the formation of an image through the correlated scanning and detection of secondary particles such as ions or electrons. In turn, this also allows the delivery of ions to a specific region on the sample [52].

The characteristics of the beam are defined by several features which dictate the primary use case of the FIB system. This results in a FIB microscope being tailored towards either high resolution, low current operation, or low resolution, high current operation, with the latter being optimum for VLE-PIXE operation due to the requirement for high currents at such low accelerating voltages.

It is important to note that many of the beam characteristics are typically only established for a single ion species operation unlike what is expected during mixed beam operation. Further investigation is required to determine the interaction of multiple species in a FIB and the potential impacts on performance such as resolution.

1.3.2.1 Beam Characteristics

Virtual Source Size:
In an ideal source, the emission point such as the tip of an LMIS Taylor cone or the output aperture of a plasma source would be considered the origin of all particles emitted from the source. In reality however, localised electric fields, the statistical nature of emission, and source instability may result in emission from a region some distance from the idealised point source, and from an area larger than an idealised point source. By tracing back the trajectory of the emitted

particles, a virtual source size can be determined based on the geometric origin of all particles emitted from a source. As shown in figure 1.11, this is typically somewhat different to an idealised source location and size [53, 35, 54].

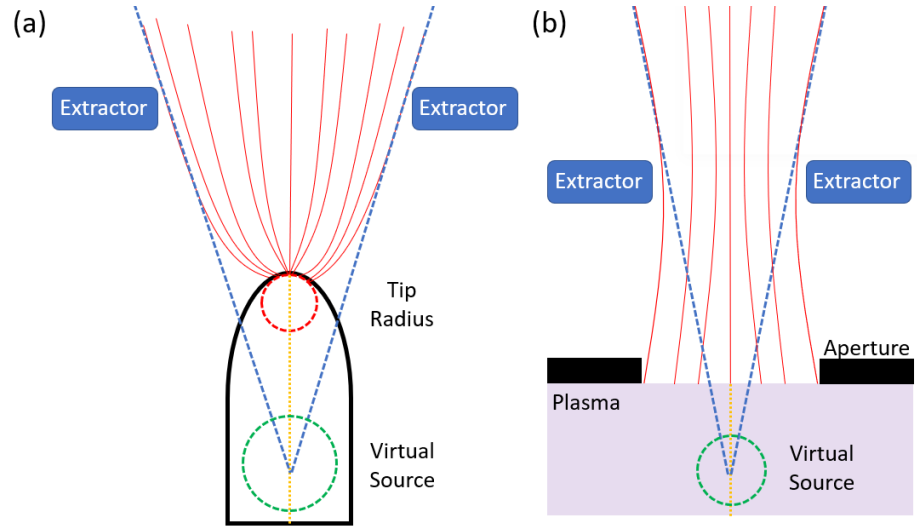

Figure 1.11: Diagram of a virtual source determination for (a) a point source such as an LMIS (b) a plane source such as an ICP plasma source (not to scale).

For point-like sources such as the LMIS and GFIS, Coulombic interactions between particles in the high density region near the tip can cause deviation from their ideal paths, and is known as the Boersch effect, which worsens with increasing extraction current. This results in a loss of resolution at higher currents. [55] This problem is reduced for more diffuse plasma ion sources, thus allowing much better resolution at the higher currents required for VLE-PIXE. [35]

Angular Intensity and Source Brightness:
The angular intensity, (I') of the source is calculated as the number of ions emitted per unit time (I) into a cone shape of solid angle (Ω):

$$I' = I/\Omega \tag{1.1}$$

The brightness (β) of the source is then calculated as the current density (J) emitted into the same cone [56]:

$$\beta = \frac{I}{\pi r^2\ \Omega} = \frac{J}{\Omega} \tag{1.2}$$

where r is the beam semi-angle. This brightness value, is typically measured in A/m^2 sr^1 and represents the amount of current delivered to any axial plane

immediately following the source. This however does not accurately represent the amount of current which can be delivered to the sample as it does not consider the effect of the optical system on brightness [53, 35, 57]. For highly divergent point sources which are susceptible to extreme Boersch effects such as the LMIS and GFIS, a significant amount of the beam is lost at the first aperture and thus the source brightness is not a meaningful value.

It is therefore most relevant to consider the practical current delivered to the image plane which in most cases is the plane of the sample. If we consider the practical current as the sum of the current density over the beam spot on the sample [57]:

$$I_p = \Omega_p \int_{sample} \beta(\vec{r}) d\vec{r} \tag{1.3}$$

where I_p is the practical current Ω_p is the solid angle at the sample plane, V_p is the beam energy at the sample and $\vec{r}$ is the radial position in the plane [57].

Resolution:
Resolution is a measure of the smallest feature size which can differentiated by an imaging system [58]. In the case of a FIB system, this resolution can be approximated by the spot size of the ion beam, due to the limited interaction volume of the beam in the sample [5].

In a FIB system, the beam spot size is determined by a convolution of the Gaussian image of the virtual source with the first order chromatic and third order spherical aberration contributions from the FIB optics. Chromatic aberration is caused by source particles of varying energy passing through a lens. Spherical aberration is caused by the varying field strength of a lens across its radius.

The final beam diameter containing 50% of the beam (d_{50}) can be calculated as [35]:

$$d_{50} = ((d_{C_s}^{1.3} + d_g^{1.3})^{2/1.3} + d_{C_c}^2)^{0.5} \tag{1.4}$$

Where d_{C_s} is the broadening contribution from spherical aberration of the lenses and is calculated as [35]:

$$d_{C_s} = 0.5^{2.5} C_s \alpha_i^3 \tag{1.5}$$

where C_s is the spherical aberration coefficient and α_i is the semi-angle of the beam as it converges onto the sample. d_{C_c} is the broadening contribution from chromatic aberration of the lenses and is calculated as [35]:

$$d_{C_c} = 0.34 C_c \left(\frac{U_{FWHM}}{U_i} \right) \alpha_i \tag{1.6}$$

where C_c is the chromatic aberration coefficient, U_{FWHM} is the FWHM of the beam energy distribution, and U_i is the energy of the beam as it converges on the sample. d_g is the linear magnification or demagnification of the virtual source diameter d_v and is calculated as [35]:

$$d_g = d_v M \tag{1.7}$$

where M is the linear magnification of the optical system as is calculated using the Helmholtz relationship [35]:

$$M = \frac{\alpha_o}{\alpha_i} \sqrt{\frac{U_o}{U_i}} \tag{1.8}$$

where α_o is the semi-angle of the beam divergence from the source and U_o is the energy of the beam at the source [35, 59].

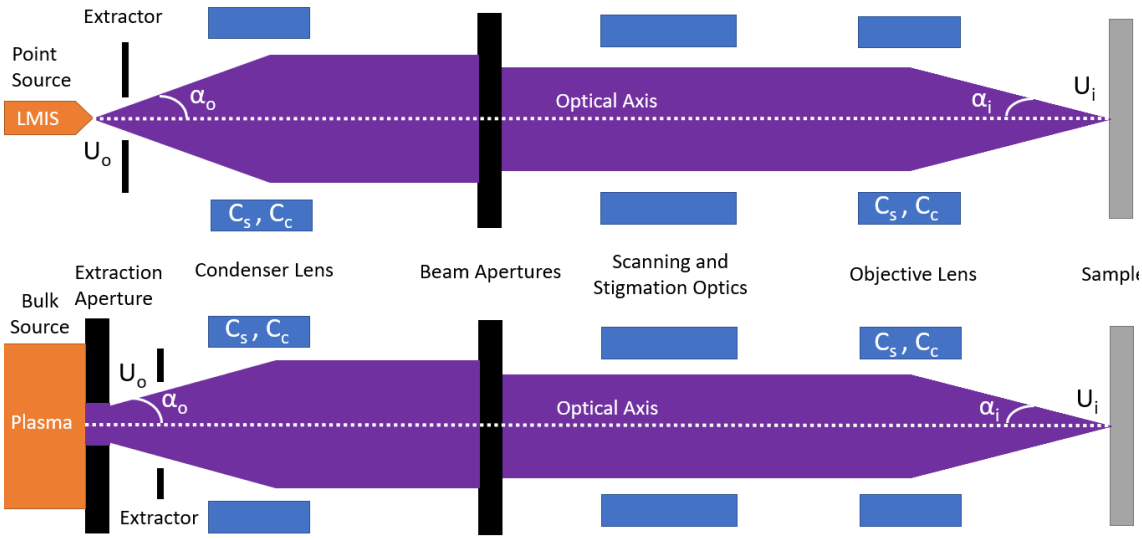

Figure 1.12: Simplified schematic of a FIB optical setup for a point ion source and bulk ion source. The contributions to the spot size equations are labelled.

Figure 1.12 shows a simplified schematic of a FIB optical setup for a point ion source and diffuse ion source, with the contributions to the equations above la-

belled. As the extraction current increases, the divergence semi-angle for planar source increases slowly as shown in figure 1.13 which results in far smaller spot sizes at higher currents for plasma sources compared to point sources [35], a critical factor for the high current operation during VLE-PIXE.

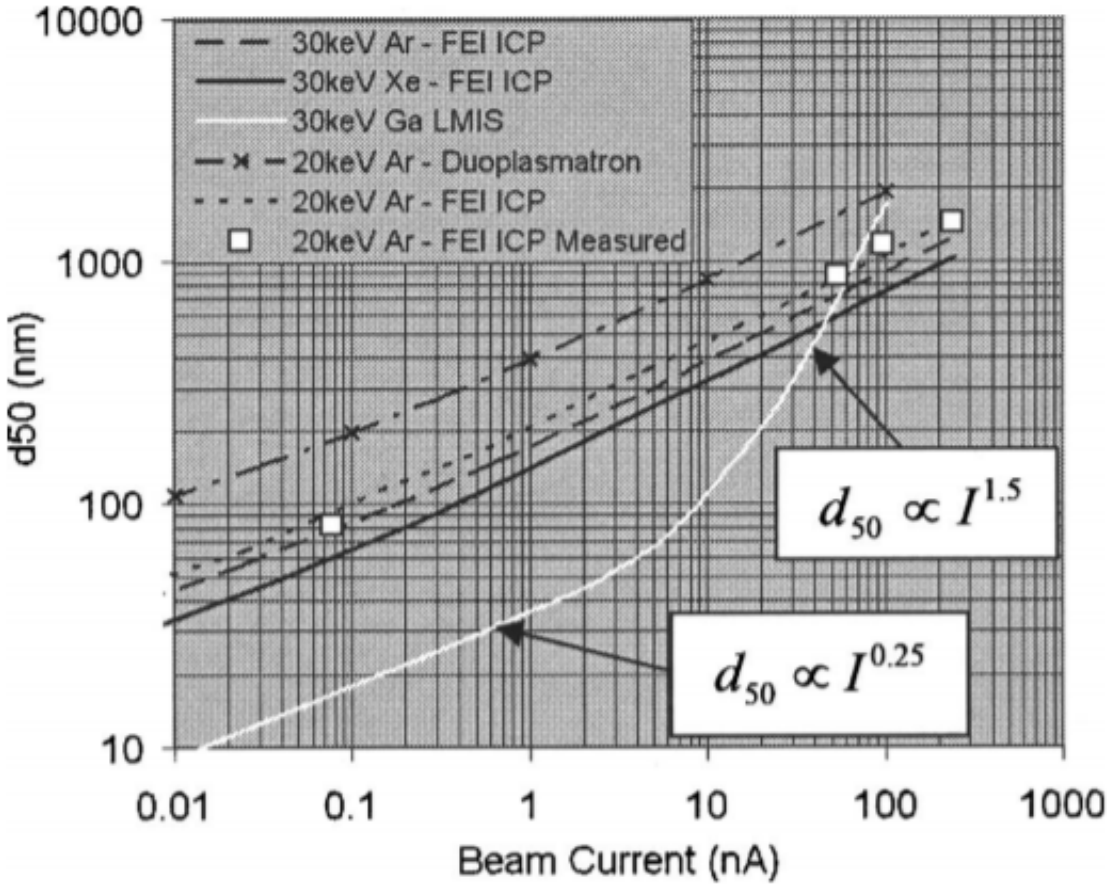

Figure 1.13: Spot size vs. current for a variety of ion sources showing the slower increase in spot for plasma sources compared to point sources. (from [35])

Energy Spread:

As seen in equation 1.6, energy spread of the source is a contributor to chromatic aberration. For a Ga LMIS, values in the range of 5-10eV are shown depending on the emitted current of the source [54, 57, 60]. In the case of a plasma ion source, the energy distribution is a result of differential ion acceleration across the sheath potential surrounding the exit aperture of the plasma source. [61] A measured value of 7eV is given for the ICP source used in the VLE-PIXE experiments. [35]

1.3.2.2 Source Comparison

Table 1.1 shows a selection of measured ion beam source metrics from literature for the most common FIB sources, the LMIS, the GFIS, and the PFIB. The bold species dictates the source used for the listed metrics.

Source Type	LMIS	GFIS	PFIB
Source Species	**Ga**, Al, Au, Alloys [62]	**He**, Ne, Ar, Kr [63]	**Xe**, Ar, O_2, N_2, Ne, H_2 [37]
Virtual Source Size	30-50nm [57]	3Å [64]	7.2 μm [35]
Min. Spot Size	5nm [57]	0.25nm [64]	25nm [35]
Angular Intensity	20 μA/sr [57]	2.5 μA/sr [64]	7.4mA/sr [35]
Source Brightness	2×10^6A/cm^{2}sr [62]	4×10^9A/cm^{2}sr [64]	1×10^4A/cm^{2}sr [35]
Max. Current	20nA [7]	100pA [32]	$>1\mu$A [7]
Energy Spread	4.5eV [57]	2×10^{-5}eV [64]	7eV [35]
Protons	$\times$	✓	✓
Mixed Species	$\times$	$\times$	✓

Table 1.1: Comparison of ion beam metrics for an LMIS, GFIS and PFIB. Bold lettering dictates the source species used for listed metrics

Based on this table, it can be seen that generally instruments which are capable of high resolution are limited in terms of deliverable current and vice versa. For VLE-PIXE, due to the low efficiency of the technique at such low energies, the PFIB is an essential development due to the very high effective current delivery to the sample due to the ICP ion source. The capability of producing protons by utilising a Hydrogen precursor is also an essential development which is required for VLE-PIXE in a FIB microscope and the ability to host multiple source species simultaneously is critical for doped beam VLE-PIXE experiments.

1.3.3 Ion Solid Interactions

When an energetic ion impacts a solid sample, a number of different processes occur as a result of energy transfer from the projectile to the sample through elastic and inelastic scattering interactions. This section will focus primarily on the interactions at energies $\leq$30keV as this is the range typically available in FIB

instruments. This energy range is considered very low compared to the energies at which PIXE are typically performed of $>$1MeV.

1.3.3.1 Nuclear and Electronic Stopping

Perhaps the most fundamental factors which govern how energetic ions interact with an atomic target are; nuclear stopping (S_n) which is the energy lost from the primary ion due to interaction with the target atomic nuclei and electronic stopping (S_e) which is the energy lost to the target electrons [65]. Nuclear stopping governs reactions involving target nuclei such as sputtering, backscattering and recoiling, whereas electronic stopping governs reactions involving electrons such as excitation, and ionisation.

Stopping power is defined as the kinetic energy (E) lost per unit distance (x) in a specific material to either target nuclei or electrons. Total stopping power is the sum of both the nuclear and electronic stopping power:

$$S_{total} = S_n + S_e = \left(\frac{dE}{dx}\right)_{nuclear} + \left(\frac{dE}{dx}\right)_{electronic} \tag{1.9}$$

The nuclear stopping can be calculated as [66]:

$$S_n = \frac{1}{4\pi\epsilon_0}\,\frac{\pi^2 e^2 a_0}{2.7183}\,\rho\,\frac{Z_1 Z_2}{(Z_1^{2/3}+Z_2^{2/3})^{1/2}}\,\frac{m_1}{(m_1+m_2)} \tag{1.10}$$

where m_1, Z_1 and m_2, Z_2 are the masses and atomic numbers of the incident ion and target atom respectively, ρ is the target density in atoms/cm^3, e is the fundamental charge of an electron, ϵ_0 is the permittivity of free space, and a_0 is the hydrogenic Bohr radius.

The electronic stopping can be calculated as:

$$S_e = \frac{1}{4\pi\epsilon_0}\,\frac{8\pi^2 a_0}{v_0}\,\rho\,\xi_e\,\frac{(Z_1 Z_2)v}{(Z_1^{2/3}+Z_2^{2/3})^{3/2}} \tag{1.11}$$

where v is the velocity of the projectile, v_0 is the Bohr velocity and ξ_e is an experimentally derived dimensionless value [67].

The ratio of nuclear to electronic stopping is highly dependent on ion mass. As shown in figure 1.14, for basically all proton energies, electronic stopping dominates over nuclear stopping. For Ga ions however, as the incident ion energy decreases, nuclear stopping dominates over electronic stopping. This may occur as the Ga ion loses energy as it passes through the material. This is why protons are highly efficient at ionisation, especially at lower energies yet have a very low sputter yield, and heavy ions have a much higher sputter yield yet do not efficiently ionise until much higher energies. For this reason, PIXE with heavy ions is typically performed at energies significantly greater than protons to maximise electronic stopping [68, 69, 70].

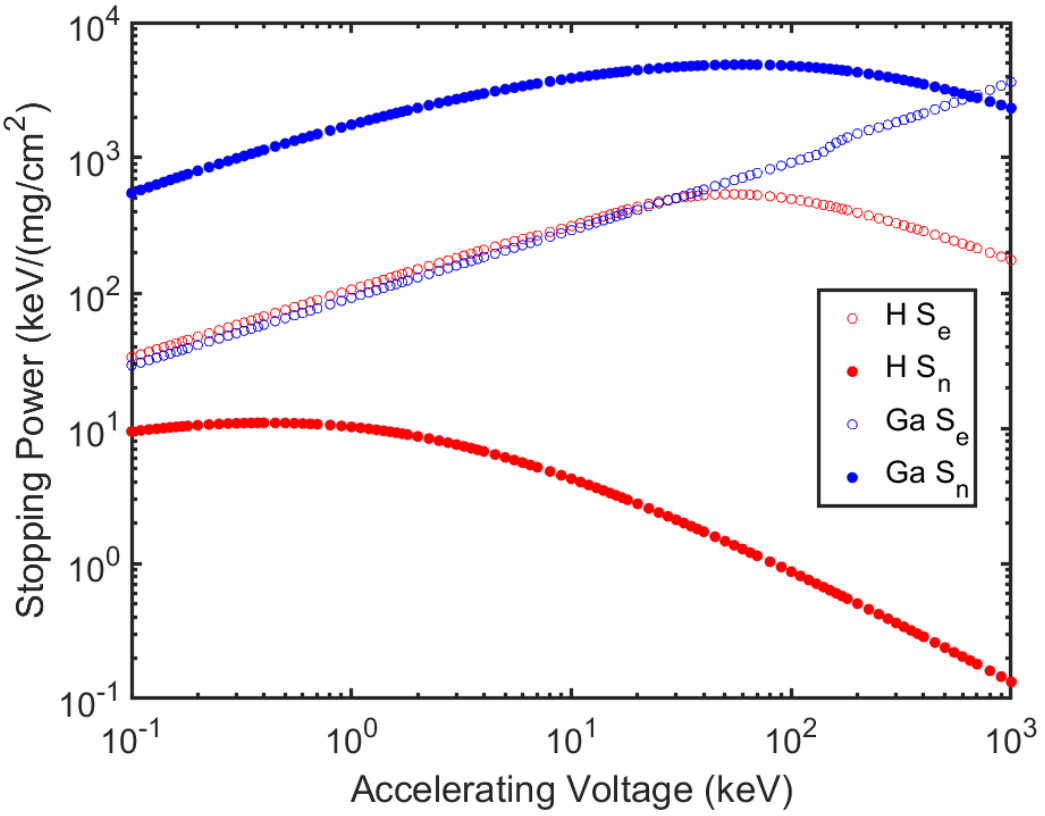

Figure 1.14: Nuclear and Electronic stopping power of protons and Ga ions, calculated using SRIM.

1.3.3.2 Ion Backscattering or Reflection

When a low energy ion approaches a surface, it will initially interact with the ions at or near the surface. If it does not possess enough energy to penetrate the surface, some of the kinetic energy of the incident ion will be transferred to a target atomic nucleus residing on the surface. Following this interaction, there is a probability that it will be reflected or backscattered from the surface with energy

equal to the initial kinetic energy, minus the energy lost through the scattering interaction. The amount of energy transferred from the projectile to the target can be derived from the conservation of momentum during the collision between the incident ion and the atomic nucleus:

$$m_1 v_0^2 = m_1 v_1^2 + m_2 v_2^2 \tag{1.12}$$

where m_1 and m_2 are the ion and target masses respectively, v_0 is the initial ion velocity, v_1 is the ion velocity following the collision, and v_2 is the velocity of the target atom following the collision.

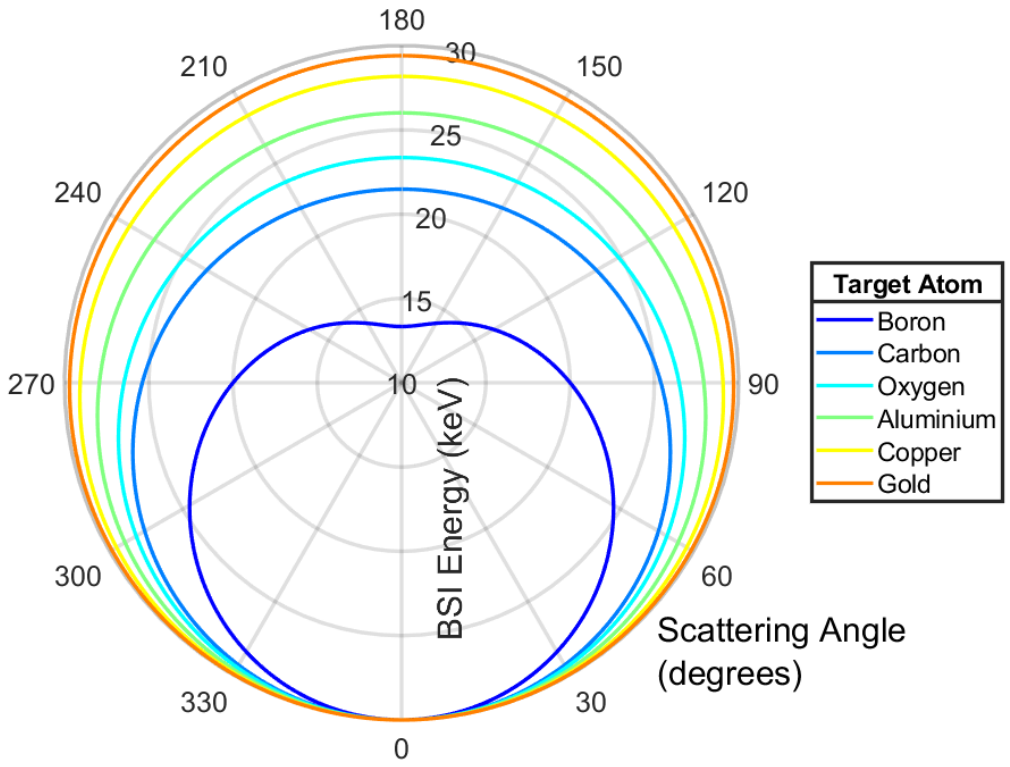

Figure 1.15: Backscattered ion energy vs. angle for a 30keV proton on a range of target masses.

The final kinetic energy of the incident ion (E_1) following the collision, where an ion with initial energy (E_0) is scattered through some angle (θ), the angle with respect to the normal of the surface, is determined by a kinematic factor (k) such that [71]:

$$E_1 = kE_0 = \left[\frac{cos\ \theta + (\mu^2 - sin^2\theta)^{\frac{1}{2}}}{\mu + 1}\right]^2 E_0 \quad for\ \mu \geq 1 \tag{1.13}$$

$$E_1 = kE_0 = \left[\frac{cos\ \theta \pm (\mu^2 - sin^2\theta)^{\frac{1}{2}}}{\mu + 1}\right]^2 E_0 \quad for\ sin\ \theta \leq \mu \leq 1 \tag{1.14}$$

where μ is the mass factor $\mu = m_2/m_1$. When this kinematic factor is calculated for a 30keV incident proton, the energy loss distribution as a function of scattering angle is shown in figure 1.15.

At normal incidence, a scattering angle of 180°, or complete reflection results in the maximum energy transferred to the target atom and equation 1.13 can then be simplified to [71]:

$$E_1 = \frac{(\mu - 1)^2}{(\mu + 1)^2} E_0 \tag{1.15}$$

The cross section for backscattering (σ_R), known as the Rutherford cross section in mb/sr is given as [72]:

$$\sigma_R = 5.18 \times 10^6 \left(\frac{Z_1 Z_2}{E}\right)^2 \frac{[(m_2^2 - m_1^2 \sin^2\theta)^{1/2} + m_2 \cos\theta]^2}{m_2 \sin^4\theta (m_2^2 - m_1^2 \sin^2\theta)^{1/2}} \tag{1.16}$$

1.3.3.3 Ion Sticking

While some proportion of low energy ions colliding with a surface may be reflected, the remainder of collisions result in the trapping of ions on or inside the target surface. The process where ions remain on the target surface is known as ion sticking. In the very low energy range where the thermal equivalent kinetic energy of the ion following collision is below the adsorption energy of a surface, the ions tend to condense on the surface. Figure 1.16 gives a representation of the sticking probability vs. energy for the case where a light ion is incident on a heavy atomic target.

As the ion energy increases such that kT ≈0.025eV at room temperature, the sticking probability begins to decrease and the ions must lose a significant amount of energy through scattering processes before they are able to remain on the surface. In the region between 0.025eV and 100eV, the scattering probability is the highest and sticking probability is the lowest as ions contain sufficient energy to

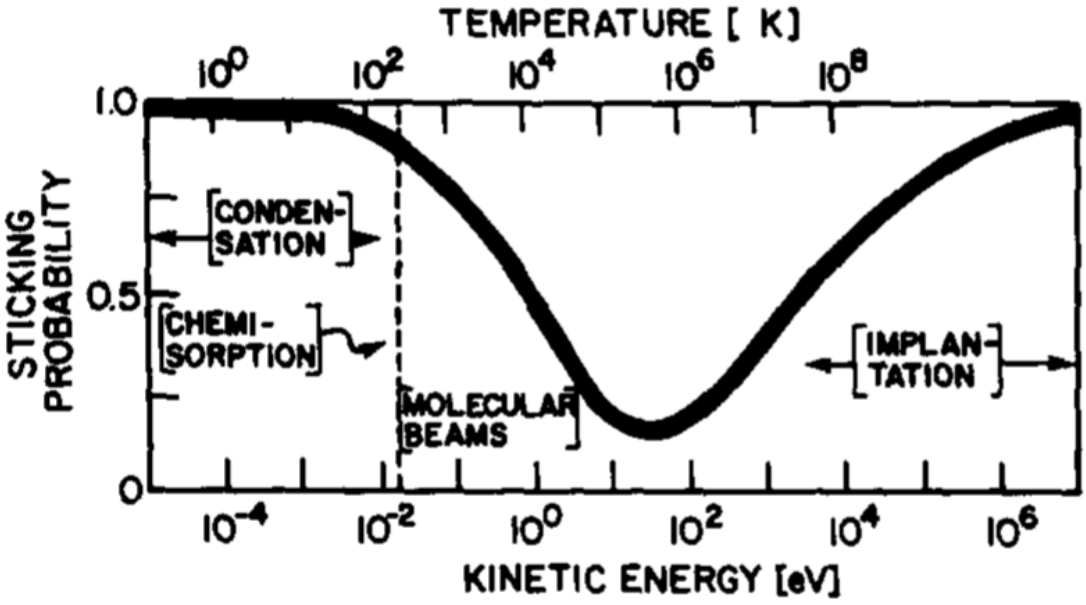

Figure 1.16: Sticking probability vs. ion kinetic energy and the respective thermal temperature. The dashed line represents room temperature, (From [73]).

overcome any surface binding yet do not possess enough energy to be efficiently implanted into the sample [73].

1.3.3.4 Ion Neutralisation

As an ion approaches a sample, there is some probability that it may either gain or lose an electron, or remain ionised as it is scattered away from the surface. The neutralisation or ionisation can proceed by a number of processes as outlined in figure 1.17, and shown schematically in figure 1.18.

These processes are:

- **Resonance neutralisation (RN):** Figure 1.18A describes a process where an electron resonantly tunnels from the the solid into the ion, neutralising the ion due to alignment of hole energy level of the ion and the electron energy level of the solid. If the energy of the remaining hole with respect to the vacuum level (VL) is larger than twice the work function, ϕ, the energy emitted by a de-exciting electron filling the hole can be transferred to another electron, resulting in the emission of this electron. This process is known as Auger electron emission.
- **Resonance Ionisation (RI):** Figure 1.18B describes the opposite process of RN, where an electron can tunnel from an ion close to the surface to

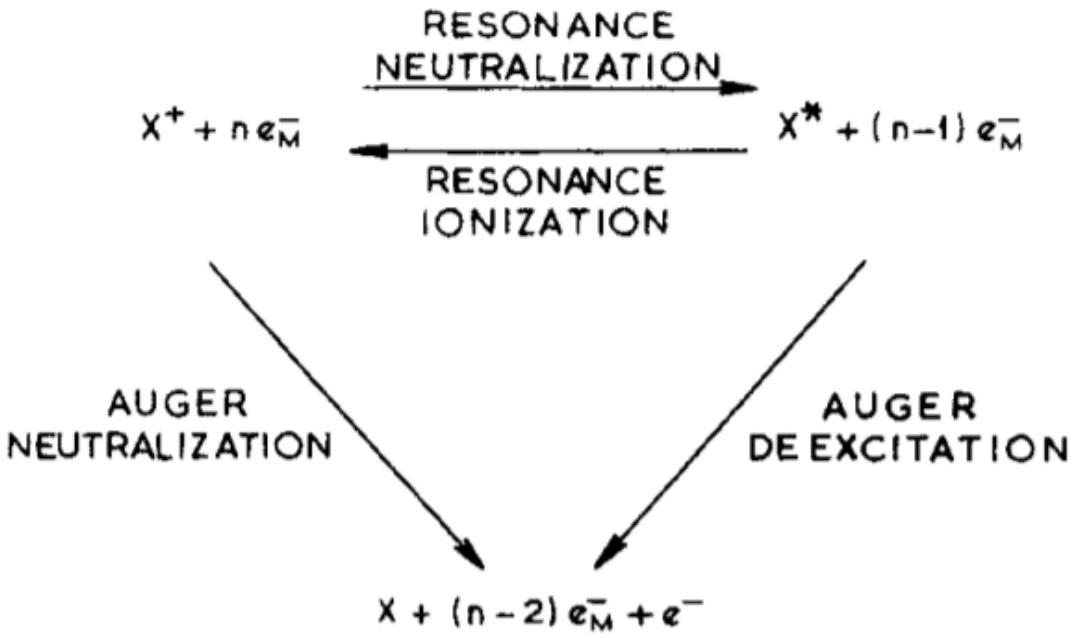

Figure 1.17: Inter-relation of neutralisation and ionisation processes. e_M^- denotes an electron originating from the bulk, e^- denotes a free electron. (From [74])

an unfilled level in the solid if the energy levels of the solid and the ion are aligned.

- **Resonance Neutralisation (Core) (RN):** Figure 1.18D describes third resonance process similar to RN where the electron comes from a core level of the surface atom. The resulting hole in the core level of the surface atom can once again decay by an Auger process resulting in Auger electron emission or the emission of an X-Ray.

- **Auger Neutralisation (AN):** Figure 1.18C indicates a process where an electron from the filled band of the solid tunnels to the ground state of the nearby ion. The energy released during this process can be taken by another valence electron resulting in Auger electron emission.

- **Radiative Electron Capture (REC):** Figure 1.18D indicates a process similar to AN whereby the energy emitted from the electron resonantly tunnelling to the ion is not captured by another valence electron. This results in the emission of a photon. This process however is so slow that AN will be greatly dominant.

- **Auger De-excitation:** Figure 1.18F indicates a process whereby an electron from the surface resonantly tunnels to the hole created by an excited, neutral ion. The resultant release of energy is sufficient to eject an Auger electron from the ion if the excitation energy (E_m) exceeds the work function,

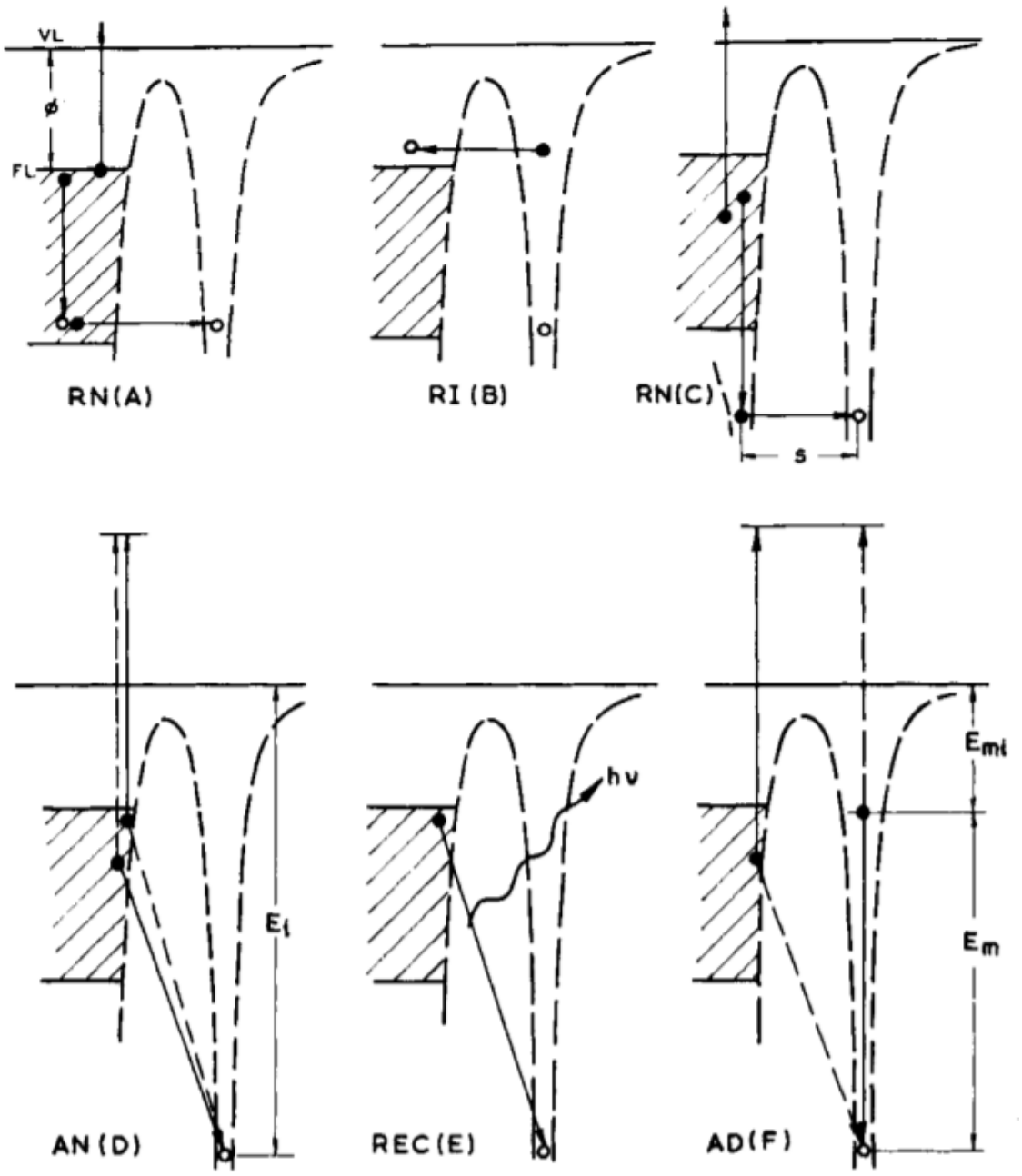

Figure 1.18: Energy diagrams of possible neutralisation or ionisation processes: (a) Resonant Neutralisation (RN), (b) Resonant Ionisation (RI), (c) Core Resonant Neutralisation (RN), (d) Auger Neutralisation (AN), (e) Radiant Electron Capture (REC), and (f) Auger De-excitation (AD). (From [74]).

ϕ of the solid.

1.3.3.5 Ion Implantation

As the energy of the incident ion increases, at some point it will overcome the surface potential of the material and enter the material surface. From here, the

incident ion may then backscatter from a subsurface atom in the same process described in 1.3.3.2 or it may continue into the bulk of the material. As the incident ion continues to lose energy through nuclear and electronic stopping, it will reach a point where its kinetic energy becomes zero and will come to rest within the material, a process known as ion implantation. [75] The final resting place of the ion may be a vacancy created through the displacement of target atoms, known as a substitution, or in between lattice sites, known as an interstitial. Ion implantation has the ability to significantly alter the properties of a target material such as the electronic, [76] optical [77], or chemical properties of the original material [78].

The average distance an ion penetrates into a material before it comes to rest is defined as the ion range and can be determined from the nuclear and electronic stopping powers [79]:

$$R = \frac{1}{N}\int_0^{E_0} \frac{dE}{S_n(E) + E_e(E)} \tag{1.17}$$

where N is the concentration of implanted ions.

When the trajectory of an ion is aligned to a crystal plane, ions can travel along the void between rows of atoms and experience minimal interaction with the atomic potentials, thus reducing the effect of the nuclear and electronic stopping. As such, the ion range can be significantly longer than what is calculated by equation 1.17. This process is known as ion channelling and can either be a hindrance in situations where a precise implantation depth is required [80] or beneficial in situations where this technique can used to determine the crystal orientation of a material, a process known as channelling contrast [81].

1.3.3.6 Target Excitation and Ionisation

During a projectile's transit through a material, some of the kinetic energy from the projectile is lost to the electrons surrounding target atoms, which is governed by the electronic stopping in the material as described in section 1.3.3.1. The energy transferred to the target electrons can be used to excite an electron from a lower energy level into a higher energy level within the target atom or form an exciton within the material. This is known as excitation, where the electron may then de-excite to a lower energy level, resulting in the emission of a photon. This process is known as ionoluminescence and can be used to analyse the electronic structure of the target material [82].

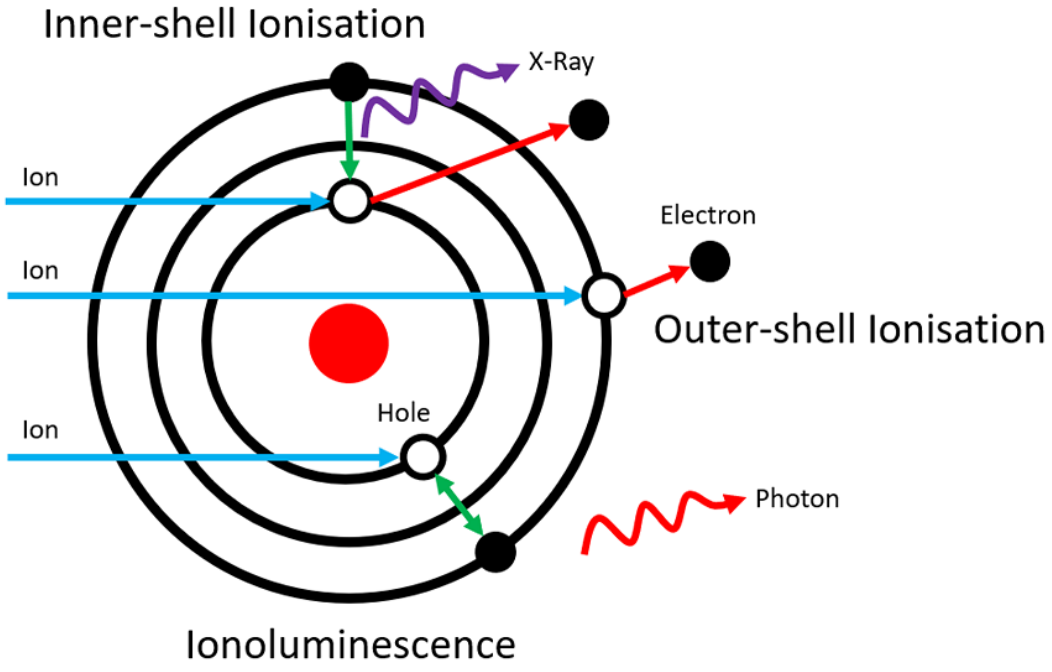

Figure 1.19: Ion-target excitation and ionisation processes.

If the energy transferred is greater than the binding energy of a particular electron in an atomic shell, an electron can be ejected from the atom, a process known as ionisation. The ejected electron is known as a secondary electron (SE). If this electron escapes from the material and is collected by a secondary electron detector (SED), this SE forms the primary signal used for imaging with a FIB [5].

The electron may be ejected either from an outer-shell or an inner shell of the target atom, with the latter requiring significantly more energy due to the increased binding energy of the negative electrons orbiting closer to the positive atomic nucleus. Following an inner-shell ionisation event, an outer-shell electron may de-excite to fill the inner-shell vacancy, ejecting a photon in the process with an energy equal to the difference in energy between the outer and inner shell. This process is known as particle induced X-Ray emission (PIXE) and is discussed in greater detail in section 1.3.4. The ionisation and excitation processes are outlined diagrammatically in figure 1.19.

1.3.3.7 Displacement and Damage

As the incident ion interacts with the target atoms within a material, a proportion of the initial kinetic energy is transferred to the atomic nuclei as dictated by the nuclear stopping power. The maximum kinetic energy transferred in a single scattering event at angle θ can be approximated using a method similar to that described in section 1.3.3.2 [83]:

$$T = \frac{4M_1M_2E}{(M_1 + M_2)^2} \sin^2(\theta/2) \tag{1.18}$$

If the energy transferred to the target atom is greater than the displacement energy of the atom, it may be displaced from its lattice site. These displaced atoms are typically referred to as recoil atoms and can then carry on to act as a primary particle for further collisions, resulting in additional recoil atoms. The result is a cascade of displaced atoms emanating from the point of the initial collision between the primary ion and its first target atom, to the final resting place of the projectile ion and is known as the collision cascade. The collision cascade results in a region of damaged material which can significantly limit the usability of ion beam processing techniques for sensitive optical and electronic applications. These damage layers often require additional processing such as post-annealing or etching which adds additional time and cost [84, 85, 86].

1.3.3.8 Sputtering

The collision cascade can extend along the direction of travel of the ion but also in the reverse direction towards the material surface. At the surface of the material, a collision with a surface atom can result in the ejection of this surface atom if its kinetic energy following the collision is greater than the energy binding it to the surface. This process is known as physical sputtering and results in the gradual removal of material from the surface. This is the primary mechanism responsible for FIB milling, the process of using the FIB to systematically remove matter from a material for the purpose of nanofabrication or sample preparation [5].

The sputter yield of a material (Y) is defined as the number of atoms sputtered, N_S per incident ion, N_I:

$$Y = N_S/N_I \tag{1.19}$$

Due to the very low sputter yield of protons, PIXE is considered a non-destructive analysis technique and is often used to analyse sensitive historical artefacts [87, 88, 89]. When performing LE and VLE-PIXE however, the greater nuclear stopping of ions at lower energies means that target damage is inevitable and must be considered when performing analysis of sensitive materials [21]. This is particularly prevalent when utilising doped beam conditions where the addition of heavy ions results in significant sample damage. This can however be utilised in situations such as simultaneous VLE-PIXE and FIB milling, which can combine

the consecutive steps of sample analysis and layer removal in serial tomography down to one simultaneous process.

1.3.4 Particle Induced X-Ray Emission

As described in section 1.3.3.6, if sufficient energy is transferred from a projectile particle to the electrons of a target atom, an inner shell electron may be ejected. An outer shell electron can then de-excite to fill the hole left by the ejected electron and an X-Ray photon may be emitted with energy equal to the difference in energy between the two levels. As the electronic energy levels in an atom are specific to the atomic species being analysed, the X-Rays are considered to be characteristic and as such, analysis of the emitted X-Ray energies can be used to identify the target atomic species. When this ionisation process is initiated by an incident electron, this technique is usually referred to as energy dispersive spectroscopy (EDS) [90], or wavelength dispersive spectroscopy (WDS) [91] depending on the method used by the spectrometer to analyse the characteristic X-Rays. When the ionisation process is initiated by a heavier particle such as a proton, alpha particle or heavy ion, it is known as particle induced X-Ray emission (PIXE) [92].

1.3.4.1 X-Ray Transition Notation

When discussing the characteristic X-Rays generated in PIXE, the X-Ray peaks are identified in terms of the electronic shell vacancy involved in the transition forming the X-Ray. Figure 1.20 displays the inter-shell transition and the corresponding transition notation. As typical in spectroscopy, the shells are labelled with the spectroscopic shell names K, L, M, N, corresponding to the electronic shell with a principal quantum number of n = 1, 2, 3, 4. The transitions are named such that the letter (eg. K) corresponds to the terminating shell of the electron transition and the following greek letter (eg. α) corresponds to the number of shells the electron has crossed with α being one, β being two etc. The subscript number corresponds to the originating sub-shell of the electron. This notation, known as the Siegbahn notation is most commonly used in literature.

The Siegbahn notation however is confusing and inconsistent and as such, the IUPAC has recommended a new notation method which simply states the final and initial shell and subshell in the transition, for example a Siegbahn Kα_1 would simply be a K-L$_3$ in IUPAC notation [93]. As the Siegbahn notation is predomi-

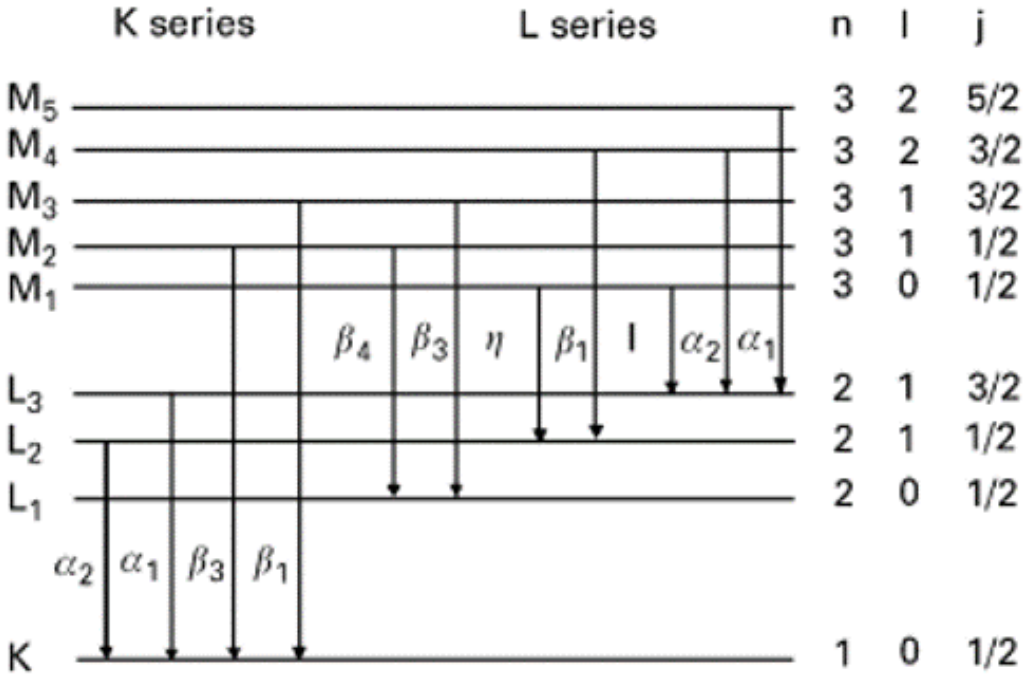

Figure 1.20: Siegbahn notation convention for X-Ray transitions

nantly used in X-Ray literature and analysis software, it will be used throughout this thesis.

1.3.4.2 Ionisation Cross Section

The X-Ray emission process must first be initiated by the ionisation of an inner-shell electron. The ionisation cross section is the probability of removing an electron upon impact, expressed in terms of an area and can be thought of as the size of the target the proton must hit in order to remove an electron. A larger ionisation cross section corresponds to a greater probability of ionisation by an incident particle and is often expressed in units of barns, with one barn equal to $10^{-28}\mathrm{m}^2$, the approximate cross-sectional area of a uranium nucleus. The theoretical description of the ionisation process is incredibly complex, with many developments made over a number of decades to better account for effects at very high, and very low energies, and heavy projectiles.

Outlined in this section is a summary of the current understanding of the ionisation cross sections by ion impact. Understanding the processes influencing these cross sections is crucial for the analysis of VLE-PIXE, particularly as operation under the extreme conditions of VLE-PIXE is at the edge of the current understanding of the ionisation processes. The effect of simultaneous impact of multiple ion species on the ionisation of target atoms is currently unknown and in-

terpretation of the doped beam results defies what is currently understood about the ionisation processes resulting in the emission of X-Rays.

Ion Velocity:

When a charged particle is accelerated through an electrostatic potential, it acquires a kinetic energy (E_k) equal to the charge of the particle (q) multiplied by the potential difference (V):

$$E_k = qV \tag{1.20}$$

and are expressed in units of electron volts (eV) or kilo electron volts (keV). Typical accelerating voltages for a FIB microscope are on the order of 2-30 keV, that is a singly charged particle accelerated through a potential of 2kV - 30kV. For two ions with identical energy however, the velocity of these particles can differ by several orders of magnitude due to the different mass of the particles. The particle velocity (ν) is a crucial factor in the calculation of ionisation cross sections, predominantly due to the fact that the electrons surrounding the atomic nuclei can also be considered to have some velocity as determined by the Bohr model of the atom. The velocity of a particle with kinetic energy can be determined using Newton's equations:

$$E_k = 1/2\ m\nu^2 \tag{1.21}$$

$$\nu = \sqrt{\frac{2E_k}{m}} \tag{1.22}$$

where m is the mass of the particle. Using the relationship from equation 1.20:

$$\nu = \sqrt{\frac{2\ qV}{m}} \tag{1.23}$$

This equation holds for a non-relativistic particle, which is the case for the energies considered in VLE-PIXE, where the relativistic effects are negligible and have no influence on the ionisation behaviour [94].

Momentum Transfer Limits:

In order to ionise an inner-shell electron, the energy and corresponding momen-

tum transferred from the projectile to the target electrons must be considered. For a projectile of atomic number Z_1, mass m_1, and velocity ν_1, colliding with a stationary target atom of atomic number Z_2, and mass m_2, the projectile loses energy:

$$E_i - E_f = (m_1/2)(\nu_i^2 - \nu_f^2) = (1/2m_1)(p_i^2 - p_f^2) \tag{1.24}$$

where E_i, ν_i, and p_i are the initial projectile energy, velocity and momentum respectively and E_f, ν_f, and p_f are the final projectile energy, velocity and momentum respectively. An important consideration is the range of momenta available in this collision process which is utilised in the ionisation process. Using the notation $q = \Delta p$, the minimum momentum change (q_{min}) in this collision is given by [95]:

$$q_{min} \equiv p_i - p_f = 2\ q_0[1 + (1 - \Delta)^{1/2}]^{-1} \tag{1.25}$$

and the maximum momentum change (q_{max}):

$$q_{max} \equiv p_i + p_f = 2\ q_0[1 + (1 + \Delta)^{1/2}]^{-1} \tag{1.26}$$

where $\Delta = (E_i - E_f)/E_i$ and $q_0 = (E_i - E_f)/\nu_1$. These two values, (q_{min} and q_{max}) form the limits over which the ionisation cross section is determined.

Plane Wave Born Approximation:

The predominant theory which is used to describe the process of ionisation is known as the Plane Wave Born Approximation (PWBA), where the initial and final states of the atom can be described in terms of a transition from the electron in an initial bound state to a state described by a continuum wave function. Utilising the PWBA method, the total ionisation cross section for the s shell, (σ_s^{PWBA}) can be expressed as a differential in terms of momentum transferred (q) into a final state (ψ_f). When the momentum transfer limits, outlined in equations 1.25 and 1.26 are considered and the definite integral is taken over these momentum limits, this is known as the the "exact" cross section (σ_i^{ePWBA}) in reference to the exact energy transfer limits. For a generalised transition from i to j, this cross section is given by [96]:

$$d\sigma_{fi}^{ePWBA}(q) = 16\pi z^2(e^2/\hbar\nu_1)^2(dq/q^3) \times \left| \int_{q_{min}}^{q_{max}} \exp(iq\cdot \mathbf{r})\psi_f^*(\mathbf{r})\psi_i(\mathbf{r})d^3r \right|^2 \quad (1.27)$$

where z is the projectile charge, ν_1 is its velocity, q is the momentum transferred from the initial (ψ_i) into final state (ψ_f), and **r** the coordinates of the electron relative to the atomic nucleus. The ionisation cross-section of a specific shell (for example the s shell), is given by a solution to equation 1.27 [96]:

$$\sigma_s = (8\pi z^2\alpha_s^2/Z_s^4\eta_s)f_s(\theta_s, \eta_s) \quad (1.28)$$

where α_S is the Bohr radius of the s shell, and Z_s is the effective charge of the shell. The effective charge is defined as the difference of the nuclear charge (Z) and a screening constant (S) such that: $Z - S = Z_{eff}$ and is induced by the screening of the net nuclear charge by the orbital electrons, leading to a reduction in binding energy [97, 98]. f_s is the result of the integration in equation 1.27 for the s shell and introduces two important dimensionless parameters, the first being the dimensionless binding energy:

$$\theta_s = n^2\frac{U_s}{(Z_2 - S_s)^2\ Ry} \quad (1.29)$$

where n is the quantum number of the s shell, U_s is the binding energy of the s shell, and S_s is the Slater screening parameter where S_s = 0.3 for the s-shell and S_s = 4.15 for the p-shell. Ry is the Rydberg energy = 13.6 eV, the ground state of a hydrogen electron.

The second dimensionless parameter, the ratio between the projectile velocity and the velocity of the s-shell electron is given by:

$$\eta_s = \left(\frac{\nu_1}{(Z_2 - S_s)\nu_0}\right)^2 = \frac{m_e}{M_1}\frac{E_1}{(Z_2 - S_s)^2\ Ry} \quad (1.30)$$

where ν_0 is the Bohr velocity, the velocity of an electron in the ground state of a hydrogen atom, and m_e is the mass of the electron [99].

Based on these two parameters, the PWBA theory starts to break down at very high and very low energies. As such, additional factors must be considered which account for the change in ionisation cross section at these extremes. These factors are particularly important when considering the very low energy range utilised

by VLE-PIXE and the use of heavy ions such as the beam doping method, where the velocity of the projectile is significantly lower than the velocity of the orbital electrons.

Diabatic vs. Adiabatic Interactions:
When a fast, light, structureless ion such as a proton, positron or alpha particle interacts with a solid material, the mechanism by which ionisation occurs is often referred to as Coulomb ionisation. When the orbital electrons of the target atom possess a significantly lower velocity than the projectile ie. where η_s is large, the orbital electrons are incapable of reacting to the presence of the projectile on a time scale relative to the transit of the projectile through the orbitals of the target atom. This is known as a diabatic interaction in that the projectile-electron system is not in a state of equilibrium. The result is a Coulombic interaction between the projectile and the orbital electrons, and a corresponding transfer of energy from the projectile to the target electrons. If the energy transferred is greater than the binding energy of the electron, it may be liberated from the target atom and ionisation will occur [96].

When the velocity of the projectile is much less than that velocity of the orbital electron, ie. when η_s is small, the electrons are now capable of rearranging themselves to counter the Coulombic field of the incoming projectile. This slow interaction is known as an adiabatic interaction in that the system of the projectile and target electrons are considered to be in equilibrium at all times [100]. This significantly decreases the likelihood of ionisation when a light structureless projectile such as a proton interacts with a target atom. This is the primary reason for the rapid decrease in the ionisation cross section of a proton at energy ranges where the projectile velocity is similar to or less than that of the electron orbital velocity [101, 102].

Additionally, the presence of a slowly moving, structureless charged particle in the vicinity of the atomic electron cloud results in a rearrangement of the electronic orbital structure of the target atom. This can lead to modification of the energy levels of the atom and can result in an increase in the binding energy of the electrons [103]. The case of more complex, heavier ions with a number of electronic orbitals will be covered in more detail in a following section. At high energies, relativistic effects must be considered which also alter the probability of ionisation [104].

Relativistic Correction:
The projectile velocity variable ξ is introduced which distinguishes fast (ξ>1) interactions from slow (ξ<1) interactions, those which occur in times comparable to or slower than the orbital period for a particular shell. For the s shell:

$$\xi_s = \frac{2n}{\theta_s}\sqrt{\eta_s} \tag{1.31}$$

where θ_s and η_s are as described in equations 1.29 and 1.30 respectively. As the projectile reaches relativistic velocities, the particle mass begins to increase, which in turn increases the ionisation cross section. The relativistic projectile mass can be calculated using the relativistic mass correction ($m^R(r)$):

$$m_s^R(r) = [1 + (Z_{2s}/2rc^2)^2]^{1/2} + Z_{2s}/2rc^2 \tag{1.32}$$

where r is the distance from the target nucleus and c is the speed of light.

A relativistic correction can also be applied to the projectile velocity variable (ξ_S^R) due to time dilation and length contraction:

$$\xi_s^R = [m_s^R(\xi_s/\zeta_s)]^{1/2}\xi_s \tag{1.33}$$

where ζ is the PSS factor which will be introduced in the next section. Additionally, a relativistic correction can be applied to the dimensionless variable η_s based on the modified mass:

$$\eta_s^R = m_s^R\eta_s \tag{1.34}$$

The relativistic correction (R) to the PWBA total ionisation cross section (σ_s^{PWBAR}) becomes [105]:

$$\sigma_s^{PWBAR} = \sigma_s^{PWBA}([m_s^R(\xi_s)]^{1/2}\xi_s, \theta_s \tag{1.35}$$

Perturbed-Stationary-State Correction:
The perturbed stationary state approximation considers a state where the presence of a moving charged particle in the vicinity of the electron cloud of an atom causes a modification of the electronic energy levels of the atom. This causes a modification of the binding energy of the electrons which results in a decrease

in the probability of ionisation for the case of Coulombic ionisation by light, structureless ions. At high energies, the PSS factor (ζ) for the s shell given as [103]:

$$\zeta_s = 1 + (2Z_1/Z_{2s}\theta_s)[g_S(\xi_s) - h_s(\xi_s)] \tag{1.36}$$

where $g_s(\xi_s)$ accounts for the increase in binding energy with decreasing velocity and $h_s(\xi_s)$ accounts for the decrease in binding energy at intermediate velocities.

The PSS correction to the PWBA cross section becomes [105]:

$$\sigma_s^{PSS} = \sigma_s^{PWBA}(\xi_s/\eta_s, \zeta_s\theta_s) \tag{1.37}$$

Coulomb Deflection Factor:
When the projectile approaches the vicinity of the target nucleus, it encounters a Coloumbic field induced between the positive nucleus of the target atom and the positive nucleus of the projectile which causes it to deflect away from the nucleus. This Coulombic field pushes the projectile away from the target, causing a decrease in incident velocity and effectively reduces the ionisation cross section.

The PWBA theory assumes that the projectile will follow a straight line (sl) trajectory which provides an accurate cross section at higher relative energies. The differential ionisation cross section for this straight path is determined as [102]:

$$(d\sigma_S/d\epsilon_f)^{sl} \tag{1.38}$$

where ϵ_f is the final kinetic energy of the ejected electron. When the deflection in the Coulombic field is considered, the projectile moves in a hyperbolic (hyp) path which produces the differential cross section:

$$(d\sigma_S/d\epsilon_f)^{hyp} \tag{1.39}$$

The Coulomb deflection factor (C) is defined as the ratio of the hyperbolic to straight line differential cross sections and considers the change in cross section caused by the deflection of the particle in the Coulombic field of the nucleus:

$$C = (d\sigma_S/d\epsilon_f)^{hyp}/(d\sigma_S/d\epsilon_f)^{sl} \tag{1.40}$$

The Coulomb deflection factor can be calculated explicitly as:

$$C(\tau dq_{0s}) = \exp(-\pi\tau dq_{0s}) \tag{1.41}$$

where τ is the time variable $\tau = 1 + \epsilon_f/\omega_{2s}$ where ω_{2s} is the electron harmonic oscillator frequency, d is the half-distance of closest approach $d = Z_1 Z_2/M_1\nu_1^2$ and q_{0s} is as described in section 1.3.4.2. For the s shell, in the slow-collision limit (ξ<1) relevant for Coulomb deflection, the Coulomb deflection factor becomes [105]:

$$C(dq_{0s}) = \int_1^\infty \frac{C(\tau dq_{0s})}{\tau^{10+2l_2}} d\tau \tag{1.42}$$

where l_2 = 0 for the K and L_1 subshells and l_2 = 1 for the L_2 and L_3 subshells.

The Coulomb corrected PWBA theory becomes:

$$\sigma_s^{CPWBA} = C_s(dq_{0s})\sigma_s^{PWBA} \tag{1.43}$$

Combined eECPSSR Theory:
When all the factors discussed above are taken into account:

- The exact energy integration limits (e)
- Energy correction (E)
- The effect of deflection and velocity change of the projectile in the Coulomb field (C) of the target nucleus on the ionisation cross section
- The modification of the electron orbitals in the target atom under the influence of the projectile as perturbed stationary states (PSS)
- Relativistic (R) effects [95]

gives the combined eECPSSR theory. The CPSSR corrected PWBA cross section becomes:

$$\sigma_s^{CPSSR} = C_s(dq_{0s}\zeta_s)\sigma_s^{PWBA}(\xi_s^R/\zeta_s, \zeta_s\theta_s) \tag{1.44}$$

The momentum limits given in equations 1.25 and 1.26 must also be modified to

include the factors described above. Smit and Lapicki outlined a reformulation to the limits [99]:

$$q_{min} = \frac{\zeta_s^2 \theta_s^2}{\eta_s^2} \left(1 + \sqrt{1 - \frac{m \zeta_s^2 \theta_s^2}{M \eta_s}} \right)^{-2} \tag{1.45}$$

and

$$q_{max} = \frac{\zeta_s^2 \theta_s^2}{\eta_s^2} \left(1 - \sqrt{1 - \frac{m \zeta_s^2 \theta_s^2}{M \eta_s}} \right)^{-2} \tag{1.46}$$

Applying the exact integral energy correction gives the final eECPSSR cross section:

$$\sigma_s^{eECPSSR} = C_s \left(\frac{dq_{0s} \zeta_s}{Z_2(1 + Z_2)} \right) f_s(Z_2) \sigma_s^{PWBA}(\xi_s^R / \zeta_s, \zeta_s \theta_s) \tag{1.47}$$

Accuracy of the eECPSSR Theory:

A significant amount of work has been performed by Lapicki et al. to determine the experimental accuracy of the eECPSSR theory. For higher impact energies such as those above 1MeV, a large body of experimental data on the X-Ray production cross sections exists, particularly for the K shell transitions. The eECPSSR theory matches very well with experimental data in this energy range and can be used to accurately fit and estimate experimental data to within less than 10% using software such as GUPIX [106] and GeoPIXE [107] which can calculate theoretical cross-sections based on the eECPSSR theory.

For lower impact energies however, the eECPSSR theory can deviate significantly from experimental values. This deviation can be partially attributed to the effect of multiple ionisation by low energy ion impact. The additional vacancies generated in an atom can cause significant changes in the fluorescence yield due to suppression of non-radiative transitions, resulting in over-estimation of the X-Ray production cross sections [108, 109, 110]. These non-radiative transitions will be discussed in the next section.

Another cause of deviation at very low energies is attributed to the shift in the electronic energy levels of the target atom due to the presence of the projectile. This is an extension of the PSS theory to account for the very slow adiabatic interactions where the electronic structure of the target atom has sufficient time to respond and reshape to the presence of the projectile as previously discussed.

This creates a situation where the ionisation cross section is different when the target and the projectile are close together, known as the united atom limit, as compared to when they are far apart, which known as the separated atom limit. The original PSS theory as outlined in section 1.3.4.2 was defined for the separated atom and does not account for the change in binding energy at very low velocities. This led to the development of the usPSS theory where the (us) corresponds to the united/separated atom treatment which compensates for the very low velocity limit.

At very low velocities, where $h_s(\xi_s) = 0$ and $g_s(\xi_s) \to 1$, the PSS factor is referred to as the united atom (UA) PSS correction [111]:

$$\zeta_s^{UA} = 1 + (2Z_1/Z_{2s})^2 \theta_s^{UA}/\theta_s \tag{1.48}$$

which replaces the original PSS factor (ζ_s) when $\zeta_s^{UA} < \zeta_s$.

The initial PWBA calculations such as those discussed above are typically performed using non-relativistic, hydrogenic wavefunctions, a simple model for the calculation of the transition of an electron from a bound to free state which assume a hydrogen-like system consisting of a single electron orbiting a positive nucleus. This model does not accurately describe multi-shell systems which are susceptible to screening by outer electrons. For this reason, the more realistic relativistic Hartree-Slater (hs) wavefunctions are often used at low velocities where the disparity between the hydrogenic and hs wave functions is shown to be significant [112].

The relativistic Hartree-Slater (hsR) correction to the eECPSS cross section model for the K shell can be calculated as [108]:

$$\sigma_s^{eECPSShsR} = hsR[\xi/\zeta_s,\ z]\sigma_s^{eECPSS} \tag{1.49}$$

where $z = Z_2/137$ and

$$\begin{aligned} hsR[\xi, z] = \exp[&0.1624 - 1.873z + 4.642z_2 - 2.256z^3 \\ &+1.480z^4/\xi - (0.2316 - 2.288z + 5.526z^2 \\ &-5.829z^3 + 2.670z^4)/\xi^2 + (0.05952 - 0.5809z \\ &+1.540z^2 - 1.745z^3 + 0.7644z^4)/\xi^3 \\ &-(0.003702 - 0.03698z + 0.1015z^2 - 0.1157z^3 \\ &+0.0490z^4)/\xi^4] \end{aligned}$$

Lapicki states that both the us and hsR factor can result in an enhancement of K-shell ionization cross sections by as much as 60% for light elements, although he does not state what he considers to be a light element, deeming Neodymium (Z=60) to be a "relatively light target." He also states that these factors are only significant in the low velocity regime that is below the typical PIXE range of ξ $<$0.2, however considering that ξ = 0.2 corresponds to an accelerating voltage of $\sim$140keV, this becomes highly significant for the energy range utilised in VLE-PIXE of $<$30keV [108]. Altogether, the theoretical total ionisation cross section can be calculated using the eECusPSShsR model:

$$\sigma_s^{eECusPSShsR} = hsR[\xi/\zeta_s^{UA}, Z_2/137]\ C_s\left(\frac{dq_{0s}\zeta_s^{UA}}{z_s(1+z_s)}\right)... \\ f_s(z_s)\ \sigma_s^{PWBA}(\xi_s^R/\zeta_s^{UA}, \zeta_s^{UA}\theta_s) \tag{1.50}$$

It is also important to note that the eECPSSR cross sections are only valid for the impact of protons on a target. Attempts have been made to apply the eECPSSR treatment to heavier projectile ions, however the results are often inaccurate and inconsistent, and do not provide an accurate description of ionisation under these conditions. Unlike protons, no unified theory currently exists to accurately describe ionisation by the impact of heavy ions upon a sample [113, 114, 115, 116].

1.3.4.3 X-Ray Production Cross Section

To determine the X-Ray Production Cross Section (XRPCS), the fate of all vacancies in a target atom must be considered. These vacancies may result in the emission of an X-Ray (radiative transitions), or de-excitation through a pathway which does not result in an X-Ray being emitted (non-radiative transitions).

X-Ray Fluorescence Yield:
The X-Ray fluorescence yield for a specific shell (ω_i) accounts for the radiative transitions and is defined as the number of X-Rays generated per vacancy [117]:

$$\omega_i = \frac{I_i}{N_i} \tag{1.51}$$

where I_i is the average number of characteristic X-Rays emitted as a result of N_i vacancies created in the i^{th} shell or subshell of an element. Fluorescence yields for the K, L and M shells as a function of target Z can be approximated by:

$$\omega_i = \sum_{n=0} a_n Z_n \tag{1.52}$$

where a_n are the fitting coefficients given by Hubbell et. al. in table 7 of [117].

Non-Radiative Transitions:
Non-radiative transitions arise when the energy of an electron de-exciting into an inner-shell vacancy is instead dissipated through a pathway which does not result in an X-Ray being emitted. The primary non-radiative transition is known as the Auger process, where the energy is transferred to a neighbouring electron. If the energy transferred exceeds the binding energy of the electron, it can then be emitted from the target atom as an Auger electron if the recipient electron is located in the same shell as the donor electron. If the energy is transferred to an electron in a higher shell, this is known as a Coster-Kronig (C-K) transition. In the case where an intra-shell Auger transition results in the ejection of an electron from the same shell as the primary vacancy, a double vacancy can be formed in the same shell and is known as a super Coster-Kronig transition. These transitions are shown diagrammatically in figure 1.21.

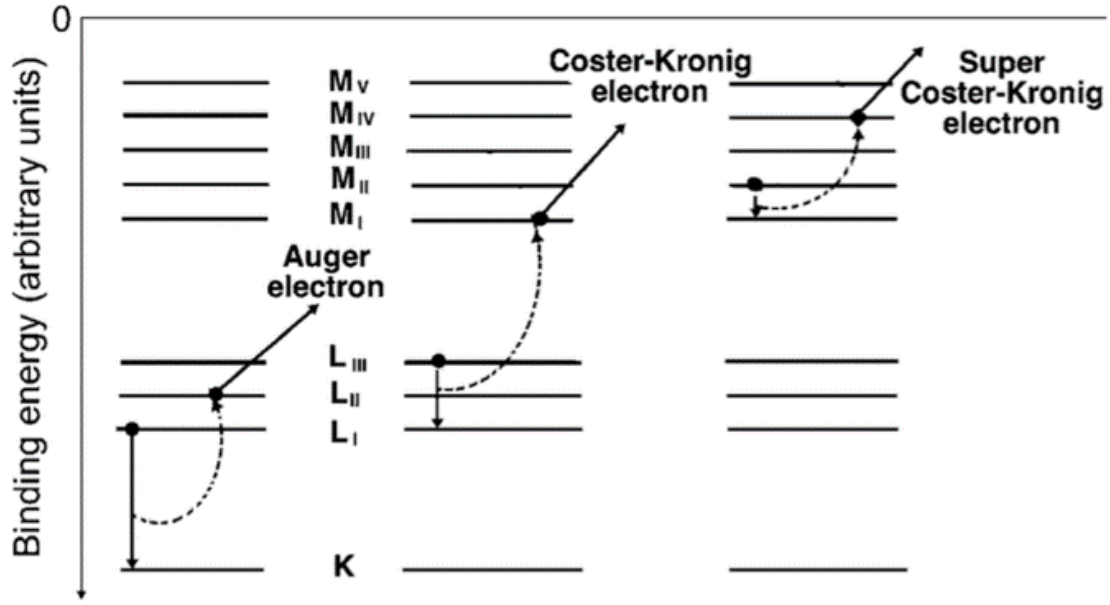

Figure 1.21: Auger, Coster-Kronig and Super Coster-Kronig transitions

It was considered that these Auger processes are carried out by first the emission of an X-Ray, followed by the absorption of the same X-Ray by an outer shell electron, however it has been shown that there is no intermediate step and that the energy is transferred from the de-exciting electron to the Auger electron instantaneously via a virtual photon [118, 117].

X-Ray Production Cross Section:
Based on the radiative and non-radiative yields, the fate of all vacancies can be accounted for by satisfying the following relationship:

$$\omega_i + a_i + \sum_{j=i+1}^{k} f_{ij} = 1 \tag{1.53}$$

where ω_i is the X-Ray fluorescence yield, a_i is the Auger yield and f_{ij} is the sum of all Coster-Kronig yields from i to j. These yields are typically derived experimentally and are considered to be fixed for a particular atomic system.

The X-Ray production cross section (σ_x) for a specific shell of an element can then by found by multiplying the total ionisation cross section by the X-Ray fluorescence yield (ω_i) [96]:

$$\sigma_x = \omega_i \, \sigma_i \tag{1.54}$$

Experimental Determination of X-Ray Production Cross Section:
An empirical formula is used to convert the intensity of X-Ray peaks under known beam and detector conditions to an X-Ray production cross section. This formula assumes a material of infinite thickness and as such, accounts for the so called matrix effects such as the energy loss of the primary ion due to the stopping power of protons in the material and self-absorption of X-Rays by the material as they escape to the surface [119]:

$$\sigma_x(E, E_X) = \frac{4\pi}{N_p \, A \, \Omega \, T_w(E_X) \, \eta(E_X)} \left[\left(\frac{dY}{dE} \right) \left(\frac{dE}{dx} \right) + \mu(E_X) Y \frac{cos\varphi_1}{cos\varphi_2} \right] \tag{1.55}$$

E_X is the energy of the X-Ray, 4π considers the isotropic emission of X-Rays into a spherical section, of which, some portion is collected by Ω, the solid angle of the detector, where φ_1 and φ_2 are the angles of the incident beam and detector respectively.

Once the X-Rays reach the detector, the detector window transmission coefficient T_w will attenuate some of the signal and η accounts for any losses due to the efficiency of the detector, both of which are functions of X-Ray energy. Y is the radiation intensity as observed in the final X-Ray spectrum. The cross sections are normalised to the total number of protons incident on the sample, N_p. A is

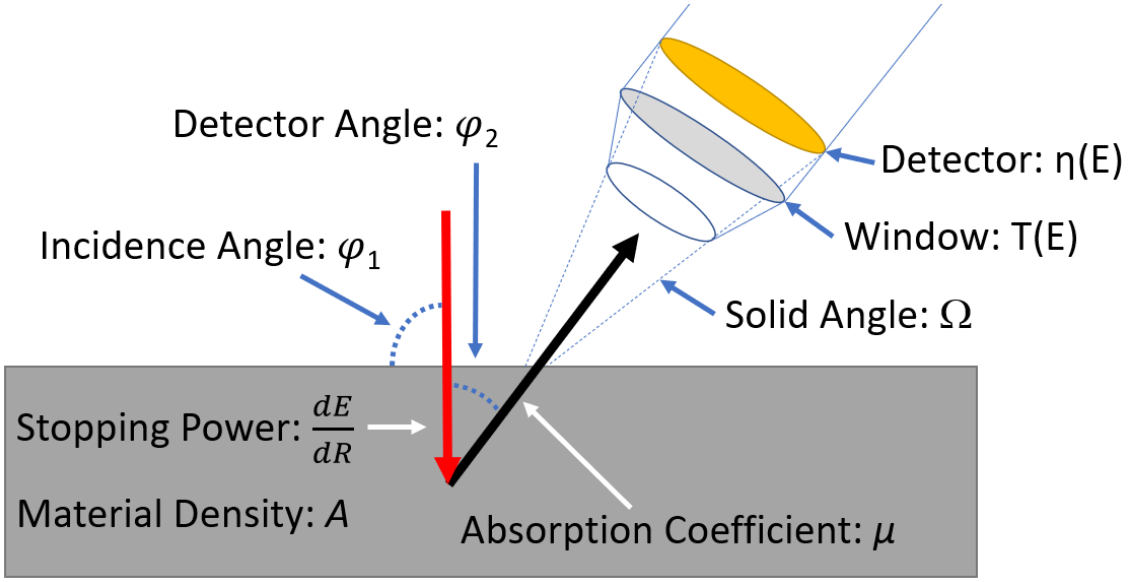

Figure 1.22: Factors contributing to the experimental X-Ray cross section calculation

the material number density, and $\left(\frac{dE}{dx}\right)$ is the total stopping power of the material, which accounts for the loss of energy of the projectile on its way to the collision site. μ is the mean X-Ray absorption coefficient of the target material for a specific transition which accounts for the attenuation of the X-Ray signal on its way out of the material. $\left(\frac{dY}{dE}\right)$ accounts for the variation in intensity with respect to energy and can be calculated by fitting slope of X-Ray peak intensity vs energy. The factors contributing to the calculation of the XRPCS are shown diagrammatically in figure 1.22. From this experimental calculation of the XRPCS, the ionisation cross section can also be calculated using equation 1.54 and tabulated values of the fluorescence yield from Hubbell et al [117].

An important consideration for the use of this technique is that it can only be considered for a single ion species at a time. This is due to the differing stopping power of various ion species resulting in a reducing penetration range with increasing ion mass. Difficulty therefore arises when considering the XRPCS of doped beams such as those utilised throughout this thesis as the method for combining the XRPCS of multiple species is as yet unknown. Therefore it is impossible to separate the XRPCS contributions from the proton and dopant ion species. The XRPCS for protons are therefore used throughout this thesis as a reference only due to the overwhelming amount of literature data for these measurements, compared to the relatively sparse XRPCS data for heavier ion species and the fact that the proton XRPCS represent the most conservative estimate for the XRPCS, with heavier ion species resulting in an increased XRPCS due to reduced ion range and therefore lower X-Ray mass absorption in the material.

1.3.4.4 Analytical Cross Sections

Analytical fits to ionisation cross sections offer a simple approximation which can be used to rapidly determine concentrations of elements in a sample. Analytical fits offer a far simpler method than calculation of the full eECPSSR cross sections for each individual element. Such analytical cross sections are often used in PIXE analysis software where near real-time analysis of data is required [107].

K Shell Analytical Cross Sections:

Based on some 117 references, Paul [120] developed an analytical fit to the experimental K shell X-Ray production cross sections for elements from 4$\leq$ Z_2 $\leq$ 92. This analytical fit can be used as an approximation for the cross sections by:

$$\sigma_x = s_c \times 10^f / Z_2^{2.2} \tag{1.56}$$

To calculate s_c, η is established which is the velocity ratio between the projectile and the velocity of the K-shell electron and is described in equation 1.30, then θ the dimensionless binding energy as described in equation 1.29, and the scaled velocity, ξ as described in equation 1.31.

s_c can then be determined using:

$$\begin{aligned} s_c &= -2.17171 - 10.8883y - 9.45875y^2 \\ &(-0.86 \leq y \leq -0.582) \\ s_c &= 0.975316 - 0.0165458\ cos[13.6(y + 0.393)] \\ &(-0.582 \leq y \leq -0.037) \\ s_c &= 1.00859 + 0.0474606\ cos[6.23(y - 0.33)] \\ &(-0.037 \leq y \leq 0.83), \end{aligned}$$

where y = $\log_{10} \xi$. f can then be calculated from:

$$f = b_1 + b_2(e - b_3)^2 + b_4 P_3(x) + b_5 P_4(x) + b_6 P_5(x) + b_7 P_6(x) \tag{1.57}$$

where $P_3 - P_6$ are the Legendre polynomials as a function of $x = e/1.15 + 2.22$ where $e = \log_{10}(E_1/Z_2^2)$.

For i = 1-3:

$$b_i = (c_1 + c_2 Z_2 + c_3 Z_2^2 + c_4 Z_2^3)/(1 + c_5 Z_2 + c_6 Z_2^2) \tag{1.58}$$

For i = 4 and 5:

$$b_i = c_1 + c_2 Z_2 + c_3 Z_2^2 + c_4 Z_2^3 + c_5 Z_2^4 \tag{1.59}$$

For i = 6 and 7:

$$b_i = c_1 + c_2 Z_2 + c_3 Z_2^2 + c_4 Z_2^3 \tag{1.60}$$

where c_x is given by the coefficients in table 3 of Paul [120]. The error for this analytical fit is as low as 2.5% for Z_2 21-30, increasing to 10% for Z_2 31-90 and as high as 21% for Z_2 11-20.

L Shell Analytical Cross Sections:
Sow et al. determined an analytical fit to the $L1$, $L2$, and $L3$ subshell ionisation cross sections as determined by a fifth degree polynomial fit [121]:

$$\ln(\sigma_{Li} U_i^2) = A_0 + A_1 x + A_2 x^2 + A_3 x^3 + A_4 x^4 + A_5 x^5 \tag{1.61}$$

where σ_{Li} is the Li subshell ionisation cross section in barn, U_i is the Li subshell electron binding energy in keV, and $x = \ln(E/\lambda U_i)$, where E is the proton energy and λ = 1836.109, is the ratio of the proton mass to the electron mass. The coefficients A_{0-5} are given in table 1 of [121] and are separated by Z_2 range, given from Z_2 = 14-92. The uncertainty of this analytical fit is within a few percent.

M Shell Analytical Cross Sections:
Pajek et al. determined an analytical fit to the most intense M shell X-Ray transitions as observed in PIXE, the $M\alpha\beta(M_{4,5}N_{6,7})$, $M\gamma(M_3N_{4,5})$, and $M_3O_{4,5}$ transitions, for select elements from Ta to Th [122]:

$$\ln \sigma_{Mx} = \sum k = 5 a_k (\ln \xi_M)^k \tag{1.62}$$

where a_{1-5} are fitting coefficients given in table 1 of [122], and ξ is the scaled velocity as discussed previously. The accuracy of this analytical fit is determined to be within 5% for proton energies 0.1-4.0 MeV.

1.3.4.5 Slow, Heavy Ion PIXE

As discussed previously, PIXE is typically performed with very light ions such as protons due to their high velocity and therefore high XRPCS. PIXE however is

not restricted to protons and can also be performed using heavier ions. Heavier ions have been shown to possess a greater ionisation cross section than protons for a similar velocity [116, 115]. Due to their increased mass however, in order to match the proton velocity, a much higher accelerating voltage must be used [123]. When the accelerating voltages available to the VLE-PIXE technique are applied to heavy ions, these ions are travelling extremely slowly relative to a proton at a similar energy. Velocities can differ by over an order of magnitude depending on the ion mass.

Several studies outlined in the literature have demonstrated that the interaction of slow, heavy ions with a solid can produce ionisation cross sections on the order of 10^3-10^5 times greater than what is expected by Coulomb ionisation by protons at the same energy, despite the much greater velocity of the protons [124, 101, 100, 96, 125]. This is counter intuitive given the extremely low velocity ratio between the projectile and the target electrons as discussed in section 1.3.4.2. The key to this phenomenon lies in the adiabatic approach of a heavy ion towards a target atom.

As described in sections 1.3.4.2 and 1.3.4.2, the rearrangement of the target electrons in the presence of the electrostatic field of the projectile can result in a shift in the electronic energy levels of both the target and the projectile. This is a condition which is typically experienced during the formation of molecules from two or more separated atoms, and can be described using Molecular Orbital (MO) theory. An understanding of molecular orbital theory is a crucial part of many of the results in this thesis and as such a brief introduction to molecular orbital theory is given

Molecular Orbital Theory:
In molecular orbital theory, the electrons surrounding an isolated atom are arranged into atomic orbitals based on their principal quantum number n = 1, 2, 3... and their angular momentum quantum number l = 0, 1, 2, 3... which for clarity is usually labelled s, p, d, f... Each atomic orbital is capable of hosting up to 2 electrons which are allowed to occupy the same orbital because of their difference in spin states, with one one spin up and one spin down.

These atomic orbitals can be described by a corresponding quantum wave function. The linear combination of the wave functions of the two electrons in each orbital results in the atomic orbital structures shown in figure 1.23 on the left, starting with two electrons occupying the oxygen 2s or lowest energy atomic orbital, then two electrons occupying the oxygen 2p atomic orbitals oriented in the

x, y and z directions respectively ($2p_x$, $2p_y$, $2p_z$).

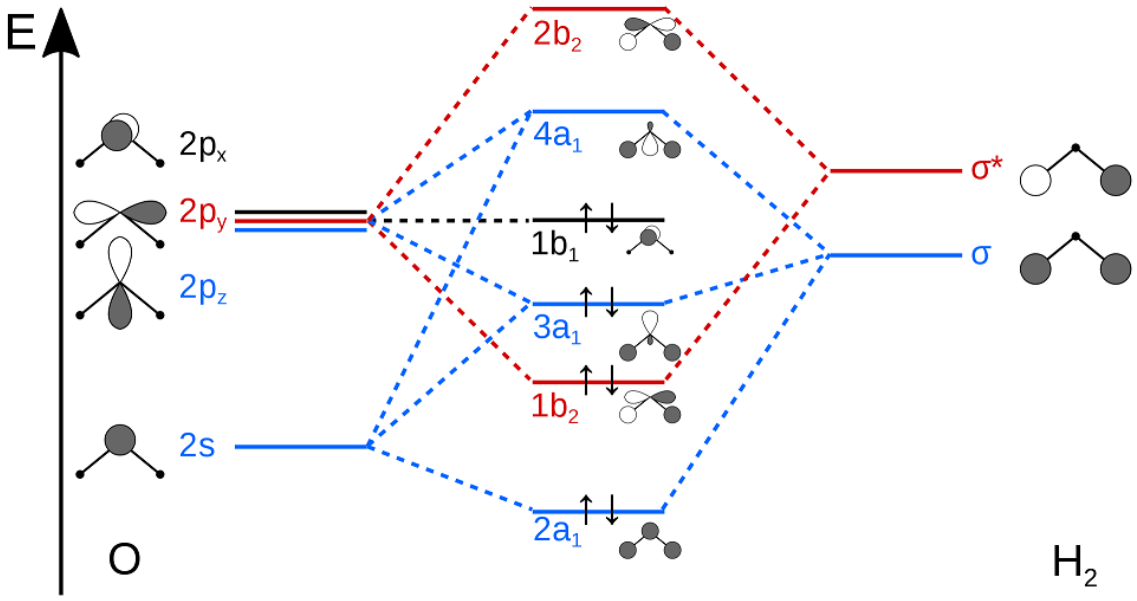

Figure 1.23: Molecular orbital diagram of water. (From [126])

As a result of this linear combination, these orbitals have associated with them a phase which is represented in this diagram as the shaded lobes of the orbitals. Similarly for the H atoms on the right, each H atom has an occupied 1s atomic orbital and is shaded due to the possible phase combinations.

When two or more atoms are brought together, the atomic orbitals of the corresponding atoms overlap and combine to form molecular orbitals. Due to the combined phase of the orbital wave functions, the molecular orbitals can either combine in phase or out of phase, with the in-phase combination being more energetically favourable or lower energy than the out of phase combination. The change in energy between the atomic and molecular orbitals is represented by the dashed lines. The in-phase combination is known as a bonding orbital and serves to stabilise the molecule, whereas the out of phase combination is known as an non-bonding or anti-bonding orbital and serves to destabilise the molecule.

The resultant molecular orbitals are a combination of all wave functions of all atoms involved, which form the electronic structure of the combined molecule. End-to-end combinations of atomic orbitals result in σ molecular orbitals and side-by-side combinations of atomic orbitals result in π molecular orbitals. The antibonding combinations of these two atomic orbitals are known as σ^* and π^* molecular orbitals. This is demonstrated diagrammatically in figure 1.24. δ and δ^* molecular orbitals are the combination of all 4 lobes of a d orbital.

Electrons will fill the molecular orbitals from the lowest energy orbital to the high-

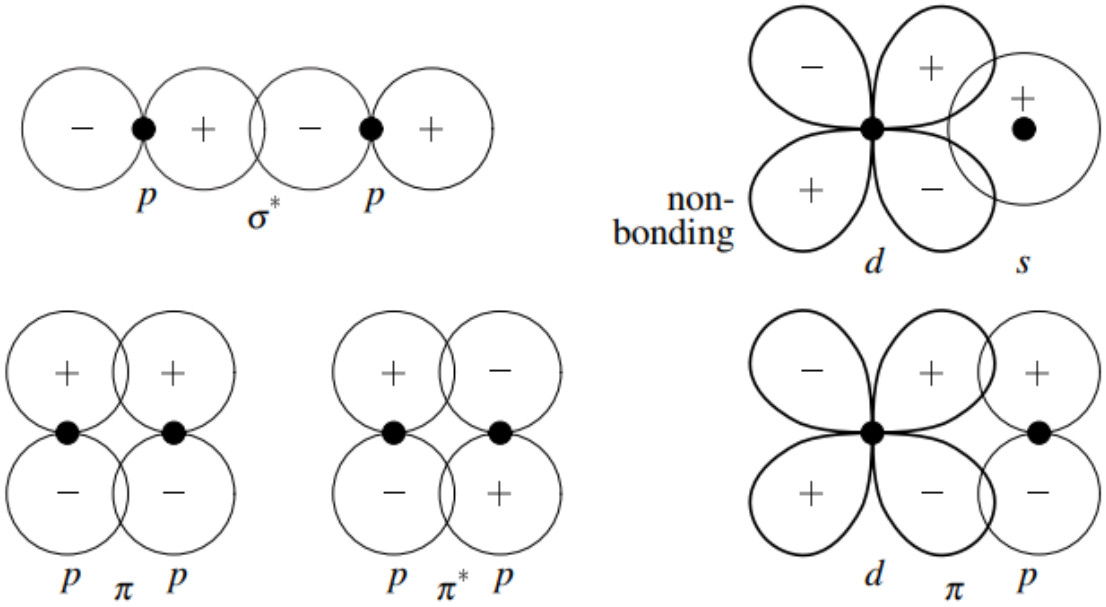

Figure 1.24: Combination of in-phase and out of phase atomic orbitals to form bonding and anti-bonding molecular orbitals. (From [127])

est energy orbital, spreading across degenerate orbitals before pairing (for example, one electron will be placed in each $2p_x$, $2p_y$, $2p_z$ before pairing) until all electrons have been placed. This is known as Hund's rule. If there are an equal number of electrons in a bonding and anti-bonding orbitals, the molecule will be unstable and the atoms will repel. This is known as the bond order of the molecule and is defined as:

$$\text{bond order} = \frac{\text{bonding electrons} - \text{anti-bonding electrons}}{2} \tag{1.63}$$

This is the reason why noble gases are incapable of forming diatomic molecules as their combination will result in an equal number of electrons in bonding and anti-bonding orbitals and an unstable molecule [127].

Of most interest to the VLE-PIXE measurements is the change in electronic energy levels as atomic orbitals transition into molecular orbitals. This results in a change in binding energies of the electrons in the target and the projectile atoms which is particularly relevant for the purpose of X-Ray emission.

Quasi-molecular Model:

Due to the high kinetic energy of the projectile, the bonding condition between the projectile and the target is only short-lived and the close, adiabatic approach of the projectile to the target results in the formation of a temporary "quasi-molecule"

between the target and the projectile. As with the molecular orbital theory discussed above, the formation of a quasi-molecule results in a rearrangement of the corresponding atomic orbitals to form a unique energy level structure [100].

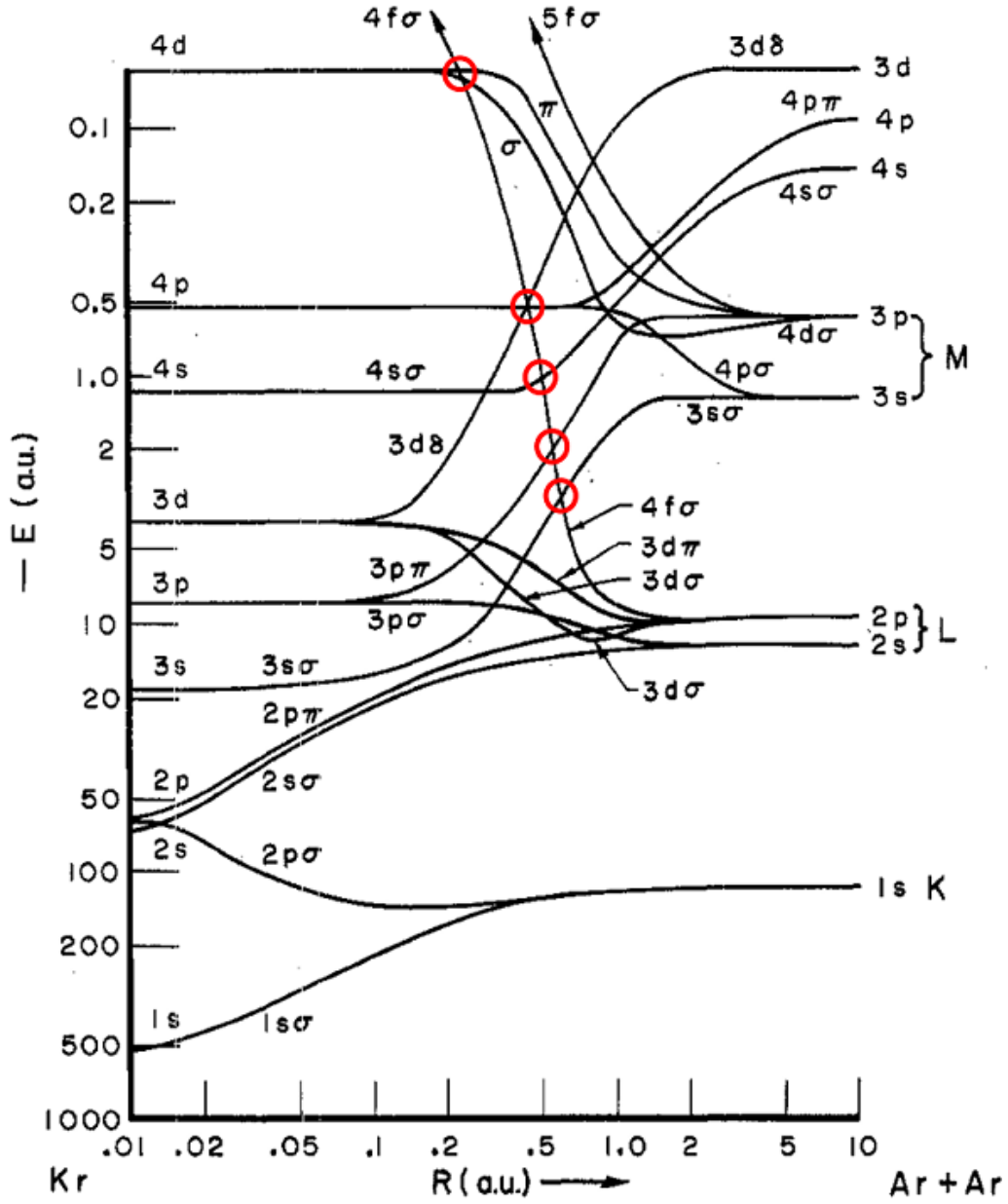

Figure 1.25: Ar-Ar molecular orbital diagram as a function of internuclear distance. Energy level crossings induced by the 4fσ molecular orbital are shown with red circles. (From [100])

The dashed lines given in figure 1.23 represent the simple yet unrealistic change in the electronic energy levels between the partner atoms as they approach each other. A more realistic depiction is given in figure 1.25 for two Ar atoms as a function of distance between the nuclei of the pair, or inter-nuclear distance. As can be seen, the shift in energy levels is continuous over the separation distance due to the non-linear combination of the atomic orbitals of both the target and the

projectile. Due to the formation of anti-bonding orbitals, which as previously mentioned are higher energy than bonding orbitals, this results in a situation where electronic energy levels can cross over and a previously inner-shell electron becomes higher in energy than an outer-shell electron. For example in figure 1.25, the rapid increase in energy of a 2p electron as it enters the 4fσ orbital results in several energy level crossings which are shown as red circles in figure 1.25.

The inversion of the energy levels can allow the electron to transfer to the transiently lower energy orbital if a vacancy in this orbital exists. Upon atomic separation, this then results in an inner-shell vacancy which is produced at a primary ion energy much lower than is possible by Coulombic ionisation alone, and an X-Ray is emitted [128, 129]. These crossing events, especially the 4fσ orbital crossings are well known to cause relatively low energy ionisation events and subsequent X-Ray emission [129, 130, 131, 132]. This process is known as electron promotion [128], and can result in an apparent increase in XRPCS when compared to the typical Coulomb derived XRPCS.

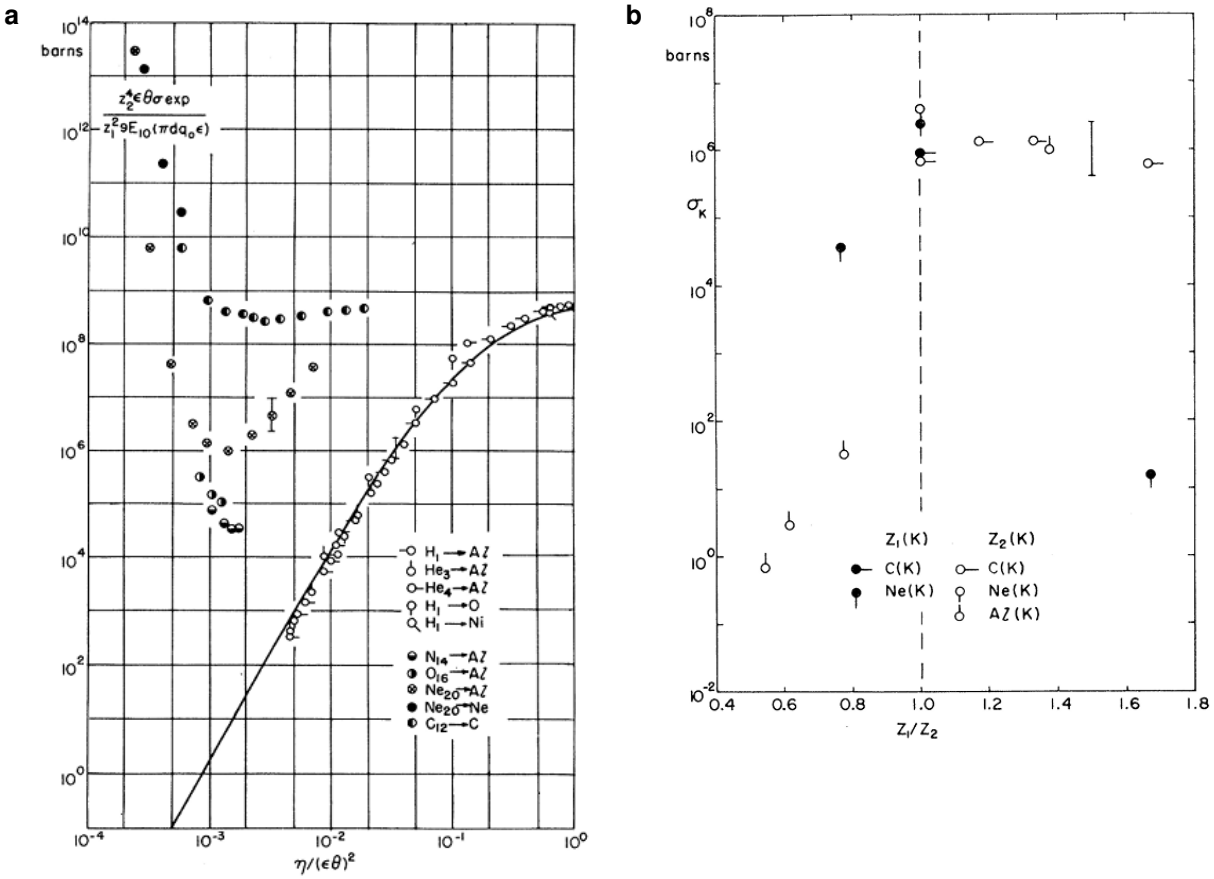

Figure 1.26: (a) K-shell ionisation cross sections of various targets as excited by the ions indicated in the figure. (b) K-shell ionisation cross sections σ_K for projectiles Z_1 and targets Z_2 as a function of Z_1/Z_2. (From [101])

An interesting result of this phenomenon is that the the ionisation cross section

increases with decreasing velocity for heavy ions as demonstrated in figure 1.26a, the opposite behaviour of what is observed with Coulombic excitation by protons as shown by the solid line in figure 1.26a [101]. The reason for this increase is the greater probability of electron promotion due to the extended lifetime of the quasi-molecule at lower velocities.

An additional consequence of the vacancy sharing model is the change in XRPCS with the ratio of the atomic numbers of the projectile and target. With the projectile atomic number expressed as Z_1 and the target as Z_2, as Z_1/Z_2 approaches 1 the ionisation cross section for the K shell of Z_2, jumps by four to five orders of magnitude, and is shown to plateau above a value of 1 [101]. This effect is summarised in figure 1.26b.

Double-Scattering:

The opposite behaviour is also possible, whereby a projectile enters the collision with an inner-shell vacancy, which can then be transferred to the target, a process known as vacancy sharing which has the similar result of increasing the XRPCS. An important condition of vacancy sharing is that the projectile must possess an inner-shell vacancy. Due to the relatively low electron energy in an ICP plasma source, for example an Ar source [133], the probability of a projectile leaving the plasma FIB source with an inner-shell vacancy is essentially zero. These ions instead possess outer-shell vacancies which allow them to be accelerated in the electrostatic potential of the source. As these ions are in the lowest atomic energy state, these outer-shell vacancies can last indefinitely in a high vacuum before they undergo a collision and de-excite [34].

Even if an inner-shell vacancy was produced in the source, the lifetime of such a vacancy is incredibly short. The excited state lifetime can be calculated from the radiative rate of the vacancy in a particular shell which for example, gives an Ar 2p shell vacancy lifetime of 5×10^{-15}s [134]. This would give the ion insufficient time to exit the plasma chamber much less travel the roughly 1m from the plasma source to the sample, thus no inner-shell vacancies would survive until impact on the sample.

Macek et al. however observed the formation of Si K X-Rays when irradiating with Ar^{++} ions, a phenomenon which should be impossible as it relies on the fully filled 2s and 2p levels of the Ar^{++} ion for vacancy transfer to the Si K shell based on the MO model [135]. They attributed this observation to a mechanism whereby an initial collision of the Ar^{++} ion with a target atom forms an inner-shell vacancy which is then transferred to the Si K shell in a secondary collision partner. This

mechanism, called the double-scattering mechanism was further confirmed by Feldman et al. [136] and Heitz et al. [137]. Saris et al. estimated that 10% of the incident Ar ions should possess a required L shell vacancy [138].

Double scattering effectively reduces the required distance travelled during the Ar 2p shell vacancy lifetime from on the order of 1m between the plasma source and the sample, down to the distance between collision partners in the sample. The minimum distance between collision partners will be equal to the lattice constant of the material as outlined by Heiland et al. [139], which for most elements is on the order of 0.2-1.1$\times 10^{-9}$m [140], well within the maximum distance travelled by the Ar^+ ion in its 2p shell vacancy lifetime of 1.90$\times 10^{-9}$m at 30keV.

In asymmetric collisions, where either the projectile or the target is heavier than the other, the probability that a projectile inner-shell vacancy is transferred to the target is given by $W = 1 - w$ or simply w if the projectile is lighter than the target. This K vacancy sharing probability (w) is given by:

$$w = [1 + \exp(2x)]^{-1} \tag{1.64}$$

where

$$2x = \pi \frac{[(U_{KH})^{1/2} - (U_{KL})^{1/2}]}{(\frac{1}{2} m_e v^2)^{1/2}} \tag{1.65}$$

where U_{KH} and U_{KL} are the K-shell binding energies of the heavier and lighter collision partners and m_e is the electron mass [141]. As the electronic binding energies for a specific shell tend to increase with increasing Z, this leads to a condition where in a collision between a projectile with an inner-shell vacancy and a target atom, the collision partner with the lower atomic number has a much larger probability of leaving the collision with a hole in its K shell and hence to produce an X-Ray.

Molecular Orbital Emission:

Upon impact of Ar^+ ions on a C and Si sample, Saris et al. observed a broad, intense X-Ray peak which could not be attributed to any characteristic peaks [138]. This same experiment was later performed by MacDonald et al. who observed the same results on Cu, C, Si, and Al, as well as a solid Ar target [142]. Most importantly, both Saris and MacDonald observed that this peak shifted with accelerating voltage, a phenomenon which is impossible if the X-Ray originates from

characteristic inter-shell transitions as these energy levels are fixed to the atomic orbital energies for a particular elemental species.

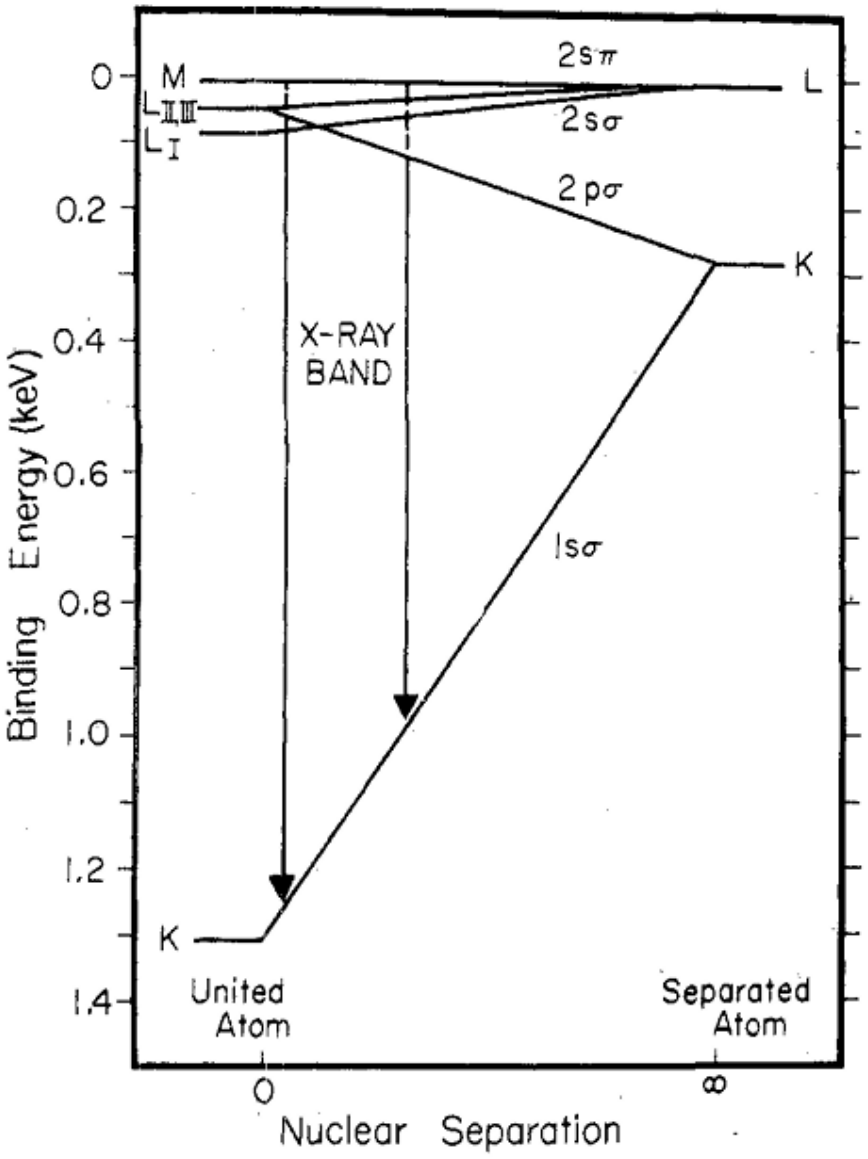

Figure 1.27: Representation of the shift in MO X-Ray energy with changing inter-nuclear distance for the C-C system. (From [143])

Saris initially attributed this emission to interaction between incident Ar ions and Ar atoms implanted in the sample, however MacDonald et al. determined that they were in fact due to interactions between incident Ar ions and the atoms in the sample. He did this by comparing the change in peak position for the Cu, C, Si, and Al targets as compared to a solid Ar target.

MacDonald concluded that this peak originated from a projectile approaching the target atom with an inner-shell vacancy. The projectile will acquire an electron from the sample, which when filling the inner-shell vacancy of the projectile, results in the emission of an X-Ray. The vacancy in the target atom will then result

in the emission of a characteristic X-Ray from the sample [143]. The peak shifting corresponded to the changing binding energy of the electrons through the formation of molecular orbitals, which differ as a function of the distance of closest approach which is dependent on the projectile energy. This phenomenon is shown diagramattically in figure 1.27, with a greater incident energy corresponding to a shift towards the left of the graph. This effect, dubbed as Molecular Orbital (MO) emission is direct evidence of both the double scattering mechanism, due to the presence of the projectile vacancy, and the quasi-molecular model, due to the shift in peak energy with formation of MOs between the projectile and target [138, 142, 143]. This phenomenon is indeed observed during doped beam VLE-PIXE and is demonstrated in section 5.4.

An important distinction is therefore made between the characteristic emission from the sample and the MO emission which arises from vacancies within the projectile incident upon the sample. Due to vacancy sharing however, MO emission will be accompanied by characteristic emission from the sample which may occur at energies lower than what would be expected by Coulomb ionisation alone.

Chemical Effects:

When an atom in a target material is bonded to surrounding atoms, the result is the formation of molecular orbitals between the target atom and the surrounding atoms. The nature of these molecular orbitals will be unique to the bonding situation between the target and the surrounding atoms, for example, if an iron atom is bonded to an oxygen atom, the resultant molecular orbitals will be different to an iron atom bonded to another iron atom. This may result in the emission of a characteristic X-Ray with an energy shifted with respect to an element's expected peak energy [144]. The resultant shift in energy is referred to as a chemical shift or chemical effect. This is the working principle behind X-Ray photoelectron spectroscopy (XPS) where the bonding structure of an atom can be probed by excitation of secondary electrons by X-Ray irradiation [145].

Chemical shifts can also be probed using PIXE [144] when some knowledge of the sample is understood. This effect is indeed quite similar to that of the quasi-molecule formation discussed above, however the peak shifts observed in those collisions can be much greater due to the closer distance of approach with a high energy projectile. For stationary atoms in a sample, the equilibrium internuclear distance is much greater than the distance of closest approach in a collision and the peak shifts are therefore very small. These shifts can only be resolved with a wavelength dispersive spectrometer (WDS), [144], or an X-Ray microcalorimeter [146, 147], which will be discussed in greater detail in a later section.

1.3.4.6 Low Energy and Very Low Energy PIXE

PIXE is typically carried out at energies greater than 1MeV, predominantly due to the significantly increased Coulomb ionisation cross section at these higher energies as discussed in section 1.3.4.3. The optimal energy range for PIXE is 3MeV where the X-Ray production cross sections are maximised and the background contributions remain sufficiently low [148]. Performing PIXE at lower energies however does come with several advantages. Low energy PIXE (LE-PIXE) offers greater sensitivity to light elements compared to higher energy PIXE. This is predominantly due to two primary factors: the much lower Bremsstrahlung signal and low secondary fluorescence yield at low energies [20]. Moriya et al. demonstrated a significantly greater sensitivity to lighter elements by excitation with 180keV protons as compared to 2MeV protons and described a signal to noise ratio for the P Kα line of 50 for 180keV protons and 0.9 for 2MeV protons. They concluded that the sensitivity for all elements with Z$\leq$18 are superior for an excitation energy of 150keV compared to 2MeV and attribute this to the lower background radiation for 150keV protons compared to 2MeV protons [149].

Light elements which only have a single X-Ray transition at lower energies such as Be, B, C, N, and O are often obscured by background signals such as Bremsstrahlung. Higher energy PIXE also requires thick Mylar windows to block backcattered ions which may possess energies up to the primary beam energy. The transmission of low energy X-Rays through such thick windows is poor due to X-Ray absorption by the window and as such, the measurement of X-Ray signals generated by light elements is impossible. As such, PIXE is often limited to elements with a mass greater than Al [150, 21].

Despite the benefits listed above, limited research has been carried out into LE-PIXE and almost none into VLE-PIXE, as the disadvantages of LE-PIXE often outweigh the advantages, such as the significantly reduced X-Ray signal at such low energies, lower sensitivity, and the inability to effectively detect characteristic peaks above $\sim$1keV [21]. As such, alternate characterisation methods such as SEM-EDS are typically used, or researchers resort to PIXE at energies above 1MeV. Only a handful of LE-PIXE systems have been developed utilising decelerated accelerator beamlines or ion implantation systems as mentioned in literature [151, 152, 150, 153, 154]. This results in a lack of experimental data below the ξ<0.2 or <140keV range which makes analysis of the ionisation mechanisms at this energy quite difficult. Lapicki called for an expanded experimental data at these energies to help clarify existing models, particularly quoting the use of LE-PIXE as one of the motivating factors for the expansion of these models [108].

As mentioned previously, the application of PIXE in the very low energy range available to a FIB microscope ($\leq$30keV) was considered to be impossible [22] and no real efforts have been taken to develop PIXE at such low energies due to the expected extremely low XRPCS. Being able to perform VLE-PIXE on a FIB microscope with the sensitivity available to PIXE performed at much higher energies would therefore signify a significant breakthrough in PIXE analysis. This was the primary motivation for the development of the doped beam VLE-PIXE method described throughout this thesis, where MeV level PIXE performance can be achieved with a FIB microscope.

1.3.4.7 Bremsstrahlung

Bremsstrahlung radiation is one of the most prevalent forms of background experienced during PIXE and SEM-EDS analysis. Bremsstrahlung is caused by a change in direction and velocity of a charged particle when it interacts with the Coulombic field of an atomic nucleus. This process results in the emission of a continuum of X-Rays [155]. Due to the light mass of the electron, deviation in the nuclear Coloumbic field is significant and results in a significant Bremsstrahlung background [155]. When a primary ion is used however, Bremsstrahlung radiation originates from a combination of four mechanisms [156]:

1. **Quasi Free Electron Bremsstrahlung (QFEB):** When the projectile velocity is significantly greater than the velocity of the electrons in the target atom, the atomic electrons can be considered free electrons in the projectile frame and produce Bremsstrahlung radiation in the Coulomb field of the projectile.

2. **Secondary Electron Bremsstrahlung (SEB):** When a secondary electron is emitted from a target atom following ion bombardment, the secondary electron can travel through the material where it can generate Bremsstrahlung through the same mechanism as a primary electron.

3. **Nuclear Bremsstrahlung (NB):** The interaction of a projectile nucleus with a target nucleus can cause a deflection of the projectile and a corresponding change of direction and loss of energy of the projectile. This lost energy is emitted in the form of continuum X-Rays.

4. **Atomic Bremsstrahlung (AB):** When an electron is ejected from an atom, this electron or another electron may de-excite to fill the previously bound electron state. In this process, the electron may emit the excess energy it gained in the process in the form of continuum radiation.

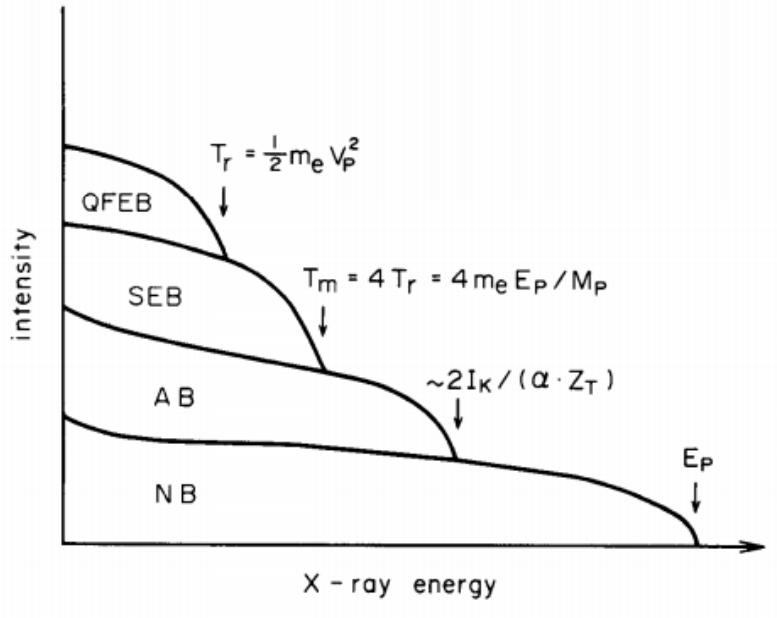

Figure 1.28: Bremsstrahlung contributions to a PIXE spectrum. From [148]

At lower projectile energies, AB and NB processes dominate significantly over SEB and QFEB processes. Both AB and NB processes however also scale inversely proportional to the projectile velocity squared (see [156], equations 6 and 7) such that at very low energies, the total Bremsstrahlung contribution to a PIXE spectra is negligible. The various Bremsstrahlung contributions to a spectrum are shown in figure 1.28.

Due to the significantly increased mass of primary ions over electrons, the deflection of primary ions in a nuclear Coulombic field is much lower than primary electrons and the Bremsstrahlung intensity decreases proportionally. For this reason, the sensitivity of PIXE is enhanced by a factor of about 100 compared to EDS and can detect trace elements on the order of parts per million (ppm) or less for most elements as these low intensity peaks would typically fall below the Bremsstrahlung background [79]. An example of the sensitivity difference due to the Bremsstrahlung contribution between SEM-EDS and PIXE is shown in figure 1.29 where several trace elements are observed using PIXE which are obscured by the Bremsstrahlung background in SEM-EDS.

1.3.4.8 PIXE Detectors

The detectors typically used for X-Ray analysis are solid state detectors such as lithium doped silicon (Si(Li)), lithium doped germanium (Ge(Li)) detectors, or recently, Silicon Drift Detector (SDD). Solid state detectors fall in the category of energy dispersive spectrometers (EDS) due to the analysis method used to

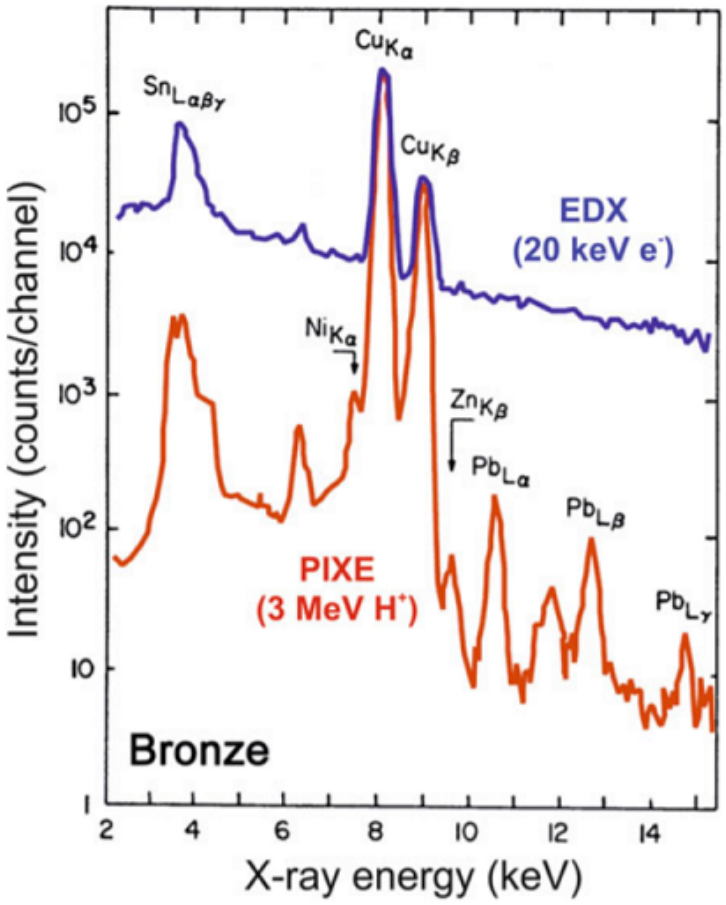

Figure 1.29: A comparison between the characteristic X-Ray spectra of a bronze sample taken using EDS and PIXE. From [79]

distinguish between X-Rays. SDDs are highly sensitive, large area detectors, with moderate resolution compared to wavelength dispersive detectors and microcalorimeters. They are capable of processing millions of X-Rays per second and do so at a temperature achievable by a simple peltier cooler, as opposed to Si(Li) or Ge(Li) detectors which require cooling using liquid nitrogen [157].

Wavelength dispersive spectrometers (WDS) are also sometimes used in PIXE analysis due to significantly increased resolution. WDS utilise a monochromator crystal to separate the X-Ray wavelengths and as such have a much lower efficiency compared to EDS due to absorption by the crystal, and are much slower than EDS due to the fact that the entire spectral range is not recorded simultaneously but scanned sequentially [158]. For these reasons, EDS spectrometers are favoured for commercial applications where resolution is less important than speed.

Microcalorimeters are another detector which is sometimes used for PIXE due to very high resolution [159]. These spectrometers work on the principle of a

superconducting junction, cooled to the point just below the superconducting-normal transition temperature. An incident X-Ray raises the temperature of the junction proportional to the energy of the X-Ray which results in a change in current across the junction [146]. Microcalorimeters are highly sensitive, capable of detecting single X-Rays, however are quite large, complex, and expensive instruments due to the need for millikelvin cooling and sensitive current measurement, and are therefore not commonly used.

SDD Operation:

In an SDD, if the radiation incident on the semiconductor surface is sufficient to penetrate the thin oxide dead-layer on the surface, it will generate a number of electron-hole pairs proportional to the energy of the incident particle. The electrons will then drift towards an anode ring, shown in figure 1.30. This accumulates electrons at the anode ring which is directly connected to the gate of the central Field Effect Transistor (FET), shown as (G) in figure 1.30 and results in a negative bias on the gate. This creates a reverse bias across the junction of the FET, resulting in a current drop through the FET proportional to the voltage applied to the gate. This change of current can be precisely measured using a low-noise amplifier [157].

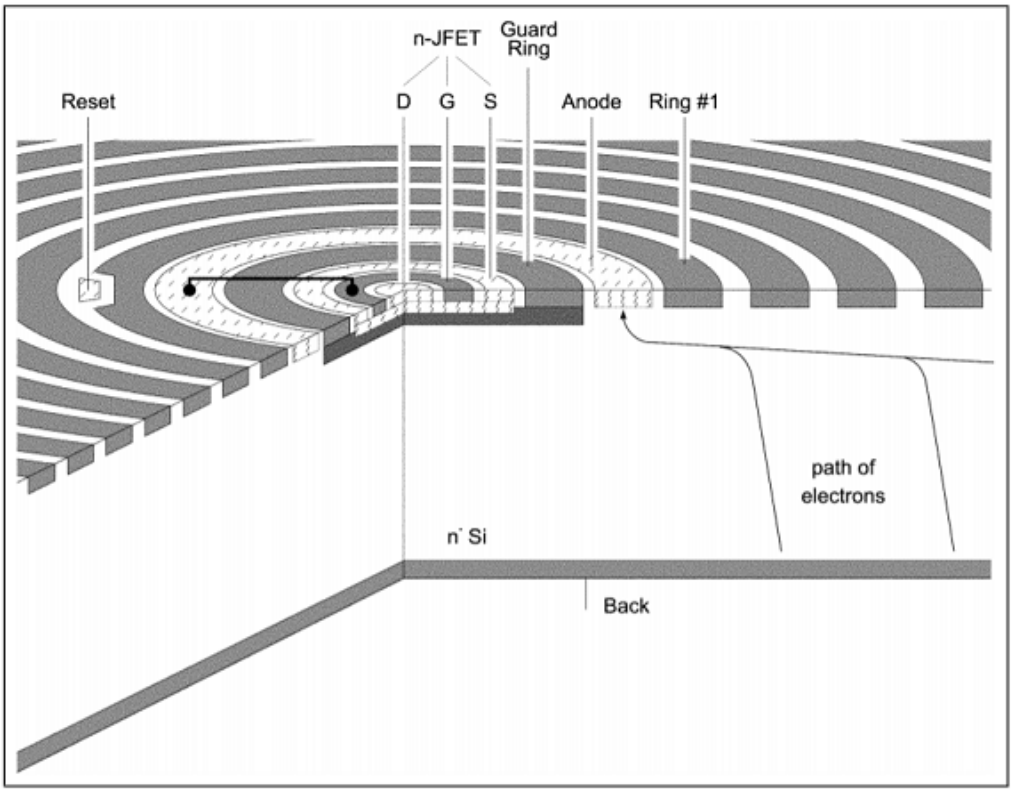

Figure 1.30: Schematic of a Silicon Drift Detector (SDD) showing the junction configuration and the path of electrons. From [160].

At a specific reverse bias of the FET, a weak avalanche breakdown of the junction is produced between the gate and drain, shown as (D) in figure 1.30. The holes generated as a result are collected at the gate and compensate for the signal electrons which previously collected at the gate. This effectively resets the junction and completes a pulse cycle [161].

Following amplification, this pulse is then sorted into a specific "channel" based on its measured current which, as mentioned before is proportional to the energy of the incident particle. After a given time period, the number of pulses sorted into each channel are counted and a histogram is produced, resulting in a spectrum of detector counts vs energy. Such a spectrum is shown in figure 1.31.

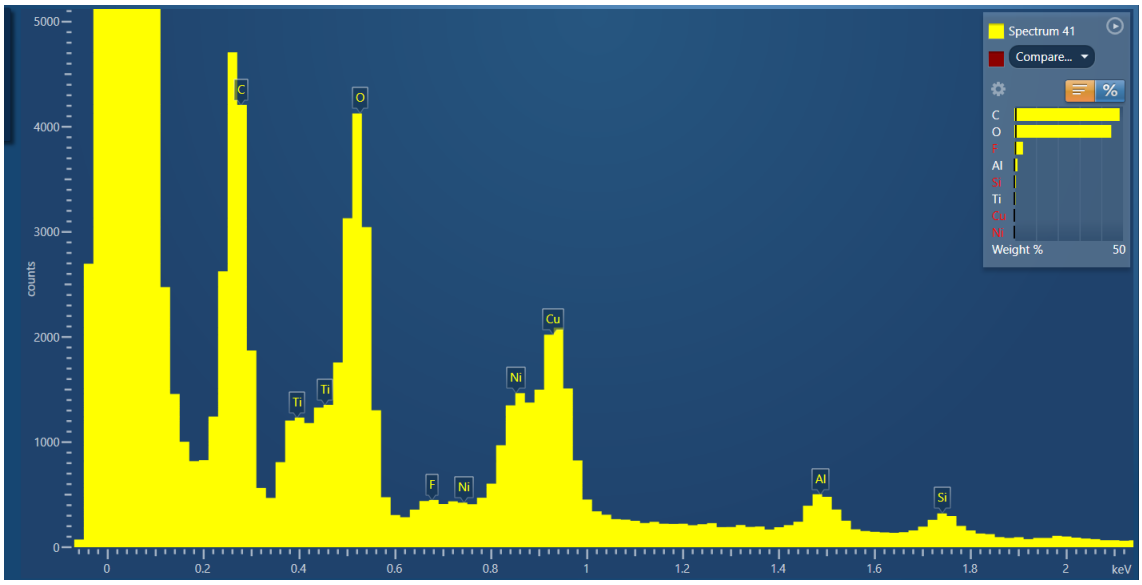

Figure 1.31: An example of a pulse-counting histogram spectrum.

Recent developments in the field of SDD detectors have focused on creating large area, high sensitivity detectors with a high throughput, capable of reducing analysis times from what was previously hours down to several minutes. It is this sensitivity which is fundamental to VLE-PIXE, where the very low X-Ray count rates generated by this technique are still capable of being detected by a modern EDS detector.

These detectors however are not only sensitive to X-Rays and may respond to any energetic particle hitting the surface which is capable of producing electron-hole pairs. This includes electrons, backscattered neutral atoms, or backscattered ions. The detection of these non-X-Ray particles however is considered to be disadvantageous when performing X-Ray spectroscopy and devices such as X-Ray collimators, and electron traps are utilised to prevent these particles from hitting the detector surface. A standard SDD detector may also be used to analyse the

energy of these backscattered ions in a technique known as backscattering spectroscopy, although loss of energy during transmission of heavy particles through the detector window must be considered. This method was used in chapter 7 for analysis of the BSIs produced during VLE-PIXE measurements. The pulse height scaling for these heavy particles may also be quite different to X-Rays due to the number of electron-hole pairs generated per keV of particle kinetic energy and some conversion must be considered.

Detector Windows:
The primary purpose of an X-Ray detector window is to protect the cryogenically cooled detector from contamination upon venting the vacuum chamber. As any energetic particle incident upon a solid state detector can generate a signal, the window also plays a role in protecting the surface of the detector from high energy particle impact, however this is typically undesirable and magnetic particle traps or detector retraction is preferred to prevent this from occurring.

In PIXE and LE-PIXE, a thin mylar or boron window is typically used to filter out high intensity backscattered ion signals which may saturate the detector or obscure the desired X-Ray signal. This window however limits the minimum X-Ray energy which can be detected due to X-Ray absorption by the window. Modern EDS detectors utilise incredibly thin polymer windows which can allow the transmission of very low energy X-Rays down to around 100eV. The super atmospheric thin window (SATW), a polymer window found on the Oxford Instruments UltimMax used in majority of the VLE-PIXE experiments is sufficient to block the vast majority of backscattered ions whilst still allowing the detection of very low energy X-Rays, making this detector optimal for VLE-PIXE measurements.

Another consideration is the support grid which is used to hold the X-Ray detector window, as the window itself is often not strong enough to withstand the pressure differential during chamber venting. Figure 1.32 shows a polymer and silicon nitride window with their corresponding support grids. For typical operation with electrons, an electron trap is used to prevent the primary particles from hitting the window and grid, which comprises a magnet located just before the window. For the case of heavier particles which will be less affected by the magnet, or particles which have been neutralised such as backscattered atoms, there is a possibility that they may hit the window support and generate an X-Ray as was demonstrated in a later chapter. In addition, the support grid will also reduce the available detector area as it prevents the transmission of some percentage of X-Rays. This results in a reported 23% loss for the window shown in figure 1.32a and 18% in figure 1.32b [162].

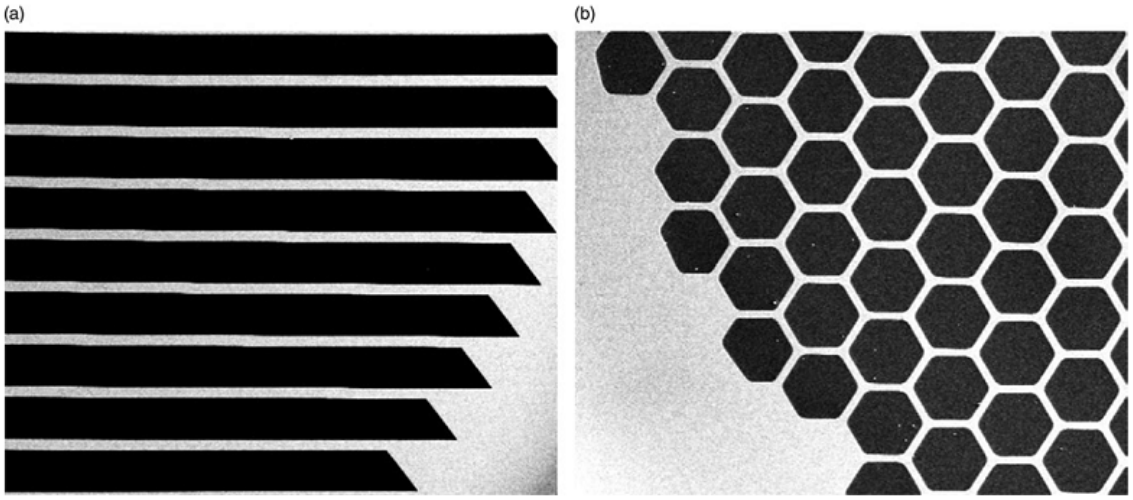

Figure 1.32: X-Ray window and support support grids for (a) a polymer window (b) a silicon nitride window. (From [162]).

Windowless Detectors:

As discussed above, the thin windows protecting the detector surface do still result in the absorption of some X-Rays at low energy. The solution was the invention of windowless X-Ray detectors which eliminate the protective window covering the exposed detector. This allows detection of extremely low energy X-Rays such as the Lithium Kα X-Rays at an energy of 55eV, a feat previously impossible with the use of a detector window. The detection of Lithium is extremely important for the development of Lithium Ion battery technology and furthermore allows X-Ray analysis of the entire periodic table, with the exception of H and He which cannot produce X-Ray transitions [163].

An example of a windowless EDS detector is the Oxford Instruments Ultim Extreme detector used in some of the measurements covered in this thesis. Predominantly the analysis of the BSIs in chapter 7 which as discussed may be blocked or modified during transmission through a detector window. In this case however, the backscattered ions are incident directly on the detector surface and there is a high probability of damage to the detector over an extended period of time. For this reason, the BSI spectroscopy measurements in this thesis were quite limited and just considered a proof of concept. Great care must be taken with windowless detectors to prevent coating or contaminating the detector with resputtered material or damage during chamber venting. This requires cooling the detector following chamber pump-down and warming the detector prior to chamber venting.

Detector Performance:
While modern detectors typically operate in an automated fashion, requiring minimal user input, there are a few input parameters which can influence the performance of an SDD detector. Processing time is perhaps the most important performance factor and relates to the amount of time which the detector software and hardware can spend processing incoming pulses. If the detector is busy processing a pulse, it cannot accept the next incoming pulse and this pulse is then thrown out. The percentage of pulses which are thrown out due to the processing overhead is known as dead time. For very high input counts, when the time between subsequent pulses is very short, the dead time can be reduced by decreasing the processing time, allowing the detector software to process a greater number of pulses in a short period of time at the expense of reduced spectral resolution [162]. As the input counts with VLE-PIXE are typically very low, the processing time is often set to maximum in order to achieve the greatest spectral resolution. In addition, the number of X-Ray channels can be selected which has a similar effect to reducing the processing time due to a smaller number of channels which the software can sort into, however at such low input counts with VLE-PIXE, this value is usually left on the highest setting of 4096 channels.

Another result of very high input count rates is a phenomenon known as pulse pile-up, where two incoming X-Rays strike the detector within a very short period of time and instead of being distinguished as two separate pulses, are counted as a single pulse with twice the pulse height ie. twice the energy. This can result in the appearance of spectral peaks at twice the energy of intense X-Ray peaks in a spectrum and are referred to as sum peaks. Modern EDS software usually automatically subtract such peaks but awareness of these peaks will prevent misidentification of characteristic X-Ray peaks during analysis.

Detector Noise:
An intrinsic feature of all SDD detectors is the presence of a noise peak at a region of $\sim$0eV, sometimes referred to as a zero-strobe peak or the zero peak, and is shown in figure 1.31. This peak arises as a result of noise in the pulse counting electronics of a detector and can typically be ignored due to the majority of X-Ray peaks being located at some distance from the noise peak. The detection of the very low energy peaks may require subtraction of the noise peak for accurate measurement, a method used in section 3.3 of this thesis.

Additional detector specific electronic noise factors include: voltage noise across the SDD detector anode, leakage current caused by the application of a bias to the SDD FET, and 1/F noise caused by internal contacts and dielectric materials

in the SDD. These factors are also referred to as shot noise and scale with the number of input counts. For N number of counts, the uncertainty or standard deviation of the signal, σ scales such that $\sigma = \sqrt{N}$. The signal to noise ratio (SNR) is then defined as the ratio of the signal to the standard deviation of the noise:

$$SNR = \frac{N}{\sigma} = \frac{N}{\sqrt{N}} \tag{1.66}$$

Another factor contributing to noise is known as incomplete charge collection. As low energy X-Rays have a very shallow penetration into the detector surface, many of the electrons generated may not make it to the FET junction. This can result in a broadening of peaks at very low energy and can be a limiting factor for spectral resolution at low energies. [164]

1.3.4.9 X-Ray Peak Shape

X-Ray emission peaks have been established to be intrinsically Lorentzian in shape, being accurately described by the function:

$$y = \frac{a}{1 + (x/b)^2} \tag{1.67}$$

where y is the peak intensity as a function of x which can be wavelength or energy, b is the half width at half maximum of the peak, and a is the maximum intensity of the peak. [165]

The process of measuring these X-Ray peaks however results in some energy deviation due to the formation of electron-hole pairs. The energy required to form an electron-hole pair is statistical in nature and specific to the material from which the detector is made. This is known as the Fano factor (F) and results in a broadening of the intrinsic Lorentzian peak shape. This broadening is Gaussian in nature, being calculated as [166]:

$$\Delta E_{FWHM} = (F)^{1/2}[8(\ln\ 2)\epsilon E]^{1/2} = 2.355(F\epsilon E)^{1/2} \tag{1.68}$$

where E is the mean X-Ray energy, F is the Fano factor, and ϵ is the average energy required to produce an electron-hole pair. The resultant spectral shape is a convolution of a Lorentzian and a Gaussian, known as a Voigt function [167].

As this Voigt function is computationally intensive, a linear combination of a Lorentzian and a Gaussian are often used instead of the convolution. This approximation is known as a pseudo-Voigt function and is given as:

$$V_p(x, f) = \eta \cdot L(x, f) + (1 - \eta) \cdot G(x, f) \tag{1.69}$$

where $L(x, f)$ and $G(x, f)$ are the Lorentzian and Gaussian functions as a function of position (x) and FWHM (f) respectively. η is the Lorentzian fraction or the proportion of Lorentzian contribution to the total function [168]. An example of such a combination is shown in figure 1.33.

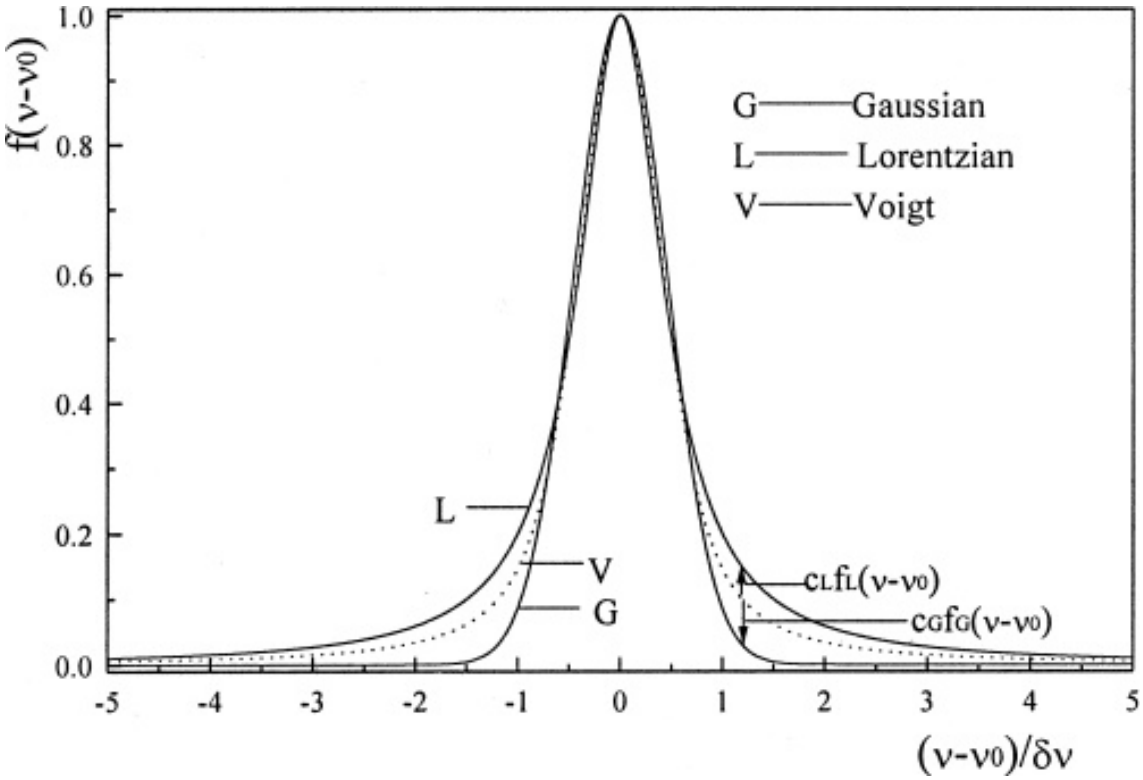

Figure 1.33: Example of a convolution of a Lorentzian and Gaussian function to achieve a Voigt function. From ([1])

1.3.4.10 Limit of Detection

A measure of sensitivity of an analytical technique is the Limit of Detection (LOD), which quantifies the lowest concentration of a specific element which can be detected within some margin of error above the signal generated by a blank sample [169]. LOD can be determined by the presence of an analyte signal peak with respect to the intrinsic noise of the system, for example the electronic noise previously discussed or the presence of background signals intrinsic to the system

such as Bremsstrahlung radiation. This value can be used to characterise the technique as a whole and takes into account factors such as production cross sections, detection limitations, signal processing, and the total noise related to a specific system.

The limit of detection is equal to the concentration of an analyte that produces a signal that is three times the noise of the system (3N). Stated another way, the LOD is equal to an analyte concentration which produces a signal 3σ times the signal to noise ratio. The factor of 3 used originates from a determination by the American Chemical Society that the LOD is the lowest concentration of an analyte that can be determined to be statistically different from a blank [169].

Experimentally, the LOD can be determined using the following technique:

- Acquire a sample with a well known composition such as a standard reference material
- Measure sample using the given analytical technique
- Determine Signal To Noise Ratio (SNR) as the ratio of the analyte signal peak prominence to the standard deviation of the noise close to the peak

$$SNR = \frac{I_{peak}}{\sigma} \tag{1.70}$$

- Using the known element concentration (C), calculate LOD using the formula:

$$LOD = 3C/SNR \tag{1.71}$$

  given in units of concentration.

An example of the determination of signal to noise ratio from a spectral peak is shown in figure 1.34.

1.3.5 Backscattering Spectroscopy

As discussed in section 1.3.3.2, some proportion of incident ions can be backscattered from or close to the target surface. Due to the nature of the scattering process, information can be gathered about the composition and structure of the scattering surface, making backscattering analysis a highly valuable analytical technique. Rutherford backscattering spectroscopy (RBS), medium energy ion scattering (MEIS), and low energy ion scattering (LEIS) are essentially the same

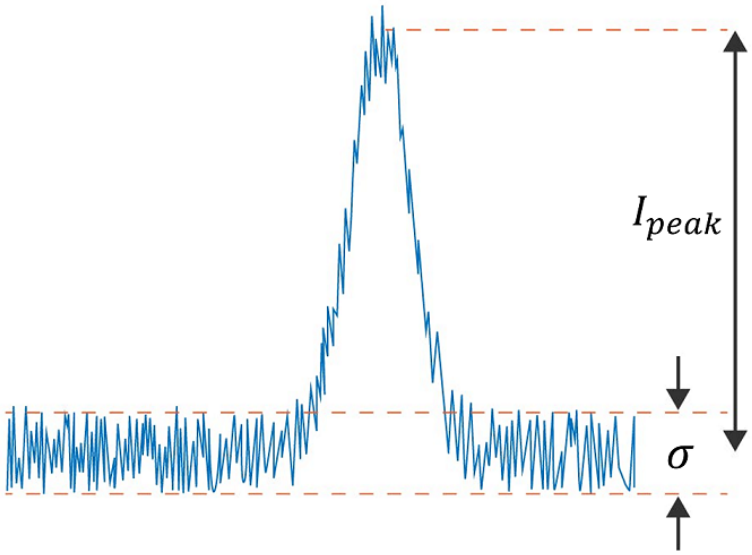

Figure 1.34: Experimental calculation of signal to noise ratio.

technique performed at an energy of >300keV, 30keV-300keV, and <30keV respectively. Analysis of the backscattered ions produced during VLE-PIXE can therefore be considered LEIS. Backscattered ions and neutrals atoms are produced during VLE-PIXE analysis, creating to potential for simultaneous analysis of both X-Rays and BSIs however several technical challenges will need to be overcome for this to be a reality.

1.3.5.1 Backscattered Ion and Neutral Detection

BSI and neutral energy following sample impact can be analysed using a windowless EDS detector such as that described in section 1.3.4.8. Windowless detectors are required so that no loss of signal or loss of energy occurs due to transmission through the thin window of a standard EDS detector. The backscattered particles will impact the detector surface directly where they will generate a number of electron-hole pairs proportional to the energy of the incident particle.

Time-of-flight detectors such as those used for BSI analysis in the He ion microscope and electrostatic analysers rely on the particles remaining charged as they escape the surface. For energies below 10keV, this can be less than 1% and for energies above 30keV, the percentage of charged particles leaving the surface remains below 10% [170]. The detection of both charged and neutral particles can therefore significantly increase the measured signal. As previously discussed, SDDs are capable of detecting both backscattered ions and neutral atoms as they do not rely on particle charge for separation or detection, and in-

stead rely on the generation of electron-hole pairs which can be achieved by any energetic particle. The number of electron-hole pairs will need to be determined for accurate energy analysis, so a sample with a known backscattering peak energy can therefore be used to calibrate the peak position and a calibration factor can be applied. [171]

1.3.5.2 Elemental Analysis

When considering the kinematic scattering process described in section 1.3.3.2, if the kinetic energy of the ions backscattering from the surface are analysed, the mass of the target atom can be determined based on the loss of kinetic energy of the primary ion during the scattering process. Using the case at a scattering angle of 180°, where the energy loss is maximised, the target mass (m_2) can be determined by rearranging equation 1.15:

$$m_2 = \frac{4E_0\, m_1}{E_0 - E_1} \tag{1.72}$$

where m_1 is the mass of the incident ion, E_0 is the initial ion energy, and E_1 is the final ion energy. At low incident ion energies, the scattering is predominantly from the top few nanometres of the target surface. This technique can therefore be used to determine the composition of a target surface [71]. For compound materials such as metal oxides, a separate scattering event can be distinguished for both the metal target atom and the oxygen target atom resulting in two distinct energy peaks. This technique can be used to analyse surface adsorbates [172].

1.3.5.3 Layer Thickness Analysis

The backscattering described above is for the case of a single collision between an incident ion and a target atom, typically residing on or near the surface of a material. As the incident ion energy increases, the ion may penetrates beneath the surface and backscatter from a target atom below the surface. As it enters the material, it will lose some energy due to nuclear and electronic stopping in the material and will also do the same as it exits the material. Backscattering spectroscopy can therefore provide depth or thickness information relating to the material in addition to the elemental composition [173]. This principle is shown in figure 1.35, where the ion energy loss peak from scattering at the surface (1' and 3') and the energy loss from scattering at some depth t (2' and 4') can be identified. The resultant spectrum will be a sum of all scattering peaks through the

thickness t which manifests as a broadening of the surface scattering peak and a shift towards lower energies. This is shown in figure 1.35b where the dashed lines represent the peaks resulting from scattering at the front and rear of the film and the solid lines represent the sum of the peaks through the thickness of the film which will be captured by the detector.

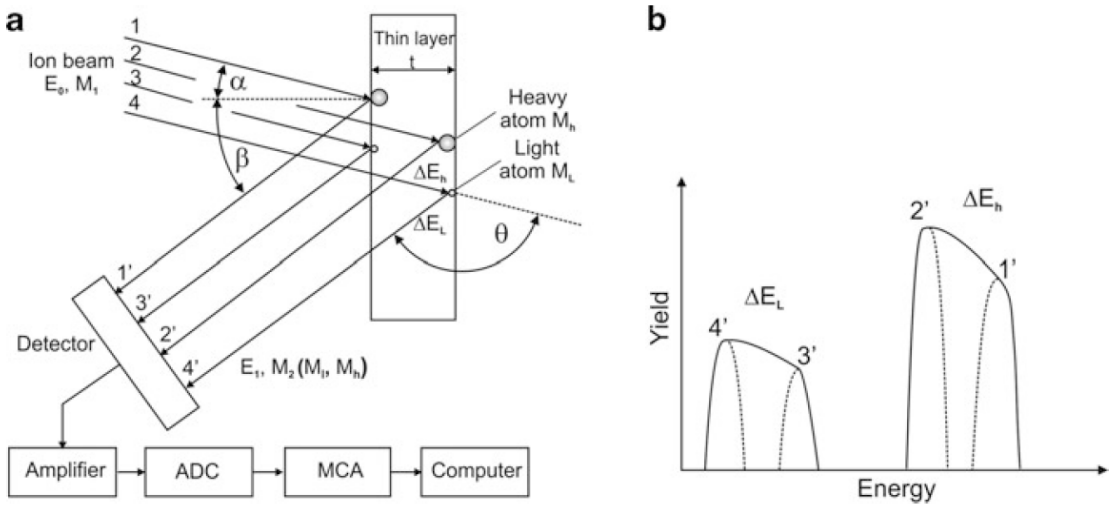

Figure 1.35: (a) Ion backscattering from a heavy atom at the surface (1), and at depth t (2), ion backscattering from a light atom at the surface (3), and at depth t (4). b. The resultant backscattered ion energy peaks from the conditions in (a). (From [79])

The expected energy loss can be calculated for an ion scattering in a material at a specific depth. Firstly the ion energy lost on its way into the material to the backscattering location can be calculated as:

$$E_x = E_0 - \Delta E_{in}(x) = E_0 - \frac{x}{cos\ \alpha}\int_0^x \left(\frac{dE}{dx}\right)_{in} dx' \approx E_0 - \frac{1}{cos\ \alpha}\left.\frac{dE}{dx}\right|_{in} .\ x \quad (1.73)$$

where E_x is the ion kinetic energy at depth x, $\Delta E_{in}(x)$ is the energy lost on at depth x, $\frac{dE}{dx}$ is the total stopping power of the material and α is the incident angle of the ion. Next, the ion kinetic energy following kinematic backscattering (E_S) at depth x is calculated based on the energy immediately prior to scattering (E_x):

$$E_S(x) = k\ .\ E_x \quad (1.74)$$

where k is the kinematic factor discussed previously. The energy lost on the transit out of the material resulting in the final kinetic energy of the ion (E_1) which

has scattered at some depth x :

$$E_1(x) = E_S(x) - \Delta E_{out}(x) = E_S(x) - \frac{x}{cos\ \beta} \int_x^0 \left(\frac{dE}{dx}\right)_{out} dx' \approx E_S(x) - \frac{1}{cos\ \beta} \left.\frac{dE}{dx}\right|_{out} . x \tag{1.75}$$

where β is the scattering angle. Combining these equations, the final kinetic energy of an ion scattering at depth x can be approximated by [79]:

$$E_1(x) = k\ .\ E_0 - \left(\frac{k}{cos\ \alpha} \cdot \left.\frac{dE}{dx}\right|_{in} + \frac{1}{cos\ \beta} \cdot \left.\frac{dE}{dx}\right|_{out}\right) . x \tag{1.76}$$

1.3.5.4 Crystalline Analysis

The scattering events described above assume a homogeneous, smooth, amorphous surface where there is no preferential scattering direction. When an ordered crystalline material is considered, the crystal structure begins to influence the backscattering behaviour, particularly the angle of emission.

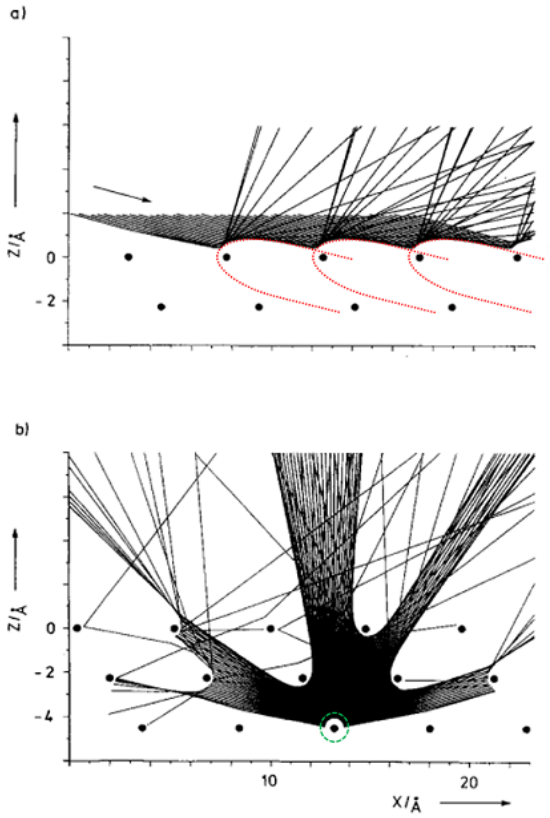

Figure 1.36: Example of a (a) shadow cone with cones marked with red dashed lines, and (b) blocking cones caused by BSIs originating from the lower centre atom, marked in green. (From [172])

As an incident ion approaches a target atom, due to the Coulombic interaction

between the incident ion and the target atom, a ”shadow” cone begins to form behind the target atom. In this region, the probability of scattering is significantly reduced, leading to a focusing effect where scattered ions are concentrated towards the edge of the shadow cone. This can result in an increased flux of ions to atoms in the second row of a crystal lattice. This effect is shown in figure 1.36a. Upon backscattering from the second or third atomic row, a similar effect happens in the reverse direction. This leads to a ”blocking” cone as the ions exit the material. As shown in figure 1.36b, when an ordered crystal lattice is present, this leads to regions of depleted backscattered ion intensity when the blocking cone aligns with a crystal orientation. When this effect is averaged over the entire crystalline surface, preferential scattering angles are formed which correlate the underlying crystalline material. If the angular dependence of the backscatter signal is measured by rotating either the sample or the detector, the crystal structure can be reconstructed based on the varying intensity across the range of angles.

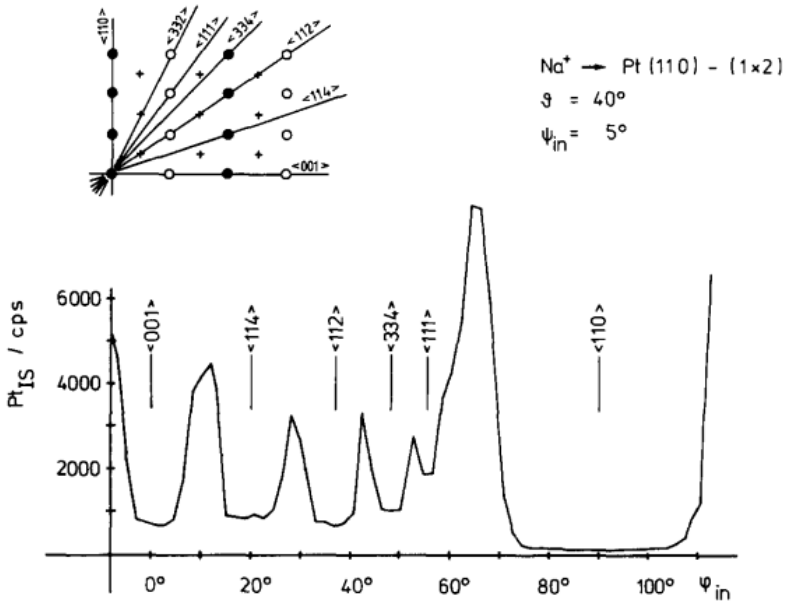

Figure 1.37: Experimental reconstruction of a Pt(110) surface using angle dependent ion backscattering. (From [172])

When an amorphous or highly polycrystalline material is considered, the number of potential scattering angles cancel each other out and there is no preferential scattering angle. In this situation, the backscattering is considered to be isotropic and the ion energy can be measured from any angle relative to the sample. A measurement angle close to 180° is preferred however as this is the scattering angle where the energy loss is maximised. Figure 1.37 shows the experimental reconstruction of a Pt(110) surface using angular resolved backscattering, where the minima of the angular intensity plot corresponds to the crystal orientations shown in the figure, where maximum blocking occurs along crystal rows [172].

Chapter 2

Implementation and Characterisation of an H_2 and Doped H_2 FIB Source

The advent of the switchable gaseous plasma ion source has allowed the application of up to 4 parallel source species, typically Xe, Ar, O_2 and N_2. Xe and Ar are chosen for their high masses, making them ideal for rapid processing due to their high sputter yields, and nonreactive nature resulting in reduced influence over the chemical and electronic properties of the sample. O_2 and N_2 are chosen due to their availability and the possibility of interesting applications due to the chemically active nature of these species. While the sputter yields of these species are much lower than Xe and Ar, they are still not negligible and can be used for the processing and preparation of materials through FIB milling. One example is the use of the O_2 beam for the processing of organic materials, as the chemical nature of the oxygen species allows volatilisation of sputtered species, preventing redeposition of carbon based materials [174].

Hydrogen, with its very light mass and therefore very low sputter yield is not suitable for the preparation and processing of materials. The potential for a hydrogen beam lies instead in the analysis of materials, with a number of possible applications highlighted in chapter 1 such as PIXE, and LEIS. Some attempts have been previously made to incorporate a hydrogen source into a FIB as outlined in section 1.3.1.1, however the very low currents available, particularly of protons make materials analysis with such instruments difficult.

The VLE-PIXE technique outlined in this thesis relies on the production of light species such as protons, with the most ready source of protons being a hydrogen

plasma. A significant current of protons is also required as the low XRPCS at such low energies can be compensated to some degree by increasing the number of protons incident on the same in a given time frame. In addition, for doped beam VLE-PIXE, the capability of supporting multiple species simultaneously is fundamental for the application of this technique.

This section outlines the implementation and characterisation of a hydrogen source and a doped hydrogen source on a plasma FIB instrument, in particular the Thermo Fisher Helios G4 Hydra plasma FIB, referred to herein as “the PFIB”.

2.1 Beam Implementation

2.1.1 Gas Delivery System

The gas delivery system on the PFIB is responsible for the supply and distribution of a gaseous precursor to the plasma chamber. Inside this plasma chamber is where ions are produced, which are then extracted and accelerated for the purpose of generating a focused ion beam. In order to generate a hydrogen beam, the standard supplied oxygen bottle was simply replaced with a bottle of high purity hydrogen. The removal of the oxygen bottle was for the purpose of safety as well, with the combination of oxygen and hydrogen on the same system creating the potential for an explosion.

The position of this hydrogen bottle is circled in red in figure 2.1 however the position is still listed as Oxygen in the user interface. From this bottle, the Hydrogen is supplied via a series of shut-off valves ((2) in figure 2.1), and the gas delivery manifold ((3) in figure 2.1) to the inlet of the plasma chamber ((4) in figure 2.1) where the plasma is ignited.

The hydrogen gas is provided to the plasma chamber via a metered orifice, circled in blue in figure 2.1 item (4), which ultimately controls the pressure within the plasma chamber. The back-pressure upon this orifice, provided by the gas delivery system dictates the flow rate through the orifice and was found to be optimal in the 2-4$\times 10^3$ mbar range as measured directly before the orifice, on the Pirani Pressure Gauge (PPG) shown in figure 2.1. The evacuation rate of the plasma chamber is fixed by the pumping speed of the turbo molecular pump (TMP) shown in item (6) of figure 2.1, resulting in a drop of pressure between the metered orifice and the exit aperture of the plasma chamber. The precise pressure in the plasma chamber is not known, however a pressure measured on the

cold cathode gauge (CCGp) after the plasma chamber, shown in item (6) of figure 2.1, of 6-7$\times 10^{-6}$ mbar was demonstrated to be optimal for hydrogen plasma ignition.

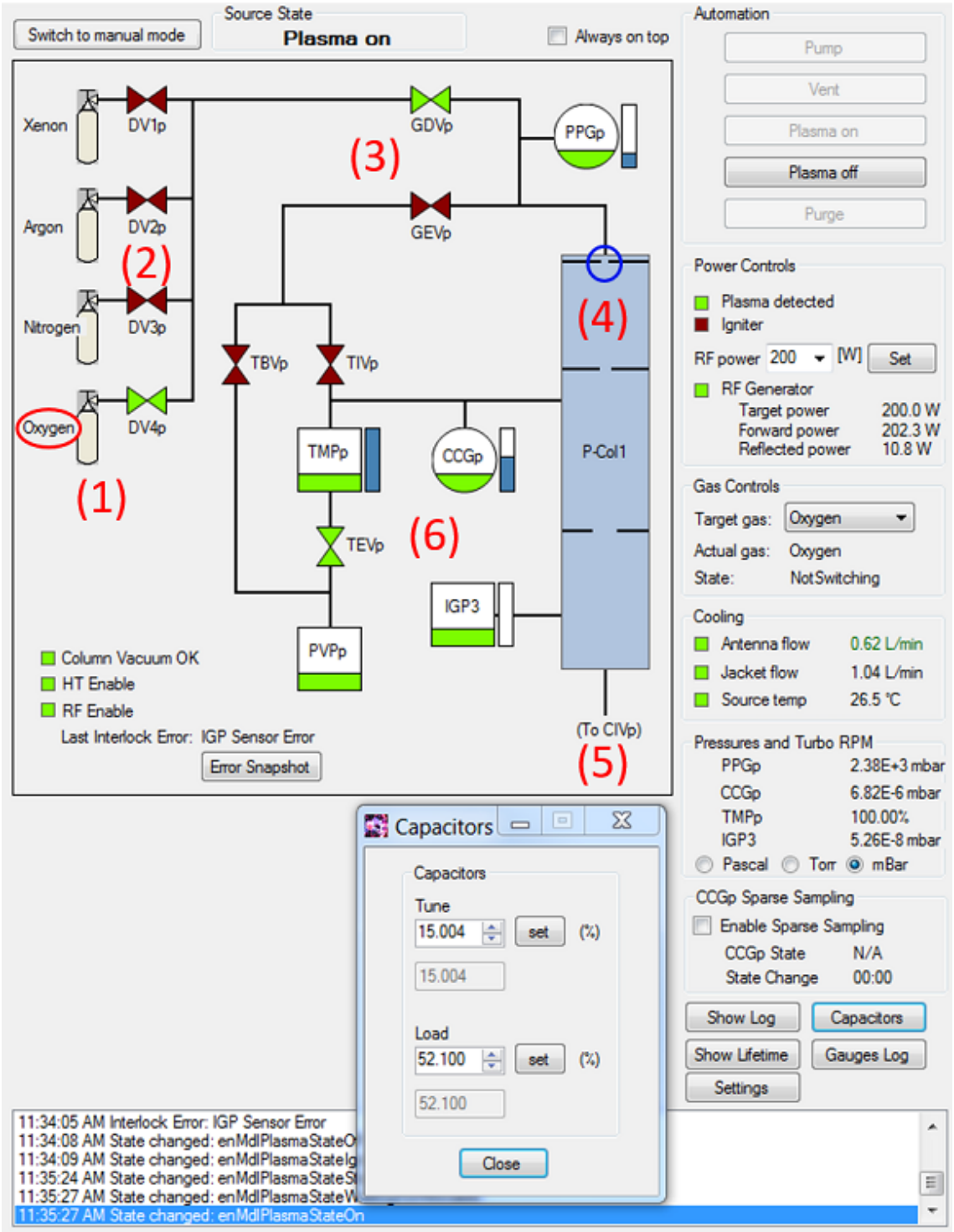

Figure 2.1: Diagnostic page for the plasma system of the PFIB with a Hydrogen plasma ignited. (1) Gas supply bottles with the Hydrogen bottle position circled in red, (2) Gas delivery shut-off valves, (3) Gas supply manifold, (4) Plasma chamber with the metered orifice circled in blue, (5) FIB column, and (6) Vacuum and bypass system

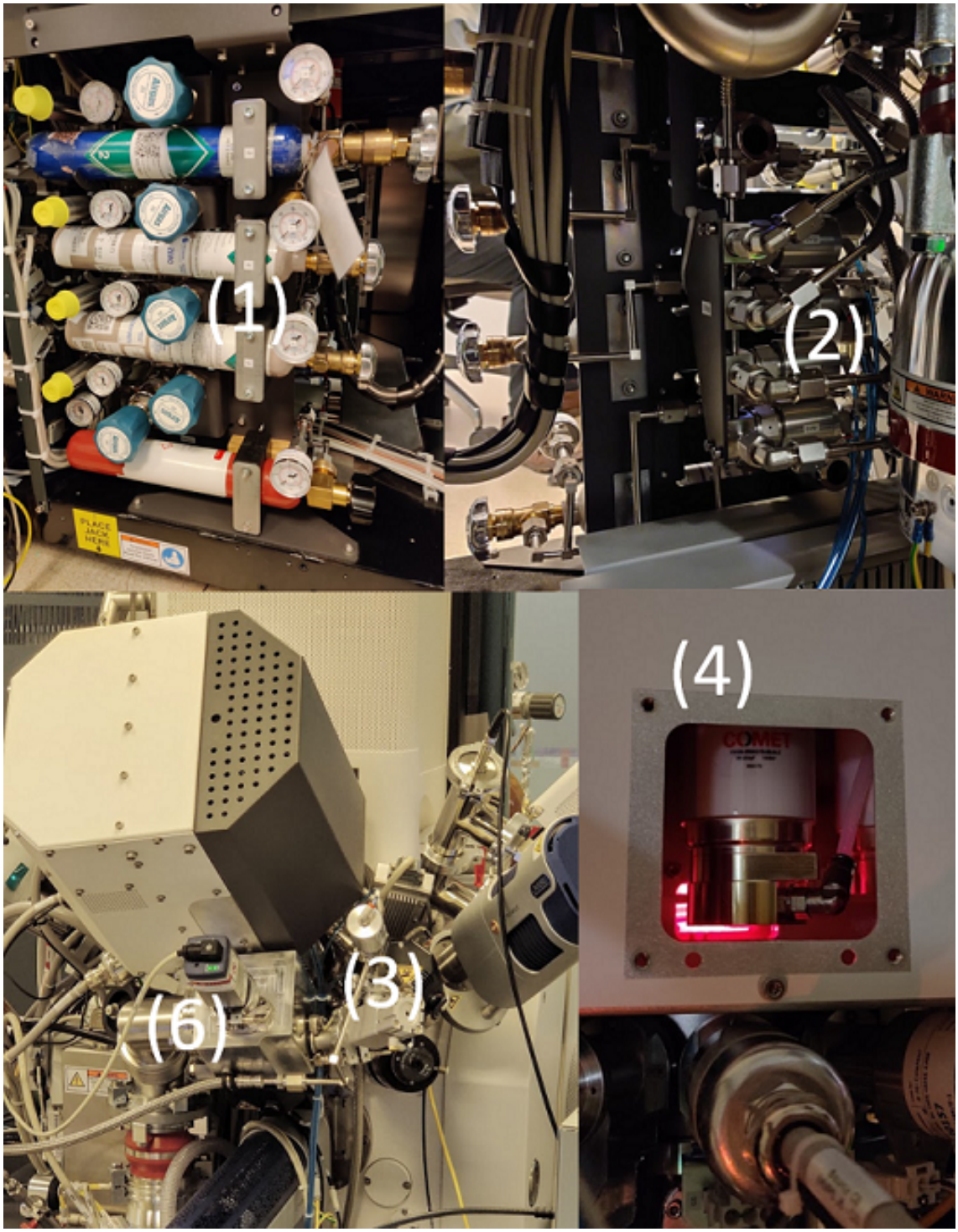

Figure 2.2: Images of the Helios Hydra PFIB hardware. (1) Gas supply bottles with the Hydrogen bottle (red) installed in the lowest position, (2) Gas delivery shut-off valves, (3) Gas supply manifold, (4) Plasma chamber with hydrogen plasma, (5) FIB column (not shown), and (6) Vacuum and bypass system

Photographs of the approximate positions of the: (1) Gas supply bottles with the Hydrogen bottle (red) installed in the lowest position, (2) Gas delivery shut-off valves, (3) Gas supply manifold, (4) Plasma chamber with hydrogen plasma, (5) FIB column (not shown), (6) Vacuum and bypass system are shown in figure 2.2.

2.1.2 Plasma Source

Once a stable pressure of gas in the plasma chamber has been established, the plasma is then ignited. This ignition process is typically performed automatically following gas species switching and proceeds as such:

- Radio Frequency (RF) impedence matching capacitors are set to pre-ignition values.
- RF generator provides an RF wave at a desired power.
- Plasma igniter is discharged which ignites the plasma in the chamber.
- Plasma detection logic is applied which relies on an increase in the reflected RF power upon plasma ignition.
- RF impedence matching capacitors move to post-ignition values and automatically tune to minimise reflected power.

Once ignited, the plasma is allowed to stabilise for a period of between 15-30 minutes before use to achieve the most stable beam. A photograph of the plasma chamber displaying an ignited Hydrogen plasma (item (4)) is shown in figure 2.2.

Operation of the plasma source during beam doping typically involved extinguishing the plasma, establishing the new precursor gas mixture and re-ignition of the plasma source. Some amount of manual RF capacitor tuning was also required as the optimum tuning values for the plasma system are established for a single gaseous species.

It was observed throughout the beam doping experiments that the addition of dopant species to the source plasma could have unexpected effects on the plasma composition and therefore the beam composition. As described in section 5.3, the changing partial pressure of Ar in the plasma source resulted in the proportion of the hydrogen molecular species in the beam differing somewhat from what was expected based on a pure hydrogen beam. This is fairly typical of multi-gas plasmas, as Bai et al. described that the plasma parameters can change significantly with the mixing ratio in inductively coupled plasmas [175]. A significant amount of modelling would need to be performed to fully understand the behaviour of the multi-species plasma in a doped beam situation.

2.2 Beam Characterisation

Understanding the molecular and isotopic composition of the FIB is fundamental to understanding the interactions of the beam with the sample and the resulting physical processes. In particular for the doped beam VLE-PIXE experiments, the plasma will generate H^+ (protons), H_2^+ and H_3^+ ions, as well as some proportion of dopant species, the ratio of which is dependent on a number of factors such as plasma power, pressure, and partial pressure of the gaseous precursors. Characterisation of the beam as it is incident upon the sample is the best way to determine the experimental conditions. This section will highlight the techniques used to characterise the beam composition, techniques which are used throughout all the experiments outlined in this thesis.

2.2.1 Beam Splitting

The magnetic immersion lens (MIL) of the electron column utilises a strong magnetic field to both act as the final lens for the electron beam and to help guide electrons to be collected by detectors located in the column [176, 177]. This magnetic field is known to cause deflection of ions as they travel from the FIB column to the sample as a result of the Lorentz force applied to the positively charged ions. A detailed explanation of the Lorentz force is provided in appendix section A.1. Importantly, this Lorentz force is dependent on the mass to charge ratio of the ion, with a greater force applied to lighter ions than heavy ions.

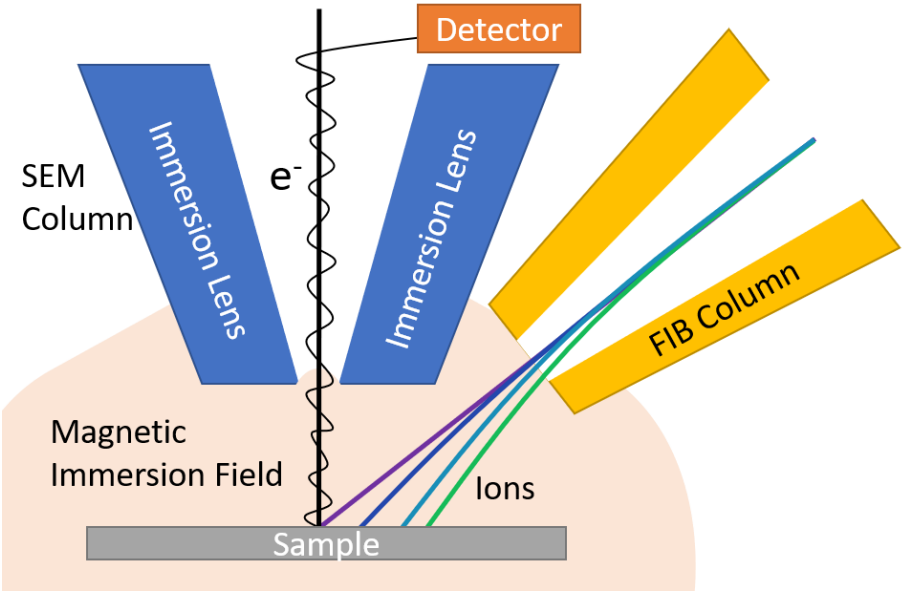

Figure 2.3: Schematic of the FIB interaction with the magnetic immersion field.

The strength of the magnetic field generated by the MIL can be adjusted by increasing or decreasing the current travelling through the MIL and can be applied with both a positive and negative polarity. This is typically used to adjust the focal point of the electron beam upon the sample. The magnetic immersion lens however contains a ferromagnetic core which serves to enhance the magnetic field generated by the coil. As a result, when the current applied to the lens coil is removed, a remanant magnetic field is still present. As such, a current is applied to the lens coil which acts to compensate for the remanant magnetic field, resulting in an effective field free condition. This is typically applied during FIB operation such that the ion beam is free to travel to the sample without deflection.

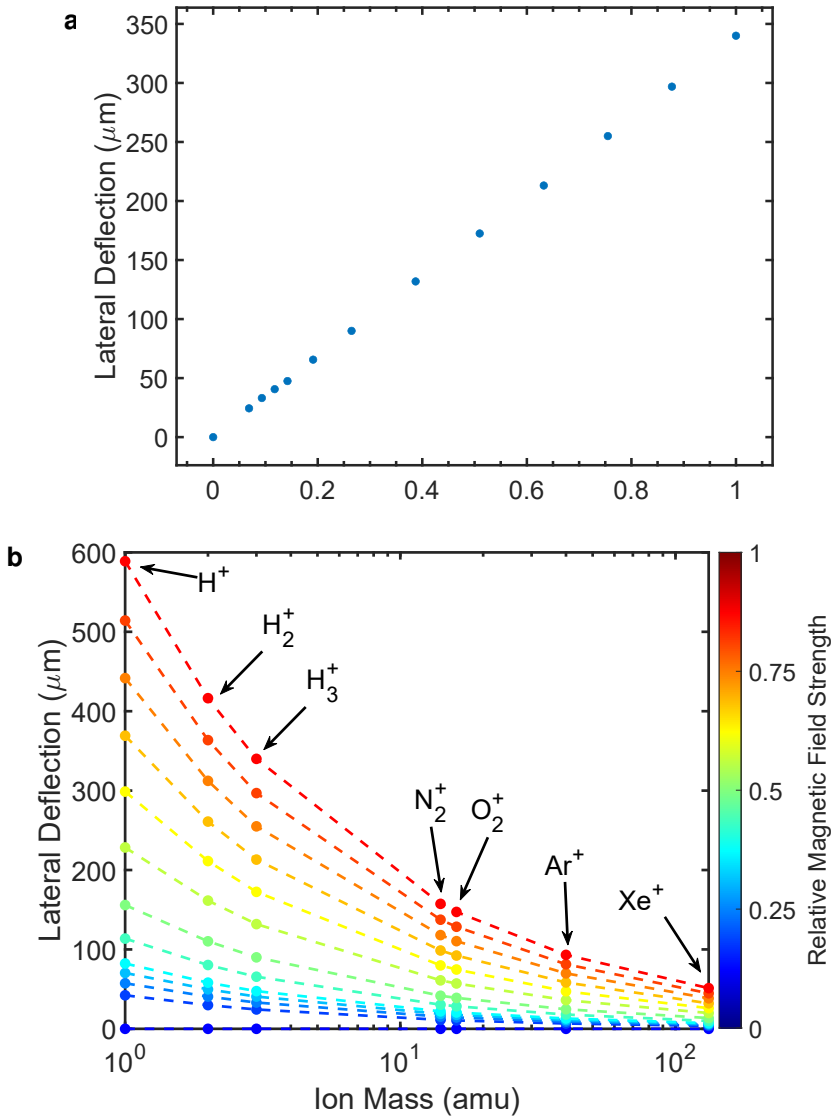

Figure 2.4: (a) Measured lateral deviation of the primary H_3^+ species as a function of relative magnetic field strength. (b) Predicted trajectories of common mass components vs relative magnetic field strength.

Changing the current of the MIL however creates the possibility of intentionally inducing a deflection to the ions in the beam. The magnetic field is aligned such

that the deflection is only in the X-direction relative to the beam scanning field of view. This results in the separation of the ion beam components by mass/charge ratio with the heaviest component falling closest to the beam axis and the lightest components falling some distance away. The degree of deflection can be described using the Lorentz equations in appendix section A.1 and can therefore be used to identify the species. A cartoon of this system is shown in figure 2.3.

The lateral deflection of the H_3^+ ion from its field-free location is shown in figure 2.4a. From these values, the strength of the magnetic field can be determined by solving the Lorentz equation. From here, the lateral deflection of some common mass components could be predicted for a specific relative magnetic field strength as shown in figure 2.4b, and was found to be very accurate when compared to spot-burn images of separated beams such as those shown in figure 2.5. Inversely the mass of the species can be calculated based on their lateral deflection, identified using a spot-burn image of a separated beam. The method for this will be covered in the next section.

Figure 2.5 shows a representative spot-burn image of the individual beam components of a hydrogen beam. Labelled are the most likely molecular species based on the mass identification method used in the following section and comparison with a molecular mass reference database [178].

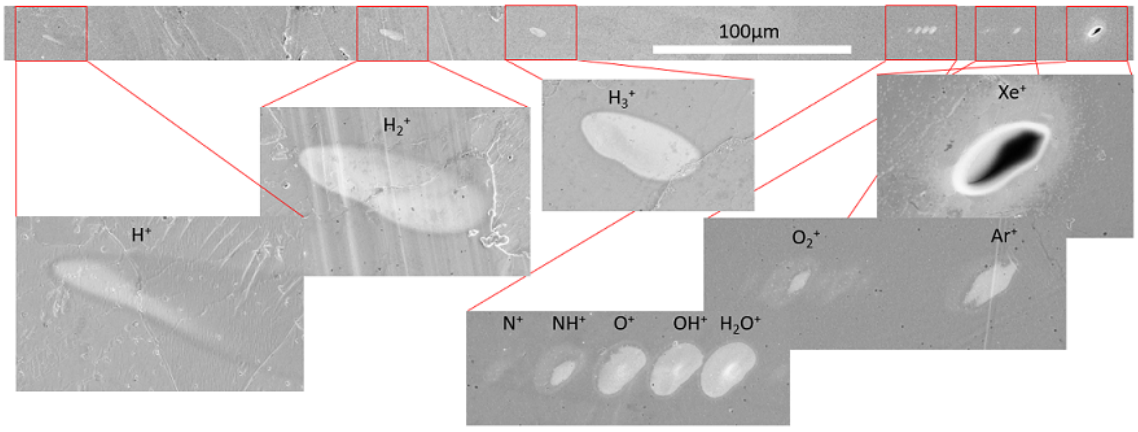

Figure 2.5: 90 second spot-burn irradiation of 1.22nA, 30keV separated hydrogen ion beam, with likely species labelled.

2.2.2 Beamlet Identification

In order to identify the mass of the each beam component, referred to as “beamlets”, a custom MATLAB script was developed which takes an image of a spot-burn irradiation of the separated beam and calculates the mass to charge ratio

in Atomic Mass Unit or Dalton (amu) of each beamlet spot using the following method:

1. The image to be analysed is imported.
2. The spots of two known masses are marked and their pixel coordinates recorded, for example Xe^+ (132 amu) and the primary beam spot, being either H_3^+ (3 amu), N_2+ (28 amu), O_2+ (30 amu), Ar^+ (40 amu).
3. The pixel coordinate values are converted to X-deflection distances using the horizontal field width (HFW) of the image.
4. The X-deflection distances and masses of the two identified spots are used to solve equation A.9 as a set of two simultaneous equations for W/E_x and W/B_y. This essentially calibrates the image in terms of the magnetic field strength, working distance and accelerating voltage.
5. Using the calculated values for W/E_x and W/B_y, equation A.9 is solved for the remaining beam spots and the component masses are calculated.
6. The species were then identified using the NIST Standards Reference Database [178].

An example of this script in operation on the spot-burn image given in figure 2.5 is shown in figure 2.6a. The result of this analysis has been added to figure 2.5 where mass components of a hydrogen beam have been matched with their most likely species identification. The Xe spot is marked against the Xe^{132} spot as this is the highest naturally abundant isotope of Xe at 26.9% [179]. Xe however has 7 naturally occurring stable isotopes, all of which could be identified under certain conditions.

Identification Considerations

In order to identify the species following their mass calculation, several considerations must be taken in order to isolate the most likely molecular or isotopic candidate. One consideration is whether the vast majority of ions generated in the plasma from the source gases are singly ionised. This is important as the mass identification is based on the mass to charge ratio (m/z), not simply the ion mass and doubly charged ions could be misidentified as an ion with half its mass. Previously reported performance of an early version of the Helios Hydra PFIB source demonstrated a doubly ionised percentage of just 0.75% for the ICP source operating with Xe at an RF power of 300W [35]. This power is significantly higher than the 37W typically used with Xe on the commercial version of this ICP

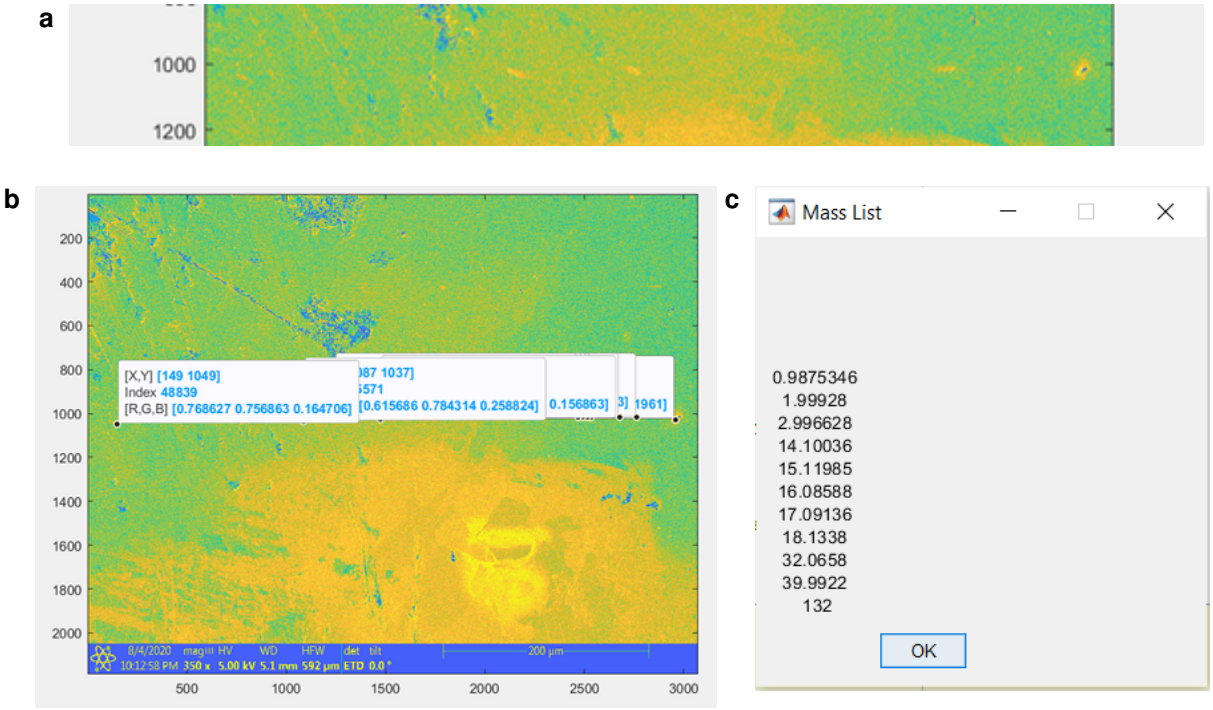

Figure 2.6: (a) The image input of a spot-burn irradiation of the separated ion beam shown in figure 2.5, (b) marking of the individual beam spots for mass identification, (c) output results table of the calculated beam component masses.

source and therefore the percentage of doubly ionised Xe would be expected to be even lower. Xe^{2+} with an average m/z of 66 amu based on its most abundant isotope could also be clearly distinguished from any other likely beam species given that the other candidate species would be transition metals such as Cu^{+}, Zn^{+}, and Ga^{+} which should not be present in the beam.

It was shown that Ar could produce doubly ionised species at the typical operating power of 200W. The Ar^{2+} spot at an m/z of 20 amu could also be attributed to Ne^{+} however given that no Ne is utilised in the PFIB system, this peak can be clearly identified as Ar^{2+}. Studies on a nitrogen ICP source at powers of up to 400W have demonstrated that the production of N_2^{2+} species is undetectable, with the dissociated N^{+} species being far more likely [180]. N_2^{2+} would also overlap with the N^{+} and distinction would be impossible. Studies on Oxygen ICP sources at powers of up to 300W have also been unable to detect doubly ionised O_2^{2+}, once again demonstrating the dissociation to O and O^{+} species to be far more likely [181]. It is impossible to doubly ionise an H_2 molecule as there would be no electrons remaining to facilitate bonding, and this would be the equivalent of two free H^{+} ions.

Another consideration is the possibility of chemical reactions occurring in the plasma source. Ar, while typically considered a non-reactive noble gas, is ca-

pable of forming molecules with various other species in the plasma. These molecules are referred to as polyatomic interferences and are particularly prevalent in ICP mass spectrometry where the Ar carrier gas can form molecules with analyte species. These interference molecules can lead to incorrect identification of species such as, $^{40}Ar^{12}C$, $^{40}Ar^{16}O$, $^{40}Ar^{35}Cl$, and $^{40}Ar^{40}Ar$, mistakenly identified as ^{52}Cr, ^{56}Fe, ^{75}As, and ^{80}Se [182]. These polyatoms fall between the primary m/z peaks of Ar at 40 amu and Xe at 132 amu. With no other ions being expected between these two masses, this makes identification of Ar polyatomics simple.

Hydrogen Molecules

Understanding the formation of the various hydrogen molecules in an ICP is fundamental to the performance of the VLE-PIXE technique. The reaction pathways taking place in the plasma leading to the formation of the primary hydrogen molecules H^+, H_2^+ and H_3^+ are [183]:

$$
\begin{aligned}
H_2 + e &\rightarrow H_2^+ + 2e \\
H_2 + e &\rightarrow 2H + e \\
H_2^+ + e &\rightarrow H^+ + H + e \\
H_2^+ + H_2 &\rightarrow H_3^+ + H \\
H + e &\rightarrow H^+ + 2e \\
H_3^+ + e &\rightarrow H + H_2 \\
H_3^+ + e &\rightarrow H^+ + 2H + e
\end{aligned}
$$

The ratio of these species however is highly dependent on the plasma conditions such as pressure, power, electron density, chamber size, and electron temperature. Fukumasa et al. demonstrated that changing the source pressure from 1×10^{-4}mbar to 1×10^{-3}mbar can drastically shift the molecular ratios of H^+, H_2^+ and H_3^+ from 70%/15%/15% to 10%/30%/60% with all other parameters remaining constant [183]. For this reason, determination of the ratio of hydrogen molecular species can only be carried out by accurate characterisation of the currents of each individual hydrogen species at the sample using the methods described in this chapter.

2.2.3 Beam Component Currents

Once the beam components have been identified, quantification of each beamlet species can be carried out. For these measurements, a standard Faraday cup

design will not work as all charged particles hitting the top surface of the cup will register a current and only the total beam current will be measured. A special Faraday cup must be used such that any particles striking the top surface of the cup are rejected and only those which enter through the aperture will be measured. The development and characterisation of this special Faraday cup, dubbed the "isolating" Faraday cup is outlined in appendix section A.2.

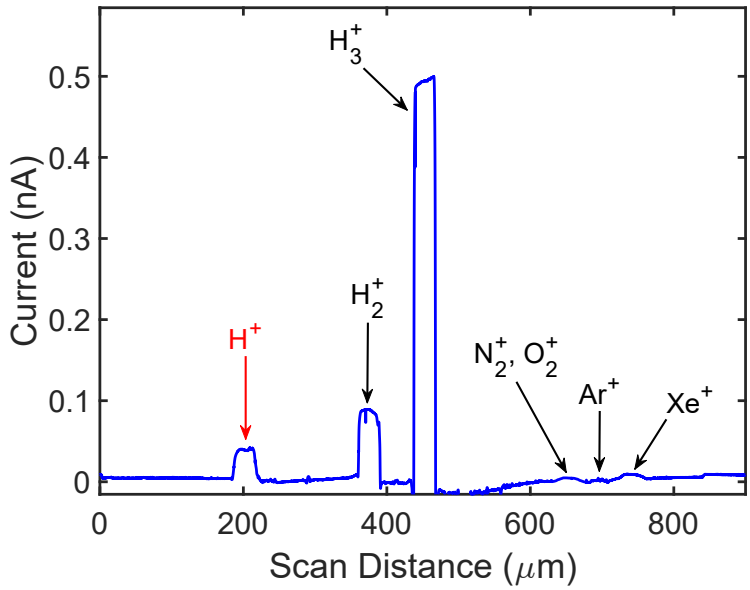

Figure 2.7: Beamlet current scan of a 650pA, H_2 beam from a 200W plasma with peaks labelled.

Figure 2.7 shows the result for a 200W hydrogen plasma where the current of each beamlet can be expressed as a percentage of the total beam composition. In this scan, the species H^+, H_2^+, and H_3^+ can be identified as well as contributions from the N_2^+, O_2^+, Ar^+ and the Xe^+ species. The percentage composition of this beam is shown in table 2.1.

Species	**Percentage Composition**
H^+	6%
H_2^+	14%
H_3^+	78%
N_2^+, O_2^+	$<$1%
Ar^+	$<$1%
Xe^+	$<$1%

Table 2.1: Percentage composition of a 650pA, H_2 beam from a 200W plasma.

Influence of Plasma RF Power on Beam Composition

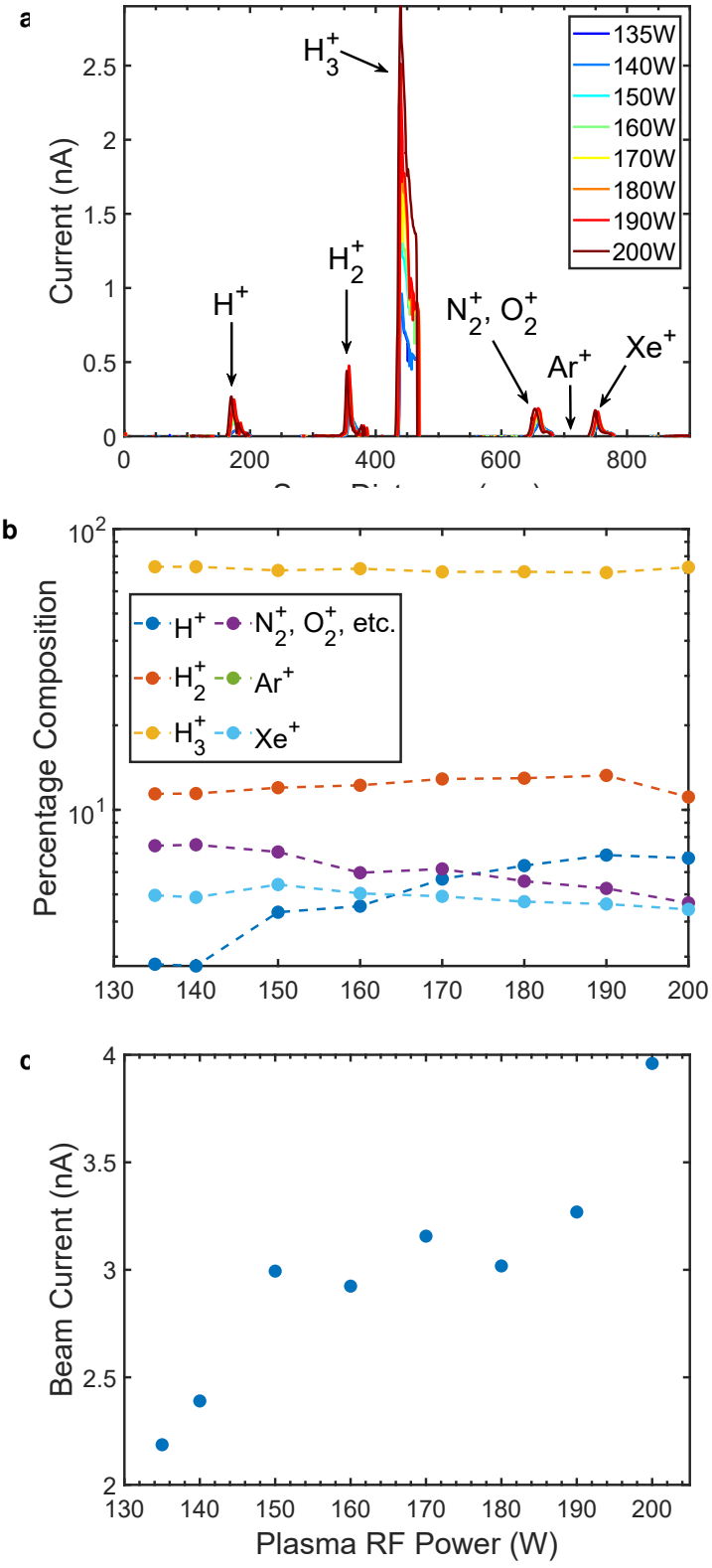

Figure 2.8: (a) Beamlet current scans vs. plasma source RF power, (b) Percentage change of beamlet current intensities vs. RF power. The dashed lines are a guide to the eye. (c) Integrated current change vs. plasma power.

The RF power used to generate the source plasma can alter the composition of the hydrogen ion beam due to changes in plasma density and electron temperature affecting reaction pathways in the source plasma [183]. The beam composition was measured as a function of plasma source RF power to establish the optimum RF power for proton production. As shown in figure 2.8b, increasing the plasma RF power results in an increase in the percentage of H^+ ions in the beam as well as a corresponding increase in the total beam current as shown in figure 2.8c. Operating the plasma source at the highest possible RF power will therefore achieve both the greatest beam current and the highest proportion of protons in the hydrogen beam. Increasing plasma power however also leads to an increase in the temperature of the plasma chamber which may result in permanent damage to the plasma source. For this reason, a power of 200W was deemed to be the maximum safe working RF power.

Influence of Total Beam Current on Beam Composition

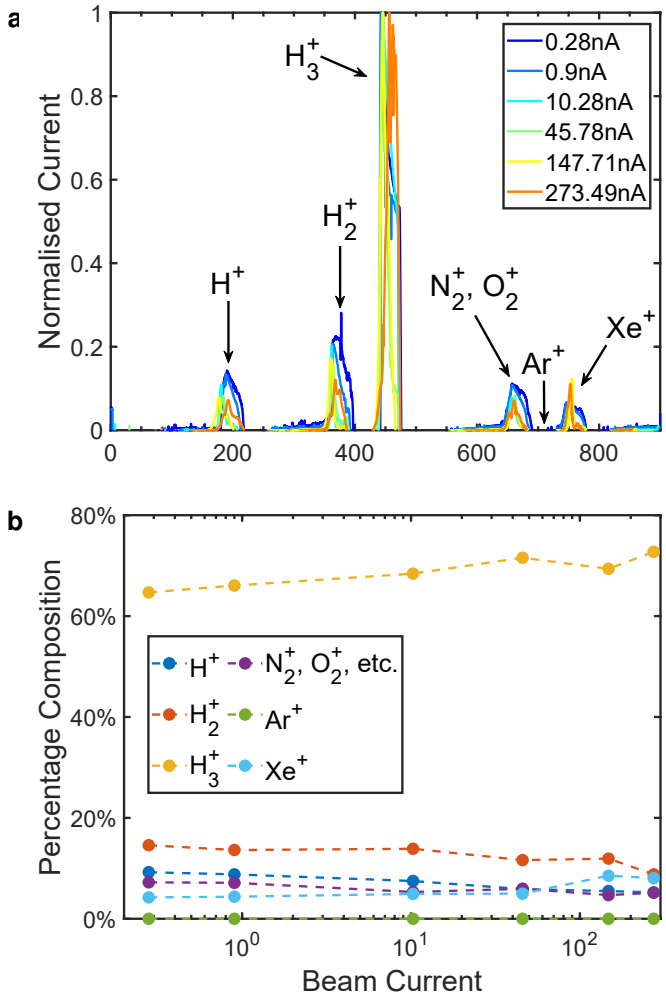

Figure 2.9: (a) Beam composition spectra vs. beam current. (b) Quantified beam composition vs. beam current. Dashed lines are a guide to the eye.

During VLE-PIXE measurements, due to the relatively low percentage of H^+ ions (protons) within the beam, high currents must be used to generate a sufficient X-Ray signal for analysis. Compositional current measurements were carried out to determine whether increasing the beam current would have any influence on the proportion of species in the beam. Figure 2.9b demonstrates only a small change in beam composition over several orders of magnitude change in beam current. For this reason, beamlet characterisation can be effectively performed at lower currents where the beam spot size is smaller, giving better separation between beamlets, as well as reduced damage to the isolating Faraday cup, particularly when characterising doped beams with a greater sputter yield due to the presence of heavy ion species.

2.2.4 Pure and Doped Hydrogen Beams

Due to the residual contamination remaining in the FIB source during source species switching, achieving a high purity hydrogen beam posed a significant challenge. Several contaminant species were commonly observed in the beam such as N_2^+, and O_2^+ likely from atmospheric contamination, and Ar^+ and Xe^+ which are due to residual contamination from previous ion source species and previous beam doping experiments.

While the gas delivery system and the plasma source are pumped using the PFIB vacuum system during gas source switching, the effectiveness of this pumping in reducing contamination is dependent on the pumping time prior to introducing the next gaseous source species. The pumping speed in this situation is limited not by the pump but by the gas flow rate, dictated by the conductance of the system [184]. Several factors such as the long, thin tubing used in the gas delivery lines, the metered orifice at the entrance of the plasma chamber, and apertures separating the differential pumping zones in the FIB column limit the conductance of the vacuum system and result in contaminant gas molecules remaining in the system if a sufficiently long pump cycle is not used.

In applications where a high purity hydrogen beam is required, the gas delivery system and plasma source chamber were manually pumped for an extended period of time, typically overnight. Figure 2.10 demonstrates the difference in beamlet current spectra when the FIB source is pumped overnight between switching from an Ar to H beam, compared to when the source gas is switched from Ar to H with a shorter pumping cycle. The overnight pumping cycle reduces the Ar value to less than 1% of the beam composition.

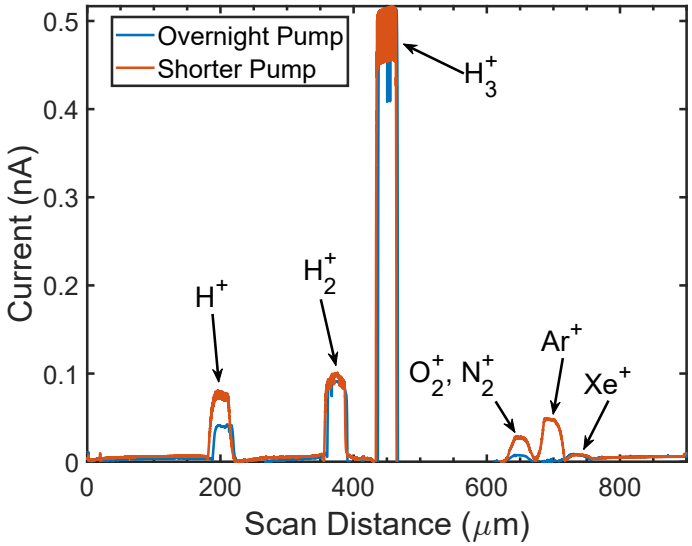

Figure 2.10: Beam compositional current measurement of Hydrogen beam after overnight pumping, and using shorter pumping cycle designed to achieve a lightly doped hydrogen beam.

To reduce the contaminant species even further, additional efforts are required such as multiple purge cycles, where the desired gas species is introduced and pumped out several times to enable scrubbing of residual gases from the system. Multiple purge cycles however waste a significant amount of high purity source gas which can be costly and require frequent changing of the source gas bottle. To perform critical experiments where no influence of other beam species is desired, the splitting technique described in section 2.2.1 is used to separate the beam components which can be directed towards different regions on a sample. This technique was used for example to isolate the X-Ray signals generated upon a sample region by a specific ion species as is described in section 3.1.1.

Utilising a shorter pump cycle allowed a small amount of Ar to remain in the beam, which is typically undesirable when a high purity hydrogen beam is required, however presented a simple way to achieve a lightly doped hydrogen beam without requiring additional gas mixing in the source gas delivery system. A lightly doped ($<$ 10%) beam could be simply achieved by starting with a source comprised of the desired dopant species and switching to the hydrogen beam with a modified pumping cycle such that a significant proportion of the dopant species remained in the plasma source and gas delivery lines. While this method did not give a significant amount of control over the proportion of dopant species, post-characterisation of the beam composition was typically performed, and the the measured beam composition could be accounted for in any experimental data. Achieving a more heavily doped beam required gas mixing in the plasma chamber, a method for which is described in section 5.3.

2.3 Beam Scattering

As the ions travel from the source plasma, through the FIB column, through the microscope chamber and eventually to the sample, they encounter several regions of varying pressure due to the construction of the FIB source. Scattering between the primary beam and the gas molecules can lead to neutralisation of the primary ion species [185, 186], loss of energy of the primary ions, [185] generation of secondary electrons through collision events [187], generation of secondary ions of the gaseous species [188], and loss of resolution of the beam through deflection of the primary ions [189, 190, 191, 192]. Of most relevance to VLE-PIXE is the generation of secondary electrons, ions and neutral molecules, as these secondary particles may be capable of producing X-Ray signals of their own which can confound the results of proton impact induced X-Ray emission. Higher pressures lead to a greater number of scattering events due to collisions between the primary beam species and the higher number of gas molecules contained within this region and as such, knowledge of the scattering behaviour of the column is essential to repeatable and reproducible VLE-PIXE experiments.

2.3.0.1 FIB Column Scattering

In a typical LMIS FIB column, the source is kept at high or ultra-high vacuum ($\sim 1 \times 10^{-8}$ mbar) which is required for field ionisation to take place. This vacuum is maintained by a combination of a Turbo Molecular Pump (TMP), and an Ion Getter Pump (IGP) which is also capable of measuring pressure. The pressure gradually increases down the FIB column towards the microscope chamber until it reaches its highest pressure in the microscope chamber, which is kept at pressures of $\sim 1 \times 10^{-6}$ mbar. The plasma FIB differs significantly from the LMIS in that the FIB source is no longer maintained at high vacuum and in fact, is the highest pressure region in the entire microscope, operating at pressures close to atmospheric pressure.

The FIB columns are separated into several pressure zones referred to as differential pumping (DP) zones, where the pressure can vary significantly. These DP zones are separated by pressure limiting apertures (PLA) which allow the beam to pass through while limiting the flow of gas between the zones [5]. Additionally, column isolation valves allow the microscope chamber to be vented to atmosphere whilst maintaining the vacuum conditions in the column. These valves are opened once the chamber has reached a sufficient vacuum level. A

rough schematic of the LMIS FIB and PFIB vacuum systems including DP zones are shown in figure 2.11.

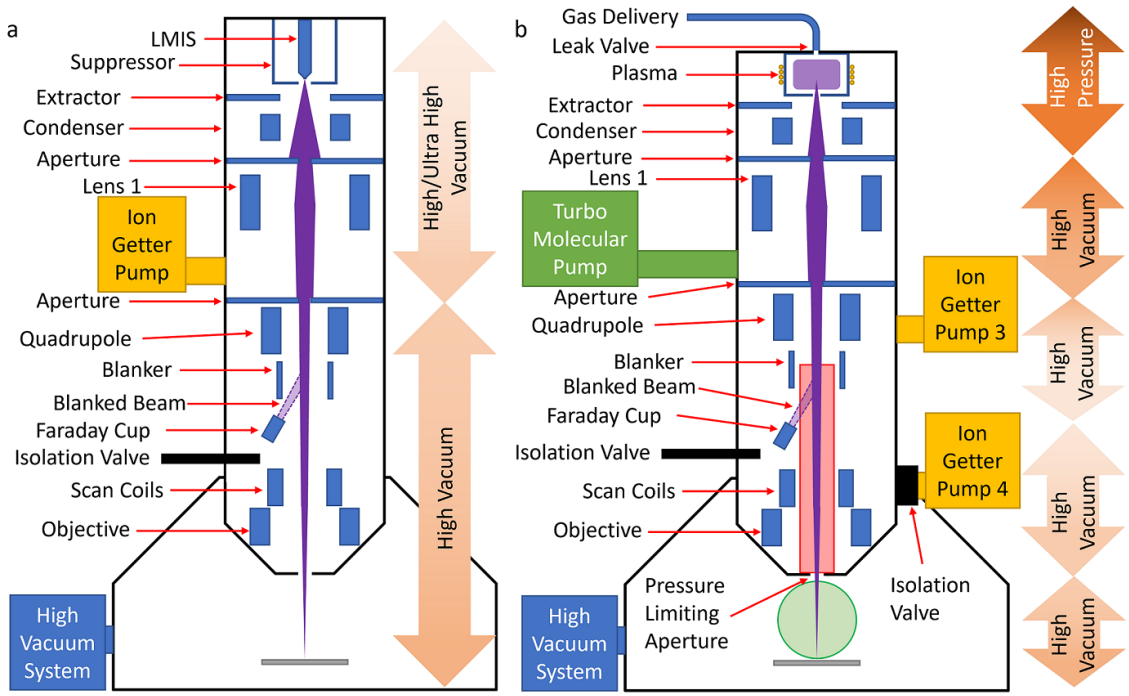

Figure 2.11: A rough schematic of the vacuum systems of (a) an LMIS FIB, and (b) a plasma FIB. Approximate pressure gradients in each configuration are displayed as orange arrows. The lower FIB column scattering region is marked with a red rectangle and the chamber scattering region with a green circle.

In the PFIB, part of the lower column region below the isolation valve is exposed to atmosphere upon microscope chamber venting. When the chamber is pumped down, this section of the column is pumped out through the microscope chamber, however due to the PLA at the base of the column, the pumping is slow and higher pressures than typical can persist in this region for several hours following chamber pump-down. Several important components are located in this region such as the internal Faraday cup, used for measuring the beam current and the objective lens, used to focus the beam onto the sample. This lower column region is approximately delineated by the start of the beam blanker and shaded in red in figure 2.11b.

In order to not expose IGP4 which is situated in the lower column region, to a higher than necessary pressure, a valve isolates IGP4 from the lower column until the vacuum in the microscope chamber reaches a sufficient value. This valve can stay closed for over an hour following chamber pump-down resulting in an even slower decrease in pressure in the lower column region. The combination of the PLA limiting gas flow away from the lower column region and the isolation valve preventing IGP4 from pumping the lower column leads to a situation where the

pressure in the lower column region can significantly impact beam performance due to beam scattering. This effect is shown to persistently influence VLE-PIXE measurements, even after this region has reached its ultimate pressure.

Scattering in the lower FIB column can be measured using the in-built Faraday cup in the column. Under normal circumstances when the beam is unblanked, the ions are free to travel down the column and interact with the sample. When the beam is blanked using the blanking electrodes, the beam is deflected into the Faraday cup and the beam current can be measured. Under unblanked operation when the beam bypasses the Faraday cup, some ions may inadvertently scatter off gas molecules in the column and enter the Faraday cup, which will register a current on the external picoammeter. The degree of scattering and therefore the number of ions entering the Faraday cup is proportional to the number of gas molecules in the column and will result in an increased current being measured. This is shown diagrammatically in figure 2.12.

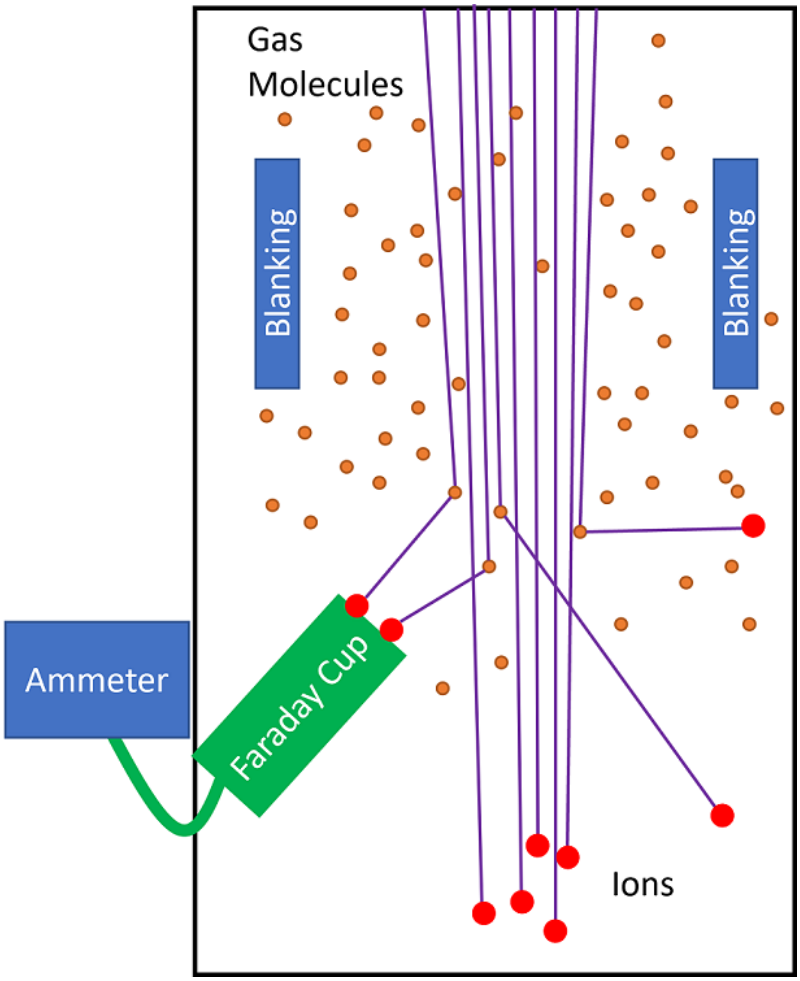

Figure 2.12: Schematic of the inadvertent scattering of ions into the Faraday cup due to interaction with gas molecules, resulting in the registration of current on the external picoammeter.

Figure 2.13 shows the current generated in the internal Faraday cup by the scattering of a 2nA, 2keV Xe beam, taken as a function of time following the vacuum ok condition after microscope chamber pump-down. The beam conditions were chosen to represent the scattering caused by the addition of a heavy ion dopant species, where the scattering cross section is maximised due to the heavy mass of the Xe ion.

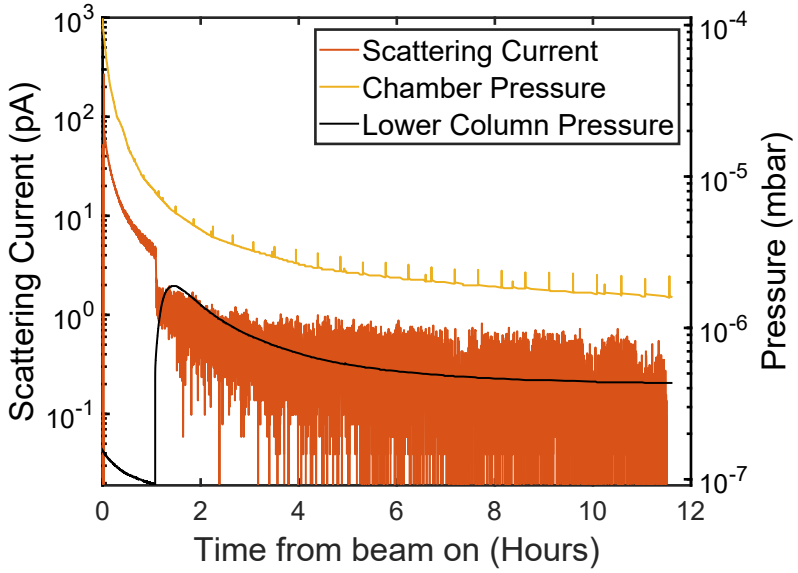

Figure 2.13: Column scattering current of a 2nA, 2keV Xe beam, chamber pressure, and lower FIB column pressure as a function of pump-down time.

The scattering current is shown to be maximum immediately after the beam was turned on, where the pressure in the lower column is at its highest point and the IGP4 has not yet been exposed to the lower column. The column scattering current reaches a maximum of $\sim$5% of the total beam current however due to the size and location of the Faraday cup, only a small portion of the scattered ions will be collected by the cup and the extent of the scattering will be much greater than is represented by this measurement.

After a period of approximately 1 hour, the valve isolating IGP4 from the lower column is opened and IGP4 begins to report the pressure of the lower FIB column. This is immediately followed by a spike in IGP4 pressure as it is exposed to the lower FIB column and demonstrates that there is still a significant pressure remaining in this region, even after an hour following chamber pump-down. As this occurs, a decrease in scattering current is observed as the gas molecules expand into the evacuated region of the IGP, resulting in a decrease in pressure and a reduction in scattering. This is further evidence that gas scattering is responsible for the measured current.

The scattering current is then shown to decrease exponentially in line with the de-

crease in pressure of both the chamber and the lower FIB column. The scattering current however is shown to never reach zero, even after an extended period of pumping and demonstrates that some level of scattering will always take place in the lower column due to its construction. This effect must be considered when performing VLE-PIXE measurements. Analysis of the products of the lower column scattering and their influence on the VLE-PIXE measurements are given in section 3.2.

2.3.0.2 Chamber Scattering

Once the ions have left the FIB column, further scattering may occur as a result of interaction with gas molecules in the microscope chamber, the region marked with a green circle in figure 2.11. This will be in addition to the scattering within the lower FIB column as some ions which scatter in the column may also be scattered in the microscope chamber.

The beam exiting the column can be separated into three components:

- The primary beam spot: Some percentage, usually 50% of the beam current is contained here and is commonly referred to as the d_{50} value or the diameter containing 50% of the beam.
- The beam tails: The majority of the remaining current which decays exponentially as a function of distance from the beam axis for Gaussian beam shapes [53].
- The beam skirt: Ions scattered to a significant distance (microns to millimetres) from the primary beam axis. A beam skirt forms due to high angle scattering events, or at locations far above the sample. Beam skirts have been studied in detail in environmental scanning electron microscopy (ESEM) where they are significant due to high angle electron-gas scattering [193].

The current contained in the beam skirts due to scattering in the the FIB column and microscope chamber could be directly measured using the isolating Faraday cup. The construction of this Faraday cup allowed measurement of only the beam current falling within the aperture and the rejection of the beam current falling outside the aperture. This allowed the primary beam spot and tail current to be distinguished from the skirt current and could be measured dynamically alongside chamber and column pressure as a function of time from chamber pump down. The details of this experiment are shown diagramatically in figure 2.14.

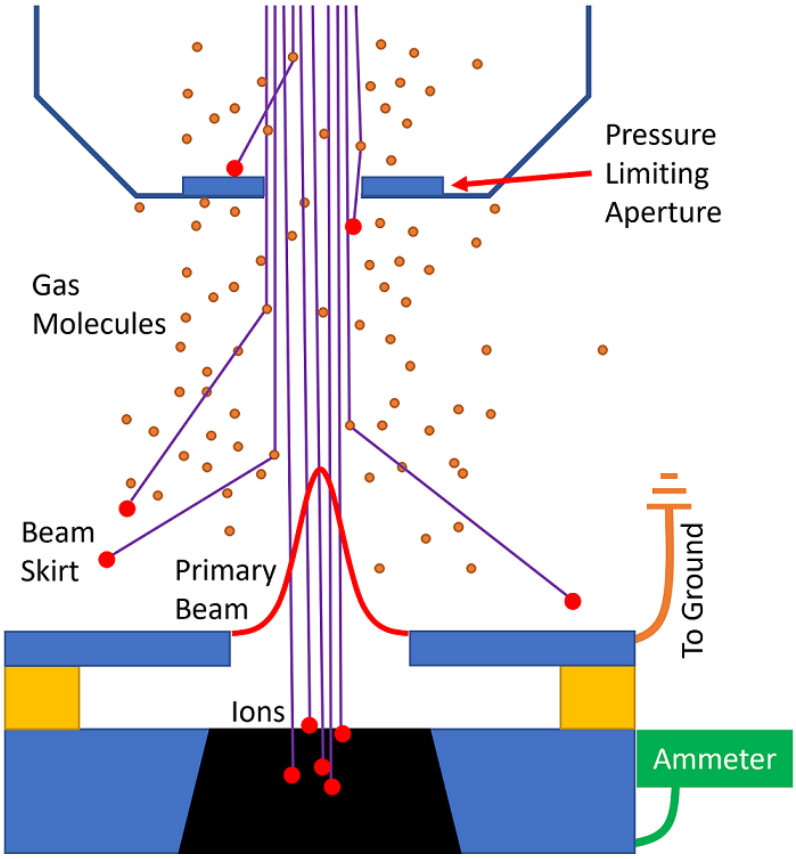

Figure 2.14: Schematic of the experiment performed to measure the current contained within the beam skirt relative to the current contained in the primary beam and beam tails.

For this experiment, the same beam conditions as the column scattering experiment were used, utilising a 2nA preset, 2keV Xe beam. A spot burn of this beam was taken during chamber pump-down in order to measure the size of the primary beam spot and tails as shown in appendix figure A.9. It was determined that an aperture diameter of 70μm was sufficient to capture the primary spot and tails whilst isolating the beam skirt.

The experiment was initiated following a vacuum ok condition at a chamber pressure of $<1\times10^{-4}$mbar. To perform this experiment, the beam was blanked in order to measure the current entering the Faraday cup in the column, then unblanked to measure the current landing upon the isolating Faraday cup at the sample. This cycle was repeated in 30 second intervals, allowing the current in each condition to settle for 15 seconds. The result of this experiment is shown in figure 2.15. The current initially measured by the Faraday cup in the column is shown to be 11.2% lower than the equilibrium column current. This is likely due to scattering of the beam in the lower column prior to entering the column Faraday cup and is reflective of the measurements shown in figure 2.13.

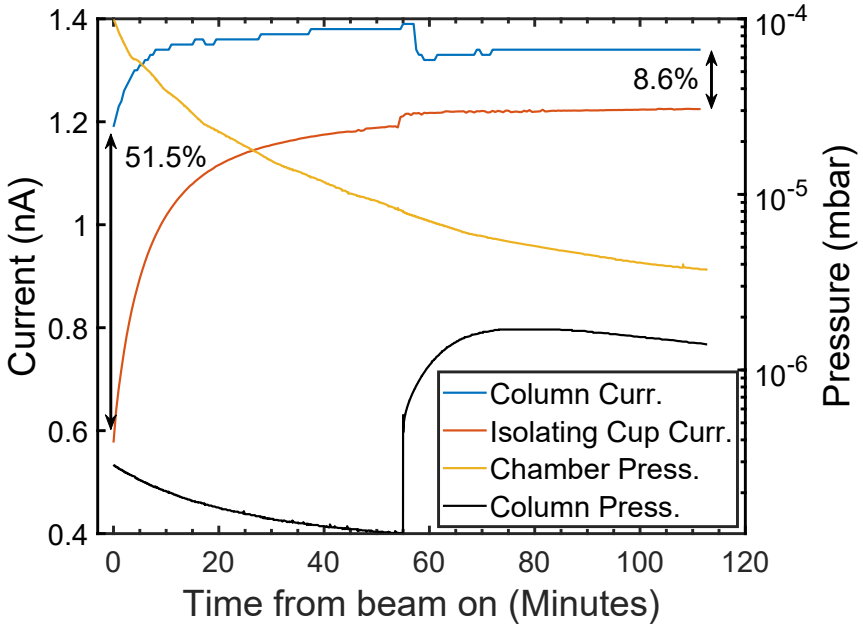

Figure 2.15: Chamber scattering current of a 2nA, 2keV Xe beam, chamber pressure, and lower FIB column pressure as a function of pump-down time.

The measured initial variation in current between the column Faraday cup and the primary beam and tails falling within the isolating Faraday cup is 51.5%. This demonstrates that the majority of the beam is lost due to scattering in the FIB column and the microscope chamber at the initial stages of this experiment. A variation of 8.6% between the column Faraday cup and the isolating Faraday cup after 2 hours demonstrates that even after a significant period of time, several percent of the beam continues to be lost due to column and chamber scattering.

The small jump in current of the isolating Faraday cup at a time of approximately 43 minutes once again corresponds to the opening of the pressure isolating valve which exposes IGP4 to the lower FIB column. The IGP4 pressure is displayed in figure 2.15 as column pressure and a corresponding spike in this pressure is seen. This demonstrates the importance of allowing the chamber and the lower column to pump for an extended period of time following chamber pump-down to attain accurate experimental results.

2.3.1 Beam Skirt Visualisation

To help visualise the extent of the beam skirts, a 20 minute spot-burn of a 2keV Xe beam on an Si(100) wafer was taken under the same conditions as the previous experiments. In this experiment however, the beam current was increased to its maximum value of approximately 40nA in order to induce a large contrast change on the sample. Figure 2.16 shows a tilted SEM image of the 2keV, 40nA Xe beam

spot burn taken during chamber pump-down with the primary beam spot, beam tails, and beam skirt labelled.

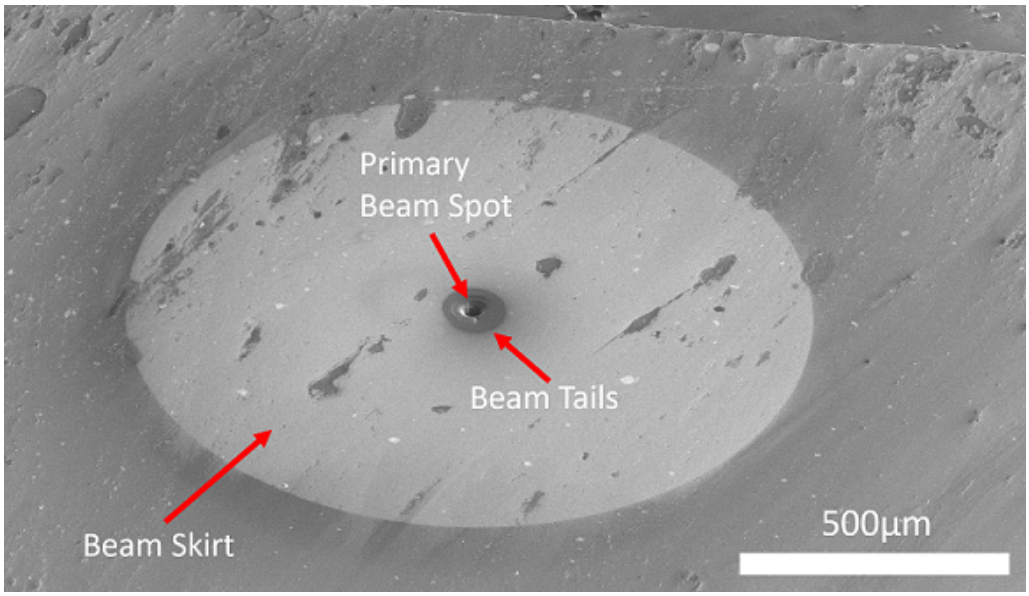

Figure 2.16: A tilted SEM image of a 2keV, 40nA Xe beam spot-burn taken during microscope chamber pump-down.

The bright region surrounding the primary beam spot and beam tails is attributed to the impact of the skirt particles upon the sample. The homogeneous distribution of this bright region is reflective of the random scattering of primary ions from the gas molecules in the lower FIB column and chamber. The abrupt edge of the beam skirt is likely caused by the PLA at the base of the FIB column blocking particles scattered in the lower FIB column from reaching the sample.

The particles scattering in the chamber will strike closer to the primary beam spot as they scatter closer to the sample plane. The particles scattering in the column will travel further radially from the beam axis if scattered through the same angle, due to their longer path length. This is likely the reason why the extent of the beam skirt is limited by the diameter of the PLA and not diffuse as a result of chamber scattering.

2.4 Optimised Operating Parameters

Source Plasma

- Gas supply regulator should be adjusted to achieve 2-4$\times 10^3$ mbar as measured on the Pirani Pressure Gauge (PPG)
- Plasma chamber outlet pressure should be in the range of 6-7$\times 10^{-6}$ mbar as measured on the Cold Cathode Gauge (CCG)
- Plasma power should be set at 200W or greater if there is no risk of damage.

Beam Splitting

- For beam splitting, the immersion lens coil 2 current should be adjusted to modify the strength of the magnetic immersion field
- A coil current of $\sim$2.04 amp turns corresponds to a converged beam and a coil current of 0 amp turns for 30keV at eucentric corresponds to a separation between the lightest (H^+) and heaviest (Xe^+) species of $\sim 550\mu$m

High Purity Hydrogen Beam

- FIB gas delivery lines and plasma chamber should be pumped ideally overnight to remove residual gas species.
- For very pure beams, the desired gas is introduced into the system, then pumped out for an extended period of time, then reintroduced for ignition.
- Beam splitting should be used for isolation of individual components.

Lightly Doped Hydrogen Beam

- Starting with a source of the desired dopant species, the beam is to be switched to hydrogen with a modified pumping cycle.
- A Pre-Vacuum Pump (PVP) delay of 10 seconds and a TMP delay of 10 seconds will achieve $\sim$10% of dopant species with a balance of hydrogen.

Beam Scattering

- Microscope chamber should be pumped for a minimum of 2 hours following vacuum OK condition before experiments commence.
- IGP4 pressure in lower FIB column should be monitored and allowed to equilibriate before commencement of experiments to avoid change in beam current or composition during experiments.

Chapter 3

VLE-PIXE: Signal Generation and Spectral Artefacts

Previous claims of PIXE observed in a FIB microscope utilising Ga+ ions [194] have been disproven. The results are an artefact caused by backscattered ions originating from a charging, insulating sample. These ions are accelerated away from a charging sample, and generate secondary electrons upon impact with grounded surfaces (e.g., the pole piece), known as type III secondary electrons. The secondary electrons are then accelerated towards the positively charged sample and generate characteristic X-Rays. The electrostatic potentials generated by such an insulating sample have been shown to be on the order of several tens of kV [22]. Another indication that the signal did not originate from the Ga^{+} ions was the presence of an intense Bremsstrahlung background, typical of a SEM-EDS spectrum, however not present in PIXE spectra at such low energies. The generation and analysis of X-Rays through the re-acceleration of secondary electrons towards a charged sample is referred to some as charge induced X-Rays (CHIX) [195].

The following chapter outlines the experiments performed to verify that the detected X-Ray signal is indeed generated as a result of proton impact on the sample. Additionally, the role of spurious signals generated by the microscope and associated equipment such as stray electrons, neutralised ions, and backscattered ions are analysed as well as other spectral artefacts, such as those originating from the EDS detector itself. Optimised operating parameters are outlined to reduce the impact of these spurious signals on the VLE-PIXE measurements.

3.1 Hydrogen Contribution to PIXE Spectra

3.1.1 Proton Contribution

As discussed in section 1.3.4, the greatest PIXE XRPCS originates from protons due to their light mass and therefore high velocity. XRPCS decreases rapidly with increasing ion mass, such that even He^+ ions with a mass of 2 amu are incapable of generating sufficient X-Rays [196]. For this reason, the greatest contribution to the VLE-PIXE is expected to be from protons.

As described in section 2.2.1 the magnetic immersion field allows the ion beam to be spatially separated into its individual mass components. The separated beam components could then be directed towards a binary sample comprised of a 1μm aluminium layer sputter coated over half of a single crystal Cu (100) substrate. By moving the separated beam over an interface between the different materials on the binary sample, the X-Ray signal contributions from each beam species could be determined. This experiment is visually represented in figure 3.1 where false colour SEM images of the irradiations are given for each condition. The Cu substrate is shaded in red, and the Al deposited layer is shaded in blue.

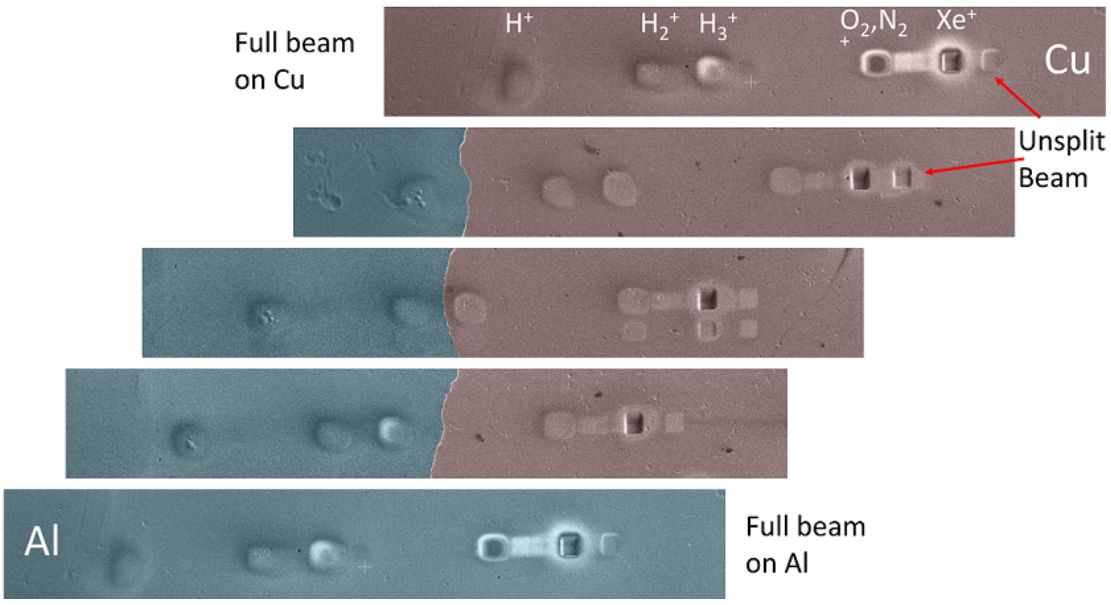

Figure 3.1: False colour SEM images of the spot-burns created as a result of the beam component contribution experiment. Cu substrate is shaded in red, Al deposited layer is shaded in blue.

A 2nA preset, 30keV hydrogen beam was measured prior to the experiment and as shown in figure 3.2a, the composition was shown to be: 10.84% H^+, 11.94% H_2^+, 53.14% H_3^+, 5.69% O_2^+ and N_2^+, and 18.37% Xe^+ with no detectable Ar signal.

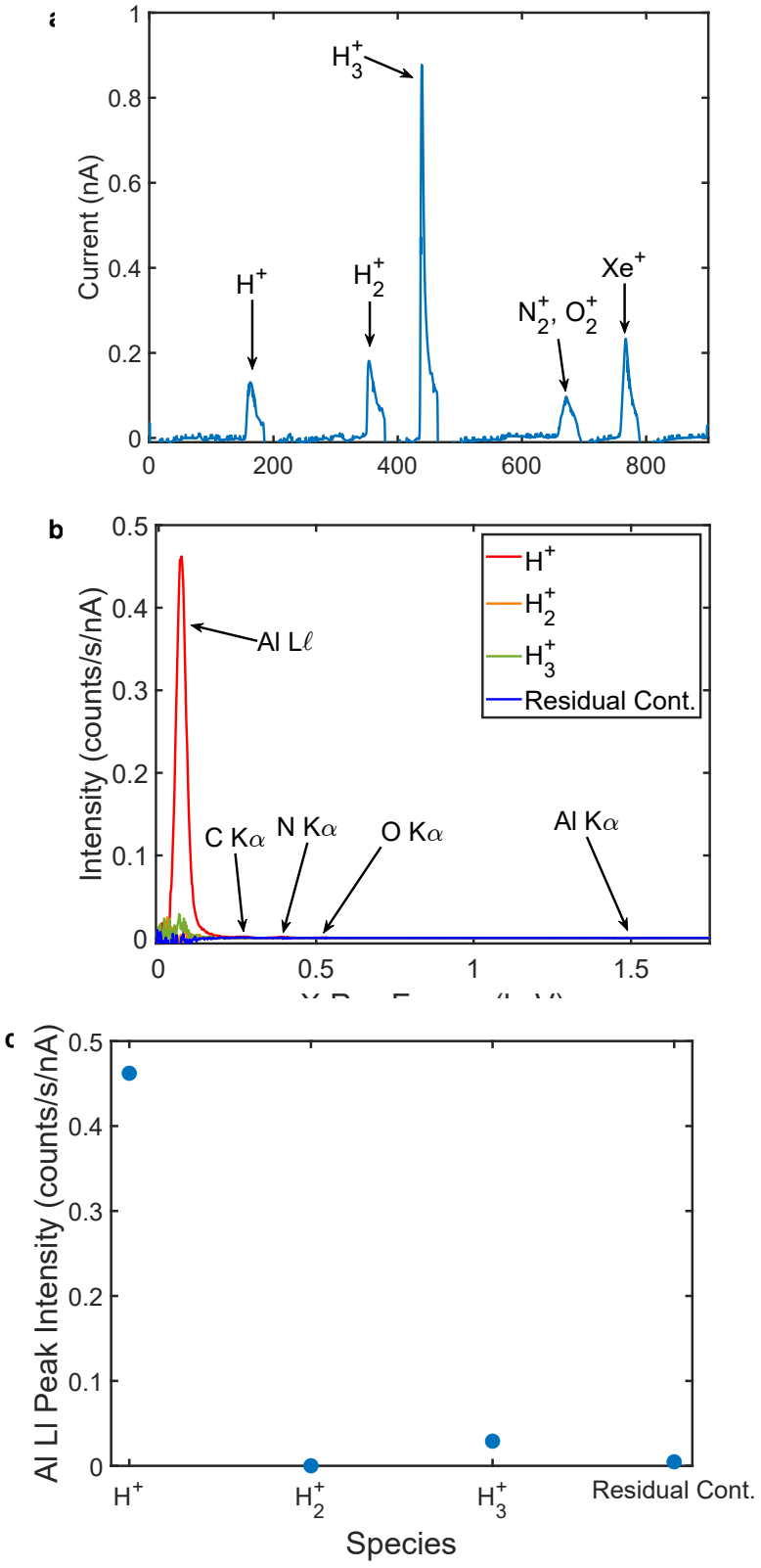

Figure 3.2: (a) Beam composition current measured prior to the experiment. (b) Successively subtracted 30keV VLE-PIXE spectra for each beam component (c) Measured spectral contribution to the Al Lℓ X-ray spectrum for each beam component demonstrating the predominant X-Ray signal originating from H^+ ions.

The beam was aligned such that only the H^+ component fell upon the Al film and the remainder of the beam fell upon the Cu substrate. An X-Ray spectrum was captured for 20 minutes. The stage was then moved such that now both the H^+ and H_2^+ components fell upon the Al film. This was repeated for the remaining beam components and the spectra for each condition were compared. The spectrum from each successive irradiation was subtracted from the prior so that the contribution from each species could be isolated. The highest intensity Al peak, the Al Lℓ line was used for identification of the signal from the Al film. Due to proximity of the Al Lℓ line to the noise peak of the detector, the noise peak was subtracted from these spectra, the details of which are covered in section 3.3.1.

As shown in figure 3.2b, majority of the X-Ray signal originates from the impact of H^+ ions (protons) upon the sample. These spectra are normalised to the irradiation time of 20 minutes and the relative current of the species based on the percentage composition of each of the species in the beam. Use of the magnetic immersion lens for beam separation in this experiment also has the added benefit that any stray electrons generated as a result of ion collision with residual gas molecules as discussed in section 2.3, would be deflected away from the sample. The contribution of these electrons to the VLE-PIXE spectra are discussed in section 3.2.3.

The signal generated by protons alone, while being the dominant contribution to the spectra, is still much weaker than the signal generated when the hydrogen beam is doped with a heavier ion species. This can be determined by the absence of the Al Kα line at 1.486keV in figure 3.2b, compared to the doped beam spectrum in figure 4.2a, despite the concentration of Al in figure 4.2a being significantly lower. The presence of the Al Kα line, with a much lower XRPCS than the Al Lℓ line, demonstrates that beam doping, and in particular the overlapping of the doped beam components is essential in producing a large quantity of X-Rays during VLE-PIXE measurements, and is important for the identification of minor and trace elements in a sample.

3.1.2 Hydrogen Molecule Contribution

Despite being higher in proportion than the H^+ ion, the contribution of the H_2^+ and H_3^+ molecules are negligible as seen in figure 3.2c. A possible explanation for this result may be the behaviour of particles upon fragmentation or dissociation at or near the sample surface. Eckstein et al. demonstrated that upon impact with a surface, the fragmentation of a molecule such as an H_n^+ molecule (or anal-

ogous D_n^+ molecules) will produce nH^+ ions with an equal proportion of energy per fragment such that:

$$E_i = \sum^{n} E_f \tag{3.1}$$

where E_i is the initial molecule energy and E_f is the energy of each fragment. If we assume that on average the energy will be perfectly equipartitioned, E_f will be equal to:

$$E_f = (1/n)E_i \tag{3.2}$$

This is shown in figure 3.3 where the energy of the dissociated molecules matches the fractional energy scaling described above.

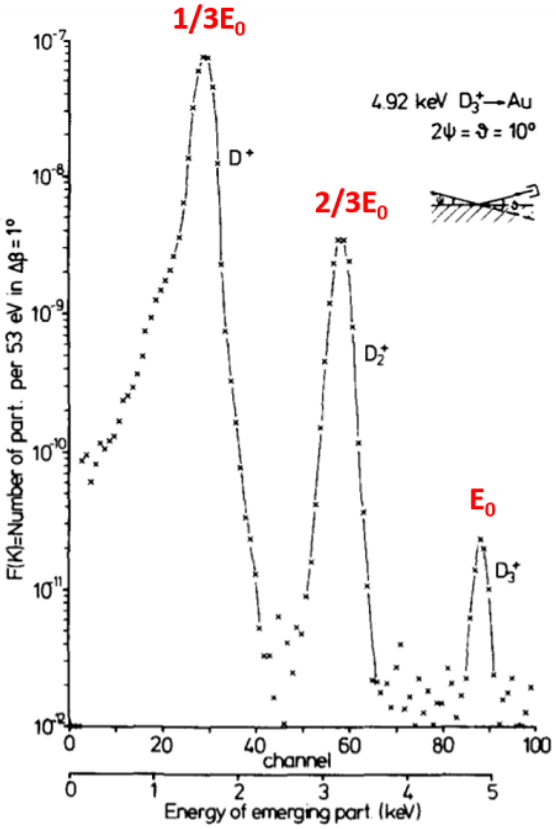

Figure 3.3: Energy spectrum of atomic, and molecular deuterium fragments reflected from a gold surface. (From [197])

It is therefore expected that the H_2^+ and H_3^+ molecules dissociate into 2 and 3 H^+ ions with 1/2 E_i and 1/3 E_i respectively, which in this case would be 15keV and 10keV. Spectra of the Al film were taken with an undoped hydrogen beam at accelerating voltages of 30keV, 15keV, and 10keV as shown in figure 3.4.

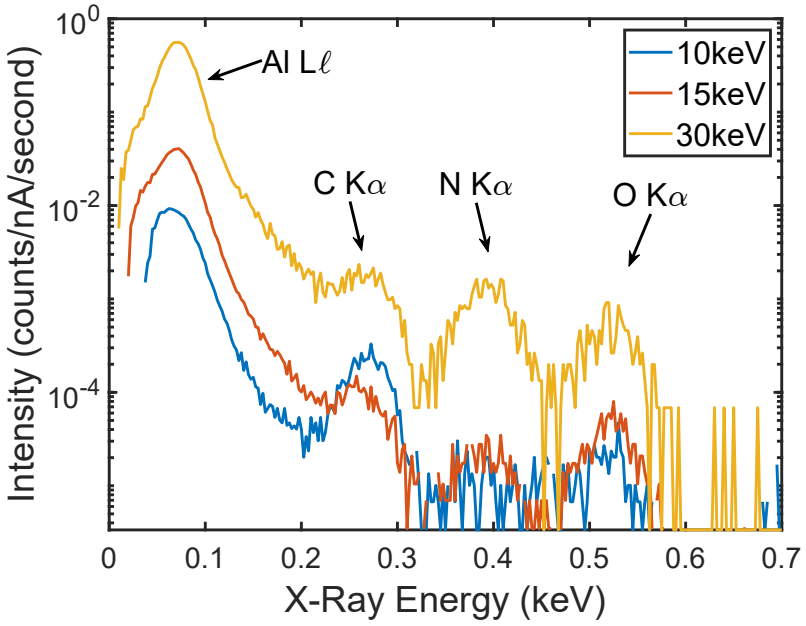

Figure 3.4: Undoped hydrogen beam VLE-PIXE spectra of the Al film vs. accelerating voltage.

Despite the lower energy, Al Lℓ peaks generated by the 15keV and 10keV beams can still be clearly identified. From the perspective of energy alone, the H_2^+ and H_3^+ molecules should therefore still be capable of producing a signal upon the Al sample following fragmentation and would produce a much greater signal in figure 3.2b. As discussed in section 1.3.4.3 however, the ionisation cross section is a function of particle velocity and not energy. It is therefore important to consider the change in momentum upon particle fragmentation. Using Newton's equation, equation 3.2 can therefore be expressed as:

$$E_f = (1/n)\frac{1}{2}m_i v_i^2 \tag{3.3}$$

where m_i and v_i are the molecule's initial mass and velocity respectively. Conservation of momentum therefore dictates that:

$$p_i = \sum^{n} p_f \tag{3.4}$$

As the fragments will all possess the same mass, and on average the same velocity, the same equipartitioning treatment can be applied as above:

$$p_f = (1/n)p_i \tag{3.5}$$

Using the relationship $p = \sqrt{2mE}$:

$$(1/n)p_i = (1/n)(2m_iE_i)^{1/2} = (1/n)(2m_i \times \frac{1}{2}m_iv_i^2)^{1/2} = (1/n)m_iv_i$$
$$p_f = m_fv_f = (1/n)m_iv_i \tag{3.6}$$

As the mass of the initial molecule (m_i) dissociates into n fragments:

$$(m_i/n)v_f = (1/n)m_iv_i \tag{3.7}$$

therefore $v_f = v_i$, ie. the velocity of each particle is unchanged during fragmentation. Given the greater mass of the H_2^+ and H_3^+ molecules compared to an H^+ ion, the initial velocity of these molecules will be 0.71 and 0.58 times that of an H^+ ion respectively. Based on this knowledge, we can calculate the equivalent energy of a primary H^+ ion needed to match the momentum of an H_n^+ molecule fragmented into nH^+ ions, as this will determine the relative performance of the molecular fragment compared to a primary H^+ ion. For this "reference" experiment, we define a final reference momentum p_r associated with our fragmented particle which can then be converted into an equivalent reference energy E_r:

$$p_r = (2m_fE_f)^{1/2} = (2m_iE_i/n^2)$$
$$E_r = p_r^2/2m_H \tag{3.8}$$

where m_H is the mass of a proton as in equation 3.7. Thus an equivalent reference energy for n hydrogen fragments can be calculated as:

$$E_r = E_i/n^2 \tag{3.9}$$

In figure 3.5, the equivalent proton energy for fragmented H_2^+ and H_3^+ ions are shown as a function of their initial accelerating voltage as calculated by equation 3.9. This demonstrates that based on the momentum argument given above, at 30keV the $2\times H_2^+$ ion fragments and the $3\times H_3^+$ ion fragments will each behave like an equivalent 7.5keV or 3.3keV primary proton respectively. This is in contrast to the energy equipartitioning model discussed above where we would expect these fragments to behave like a 15keV and 10keV proton respectively. The momentum argument is likely the reason why the VLE-PIXE contribution from the H_2^+ and H_3^+

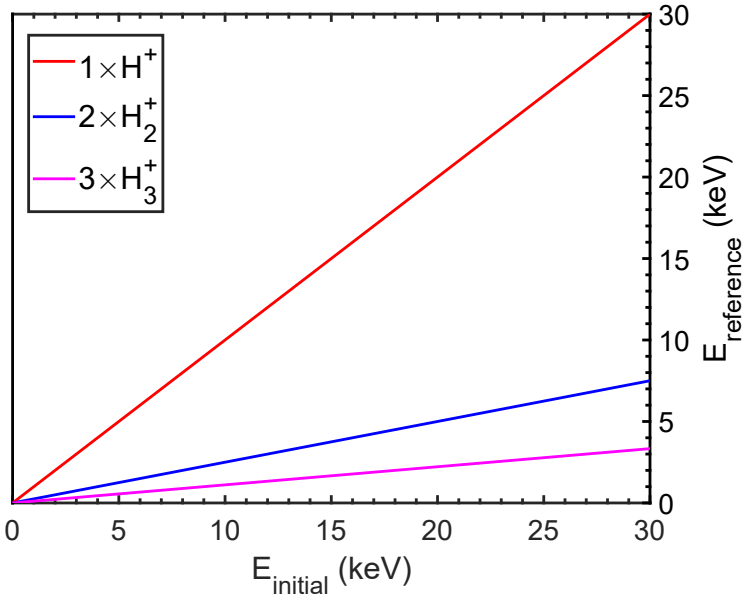

Figure 3.5: Equivalent reference proton accelerating voltage for given hydrogen molecular fragments with a specified initial energy.

molecules are negligible when compared to the primary H^+ species as shown in figure 3.2c, despite being much greater in quantity.

3.2 Investigation of Spurious Signal Contributions

3.2.1 Charging Effects

To overcome the charging related phenomenon experienced by Gianuzzi et al. [194] and described by Joy et al. [22], all the samples measured in this study were conductive and well grounded. To confirm that the charging related issues had been alleviated and that charging did not cointribute to the VLE-PIXE spectra, this effect could be reproduced on a conductive sample by applying a bias to the sample relative to the microscope ground plane.

A positive bias was applied to a single crystal copper sample to simulate the positive charging of a sample by the ion beam, the same condition experienced by Gianuzzi et al. The electrons generated by backscattered ions striking surfaces within the chamber, known as type III secondary electrons, would then be re-accelerated back towards the positively charged sample where they would produce X-Rays. The sample was irradiated by a 30keV, 100nA hydrogen beam and a 20 minute X-Ray spectrum was captured. The results of this experiment are shown in figure 3.6a.

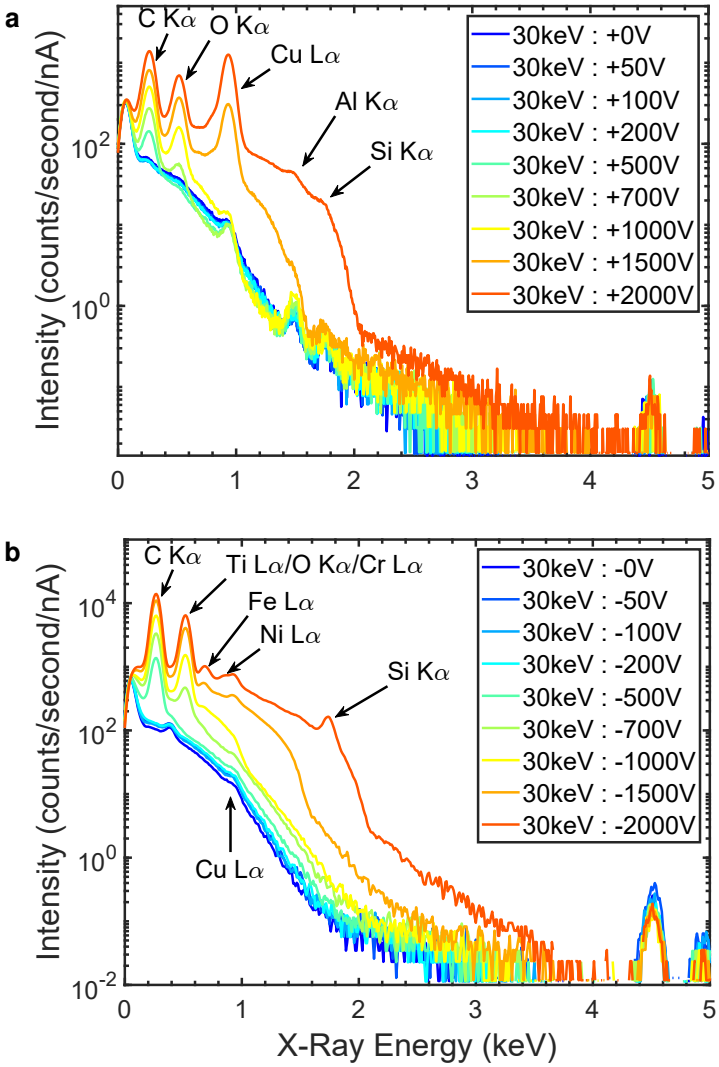

Figure 3.6: VLE-PIXE spectra from (a) a positively biased, and (b) a negatively biased Cu substrate demonstrating the effects of secondary electron re-acceleration.

At zero bias, the Cu signal is quite weak however as the bias increases, the intensity of the Cu signal begins to increase, reaching a maximum at the highest voltage bias applied of +2000V. This signal originates from the re-accelerated type III secondary electrons. A broad Bremsstrahlung background also starts to appear at higher biases with a maximum energy corresponding to the voltage bias applied to the sample. This Bremsstrahlung background is characteristic of electron induced X-Ray emission and is distinct from the VLE-PIXE signal which does not contain Bremsstrahlung. The broad background in the signal at zero voltage bias is due to backscattered ions and will be discussed in section 3.2.4. A simultaneous increase in the C and O signal likely originates from a combination of the increased deposition of carbon and oxidation of the sample surface by the incident electrons as well as the more efficient excitation of surface X-Rays by the low energy electrons.

A negative bias was then applied to the same sample. This would ensure than any type III secondary electrons generated in the chamber do not impact the sample surface. The sample was irradiated by a 30keV, 100nA hydrogen beam and a 20 minute X-Ray spectrum was captured. The results of this experiment are shown in figure 3.6b. As the negative voltage bias is increased, the Cu signal does not increase significantly, which was shown with the positive bias. This demonstrates that this Cu signal originates from the ion beam striking the surface and is not caused by the re-acceleration of type III secondary electrons. The ion beam would not be influenced significantly by the negative bias, with only a slight deceleration of the positive beam from 30keV to 28keV.

A secondary signal is also shown to appear, comprising of Fe and Ni. This signal likely originates from the secondary electrons generated at the sample, being accelerated away from the sample by the negative bias, and generating X-Rays from surfaces within the microscope chamber. Given the peak assignments of Fe, C, Ni, Si and the potentially overlapping peaks of Ti and Cr, it is likely that the electrons are striking a stainless steel surface inside the microscope chamber. Once again, a Bremsstrahlung signal appears at high biases with a maximum energy corresponding to the bias applied to the sample and likely originates from the secondary electrons striking the chamber. It can be concluded that the charging effects observed by Gianuzzi et al. [194] are not responsible for the VLE-PIXE results observed.

3.2.2 Beam Skirt Contribution

As described in section 2.3.0.1, the scattering of primary ions in the FIB column and chamber can be significant. There is a possibility that primary ions are neutralised through collisions with the gas molecules in the lower column, forming a diffuse beam skirt. These skirt neutral atoms may be capable of generating an X-Ray signal upon the sample and their contribution to the overall VLE-PIXE signal by the beam skirt must be considered.

In order to measure the skirt contribution to the X-Ray spectra, an experiment was performed using a standard Faraday cup whereby the 30keV, 100nA primary hydrogen beam was fully contained within the platinum aperture and any X-Rays generated inside the cup would be absorbed by the walls of the cup. The beam skirt would strike the platinum surface surrounding the aperture and any X-Rays generated on the surface of the cup could be detected. Using this method, the X-Ray signal contribution from the primary beam could be eliminated and the X-Ray

signal generated by only the beam skirt could be measured. These spectra were compared to spectra taken with the entire beam striking the platinum aperture surface. A schematic of the experiment is shown in figure 3.7a. The experiment was carried out during chamber pump-down where the pressure in the lower column and therefore scattering into the skirt would be the highest. These results were compared to when the chamber had been pumping for a period of 2 hours.

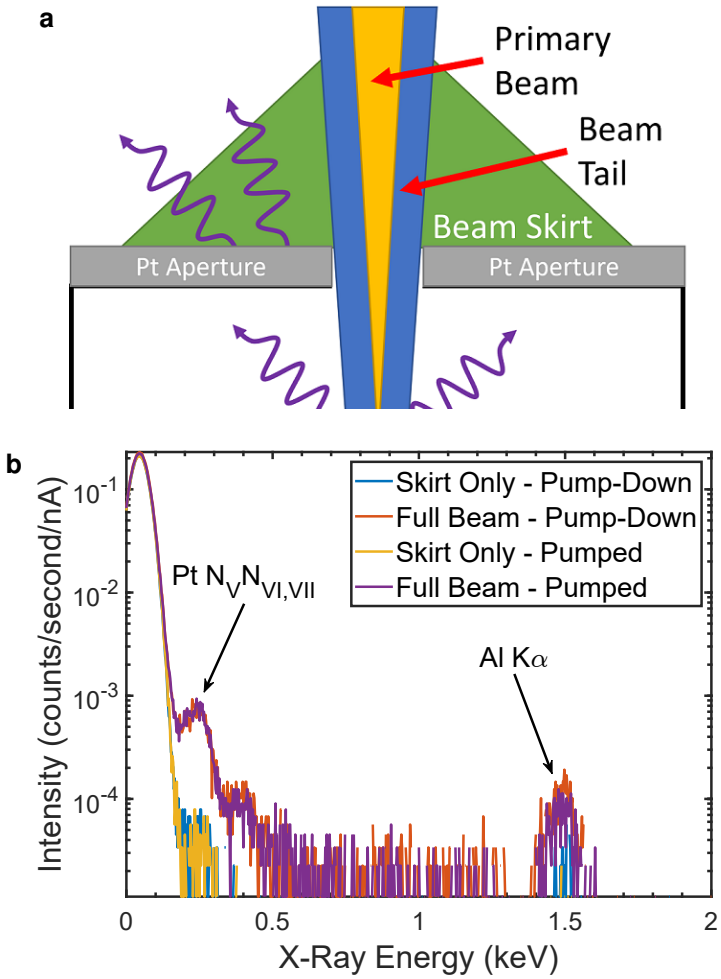

Figure 3.7: (a) Schematic of the beam skirt species isolation experiments. (b) Experimental determination of the skirt species contribution to a 30keV, 100nA VLE-PIXE spectra.

It can be seen in figure 3.7b, that by isolating the primary beam, a very weak spectrum is observed compared to when the full beam is incident upon the platinum aperture. The full beam spectrum is also quite weak due to the low XRPCS of Pt at this energy, however the results can still be used as a comparison. As there is almost no change in spectra from when the chamber is pumping down, compared to when the chamber has pumped for a period of 2 hours, it is likely that the majority of the signal is due to the primary beam tails striking the edge of the platinum aperture. It can be concluded that the contribution of the beam skirt to the VLE-PIXE signal is negligible.

3.2.3 Electron Contribution

As was established in section 2.3.0.1, there is a possibility that secondary electrons may be generated as a result of ion collisions with gas molecules in the lower FIB column. It was also established that the majority of the beam scattering occurs in the vicinity of the electrostatic objective lens, also referred to as the C2 lens. Above an accelerating voltage of 8keV, the polarity of C2 lens potential is positive and it was found that the majority of electrons generated in the lower column region could be collected by the positive lens potential. In addition, at increasing accelerating voltages the scattering cross section is reduced and as a result, less electrons would be created. Below 8keV however, the lens potential polarity becomes negative which is required to enhance FIB resolution at lower accelerating voltages. It was found that any electrons generated in the lower column region below 8keV were accelerated towards the sample by the negative potential of the lens, where they would strike the sample and generate X-Rays. A solution to this issue was to manually reverse the polarity of the C2 lens from negative to positive below 8keV. This resulted in a negligible reduction in resolution and an almost complete elimination of the electron X-Ray signal.

To demonstrate the effectiveness of this technique, an experiment was performed where X-Ray spectra were collected immediately following microscope chamber pump-down, where the pressure in the lower column is highest and therefore the gas scattering and subsequent electron emission will be maximised. Spectra were taken with both a positive and negative C2 lens voltage on the same platinum aperture sample as the skirt contribution experiments. For comparison, spectra were also taken when the microscope had been pumped for 2 hours.

In figure 3.8a, a typical electron induced X-Ray spectrum with a broad Bremsstrahlung background is observed, with the Bremsstrahlung energy extending to an energy equivalent to the lens potential, -10,649V. During pump-down, the signal is significantly higher than when the chamber has pumped for a period of 2 hours, another indication that the electrons are generated as a result of gas scattering in the column, and are responsible for the observed signal. When the lens polarity is switched from negative to positive as shown in figure 3.8b, the vast majority of electrons are collected by the C2 lens and the signal is significantly reduced. This demonstrates the effectiveness of this technique for removing stray electrons generated as a result of gas scattering in the lower column. For this reason, all VLE-PIXE spectra taken with an accelerating voltage below 8keV are taken with a positive C2 lens polarity.

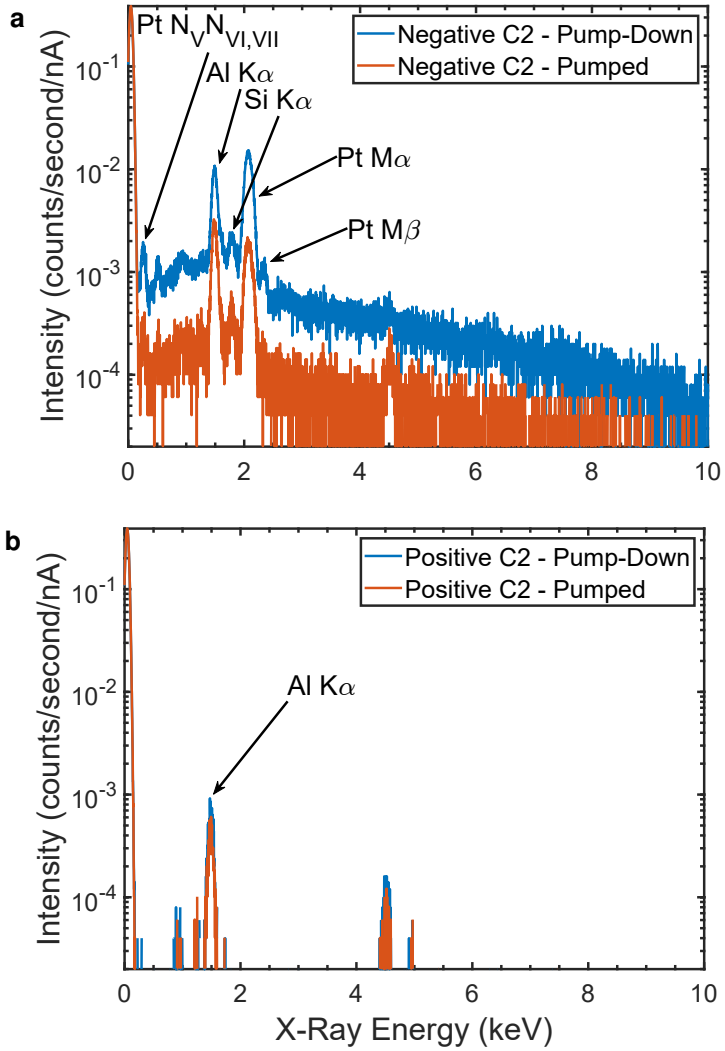

Figure 3.8: The X-Ray signal collected from a Pt aperture sample at 8keV, 50nA with (a) negative (-10649V) C2 lens voltage, and (b) a positive (+4995V) C2 lens voltage

3.2.4 Backscattered Ions

At accelerating voltages greater than 24keV a broad, intense background signal was found to appear at low X-Ray energies. Such an example is shown in figure 3.9, for a 30keV, 100nA beam on pure Mg, Cu, and Au, where th broad background can be seen extending up to an energy of 3-4keV. While initially believed to be Bremsstrahlung radiation as a result of primary ion impact on the sample surface, proton impact at such low energies is not expected to generate any appreciable Bremsstrahlung. Additionally, the background was shown to scale significantly in intensity with increasing target mass: Mg (Z = 12), Cu (Z = 29) and Au (Z = 79), a phenomenon which is not typically observed to such a degree with Bremsstrahlung radiation.

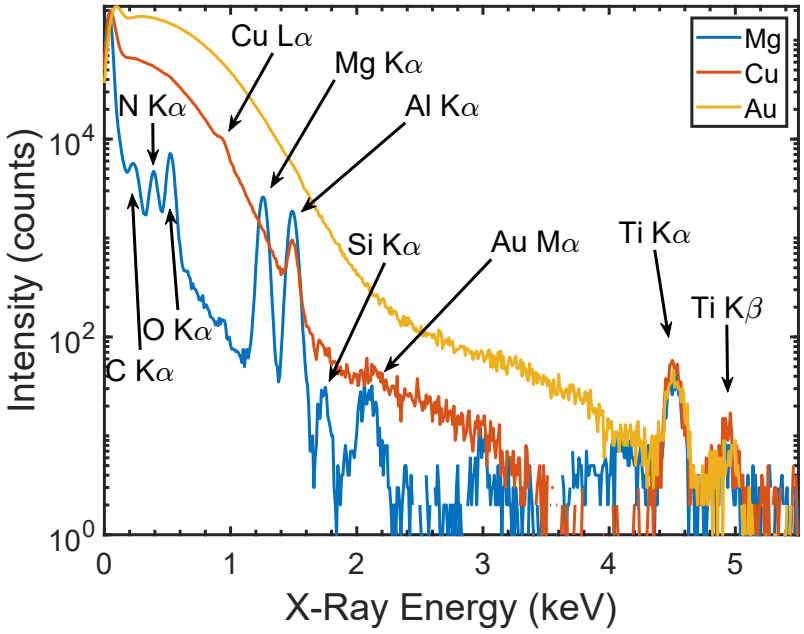

Figure 3.9: 30keV VLE-PIXE spectra of an Mg, Cu and Au sample demonstrating the scaling of the BSI signal with target mass.

To confirm the nature of this background, two spectra were collected on the same single crystal Cu sample with a windowed EDS detector and a windowless EDS detector at 8.1keV; below the threshold for this background. As shown in figure 3.10, the background was present when the spectrum was captured with the windowless detector, yet was not when the windowed detector was used. This demonstrates that the window is responsible for blocking the background signal.

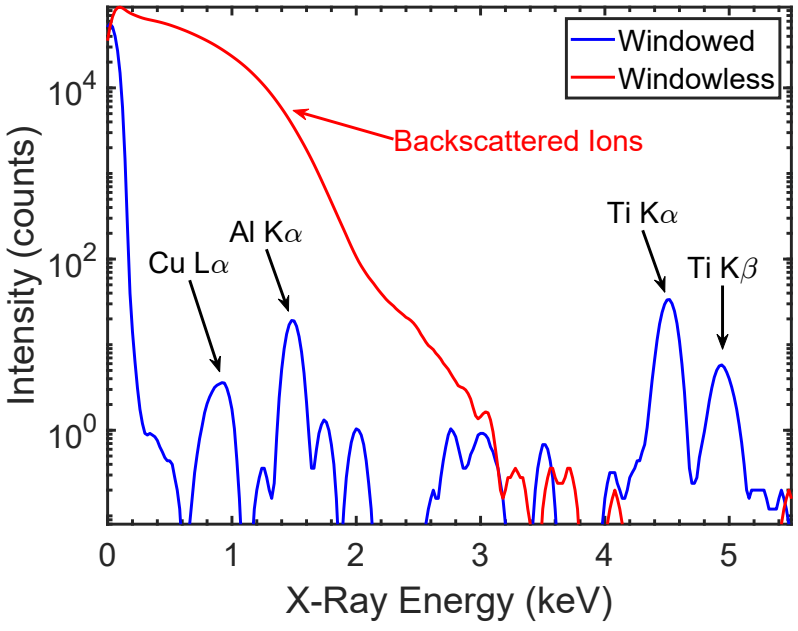

Figure 3.10: VLE-PIXE spectra of a Cu sample taken using the windowed and windowless EDS detector.

It was concluded that this background signal was due to ions backscattering from the sample, impacting the EDS detector surface and generating a signal. When the windowed detector is used, this signal does not appear until an energy of 24keV due to the transmission threshold of the BSIs through the window however when the windowless detector is used, the BSIs are free to strike the detector surface. The fact that the thin detector window is capable of blocking all BSIs up to an energy of 24keV whilst still allowing transmission of very low energy X-Rays is a significant advantage of VLE-PIXE over LE-PIXE and PIXE techniques.

VLE-PIXE spectra were typically performed at energies $<$24keV to avoid the influence of BSI background however spectra may be taken above 30keV if there is no risk of interference between the BSI background and the analyte peaks. As described in section 1.3.5, these BSIs carry information regarding the composition and thickness of a target and can be utilised to analyse a sample surface. A practical application of this BSI spectroscopy is outlined in chapter 7.

3.3 Detector Artefacts and Contributions

3.3.1 Detector Noise Peak

As described in section 1.3.4.8 an intrinsic feature of all SDD detectors is the presence of a noise peak around 0eV due to the pulse counting electronics. Very low energy X-Ray peaks may overlap with this noise peak and as such, it must be removed from the spectrum in situations where this may prevent accurate measurement of these peaks. The noise peak is also dependent on the dead time of the detector as described by Alvarez [198], however as the dead time for VLE-PIXE measurements is typically around 0% due to the low input count rates, the change in noise peak with dead time was not a concern.

To establish scaling of the noise peak, a series of X-Ray spectra were taken as a function of time with all signal sources removed and are shown in figure 3.11a. The intensity of the noise peak was shown to scale linearly with time as demonstrated in figure 3.11b. This allowed efficient subtraction of this noise peak from a spectrum based on the experimental capture time. An example of the noise peak subtraction is shown in figure 3.11c for the Al Lℓ peak. Noise spectra would ideally be captured immediately prior to experiments where subtraction is necessary as the noise spectra may change due to a variety of detector conditions such as detector temperature, room temperature, and processing time [199].

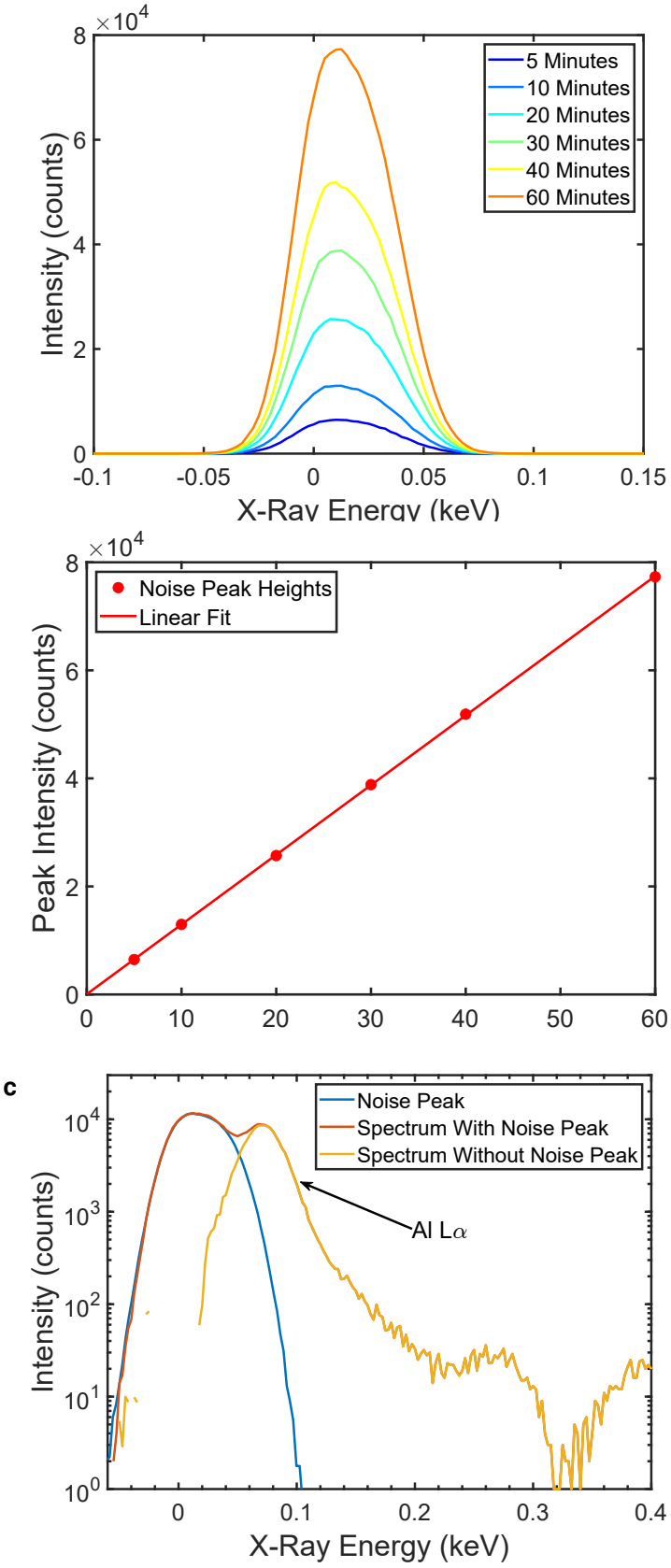

Figure 3.11: (a) Noise peak spectra as a function of capture time. (b) Noise peak heights as a function of capture time. (c) An example of noise peak subtraction from a VLE-PIXE spectrum

This technique may be effectively used when there is a significant risk of overlap between the noise peak and the desired characteristic peak, however in situations where characteristic peaks are located some distance from the noise peak, peak subtraction is not used due to unnecessary modification of the raw X-Ray spectrum. All spectra used throughout this thesis are unmodified unless specified for the purpose of noise peak removal.

3.3.2 Detector Window Signal

A spurious Ti Kα peak was found to be present in some VLE-PIXE spectra, which disappeared when a windowless EDS detector was used, as seen in figure 3.10. This suggests that the Ti peak originates from BSIs striking the support grid of the window covering the X-Ray detector. These Ti K peaks also appear in high energy SEM-EDS spectra, where the energy of the BSEs may be sufficient to overcome the magnetic field of the electron trap and strike the window support grid. An example of a 30keV SEM-EDS spectrum showing this spurious Ti peak is shown in figure 3.12. Such background peaks are not uncommon and can originate from many sources within the detector [200]. While this peak cannot be eliminated, awareness of this peak may prevent mis-identification of sample components. Collection of a VLE-PIXE spectrum with a windowless detector may help distinguish this peak from a genuine analyte peak.

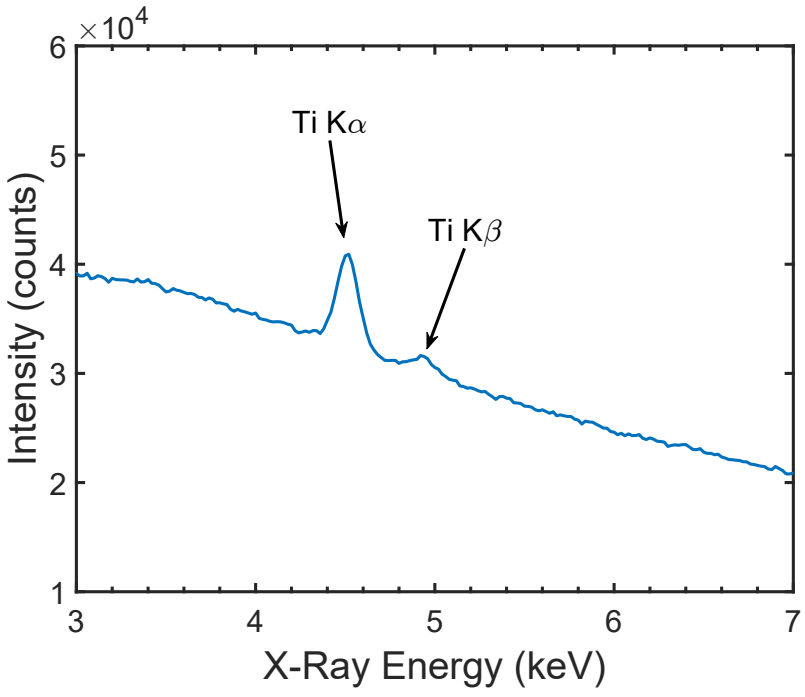

Figure 3.12: SEM-EDS spectrum demonstrating the presence of the spurious Ti peak believed to be due to BSE impact on the window support grid.

Another concern is the possibility of material sputtered during the process of the doped beam VLE-PIXE measurement coating the detector window. This is particularly prevalent with the use of heavy ion species such as Ar or Xe which will remove a significant amount of material during measurements, coating the detector which is inserted during spectral collection. Backscattered ions may once again impact the detector window and produce X-Ray peaks originating from the redeposited material on the window. Such a situation may be inevitable when performing doped beam VLE-PIXE and awareness of the origin of X-Ray peaks may be the only real solution.

Measurement of samples using a windowless detector may help distinguish real peaks from spurious peaks however care must also be taken to not coat the windowless detector surface with sputtered material which may increase the thickness of the detector dead layer and thus reduce sensitivity. Alternatively, periodic measurement of a standard sample with very few X-Ray peaks may help determine if any new peaks appear which are a result of sputtered material coating the detector window. Such a standard spectrum may be subtracted from any subsequent spectra. Comparison with SEM-EDS spectra may also be beneficial, as electrons are more likely to be stopped by the electron trap in the detector and will not generate a signal on the coated window or support grid. Bremsstrahlung background however may obscure any low intensity peaks such as trace elements, and effective delineation may not be possible.

3.4 EDS Mapping Capability

An important capability of analytical techniques such as SEM-EDS, and micro-PIXE is the ability to spatially resolve elemental components in a sample. This offers a significant advantage over bulk analytical techniques whereby the distribution of elements within a sample can be established with a resolution limited by the instrumentation being used. An example of a composite VLE-PIXE elemental map, collected with a $\sim$50nA Xe doped hydrogen beam ($\sim$6% Xe with a balance of hydrogen) is shown in figure 3.13a. These intensity maps are the result of integrating across a small spectral window containing the desired X-Ray peak. A thin MoS_2 flake exfoliated on a Si(100) wafer can be clearly identified, as well as some smaller flakes above the main flake which could not be initially identified using the FIB secondary electron (SE) contrast image alone. The elemental maps of Mo and S, shown in figures 3.13b and 3.13c correlate well with the position and shape of the flake identified using the SE image.

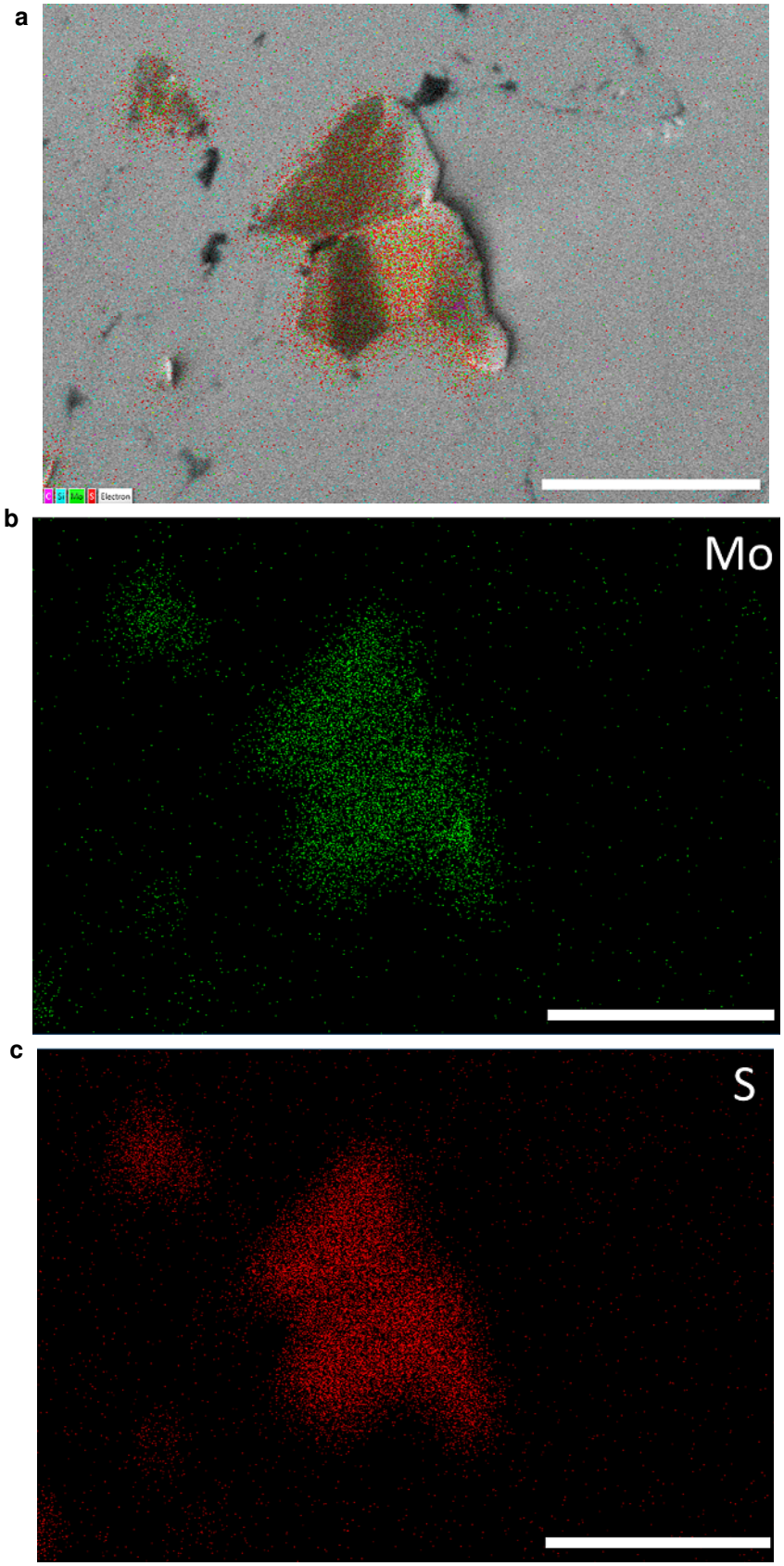

Figure 3.13: VLE-PIXE elemental map of an MoS_2 flake on Si collected with a $\sim$50nA Xe doped hydrogen beam. (a) Layered composite image, (b) FIB-SE image (c-d) Mo, and S VLE-PIXE elemental maps. Scale bar is 25 μm

These maps were captured in an automated fashion using the supplied Oxford Instruments AZtec software package and corresponding external scan generator, which were installed as standard on the FIB microscope. This means that these experiments could be performed with essentially no modification to the instrument.

There are several methods used by software packages such as AZtec for standardless quantitative spectral mapping, such as:methods utilising databases of standards, algorithms based on peak-to-background ratios, methods developed on the basis of Monte Carlo simulations, altering the incidence angle, and procedures relying on the application of fundamental equations of microanalysis. All these methods are specific to the exciting species and as such, will be appropriate only for electrons [201]. Quantitative mapping for VLE-PIXE will require the use of a specified PIXE mapping software such as the previously mentioned GUPIX [106] and GeoPIXE [107]. These software packages however rely on calculation of the XRPCS, typically in comparison with well established eECPSSR or analytical cross sections. As discussed in section 1.3.4.3, challenges arise when calculating the XRPCS for multiple ion species, challenges which must be overcome in order to perform fully quantitative doped beam VLE-PIXE mapping.

There are several challenges involved with the mapping capability of this technique which will need to be overcome. The high currents required for the VLE-PIXE measurements result in significantly reduced resolution compared to optimal imaging conditions for the FIB. Generational advancements in the PFIB instrument will however improve high current resolution and the impact of this will be reduced. Due to the relatively low signal generated even by the doped hydrogen beam, map capture times were quite significant, reaching on the order of 1 hour for the map shown in figure 3.13a. Improvements in detector sensitivity may help reduce map capture times. Additionally, increasing the proportion of dopant species may also increase the generated X-Ray signal as demonstrated in section 5.9a however will do so at the expense of increased sample damage due to sputtering.

The presence of the dopant species will inevitably result in the sputtering of the underlying sample, meaning that the sample will be continuously modified during map capture. While this is something which must be considered during doped beam VLE-PIXE mapping, this may however be beneficial in certain situations, for example where each map can originate from a subsequent layer of the sample. If these maps are then stacked together, a 3-dimensional elemental map can be established, a technique known as tomography. Current tomography workflows

are typically performed in a serial fashion, by first removing a layer of material, followed by sample analysis. The use of doped beam VLE-PIXE mapping may however replace serial tomography procedures with a single-step method of both layer removal and analysis.

This may also be used as an endpointing technique, whereby the X-Ray signal is analysed during milling. This will allow milling to be stopped precisely at the interface of two layers due to the appearance of a new characteristic X-Ray peak corresponding to the start of the next layer and can also be performed in real-time as opposed to other methods which may require serial delayering and analysis.

3.5 Optimised VLE-PIXE Parameters

Beam Composition

- IGP4 pressure in lower FIB column should be monitored and allowed to equilibriate before commencement of experiments to avoid change in beam current or composition during experiments.
- Beam composition should be measured with isolating Faraday cup before experiments to determine the proportion of dopant species or contaminant species for pure hydrogen beams
- Beam composition should be measured at 30keV, $\sim$1nA, 10 minute capture

Spurious Signal Mitigation

- VLE-PIXE should ideally be performed on conductive or coated samples to avoid charging related effects.
- To minimise the effect of gas scattering generating unwanted particles, chamber should be pumped for a minimum of 2 hours following vacuum OK condition before experiments commence.
- C2 lens voltage should be changed from negative to positive below an accelerating voltage of 8keV to collect stray electrons.

Backscattered Ions

- VLE-PIXE spectra should be taken with a windowed detector to block BSIs.

- VLE-PIXE should be performed at an accelerating voltage of 24keV or less to prevent BSI transmission through detector window unless X-Ray peaks are above $\sim$4keV and do not interfere with BSI background.
- BSI spectroscopy should be performed with a windowless detector, with as low a current as possible due to efficient backscattering and to avoid detector damage.

Detector Artefact Mitigation

- Detector noise peak may be subtracted to help identify very low energy X-Ray peaks.
- Be aware of spurious signals generated by ion impact on the detector window or window support grid.
- Collection of a spectrum using a windowless detector may help determine whether a peak originates from the sample or is the result of interaction with the detector support grid.
- Periodic measurement of a standard sample with very few X-Ray peaks may help determine if any new peaks appear which are a result of sputtered material coating the detector window.
- Comparison with EDS spectra may be beneficial as electrons are more likely to be stopped by the electron trap and will not generate a signal on the detector window or support grid.

Chapter 4

Doped Beam VLE-PIXE Trace Element Analysis

This chapter will demonstrate the trace element analysis of two well characterised materials using a Xe doped hydrogen beam. These Standard Reference Material (SRM) provided by the National Institute of Standards and Technology (NIST) are used, as they possess a well defined, certified composition with a range of major, minor, and trace elements. These results are directly compared to SEM-EDS, an analogous technique which is routinely performed for elemental analysis in an SEM. The relative sensitivity of the two techniques are assessed.

4.1 Comparison of Doped Beam VLE-PIXE to SEM-EDS

Energy dispersive spectroscopy performed with a scanning electron microscope (SEM-EDS) is an analogous technique to PIXE, where both rely on the impact of particles for inner-shell ionisation, resulting in the emission of X-Rays characteristic to the element being analysed. Where PIXE uses ions, typically protons for ionisation, SEM-EDS utilises electrons for the same purpose [202].

The XRPCS for electrons is an order of magnitude greater than protons at the energy ranges used in VLE-PIXE of $\leq$ 30keV. The generation of X-Rays by electrons is therefore expected to be far more efficient [203, 204], however SEM-EDS also possesses a significant disadvantage, the appearance of intense Bremsstrahlung radiation which can obscure low-intensity X-Ray peaks. Bremsstrahlung is discussed in detail in section 1.3.4.7. This background effectively reduces the sen-

sitivity of SEM-EDS to an LOD of approximately 100-500 parts per million (ppm), [16] compared to the LOD of PIXE in the MeV range near or below 1 ppm [14]. LOD is discussed ion greater detail in section 1.3.4.10. The LOD for VLE-PIXE however is expected to be several orders of magnitude higher due to the diminishing XRPCS for protons in the VLE-PIXE energy range [205].

Direct comparison between PIXE and SEM-EDS is often difficult due to the significant differences in instrumentation between the two techniques. Implementation of VLE-PIXE on a dual-beam PFIB/SEM microscope allows both techniques to be performed consecutively using the same detector, X-Ray window, software, and vacuum conditions, allowing more direct comparison.

4.1.1 NIST SRM 654b

The first sample measured was the NIST SRM 654b, a Ti base alloy with a range of bulk and trace elements. The certified composition is shown in table 4.1, with a balance of Ti (not listed).

Element	Value	Error (± Value)
Chromium	0.025	0.006
Copper	*80**	30
Molybdenum	0.013	0.003
Iron	0.23	0.03
Aluminum	6.34	0.06
Vanadium	4.31	0.06
Nickel	0.028	0.006
Tin	230*	60
Silicon	0.045	0.003
Zirconium	0.008	0.003
Hydrogen	(0.002)	0.002
Sulfur	(0.001)	0.001
Oxygen	(0.17)	0.17
Boron	*1.12**	0.13

Table 4.1: NIST SRM 654b certified concentration values. Concentrations are expressed as mass fraction, in % (unless noted by an asterisk * for mg/kg). Certified values are normal font, reference values are italicized, values in parentheses are for information only.

The beam composition measurement prior to analysis is shown in figure 4.1a and is expressed as a percentage of the total beam current in figure 4.1b. This established a hydrogen beam doped with approximately 6.9% Xe. As determined

in section 5.3, a greater proportion of dopant species will result in enhanced X-Ray signal production however will do so at the expense of increased sample damage due to sputtering by the heavier ion species. As such, a small percentage of dopant species was chosen for these experiments to maintain the integrity of the sample.

a

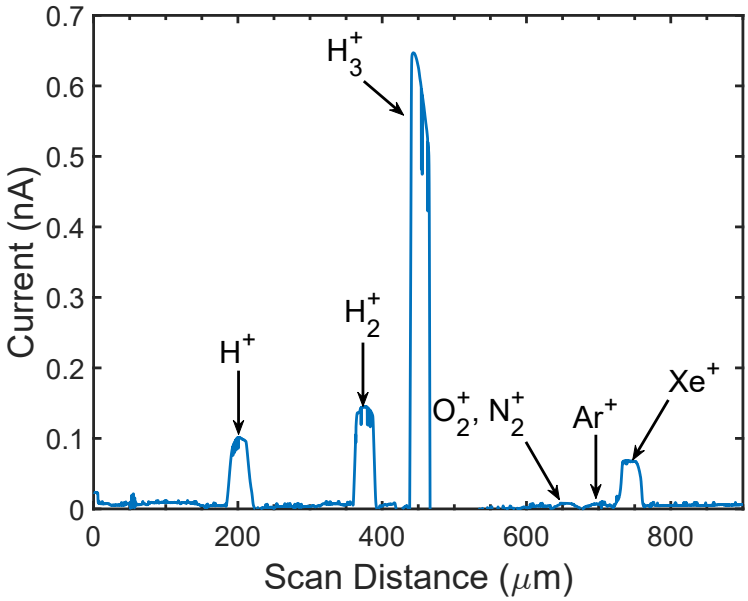

b

Species	%
H^+	10.37
H_2^+	14.81
H_3^+	66.15
O_2^+, N_2^+	<1
Ar^+	<1
Xe^+	6.90

Figure 4.1: Beam composition prior to SRM 654b trace element analysis. (a) Beamlet compositional current measurement. (b) Beam composition expressed as percentage of total beam current.

To account for the relatively lower X-Ray production with a smaller percentage of dopant species, the capture times for SEM-EDS and doped beam VLE-PIXE of 20 minutes and 4 hours respectively were chosen such that both spectra were acquired with a similar number of total X-Ray counts ($\sim$10M counts).

The Xe doped VLE-PIXE spectrum at an accelerating voltage of 24keV and a SEM-EDS spectrum at an accelerating voltage of 5keV are shown in figure 4.2a. A 24keV ion beam was used to minimise the transmission of BSIs through the X-Ray detector window as discussed in section 3.2.4 and a 5keV electron beam was chosen for increased sensitivity to the peaks in the X-ray energy range $<$2.5keV, an effect known as the overvoltage ratio [206]. An equivalent comparison in the X-ray energy range, 4-10keV is shown in figure 4.2b where a 30keV electron beam is used for increased sensitivity to the X-Ray peaks in this range. The SEM-EDS spectrum continues up to a value of 30keV however only Bremsstrahlung background is observed at an energy greater than 10keV, therefore the spectra are truncated for clarity. The full collection of SEM-EDS spectra are given in appendix section A.4 at a range of energies.

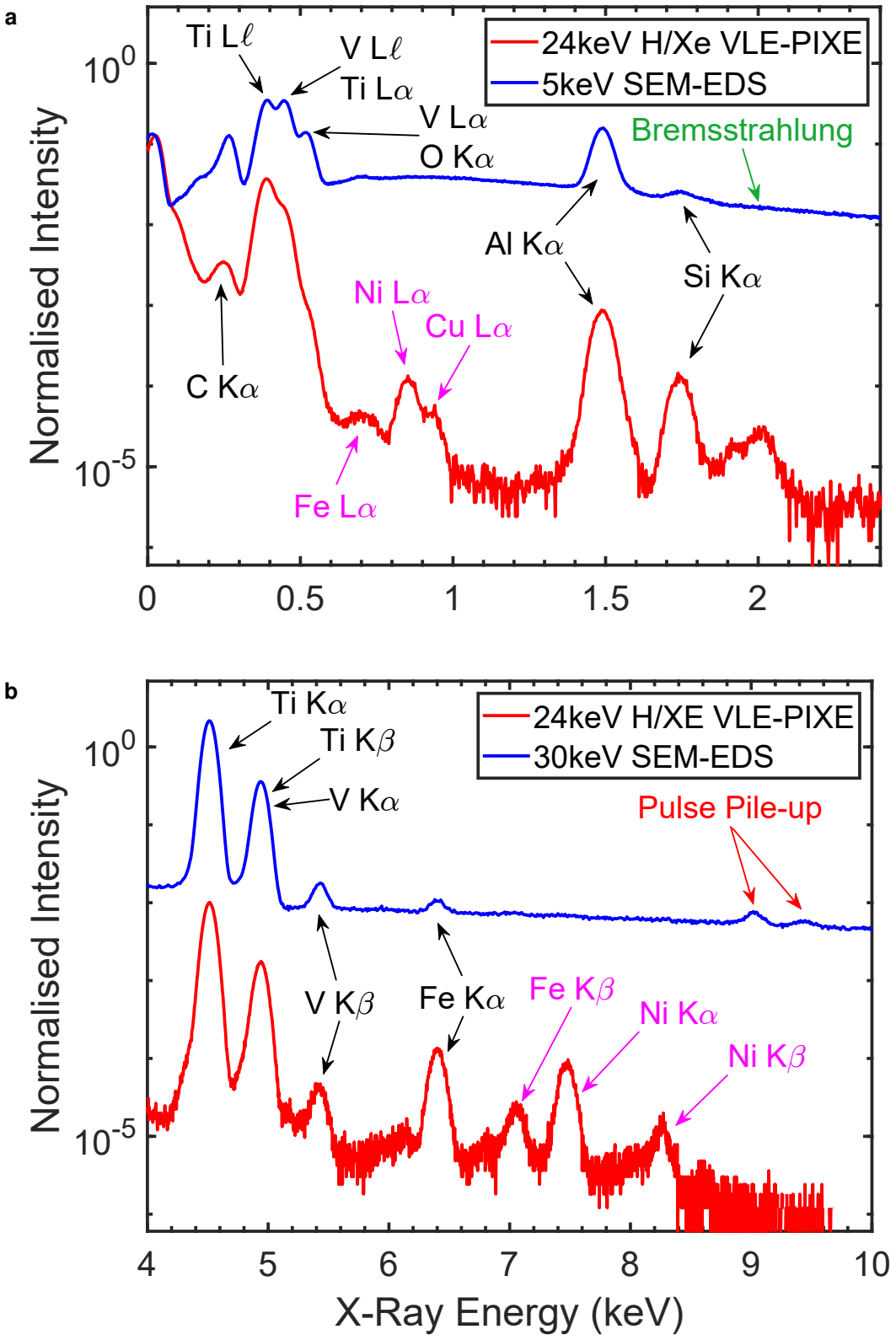

Figure 4.2: NIST SRM 654b: Comparison of a 24keV VLE-PIXE spectrum with, (a) a 5keV SEM-EDS spectrum and, (b) a 30keV SEM-EDS spectrum. Peaks identified in both SEM-EDS and VLE-PIXE are labelled in black, peaks identified in VLE-PIXE but not SEM-EDS are labelled in magenta, spectral artefacts are labelled in red.

Qualitatively, the VLE-PIXE spectra can be characterised by the almost complete absence of Bremsstrahlung background, in contrast to the broad, intense Bremsstrahlung background typical of the SEM-EDS spectrum. An example of this Bremsstrahlung background is labelled in green in figure 4.2a. As a result, several peaks are present in the VLE-PIXE spectrum which cannot be identified in the SEM-EDS spectrum, leading to the identification of two additional minor components; Ni and Cu. Ni can be identified based on the presence of the Ni Lα peak, and the Ni Kα and β peaks. Cu can be identified based on the Cu Lα peak.

The identification of additional peaks, Fe Lα and Fe Kβ can be used to confirm the presence of Fe in the sample, an important feature in the case of overlapping peaks. Peaks corresponding to elements not outlined in the COA such as the P Kα peak at 2.013keV were also observed, however the lack of certification makes identification of this element speculative and thus were not included. At an X-Ray energy of 3keV, several spectral features are present which are believed to be a detector artefact as they do not match any known X-Ray characteristic peaks. For this reason, this section of the spectra has been removed for clarity.

4.1.2 NIST SRM 1242

To assess the validity of the doped beam VLE-PIXE technique, a second sample was measured utilising the same procedure as above. This sample was chosen such that the primary component of the SRM 654b, titanium was not present in the SRM 1242 and the primary components of the SRM 1242, cobalt and tungsten were not present in the SRM 654b. This also helped eliminate the possibility of the X-Ray spectra being due to some artefact of the system, as both samples would likely produce identical X-Ray spectra in this situation. The full composition of the SRM 1242 is shown in table 4.2.

The beam composition measurement prior to analysis is shown in figure 4.3a and is expressed as a percentage of the total beam current in figure 4.3b. Similar to the 654b, a hydrogen beam was established with a dopant proportion of 6.2% Xe.

Comparison of the SEM-EDS and VLE-PIXE spectra for this sample is shown in figures 4.4a and 4.4b, again utilising the 5keV electron beam for peak comparison in the low energy region and a 30keV beam in the high energy region. The full SEM-EDS spectra are given in appendix section A.4 for a range of energies.

Element	Value	Error (±Value)
Carbon	0.126	0.003
Manganese	1.58	0.05
Phosphorus	0.002	0.001
Sulfur	0.0007	0.0002
Silicon	0.016	0.003
Copper	0.0010	0.0004
Nickel	9.78	0.08
Chromium	20.0	0.1
Vanadium	0.005	0.002
Iron	1.80	0.04
Tungsten	15.1	0.1
Cobalt	51.5	0.3
Nitrogen	0.026	0.001
Aluminium	(<0.01)	N/A
Tantalum	(<0.01)	N/A
Niobium	(<0.005)	N/A
Boron	(<0.0001)	N/A

Table 4.2: NIST SRM 1242 certified concentration values. Concentration are expressed as mass fraction, in %. Values in parentheses are for information only.

a

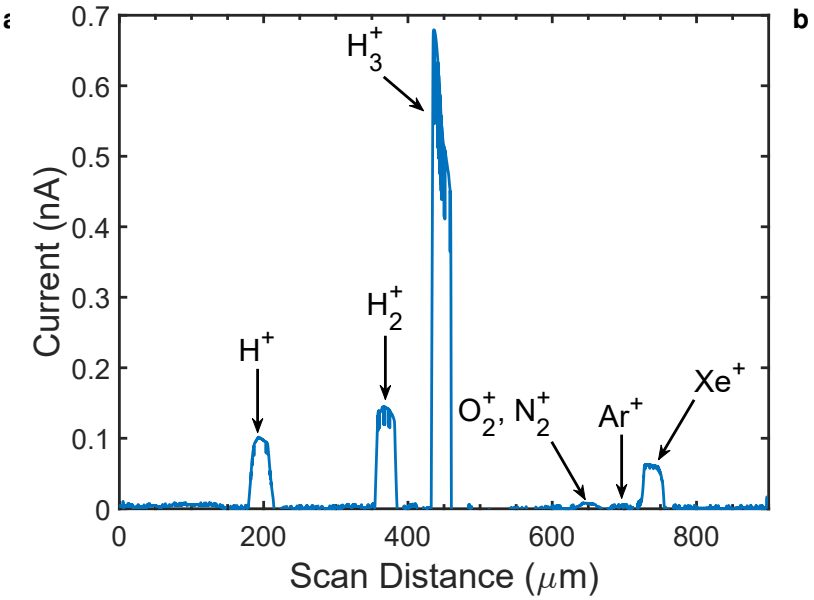

b

Species	%
H^+	10.10
H_2^+	14.41
H_3^+	67.82
O_2^+, N_2^+	<1
Ar^+	<1
Xe^+	6.24

Figure 4.3: Beam composition prior to SRM 1242 trace element analysis. (a) Beamlet compositional current measurement. (b) Beam composition expressed as percentage of total beam current.

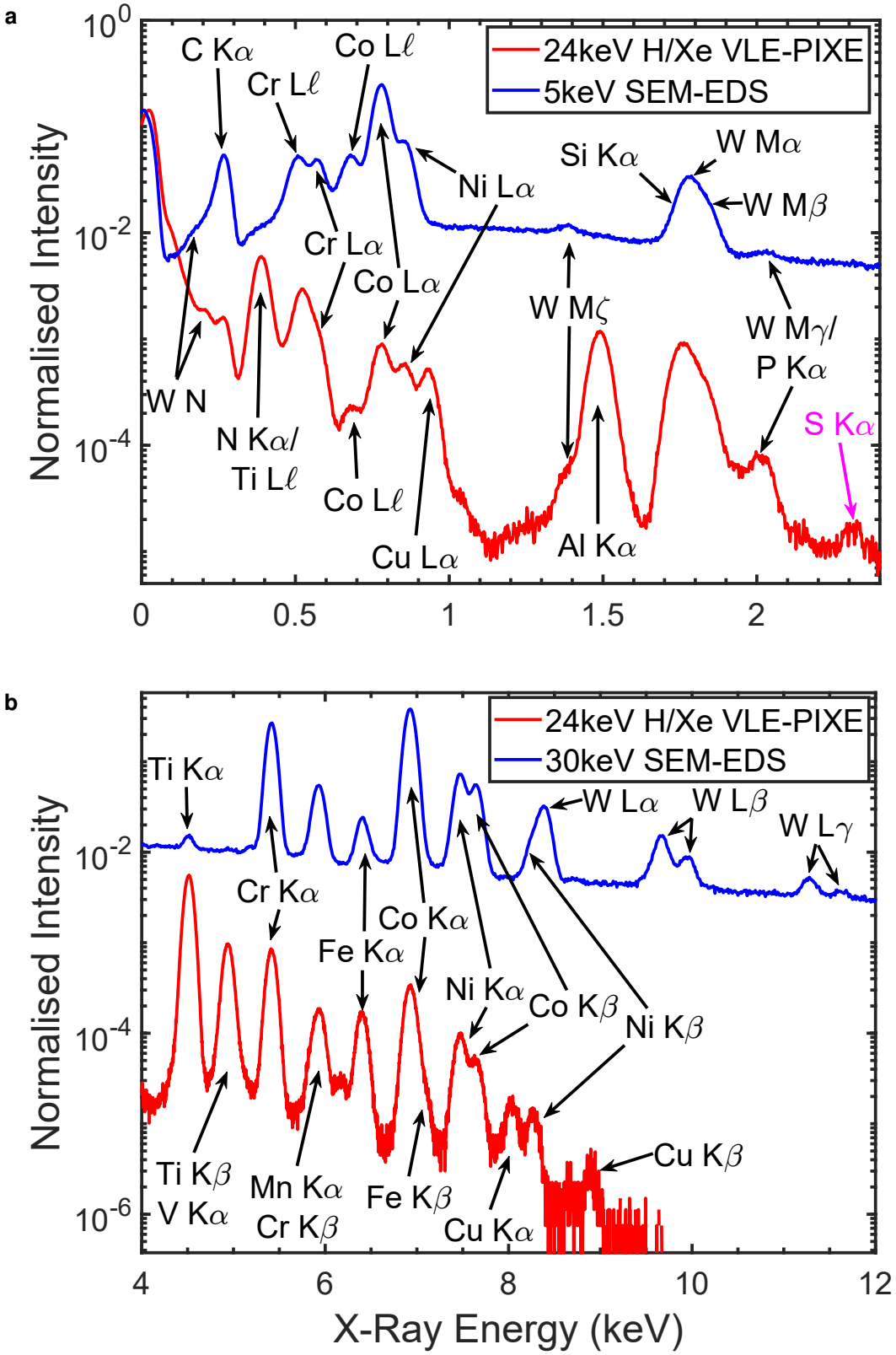

Figure 4.4: NIST SRM 1242: Comparison of a 24keV VLE-PIXE spectrum with (a) a 5keV SEM-EDS spectrum and (b) a 30keV SEM-EDS spectrum. Peaks identified in both SEM-EDS and VLE-PIXE are labelled in black, peaks identified in VLE-PIXE but not SEM-EDS are labelled in magenta, spectral artefacts are labelled in red.

When the VLE-PIXE spectra of the SRM 1242 are compared to the VLE-PIXE spectra of the SRM 654b, several peaks can be seen which are unique to each specific sample and have been identified as both major and minor components of their respective samples. In the SRM 1242, the tungsten M series of peaks as well as the Co K and L series of peaks can be clearly identified, neither of which were present in the SRM 654b. The intensity of the Cr Kα peak has also increased significantly, reflective of its higher concentration of Cr in this sample. The heavy element tungsten is of particular interest due to the presence of the outer shell M and N transitions, demonstrating the full range of K, L, M and N X-Ray transitions present in one sample.

The appearance of these new peaks corresponding to W and Co demonstrates the validity of this technique and eliminates the possibility of this X-Ray signal originating as the result of an artefact of the instrumentation. The same unidentified spectral features at $\sim$3keV were still present and once again cropped out in figure 4.4a in order to better identify the spectral lines in the low energy region.

Several peaks appeared in the characterisation of the SRM 1242 which should not be present, specifically the Ti and Al Kα peaks. As discussed in section 3.3.2, the Ti peak may result from particles striking the X-Ray detector window support grid or striking resputtered material coating the X-Ray detector window. The fact that this Ti peak is present in both the VLE-PIXE and SEM-EDS spectra suggests that this is the case and this peak should be ignored. These peaks can also be seen in the SEM-EDS spectra shown in figures A.11e-A.11g, demonstrating that as the electron energy increases, some backscattered electrons may bypass the electron trap and begin to generate a Ti Kα signal. Several techniques for mitigating or identifying such spurious peaks are outlined in section 3.5.

4.1.3 Comparison of Limits of Detection Between Doped Beam VLE-PIXE and SEM-EDS

The signal to noise ratio (SNR) and limits of detection (LOD) using a standard threshold of 3σ [169], as discussed in section 1.3.4.10, were calculated for the elements identified in the spectra shown in figures 4.2a and 4.2b for the SRM 654b, and 4.4a and 4.4b for the SRM 1242.

The full table of values are listed in table 4.3 for the SRM 654b and 4.4 for the SRM 1242 with the better of the two techniques coloured in red. These results are summarised in figure 4.5 where the minimum LODs for each element measured using doped beam VLE-PIXE and SEM-EDS are compared.

Element	Peak	COA Conc. (ppm)	SEM-EDS SNR	SEM-EDS LOD (ppm)	VLE-PIXE SNR	VLE-PIXE LOD (ppm)
Ti	Kα	880000	**4694.9**	**562.32**	3966.0	665.65
Al	Kα	63400	531.11	358.11	**908.52**	**209.35**
V	Kβ	43100	**21.45**	**6029.2**	15.11	8557.2
Fe	Kα	2300	7.81	883.33	**53.01**	**130.18**
Si	Kα	450	10.16	132.86	**148.94**	**9.06**
Ni	Kα	280	N/D	N/D	**37.66**	**22.30**
Cu	Lα	80	N/D	N/D	**20.63**	**11.64**

Table 4.3: SRM 654b calculated signal to noise ratios and limits of detection for the representative doped beam VLE-PIXE and SEM-EDS spectra. The greater SNR/Lower LOD between SEM-EDS and VLE-PIXE is listed in red. N/D signifies that the peak was not detected.

Element	Peak	COA Conc. (ppm)	SEM-EDS SNR	SEM-EDS LOD (ppm)	VLE-PIXE SNR	VLE-PIXE LOD (ppm)
Co	Kα	515000	25.30	61052	**216.82**	**7125**
Cr	Kα	200000	99.15	6051.66	**532.45**	**1126.86**
W	Mα	150000	230.51	1952.1	**578.98**	**777.23**
Ni	Kα	97800	59.59	4923.98	**62.60**	**4686.98**
Fe	Kα	18000	**142.93**	**377.81**	106.73	505.95
Cu	Lα	10	N/D	N/D	**10.79**	**2.78**
S	Kα	7	N/D	N/D	**7.20**	**2.92**

Table 4.4: SRM 1242 calculated signal to noise ratios and limits of detection for the representative doped beam VLE-PIXE and SEM-EDS spectra. The greater SNR/Lower LOD between SEM-EDS and VLE-PIXE is listed in red. N/D signifies that the peak was not detected.

It can be seen that for the majority of elements, the LOD is lower for doped beam VLE-PIXE compared to SEM-EDS, demonstrating a greater sensitivity for doped beam VLE-PIXE. This is predominantly due to the lack of Bremsstrahlung background generated during the impact of ions compared to electrons. The reduced background allows the identification of elemental peaks at a lower concentration

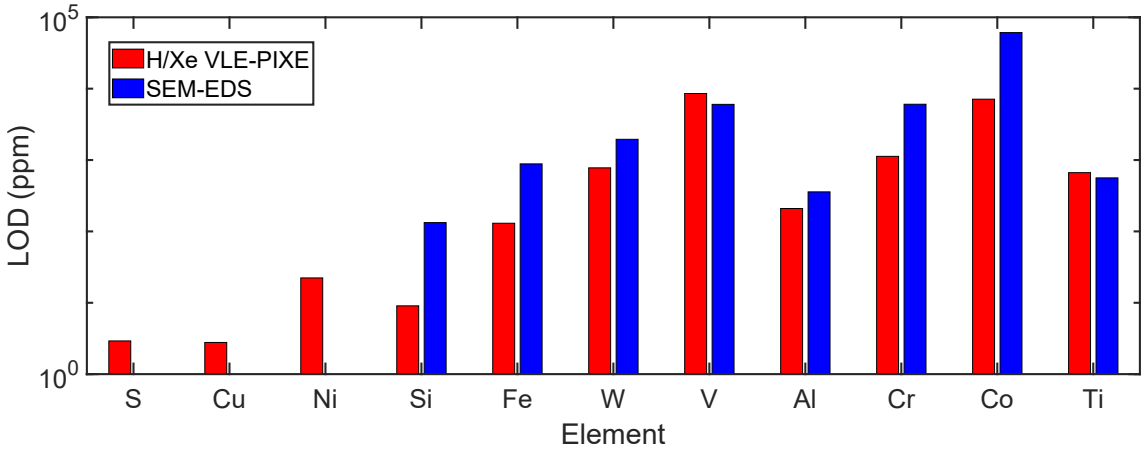

Figure 4.5: Comparison of limits of detection for SEM-EDS and H/Xe doped beam VLE PIXE produced with the beam composition shown in figure 4.1a.

than would be possible if the background were present. Additional minor and trace components were identified however due to overlapping peaks, determination of the SNR and LOD of these components could not be carried out. An example is the overlap of the phosphorus Kα peak with the tungsten Mγ peak.

The maximum improvement in LOD for doped beam VLE-PIXE compared to SEM-EDS is 14.66$\times$ for Si, and the average improvement is 4.30$\times$ for elements detected by both techniques (n = 10). The minimum LOD for Xe doped VLE-PIXE was 2.78ppm for Cu on the SRM 1242, compared to the minimum LOD for EDS at 132.86ppm for Si on the SRM 654b. These LOD values are in line with the expected literature values of 100-500 ppm for EDS [16], and near or below 1 ppm for PIXE, however this value is quoted for PIXE performed at MeV energies [14].

This result demonstrates that the addition of a small amount ($\sim$6%) of Xe to a hydrogen beam is capable of increasing the sensitivity of the VLE-PIXE to levels approaching PIXE performed at MeV energies. El Ghawi et al. described that the LOD for 250keV protons should be several orders of magnitude higher than for 2MeV protons [205], with the LOD for $\leq$30keV expected to be even higher still.

4.1.4 Advantages and Disadvantages of VLE-PIXE and SEM-EDS

While VLE-PIXE is shown to be more sensitive than SEM-EDS, there are however several disadvantages to doped beam VLE-PIXE which must be considered when choosing between the two techniques:

- The greater XRPCS for electrons compared to protons at this energy results

in significantly reduced experimental time for SEM-EDS compared to doped beam VLE-PIXE.

- The spatial resolution of SEM-EDS is significantly better than doped beam VLE-PIXE due to the much smaller electron probe size.
- The ions used in doped beam VLE-PIXE will result in sample damage due to implantation by protons and heavy ions, and sputtering due to heavy ions.

Doped beam VLE-PIXE and SEM-EDS can therefore be considered complementary techniques, with SEM-EDS being beneficial in situations where rapid identification of bulk and minor components, or high spatial resolution is required, and VLE-PIXE finding application where identification of trace elements is required at the expense of experimental time.

4.2 Comparison of Doped Beam VLE-PIXE Performance to LE-PIXE and PIXE

While LE and PIXE data was unavailable for the specific SRM samples measured in these experiments, table 4.5 lists a collection of some literature PIXE LOD values for comparison with doped beam VLE-PIXE. This list is not exhaustive and is only to provide comparison for the VLE-PIXE technique. The LOD values listed are the optimum LOD values for the given experimental conditions.

Z Range	Energy	Best LOD	Notes	Ref.
20-50	3MeV	∼1ppm	Low mass matrix elements	[207]
20-50	3MeV	10-50ppm	Medium mass matrix elements	[207]
20-50	3MeV	10ppm	High mass matrix elements	[207]
20-46	2.61MeV	∼1ppm	Organic matrices	[208]
20-46	4.22MeV	∼1ppm	Organic matrices	[208]
28-57	3MeV	5-10ppm	Micro-PIXE	[209]
25∼90	?MeV	1.5-10ppm	Micro-PIXE	[210]
39	2MeV	2.2ppm	Micro-PIXE with WDS	[211]
15	600keV	850ppm	LE-PIXE	[212]
24	750keV	<0.003 nm	LE-PIXE layer detection	[213]

Table 4.5: Comparison of various PIXE and LE-PIXE LOD values from literature.

For PIXE performed at energies of $\geq$1MeV, typical LODs of between 1 and 10ppm are consistently given. There is however very limited information regarding the LODs achieved by LE-PIXE. Nouli et al. demonstrated an LOD for P of 850ppm for LE-PIXE at 600keV [212]. Zahraman et al. demonstrated that their measured SNR increased with decreasing energy down to 750keV which resulted in a decrease in the LOD. They attributed this to the reduced background signal with decreasing energy which served to better identify the underlying PIXE signal. Overall, this table of literature results demonstrates that best LOD for doped beam VLE-PIXE as calculated above at 2.78ppm demonstrates a performance similar to PIXE performed at much higher energies.

4.3 X-Ray Production Cross Sections

As discussed in section 1.3.4.2, an important metric to describe the underlying physical process of X-Ray production is the X-Ray production cross section. These values account for a number of factors such as detector performance, total stopping power in the material, and mass absorption of the X-Rays as they escape the material.

The method used to calculate the XRPCS from experimental data is outlined in section 1.3.4.3 with an explanation of each contribution to the calculation. It is important to mention that these XRPCS are calculated for the impact of protons alone and do not take into account the addition of the dopant species. These values are instead utilised to demonstrate the performance of doped beam VLE-PIXE in comparison to PIXE performed by protons alone.

Cross section values calculated from doped beam VLE-PIXE experimental data were compared to proton XRPCS from the literature. Empirical, analytical and pre-calculated ECPSSR values are presented from the following sources:

K Shell:

- Analytical cross sections calculated using the method of Paul [120] as outlined in section 1.3.4.4.
- Empirical cross sections taken from the compilation of Paul and Sacher from a variety of sources [214].
- ECPSSR+HS+HE+UA cross sections as calculated by Pia. et al. [215].

L Shell:

- Analytical cross sections calculated using the method of Sow et al [121] as outlined in section 1.3.4.4
- Empirical cross sections taken from the compilation of Miranda and Lapicki from a variety of sources [216].
- ECPSSR+UA cross sections as calculated by Pia. et al. [215].

M Shell:

- Empirical M shell cross sections for W taken from Rodriguez et al. [217]
- ECPSSR cross sections as calculated by Pia. et al. [215].

4.3.1 XRPCS Calculation

The following material parameters were used for the calculation of the XRPCS:

- Material Densities: From NIST Standard Reference Database 126, Table 1 [218]
- X-Ray Mass Attenuation Coefficients: From NIST Standard Reference Database 126, Table 3 [218]
- Total Stopping Powers: Calculated using Ziegler-Biersack method from [219]

The following detector parameters were used for the calculation of the XRPCS:

- Detector Takeoff Angle: 21.5°
- Detector Distance: 16.5mm
- Detector Area: 100mm^2
- Solid Angle: 0.302 sr
- Window Transmission: Approximate transmission curve for SATW window extracted from Duncumb et al. [220]
- Detector Efficiency: Approximate detector efficiency curve extracted from Schlosser et al. [221]

Peak Fitting Routine

To extract the intensity of the X-Ray peaks used for XRPCS calculations, an automated peak finding and fitting routine was used:

- Use peak finding function to determine the positions and approximate widths of any X-Ray peaks. An example of this result is shown in figure 4.6a.
- Use approximate peak locations and widths as starting guesses for pseudo-Voigt fitting routine. The pseudo-Voigt function is described in section 1.3.4.9
- Use nonlinear least squares optimiser to determine accurate peak positions, heights, and Gaussian and Lorentzian widths for pseudo-Voigt fit.

The parameters extracted from figure 4.6b are shown in table 4.6:

Peak	Energy (keV)	Intensity (cts)	Gauss. Width (keV)	Lor. Width (keV)
Ti Kα	4.51	16865	0.0539	0.0018
V Kα / Ti Kβ	4.94	2856	0.0559	0.0033

Table 4.6: Extracted peak positions, heights, and Gaussian and Lorentzian widths for example pseudo-Voigt fit in figure 4.6b

Example XRPCS Calculation

An example XRPCS calculation is shown for a 30keV proton beam on Ti, resulting in the emission of a Ti Kα peak (4.5keV). Using the equation given in 1.55:

$$\sigma_x(E, E_X) = \frac{4\pi}{N_p\ A\ \Omega\ T(E_X)\ \eta(E_X)} \left[\left(\frac{dY}{dE} \right) \left(\frac{dE}{dx} \right) + \mu(E_X) Y \frac{cos\varphi_1}{cos\varphi_2} \right]$$

$$\sigma(24keV, 4.5keV) = \frac{4\pi}{1.04 \times 10^{13}\ protons \cdot 5.67 \times 10^{22} cm^{-3} \cdot 0.302\ sr \cdot 1.00 \cdot 0.98}$$
$$\times \left[22.00\ cts/keV \cdot 2.19 \times 10^5\ keV/cm + 377.68\ cm^{-1} \cdot 16865\ cts \frac{cos(0)}{cos(21.5^\circ)} \right]$$

$$\sigma(24keV, 4.5keV) = 1.08 \times 10^{-27} cm^2$$
$$as\ 1\ barn = 1 \times 10^{-24} cm^2$$
$$\sigma(24keV, 4.5keV) = 1.08 \times 10^{-3} barn$$

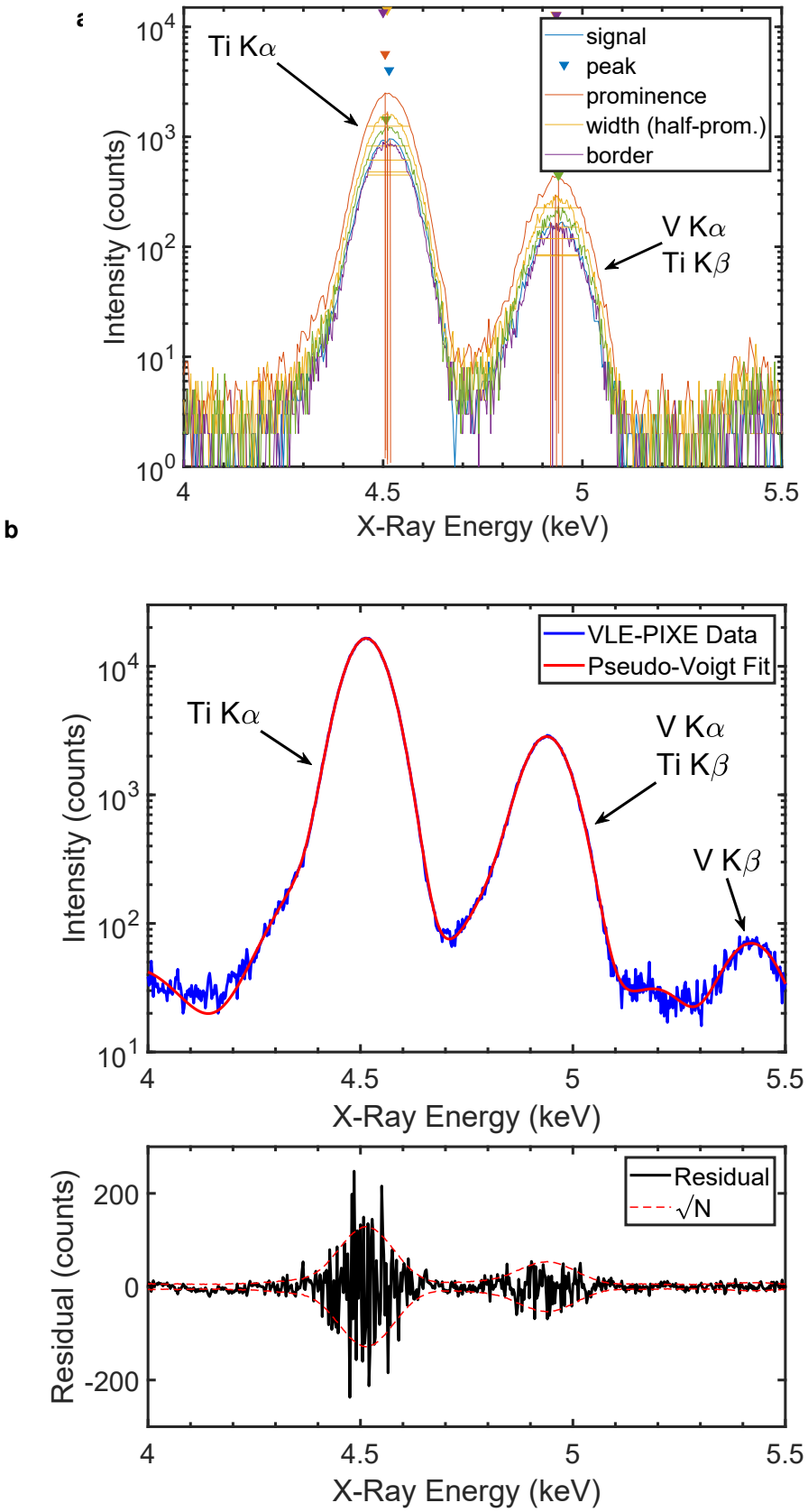

Figure 4.6: An example of the automated peak finding and fitting routine utilised during the XRPCS calculations. (a) Peak finding to locate approximate positions, widths and height of peaks. (b) Pseudo-Voigt fit of the peaks shown in (a) with residuals of fit.

4.3.2 Calculated XRPCS

The calculated XRPCS for the elements identified in SRM 654b and 1242 as outlined in tables 4.3 and 4.4 are shown below alongside comparative literature values if available. For full pseudo-Voigt peak fitting of data, please refer to Appendix section A.7.

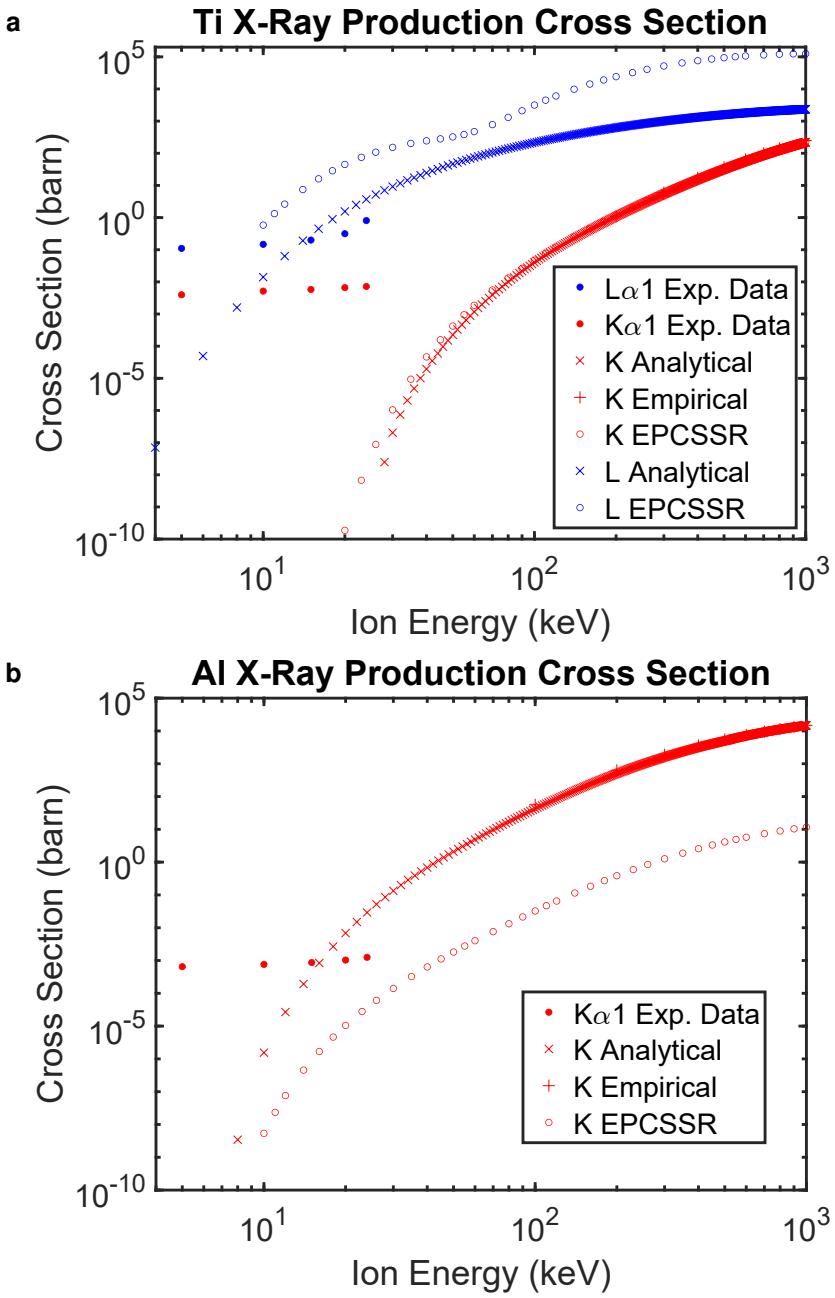

c

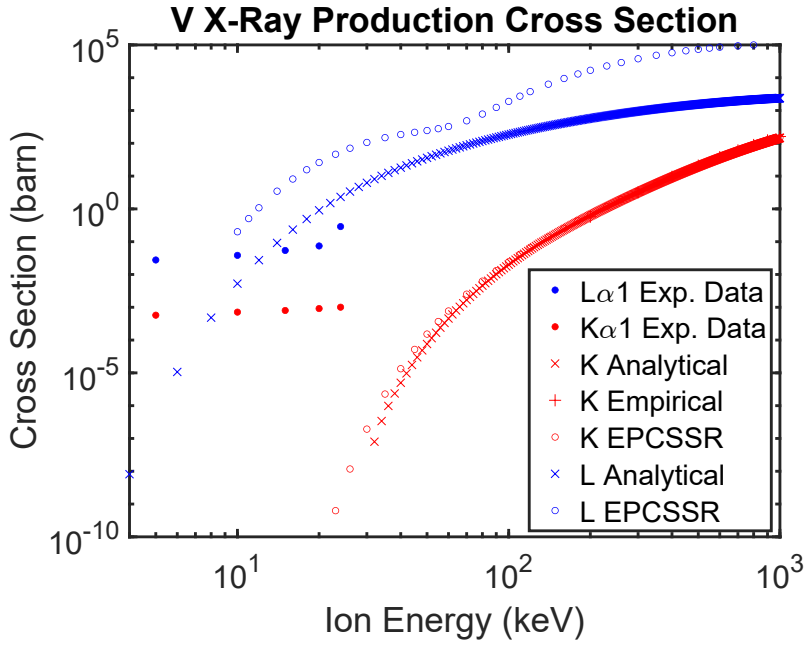
V X-Ray Production Cross Section
Cross Section (barn)
Ion Energy (keV)
Lα1 Exp. Data
Kα1 Exp. Data
K Analytical
K Empirical
K EPCSSR
L Analytical
L EPCSSR

d

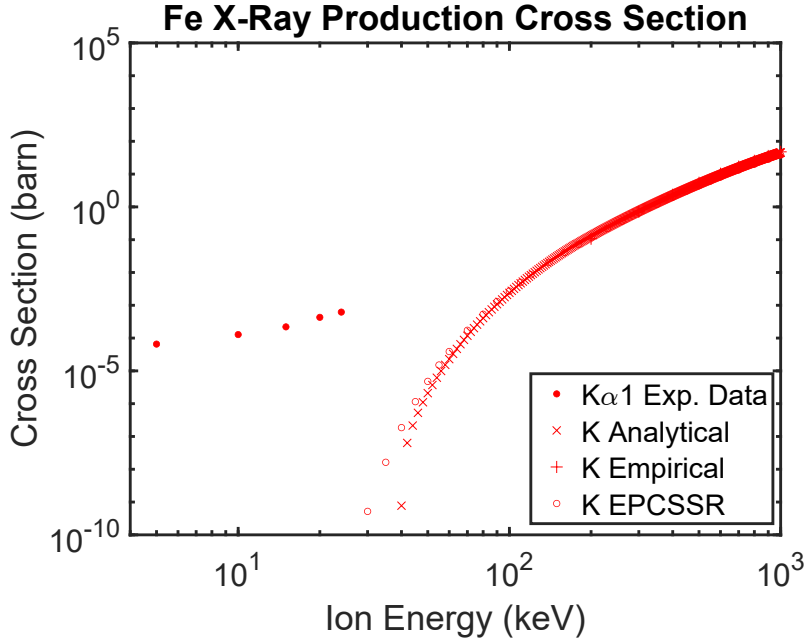
Fe X-Ray Production Cross Section
Cross Section (barn)
Ion Energy (keV)
Kα1 Exp. Data
K Analytical
K Empirical
K EPCSSR

e

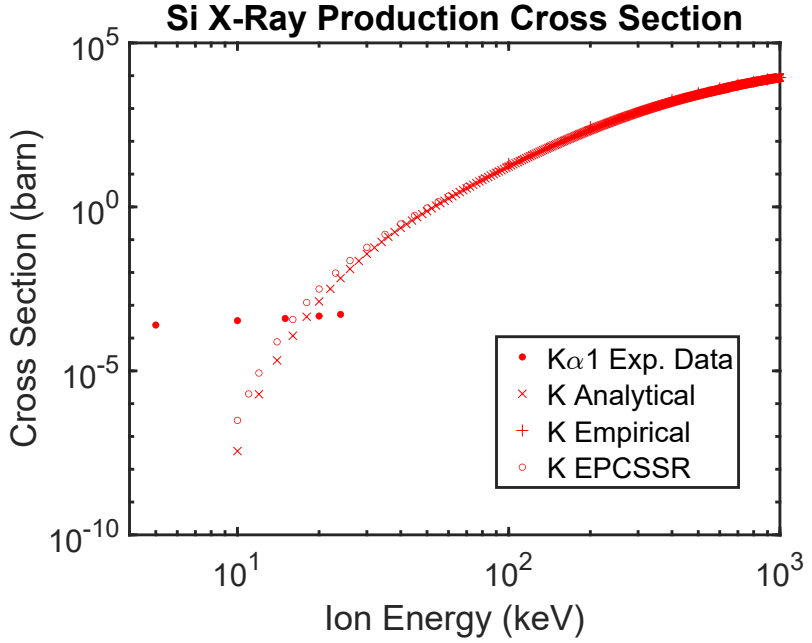
Si X-Ray Production Cross Section
Cross Section (barn)
Ion Energy (keV)
Kα1 Exp. Data
K Analytical
K Empirical
K EPCSSR

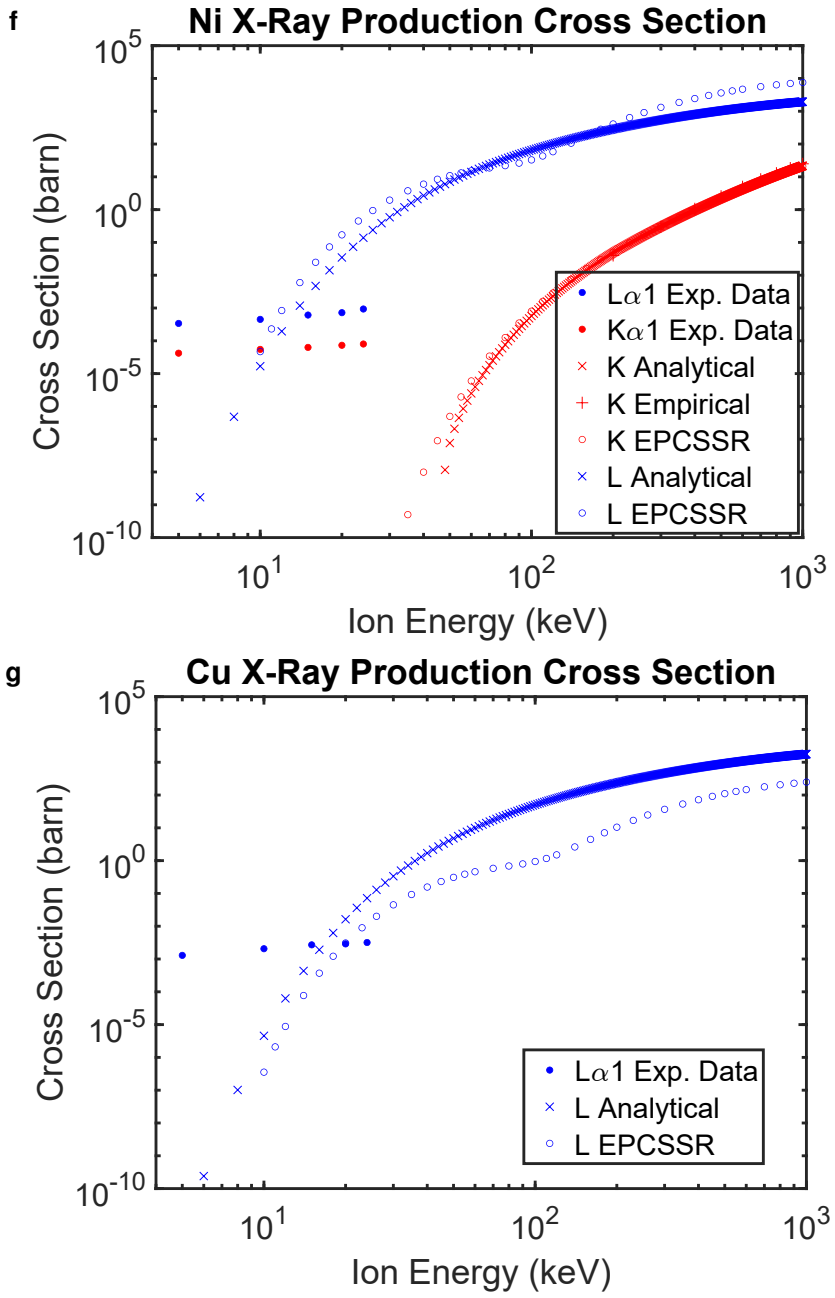

Figure 4.9: Calculated XRPCS for selected elements in the SRM 654b, compared to analytical, empirical, and ECPSSR cross sections. The beam composition used for the calculated XRPCS is given in figure 4.1a.

a

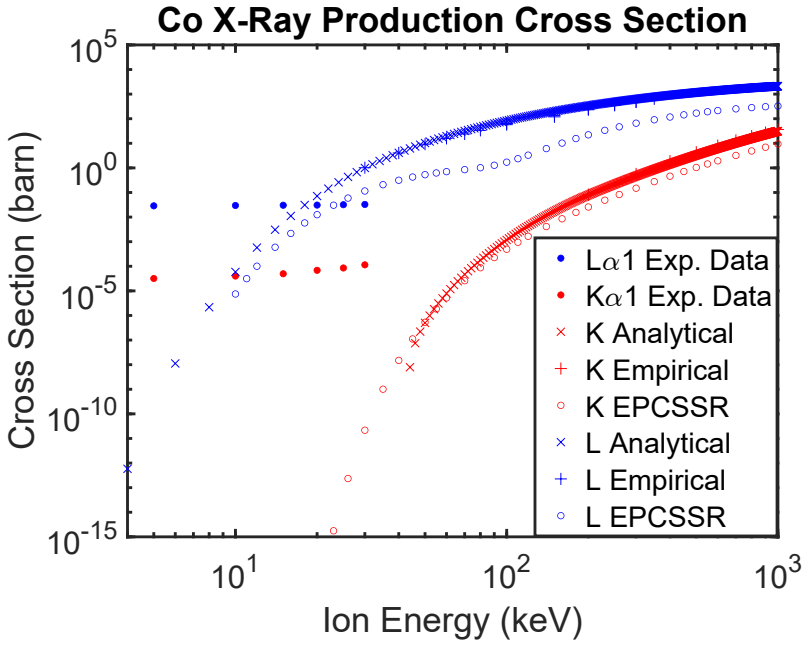
Co X-Ray Production Cross Section
Cross Section (barn)
Ion Energy (keV)
Lα1 Exp. Data
Kα1 Exp. Data
K Analytical
K Empirical
K EPCSSR
L Analytical
L Empirical
L EPCSSR

b

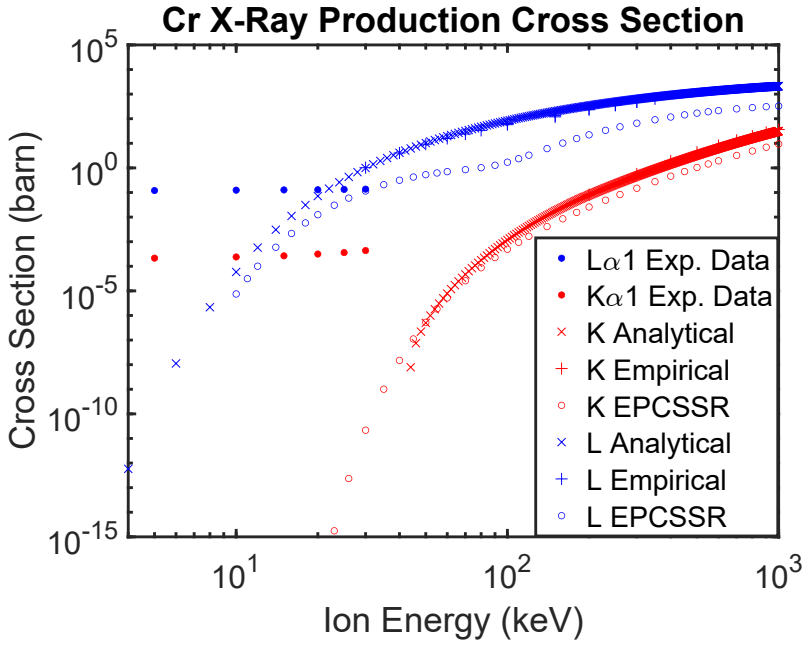
Cr X-Ray Production Cross Section
Cross Section (barn)
Ion Energy (keV)
Lα1 Exp. Data
Kα1 Exp. Data
K Analytical
K Empirical
K EPCSSR
L Analytical
L Empirical
L EPCSSR

c

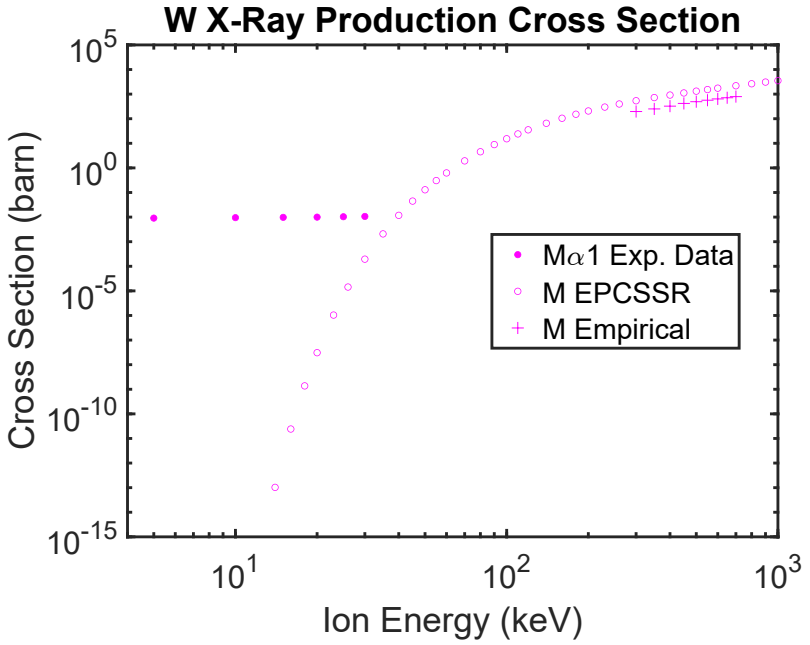
W X-Ray Production Cross Section
Cross Section (barn)
Ion Energy (keV)
Mα1 Exp. Data
M EPCSSR
M Empirical

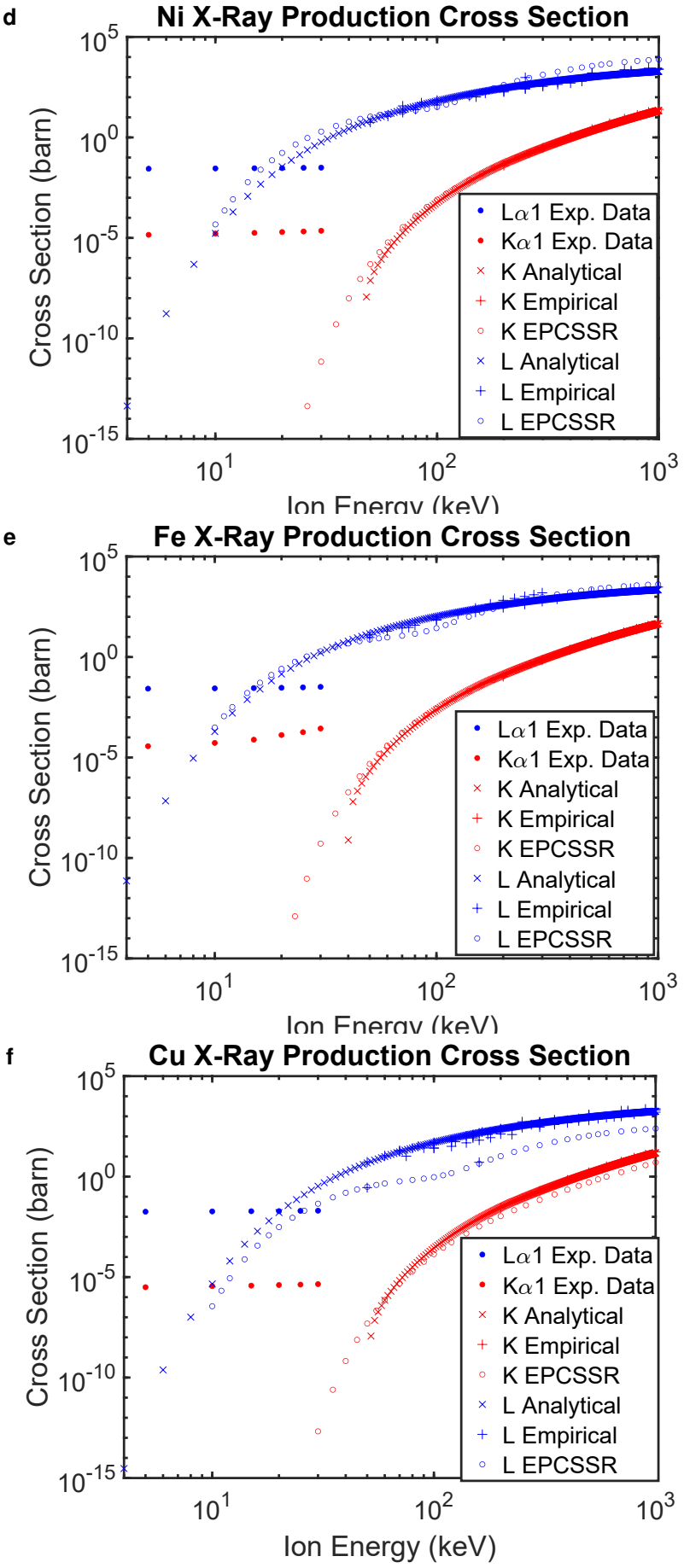

Figure 4.11: Calculated XRPCS for selected elements in the SRM 1242, compared to analytical, empirical, and ECPSSR cross sections. The beam composition used for the calculated XRPCS is given in figure 4.3a.

An interesting observation in both samples is the ratio of L to K shell XRPCS. As an example in figure 4.9a, at an accelerating voltage of 30keV the L/K ratio of the analytical XRPCS is 9×10^{6} whereas the experimental L/K ratio is 38.82, with similar values for other elements where both L and K shell peaks are identified. The experimental L shell values however are much closer to the literature analytical, empirical, and ECPSSR values. This discrepancy suggests that the beam doping method disproportionately affects K shell transitions to a greater degree than L shell transitions.

The response of the calculated XRPCS for doped beam VLE-PIXE with respect to accelerating voltage is significantly different to what is expected based on the literature analytical, empirical and ECPSSR proton XRPCS. The calculated XRPCS decrease quite linearly with respect to decreasing energy, compared to the exponential decrease in XRPCS shown by protons. This behaviour however closely resembles that described by Brandt and Laubert, as is demonstrated in the plot shown in figure 4.12a. The XRPCS for the heavier ions in this plot increase with respect to decreasing velocity with sections of linearity as shown by the red arrows in figure 4.12a. This is in contrast to the exponentially decreasing XRPCS for protons. The doped beam VLE-PIXE XRPCS also bear striking resemblance to XRPCS calculated for heavy ion impacts by Saris as shown in figure 4.12c. The heavy ion impacts demonstrate XRPCS several orders of magnitude greater than H and He impacts [222]. Additionally, several ions demonstrate a roughly linear change in XRPCS with decreasing energy in much the same fashion as observed in the calculated XRPCS above. These plots are denoted by red arrows in figure 4.12c. The reason for this linear trend is not discussed by Saris, or Brandt and Laubert.

Brandt and Laubert attributed the increase in XRPCS with decreasing energy directly to the quasi-adiabatic approach of a projectile to a target atom, and subsequent overlapping of molecular orbitals resulting in electronic energy level crossings. This effect is now commonly referred to as the quasi-molecular model. The results given by the XRPCS as calculated above, provide direct evidence that the heavy ions are responsible for the increased production of X-Rays during doped beam VLE-PIXE and suggest that the responsible mechanism may be the formation of quasi-molecules between the target and the projectile. This effect is discussed in detail in section 1.3.4.5 and investigated further in section 6.1.

As the impact energy increases, the calculated doped beam VLE-PIXE XRPCS are seen to intercept and in many cases, become lower in value the literature analytical, and ECPSSR values. This is particularly prevalent for the L shell cross

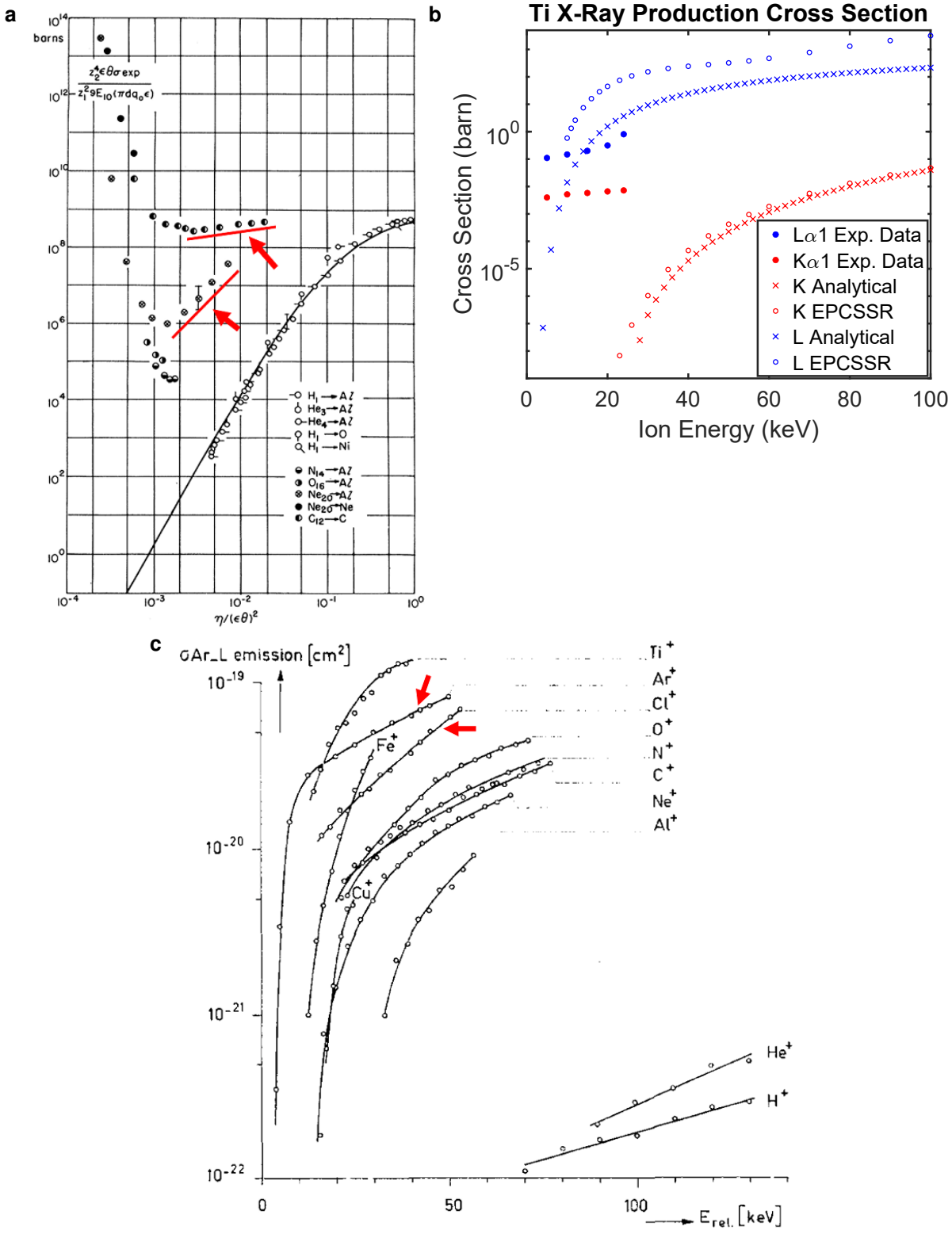

Figure 4.12: (a) K-shell XRPCS of heavy ions on various targets. XRPCS with a linear decrease are denoted with red arrows. (From [101]) (b) Experimental, analytical, empirical and ECPSSR XRPCS from figure 4.9a shown for comparison. (c) Ar L XRPCS for heavy ion impacts on an Ar target compared to H and He. XRPCS with a linear decrease are denoted with red arrows. (From [222])

sections which seem to plateau at a value which is lower than the literature XRPCS, giving the appearance that the introduction of heavy ion dopants is somehow suppressing the emission of X-Rays at increasing energies, a phenomenon which in not reflected in data sets throughout this thesis, such as in figure 5.1a, where the separation of the dopant and proton species should result in an increase in L shell emission. There is an expectation that at higher energies, the effect of heavy ion dopants will begin to decrease due to the high velocity and therefore shorter lifetime of the quasi-molecules formed between the target and the projectile, leading to a reduction in the enhancement by the dopant species, a phenomenon which is discussed in more detail in section 6.2.4. As such, with increasing energy, the ionisation by proton impact is expected dominate X-Ray emission and the proton only XRPCS as provided by the literature can be considered be a valid estimate of the XRPCS. This however relies heavily on the expectation that the literature proton XRPCS are accurate at energies just greater than the maximum FIB energy of 30keV.

As discussed extensively in section 1.3.4.2, the ECPSSR cross sections are well known to be inaccurate at energies where $\xi < 0.2$ or $<$140keV and thus the intercept of the measured VLE-PIXE XRPCS with the ECPSSR values may not be an accurate representation of the real behaviour at energies above 30keV. Likewise, the analytical XRPCS given by Paul and described in section 1.3.4.4 are based on fitted literature empirical XRPCS data which is severely lacking at low energies as described by Lapicki [108]. For these reasons, the comparison of the doped beam XRPCS data to the literature analytical, empirical, and ECPSSR data cannot be compared directly in this situation and should be considered carefully.

For the case of heavy ion impact XRPCS such as those expected by the dopant ions, the theoretical cross sections are considerably less accurate than those of protons alone. Msimanga et al. compared experimental XRPCS data to that of the PWBA, SCA-UA and ECPSSR theories and found that no unified theory could be applied to all ions under all experimental conditions [113]. Similar results have been observed by several other groups [223, 116, 224], with results varying wildly for different energies and projectile masses, in many cases the measured XRPCS values vary by many orders of magnitude compared to theoretical values in a manner not dissimilar to that seen in this research. Even within different theories such as ECPSSR and PWBA, the calculated values can vary drastically. Thus, when heavy ions are considered, the current theoretical explanations for X-Ray production are insufficient and cannot accurately describe experimental observations. This is of course further compounded by the mixing of both heavy and light ions such as that experienced during doped beam VLE-PIXE measurements, the

combination of which is demonstrated throughout this thesis to produce X-Ray production which defies theoretical explanations of both proton X-Ray production and heavy ion X-Ray production alone. This effect has significant implications for accurate VLE-PIXE quantification, with significantly higher than expected X-Ray yields resulting in an over-estimation of elemental concentrations within a sample. For this reason, the ionisation behaviour of multiple simultaneous ion species must be investigated and an analytical model developed to determine accurate X-Ray production by multiple species. This will be discussed further in chapter 6.

4.4 Conclusions

This chapter demonstrated that the sensitivity of VLE-PIXE performed with a lightly doped Xe beam is comparable to PIXE performed at much higher energies. When compared to SEM-EDS, the sensitivity of doped beam VLE-PIXE was superior in almost all cases however this sensitivity was achieved at the expense of significantly increased experimental time due to the very low X-Ray production. Doped beam VLE-PIXE can therefore be considered a complimentary technique to SEM-EDS which can be utilised for the identification of elements which are obscured by the Bremsstrahlung background typical of SEM-EDS spectra.

The calculated XRPCS shown above demonstrate that the addition of a small proportion of Xe to a hydrogen beam can enhance the XRPCS well beyond what is expected by the impact of protons alone at the given energies. This was particularly prevalent for the K shell XRPCS which deviate from expected values by many orders of magnitude. This provides evidence that the doping method affects K shell transitions to a greater degree than L shell transitions.

While the impact of beam doping on VLE-PIXE performance is clear, the mechanism surrounding the enhancement of X-Ray production is not well understood. The following chapters will attempt to provide some explanation based on the underlying physics of ionisation and the wealth of knowledge provided in the literature over several decades.

Chapter 5

Role of Heavy Ion Dopants in VLE-PIXE

As demonstrated in the previous chapter, the performance of doped beam VLE-PIXE was shown to approach undoped beam VLE-PIXE performed at much higher energies. This chapter outlines an investigation into the performance and underlying mechanisms of the beam doping technique. Methods to improve the performance of this technique are discussed including the use of different dopant ion species and different proportion of dopant ion species.

5.1 VLE-PIXE Response to Magnetic Field Strength

As discussed several times throughout this thesis, the magnetic immersion field of the SEM results in a deviation of ion trajectories as they travel from the FIB column to the sample. The force applied to each ion is inversely proportional to the mass of the ion species, such that the beam can be separated into its individual mass components. The magnetic field strength can be adjusted so that the beam components overlap when no field is present, or fully separated when the magnetic field strength increases. In the case of doped beam VLE-PIXE, the separation of the proton and dopant species is not expected to have any significant impact on the signal strength as, regardless of where the components strike the homogeneous sample, they should be capable of producing the same quantity of X-Rays. What was observed however is that as the proton and dopant species were separated, the X-Ray signal rapidly decreased. This is shown in figure 5.1a where VLE-PIXE spectra of the SRM 654b are shown as a function of relative magnetic field strength. Figure 5.1c shows the intensity of some prominent peaks, shown as the ratio of the peak intensity when the beam is fully separated. These peaks were chosen as they remain present in all spectra.

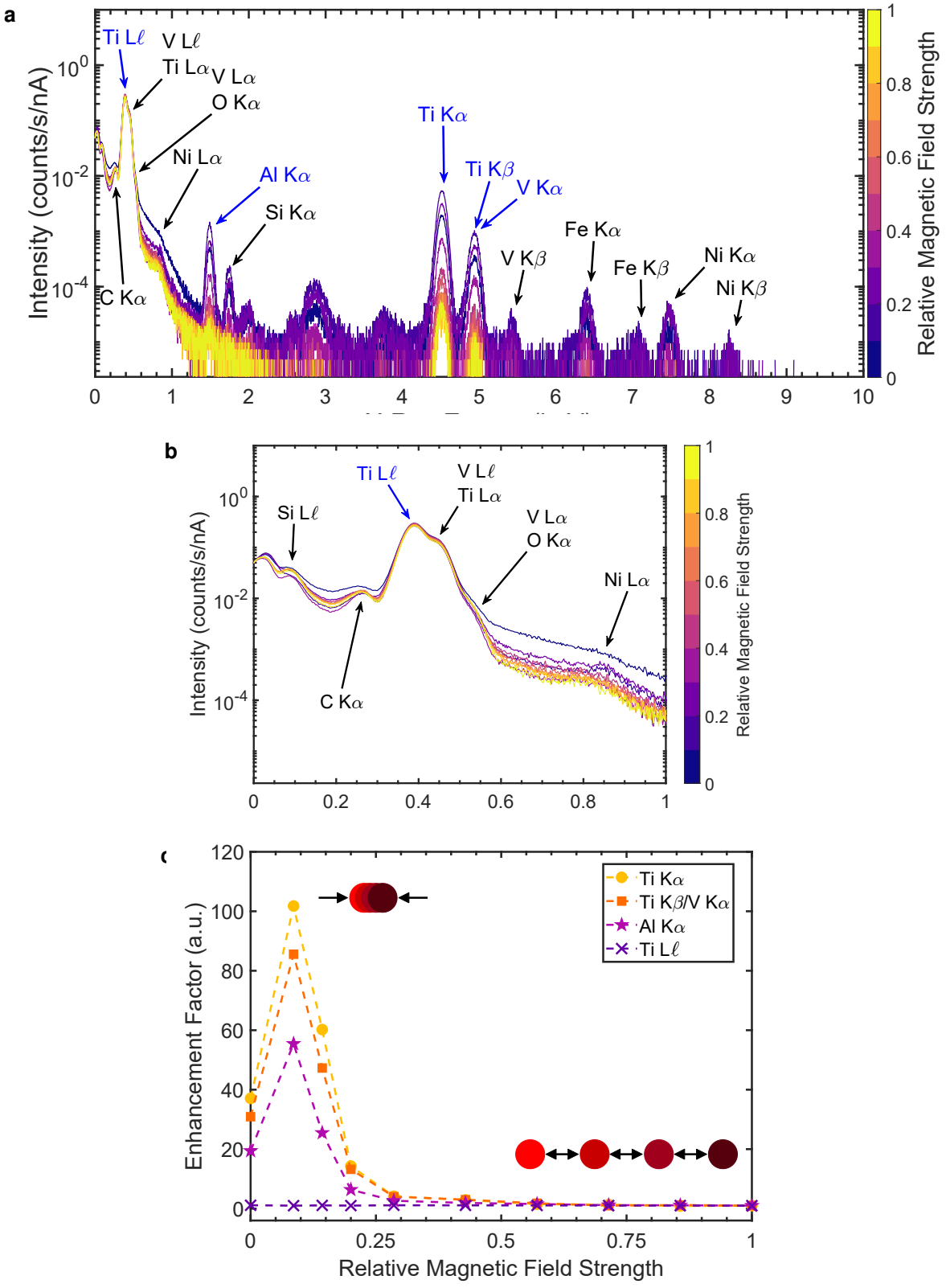

Figure 5.1: VLE-PIXE spectra of the NIST SRM 654b vs. relative magnetic field strength (a) 24keV VLE-PIXE spectrum vs. relative magnetic field strength. (b) Isolated region of (a). (c) Relative intensities of some prominent peaks marked in blue in (a) and (b). Peaks $<$1keV are marked with crosses. Dashed lines are a guide to the eye. Red discs represent separation of beam components.

This result demonstrates that the impact of protons and heavy ion dopant species upon the same location on the sample results in an X-Ray signal greater than the sum of the hydrogen and heavy ion dopant signals independently. SEM images of the irradiations shown in figure 5.1a are provided in appendix section A.5 and demonstrate the changing overlap of the beam components with increasing magnetic field strength.

The decrease in VLE-PIXE signal is however not equal across the entire spectrum. This decrease is only observed for the portion of the spectra with an X-Ray energy of greater than ∼1keV. An excerpt of the spectra below 1keV is shown in figure 5.1b where it can be seen that this region is relatively invariant to the magnetic field strength. This is also reflected in figure 5.1c where the Ti Lℓ line does not change with respect to magnetic field strength. An important observation is that the peaks above 1keV are predominantly K shell X-Ray peaks whereas the peaks below 1keV are predominantly L shell peaks. This can be correlated with the calculated XRPCS as shown in figures 4.9a-4.9b, where the L shell XRPCS were much closer to the expected literature values than the K shell XRPCS. This evidence leads to the conclusion that the peaks observed below an energy of ∼1keV are likely due to the impact of protons alone, as these peaks are observed even when the beam components are separated.

It is also observed in figure 5.1c that the maximum X-Ray intensity with magnetic field strength is offset from the 0 relative magnetic field position by ∼20%. This is most likely due to an offset in setting the magnetic field strength required to counteract the remnant magnetic field of the magnetic immersion lens coil as discussed in section 2.2.1, which when adjusted becomes the reference point for the 0 relative magnetic field strength. The 0 relative magnetic field strength position is set by manually changing the magnetic immersion lens coil strength until all the beam component secondary electron images visually converge. This is also known as the ”double spot compensation” due to the remnant magnetic field causing multiple secondary electron images, one for each beam species due to their spatial separation. The very weak intensity of the H^+ beam relative to the more intense H_2^+ and H_3^+ species, makes it very difficult to visually align the image generated by the H^+ ions. As such, visually aligning the beam images may not result in a complete overlap of the H^+ species with the remaining beam components at the 0 relative magnetic field strength point. The very light mass of the H^+ ion results in a significant spatial deviation with the small offset in magnetic field strength. As the magnetic field strength is increased during the experiments in figure 5.1a, the H^+ beam comes into full convergence with the remaining beam species and a resulting increase in X-Ray intensity is observed.

5.1.1 Current Change vs. Magnetic Field Strength

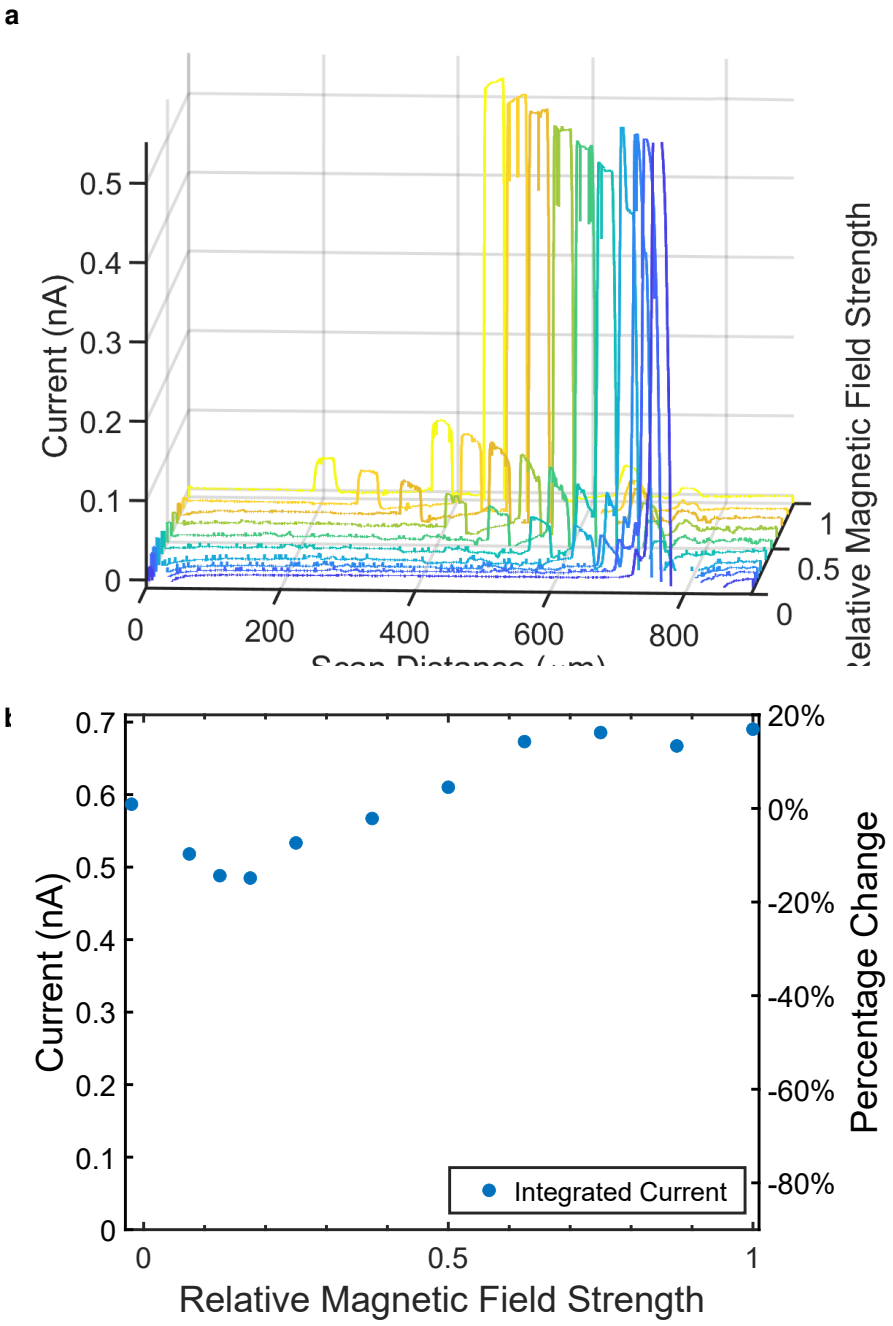

Figure 5.2: (a) Beamlet current measurement vs. relative magnetic field strength. (b) Change in integrated current from (a) vs. relative magnetic field strength.

The increasing magnetic field may also result in a change in total beam current and must be considered as a possible explanation for the reduction in X-Ray signal intensity as observed in figure 5.1a with increasing magnetic field strength. To test this, the beam current was measured as a function of magnetic field strength as shown in figure 5.2a and quantified in figure 5.2b as an integration of the beam component current spectrum. It can be seen that the total beam current fluctuates

with changing magnetic field strength, first decreasing by approximately 20%, then increasing by approximately 20%, in the opposite behaviour to what is observed in figure 5.1c with respect to the change in X-Ray intensity with magnetic field strength.

To determine the influence of such a change in beam current on the VLE-PIXE spectra and whether this can be attributed to the effect seen in figure 5.1a, several VLE-PIXE spectra of the SRM 654b were taken as a function of beam current spanning greater than an order of magnitude. These spectra are shown in figure 5.3a, and the total X-Ray counts are shown in figure 5.3b. Based on the reduction in total X-Ray counts between the most intense spectrum, and the spectrum at the maximum magnetic field strength in figure 5.1a, it was determined that a current decrease of $>$90% is required to observe the measured change in VLE-PIXE signal. As a current change of no greater than 20% is shown over the full range of magnetic field strengths as shown in figure 5.2b, a change in current with magnetic field cannot be responsible for the observed effect.

Additionally, the change in VLE-PIXE signal observed in figure 5.2a with respect to current affects the entire spectrum equally, whereas the change in VLE-PIXE signal in figure 5.1a with respect to magnetic field strength only affects the region above 1keV. This provides additional evidence that a change in beam current cannot be responsible for the decrease in VLE-PIXE signal with changing magnetic field.

5.1.2 Electron Contributions

As discussed in section 3.2.3, stray electrons generated from gas scattering in the chamber and FIB column must be considered when using the VLE-PIXE technique. While efforts were taken to reduce the influence of electrons such as ensuring the C2 lens voltage bias was positive, and ensuring that the FIB column and chamber were pumped for an extended period of time, the possibility of electrons escaping the column must still be considered. The addition of a heavier ion species to the hydrogen beam may result in the generation of a greater number of electrons in the lower FIB column due to the larger scattering cross section of the heavy ions with the gas molecules. As the magnetic field strength increases, these electrons may then be deflected away from the sample, resulting in the behaviour observed in figure 5.1a.

A significant feature of electron induced X-Ray spectra however is the presence of the broad Bremsstrahlung background which was previously demonstrated to

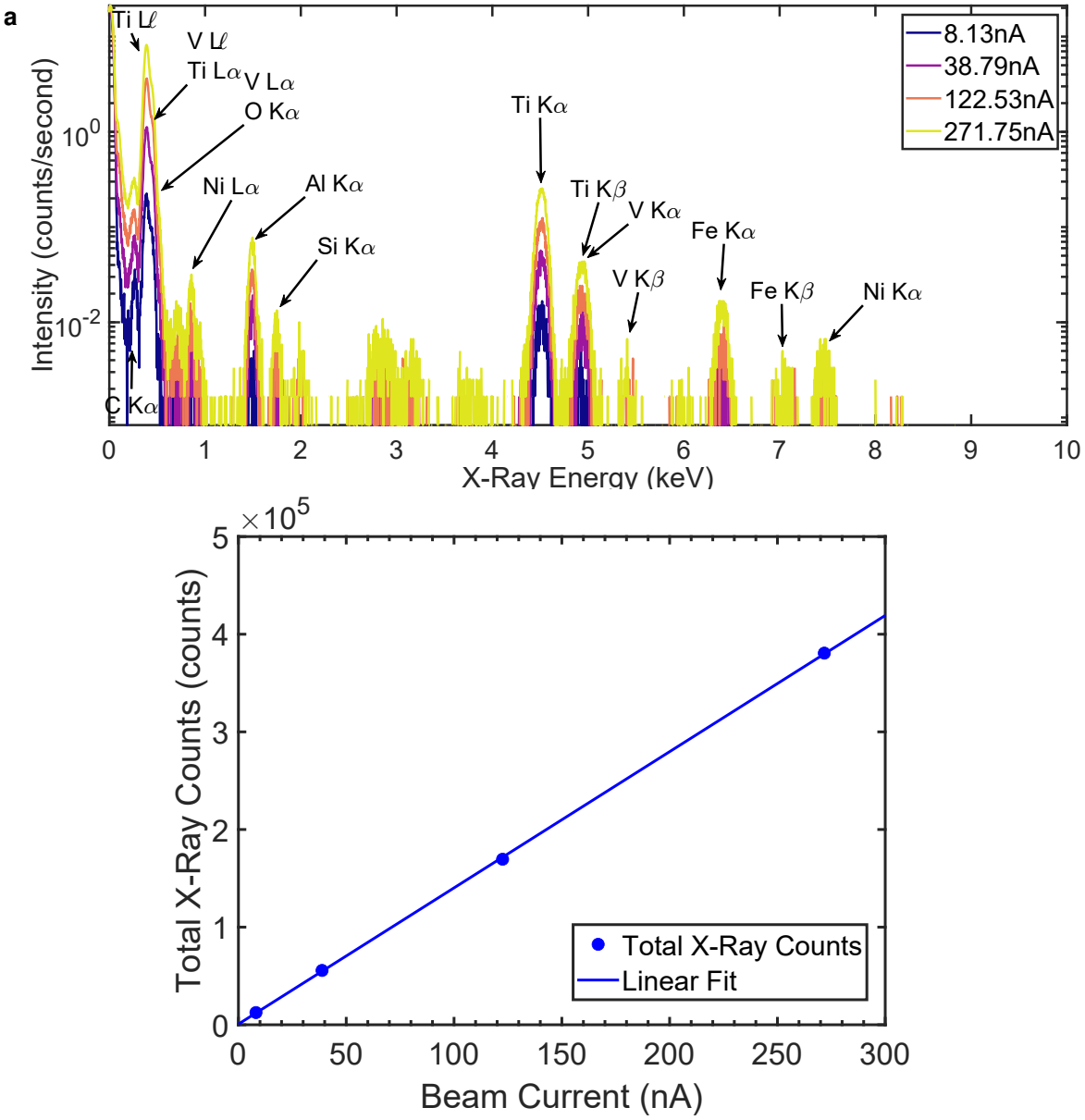

Figure 5.3: (a) Current dependence of VLE-PIXE spectra (b) Measured change in total X-Ray counts as a function of beam current

obscure low intensity peaks, as shown in figure 4.2a and 4.2b, and is consistent across all electron accelerating voltages as shown in appendix section A.4. As this Bremsstrahlung background is not seen in doped beam VLE-PIXE spectra, this helps eliminate the role of electrons in the generation of the VLE-PIXE signal.

There may however be a possibility of enhancement caused by the co-irradiation of protons and a low current of electrons such as those emanating from the FIB column. Such electrons may cause additional ionisation of target atoms, resulting in a greater number of X-Rays emitted and an increase in XRPCS, or additional ionisation may result in the suppression of non-radiative transitions which is discussed in more detail in section 6.1.1. To test the effect of simultaneous electron

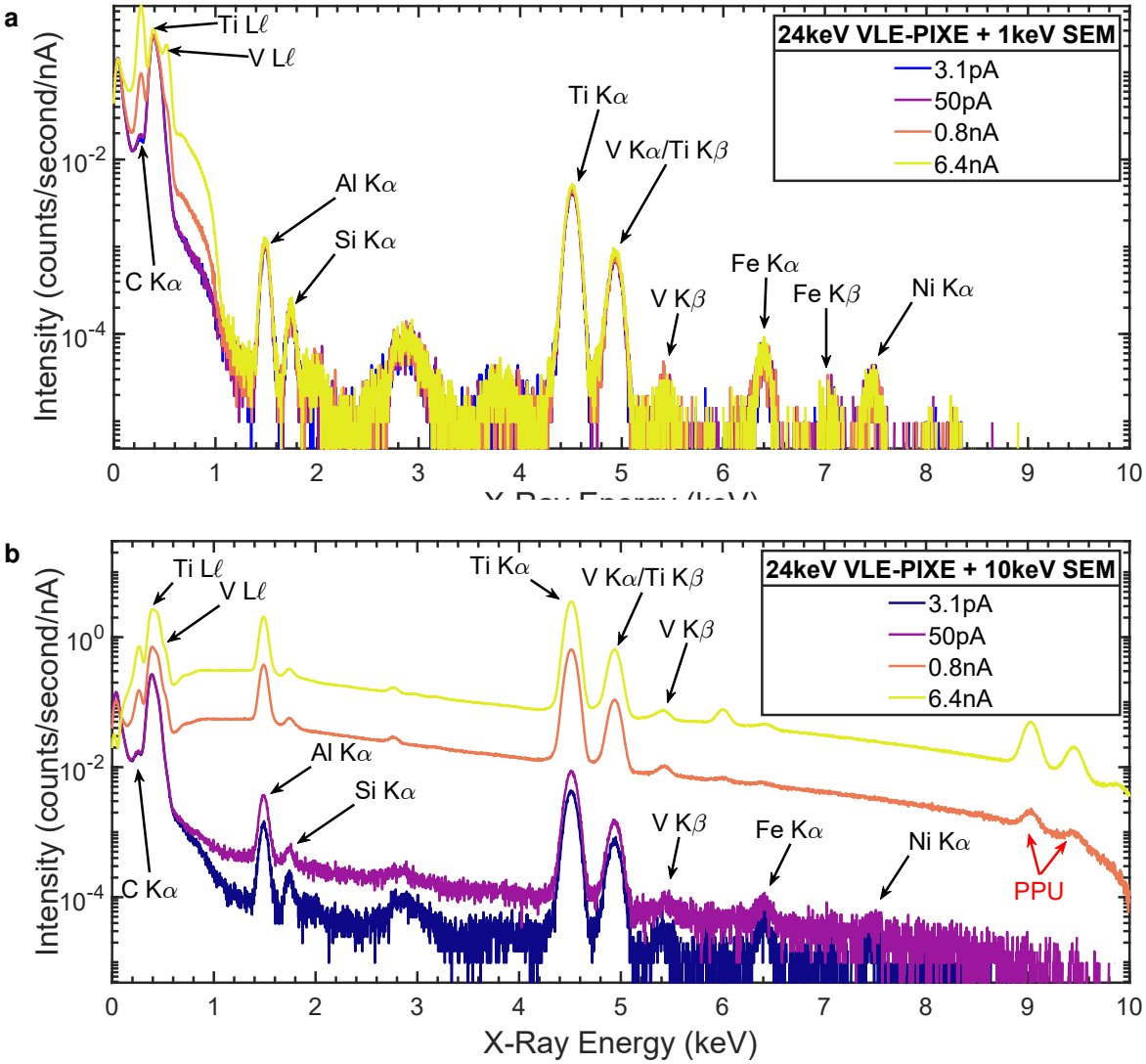

Figure 5.4: X-Ray spectra taken on the SRM 654b during co-irradiation of a hydrogen beam and (a) a 1keV electron beam and (b) a 10keV electron beam, as a function of electron beam current. Pulse pile up (PPU) peaks are labelled in red.

impact, an experiment was performed by first reducing the enhanced VLE-PIXE signal by increasing the magnetic field strength, as was shown in figure 5.1a, then exposing the SRM 654b to both protons and electrons on the same sample region. A 1keV electron beam was used as this represents the upper energy limit of the low X-Ray spectral region as shown in figure 5.1b and a 10keV electron beam was used as this represents the upper energy limit of all X-Ray peaks shown in figure 5.1a. The results of this experiment are shown in figure 5.4a for a 24keV hydrogen beam and a 1keV electron beam, and figure 5.4b for a 24keV hydrogen beam and a 10keV electron beam.

1keV electron beam is shown to only cause an increase in signal and Bremsstrahlung at an X-Ray energy of $<$1keV as expected. The 10keV electron beam enhances all the observed X-Ray transitions but also causes an increase in Bremsstrahlung

which obscures low intensity X-Ray peaks. These experiments demonstrate that while electrons may cause enhancement of the VLE-PIXE signal, they do so at the expense of increased Bremsstrahlung background. The VLE-PIXE signal enhancement induced by beam doping therefore cannot originate from the increased production of electrons in the lower column due to the enhanced scattering from gas molecules by the dopant heavy ion species. Additionally, during the negative sample biasing experiments in section 3.2.1, such low energy electrons would be reflected by the bias prior to reaching the sample and would not influence the VLE-PIXE spectra, as was observed in the biasing experiments in figure 3.6b.

The electron contribution can also be established by fitting doped beam VLE-PIXE data using the pseudo-Voigt fitting routine described in section 4.3.1. As shown in figure 5.5a, the low energy region of a Xe doped beam VLE-PIXE spectra can be fit precisely to the prescribed characteristic peaks of the SRM 654b with the residual plot displaying a linear background. Should there be a contribution from electron Bremsstrahlung, this residual plot would not be linear but would instead increase towards an X-Ray energy of zero. As this is not the case, this demonstrates that the only contribution is from the VLE-PIXE spectrum. The residual noise is proportional to the signal intensity of the VLE-PIXE spectrum which scales as expected with $\sqrt{N}$ as described in section 1.3.4.8. The small features observed in the residual spectrum at an X-Ray energy of 0.2-0.35 keV are due to non-ideal fitting conditions.

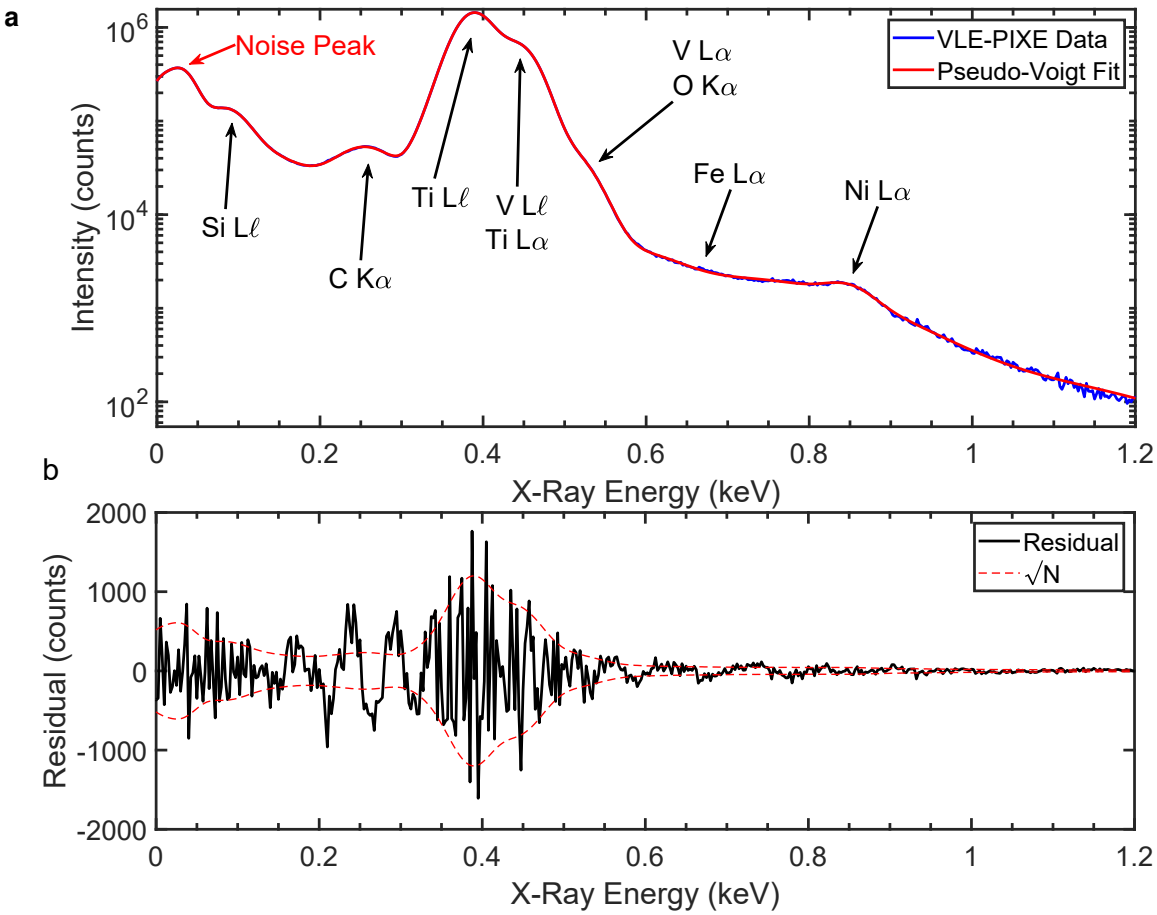

Figure 5.5: (a) Pseudo-Voigt fit and (b) residual plot of a Xe doped VLE-PIXE spectrum demonstrating the lack of contribution from electron Bremsstrahung background at low energies.

5.2 Influence of Dopant Species on VLE-PIXE Performance

As was established in section 5.1, the impact of the proton and heavy ion dopant species on the same region of the sample is essential for generating an enhanced X-Ray signal. To establish the influence of the dopant ion species on X-Ray production, beams were prepared with >99% hydrogen, and hydrogen doped with N, Ar, and Xe. To establish the >99% undoped beam, the FIB column was pumped overnight to remove residual gaseous species. To establish the lightly doped beam, the procedure described in section 2.4 was used. The composition of these beams before and after the measurements are shown in appendix section A.6. VLE-PIXE spectra of the SRM 654b are shown in figures 5.7a-5.7d with respect to relative magnetic field strength.

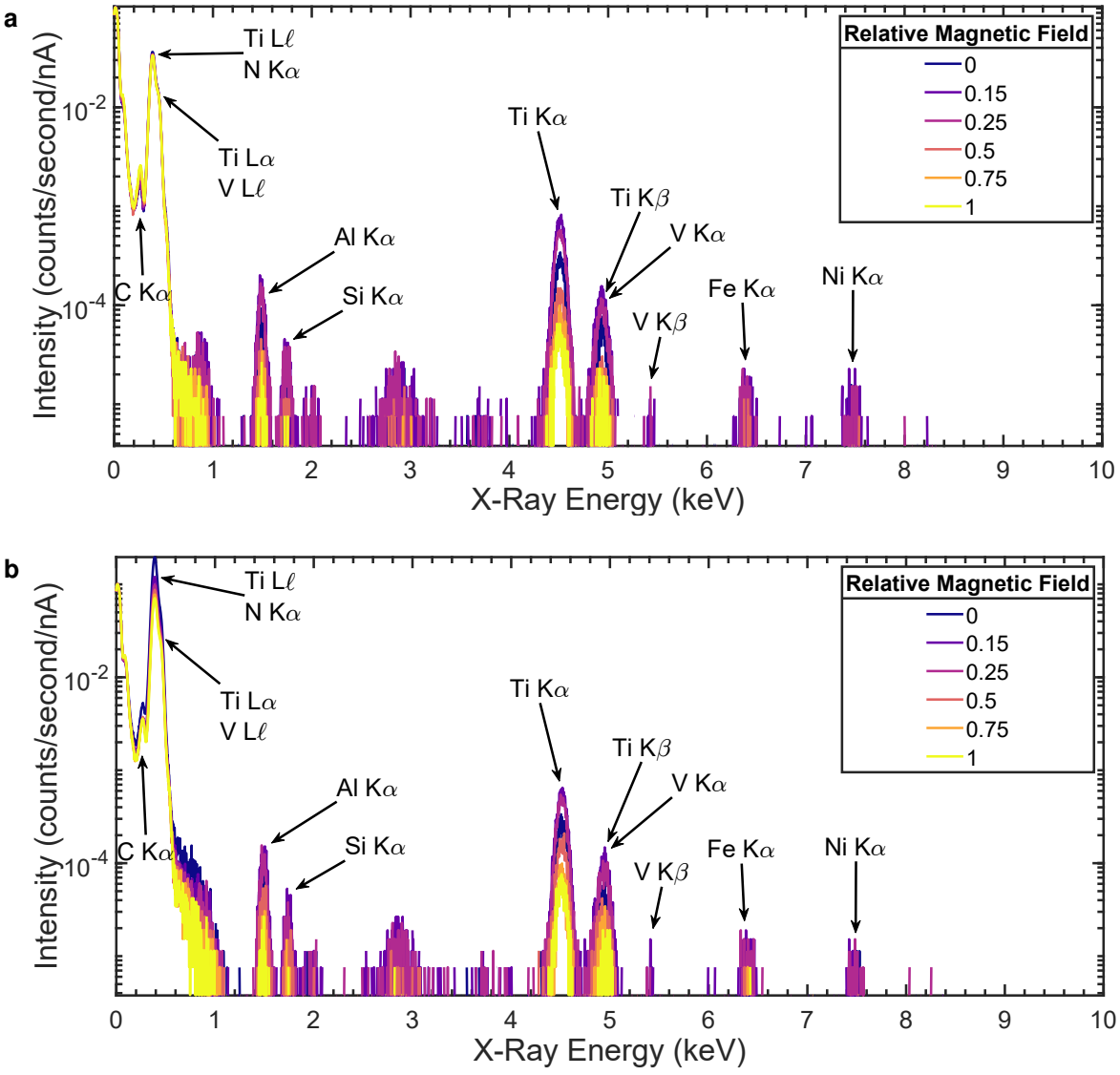

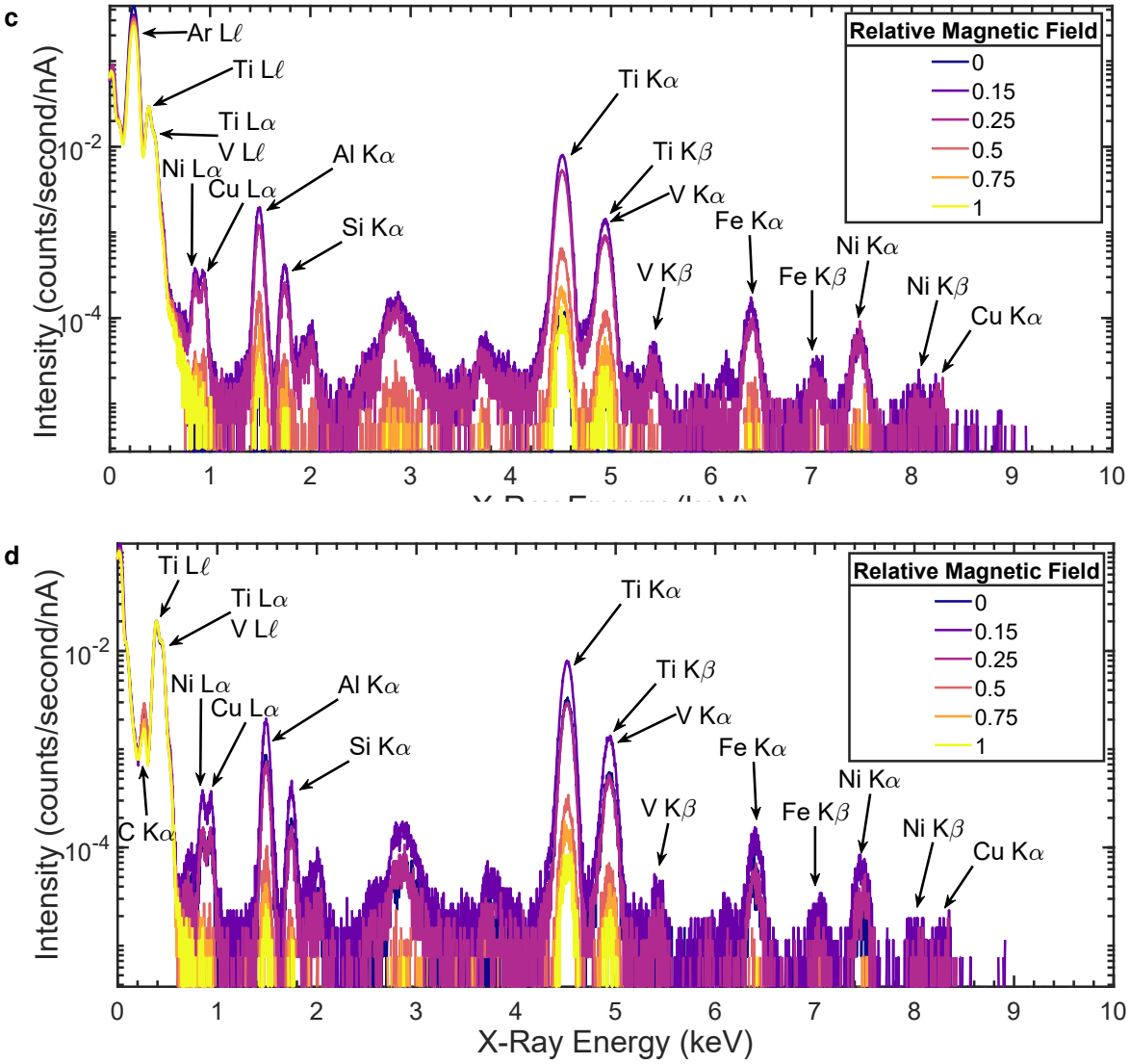

Figure 5.7: Doped hydrogen beam spectra vs relative magnetic field strength. (a) >99% hydrogen beam, (b) N doped hydrogen beam, (c) Ar doped hydrogen beam, and (d) Xe doped hydrogen beam. In all spectra, the intensity with magnetic field strength follows the trend as outlined in section 5.1.1, first increasing from low intensity, then decreasing.

As can be seen in figure 5.7a, the response of the undoped (>99% hydrogen) VLE-PIXE to the magnetic field shows that some residual contamination is still present despite the best efforts establish a very clean beam. This also demonstrates that even a trace amount of contamination is sufficient to enhance the production of X-Rays. The intensity with respect to magnetic field strength for all spectra once again follows the trend as outlined in section 5.1.1, first increasing, then decreasing. The undoped and nitrogen spectra are quite similar with the exception of a significantly enhanced peak at ~0.392 keV which can be attributed to emission from the nitrogen projectile. The similar change with respect to magnetic field for both these spectra suggests that the nitrogen has a negligible affect

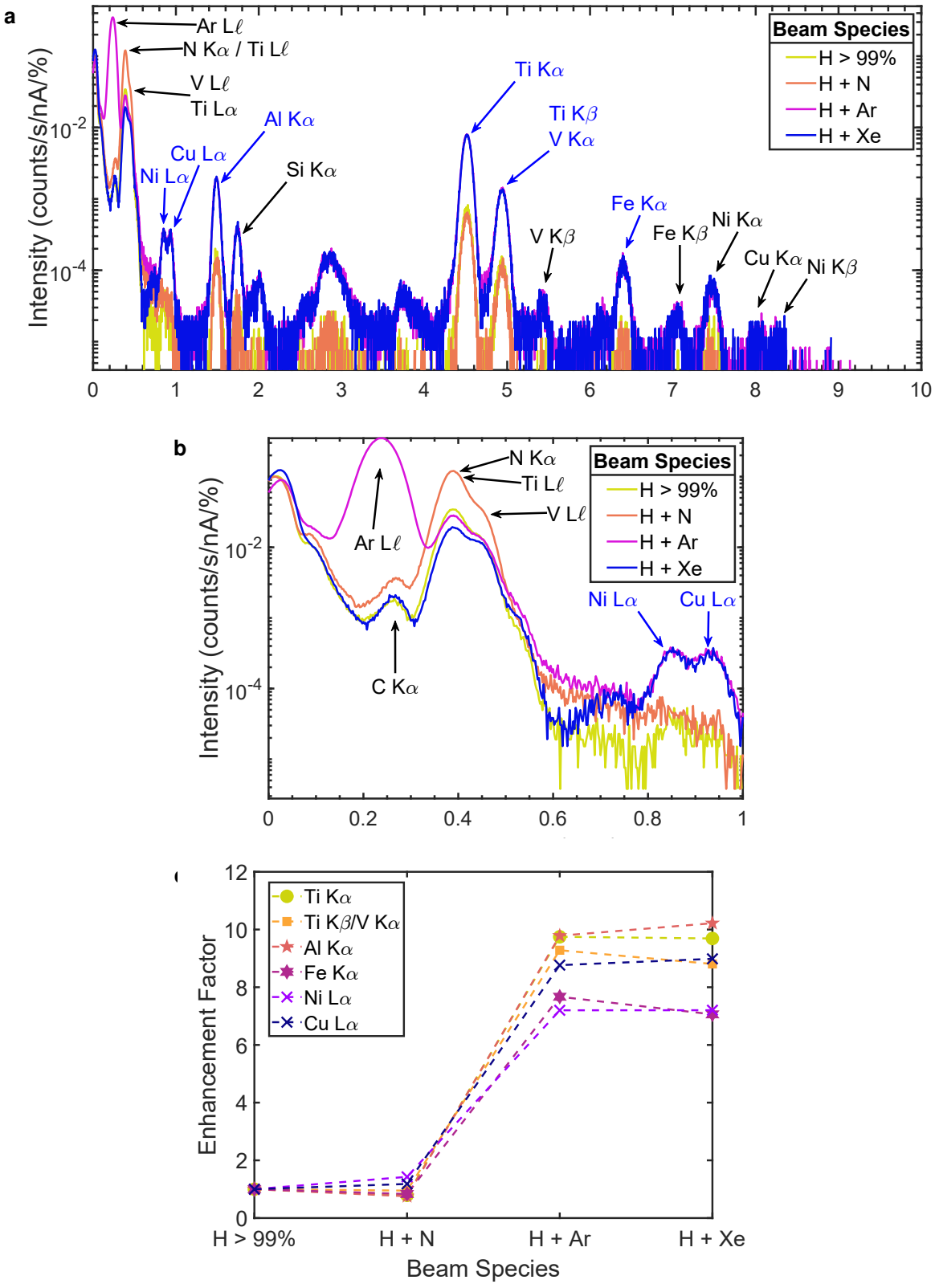

Figure 5.8: Influence of dopant species on VLE-PIXE performance. (a) VLE-PIXE spectra for the various dopant species. (b) Isolated region of (a). (c) VLE-PIXE enhancement factors relative to >99% hydrogen ion beam for the various dopant species marked in blue in (a) and (b). L shell transitions are marked with crosses. Dashed lines are a guide to the eye.

on the enhancement of the VLE-PIXE spectra and that any enhancement relative to the separated beam may be due to residual Ar or Xe contaminants. The Ar and Xe spectra shown in figures 5.7c and 5.7d show a significant enhancement relative to the fully separated beam across the entire spectrum greater than 1keV. When compared to the Xe spectra, an intense peak at an X-Ray energy of $\sim$0.22keV is observed and attributed to emission from the Ar projectile. This peak is investigated further in section 5.4.2. The Xe spectrum however does not show any additional peaks and as such, is the favourable species for analysis of low energy peaks in the region where the influence of Ar or N may obscure sample characteristic peaks.

A comparison of the most intense VLE-PIXE spectra with respect to magnetic field strength, taken with the undoped and doped beams are shown in figure 5.8a, normalised to beam current, capture time, and the percentage of dopant species in the beam. Enhancement factors relative to the undoped hydrogen beam are shown in figure 5.8c for each dopant species. As shown in figure 5.8c, a significant increase in X-Ray production is demonstrated with the introduction of the Ar and Xe species, however the effect of the N species was negligible.

The low performance of nitrogen may be due to the simple nature of the N electronic structure compared to Ar and Xe, resulting in a less significant change in the electronic structure of the target atoms due to the formation of quasi-molecules. The higher velocity of the N species, as well as the smaller atomic radius may also also result in a shorter lived quasi-molecule compared to Ar or Xe. As calculated in section 6.2.4, the collision time for N will be approximately 0.58$\times$ that of Ar and 0.37$\times$ that of Xe, which also reduces the probability of coincident interaction with the sample as discussed in section 6.3. All these factors will result in a reduction in performance for N compared to Ar and Xe as reflected in figure 5.8c.

The increase in performance between the Ar and Xe dopant species was small. This effect may be due to the much larger distance of closest approach for Xe compared to Ar, defined as the smallests internuclear distance achieved during a collision. This metric, calculated as 5.76×10^{-11}m and 5.18×10^{-10}m for Ar and Xe respectively, influences the shift in energy levels associated with the formation of a quasi molecule, with a smaller distance of closest approach resulting in a greater shift in projectile and target energy levels. This effect will be discussed in greater detail in section 6.2.3. In the case of N, despite the much smaller distance of closest approach compared to Ar and Xe at 8.71×10^{-12}m, the simple nature of the N electronic structure and the short lived quasi-molecule will negate the influence of the smaller distance of closest approach.

Both the low performance of N and the low increase in performance between Ar and Xe may also be explained by the ratio of the projectile to target atomic numbers (Z_1/Z_2). Brandt and Laubert explained that as the Z_1/Z_2 ratio increases above 0.6, the result is a rapid increase in XRPCS due to the Pauli excitation model attributed to the formation of quasi-molecules [101]. When the Z_1/Z_2 ratio exceeds 1 however, the XRPCS does not increase any further. This is represented in figure 1.26b. The Z_1/Z_2 ratios for the dopants used throughout the VLE-PIXE experiments compared to the elements identified in the SRM 654b are listed in table 5.1. For the case of Nitrogen, the only element which the Z_1/Z_2 ratio exceeds 0.6 is carbon, which is only present as a surface contaminant in the SRM 654b. Indeed, the C Kα line is shown to be more intense for the N doped VLE-PIXE spectrum in figure 5.8b compared to the undoped beam spectrum. For the case of Ar, all Z_1/Z_2 ratios exceed 0.6 and only C, Al, and Si exceed a value of 1. For Xe, all measured elements exceed a value of 1 and thus it is expected that the increase in XRPCS will be low relative to Ar, as was demonstrated in figure 5.8c.

Element	Z_2	N/Z_2	Ar/Z_2	Xe/Z_2
C	6	**1.17**	**3**	**9**
Al	13	0.54	**1.38**	**4.15**
Si	14	0.5	**1.29**	**3.86**
Ti	22	0.32	0.82	**2.45**
V	23	0.30	0.78	**2.35**
Fe	26	0.27	0.69	**2.08**
Ni	28	0.25	0.64	**1.93**
Cu	29	0.24	0.62	**1.86**

Table 5.1: Z_1/Z_2 ratios for the dopants used throughout the VLE-PIXE experiments compared to the elements identified in the SRM 654b. Bold numbers denote Z_1/Z_2 ratios which exceed a value of 1.

5.3 Influence of Proportion of Dopant Species on VLE-PIXE Performance

An experiment was carried out to determine the influence of the proportion of dopant species on VLE-PIXE performance. This experiment was performed using Ar as a dopant as opposed to Xe, despite Xe being preferable due to the absence

of additional peaks as shown in figure 5.8a. This was due to a limitation of the Xe source plasma, where operation above an RF power of 100W may result in permanent damage to the source, specifically overheating of the metered orifice discussed in section 2.1.1 which can cause closure of the orifice. Both hydrogen and argon beams are typically operated at an RF power of 200W and therefore could be mixed together without risk of damage to the source. It is expected that Ar will give similar results to Xe as demonstrated by the performance increase relative to the $>$99% hydrogen beam as shown in figure 5.8c.

To perform this experiment, first, a VLE-PIXE spectrum was taken on the SRM 654b with a $>$99% Ar beam. Contamination from previous source species meant that some amount of hydrogen was still present which could result in the generation of some amount of X-Rays. With the gas supply lines for the plasma source filled completely with Ar, the hydrogen beam was switched on, introducing a small amount of hydrogen gas. The beam composition was measured and a VLE-PIXE spectrum was captured. The source plasma was then switched off and a small section of the gas supply lines was evacuated using the plasma source vacuum system. The plasma source was once again ignited, resulting in a dilution of the initial Ar content with a balance of hydrogen. This was performed several times, resulting in a number of VLE-PIXE spectra vs. the partial pressure of argon in hydrogen. The percentage composition of the beam with each pumping cycle is shown in figure 5.9a where the Ar content is shown to decrease from 99% to 1.7% over the course of the measurements.

It is noted that using the method described above will result in significant contamination to the gas delivery lines up to the hydrogen gas source bottle. Thorough flushing and pumping of the lines is recommended following this measurement. For commercial applications where a desired proportion of hydrogen to dopant species is required, ideally a pre-mixed gas source will be used such that the beam composition remains fixed over the course of the experiments and the beam composition can be reproduced in a more predictable manner. For more flexible beam mixing, mass flow controllers (MFC) may be used to precisely determine the mixing ratio of each beam species.

Figure 5.9b shows the VLE-PIXE spectra vs. Ar percentage. An increase in the total signal intensity is demonstrated as the Ar percentage increases from 1% to $\sim$80% as shown in figure 5.9c. This is followed by a rapid decrease in the VLE-PIXE signal as the Ar content approaches 99%, and hydrogen content in the beam approaches zero. This demonstrates that some proportion of hydrogen is required to generate the VLE-PIXE signal. This experiment demonstrates that the

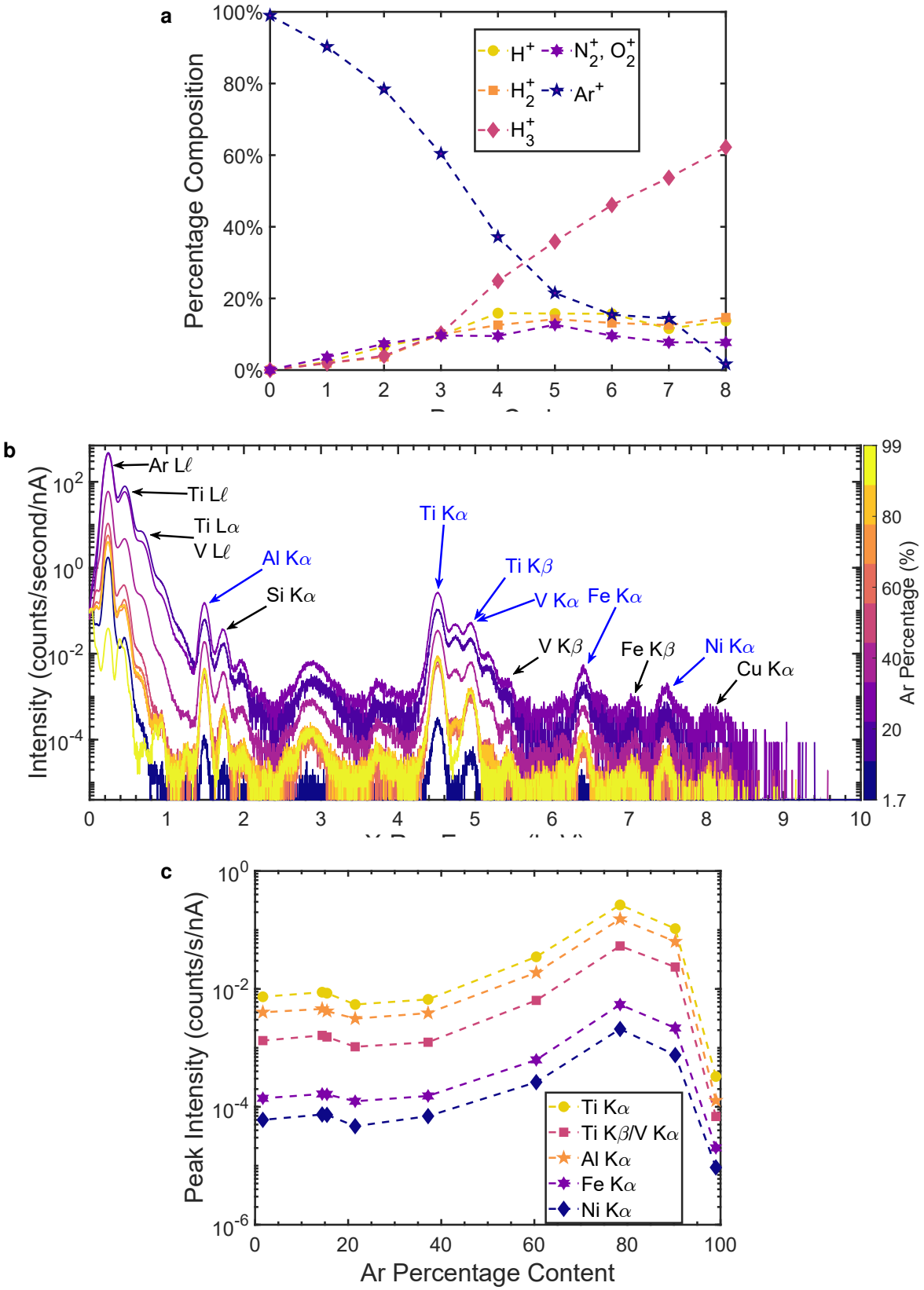

Figure 5.9: (a) Percentage content of beam species vs. pumping cycle. (b) VLE-PIXE spectra vs Ar percentage. (c) Peak intensities of some X-Ray transitions marked in blue in (b) vs. Ar percentage.

addition of even a small percentage of a heavy ion species to a hydrogen beam results in a significant enhancement of the VLE-PIXE signal. Conversely, adding a small percentage of hydrogen to a heavy ion species beam can result in a heavy ion beam which is also capable of producing a characteristic X-Ray signal. This opens up the possibility for techniques such as an endpointing method, where the X-Ray signal can be analysed during FIB milling with a heavy ion beam, allowing precise control over sample delayering. Also, this could provide an alternative to serial tomography, where both the milling and characterisation steps can be combined into one, potentially reducing the experimental time taken to perform this technique. Future work relating to these techniques is outlined in section 8.2.2.

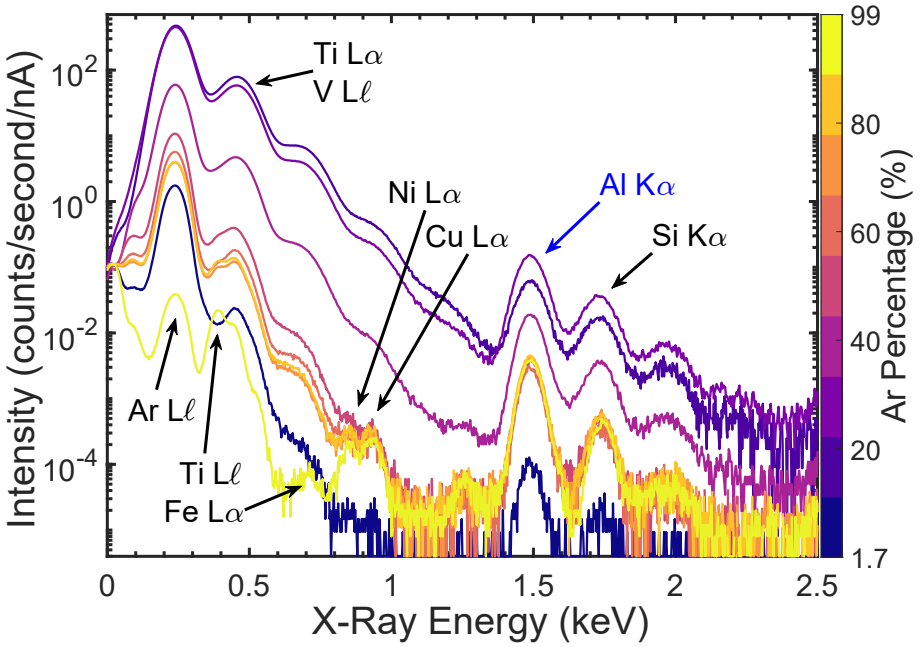

Figure 5.10: Isolated region of the VLE-PIXE spectra vs Ar percentage shown in figure 5.9b.

In the $<$1.4keV region as shown in figure 5.10, the much greater intensity of the overlapping X-Ray peaks results in greater difficulty distinguishing between these peaks. The most intense peak which remains throughout all spectra is situated close to the Ar Lℓ line at 0.22keV. When the high percentage Ar spectrum in the high X-Ray energy region is fitted with a pseudo-Voigt function, several additional peaks are identified which cannot be attributed to any known characteristic X-Ray transitions and are shown in figure 5.11 with magenta labels. These peaks disappear at low and high percentages of Ar and as such, it is likely that these peaks arise due to interaction of the Ar projectile and protons with the sample, possibly arising from the energy shifts associated with the formation of molecular orbitals between the Ar projectile and the sample.

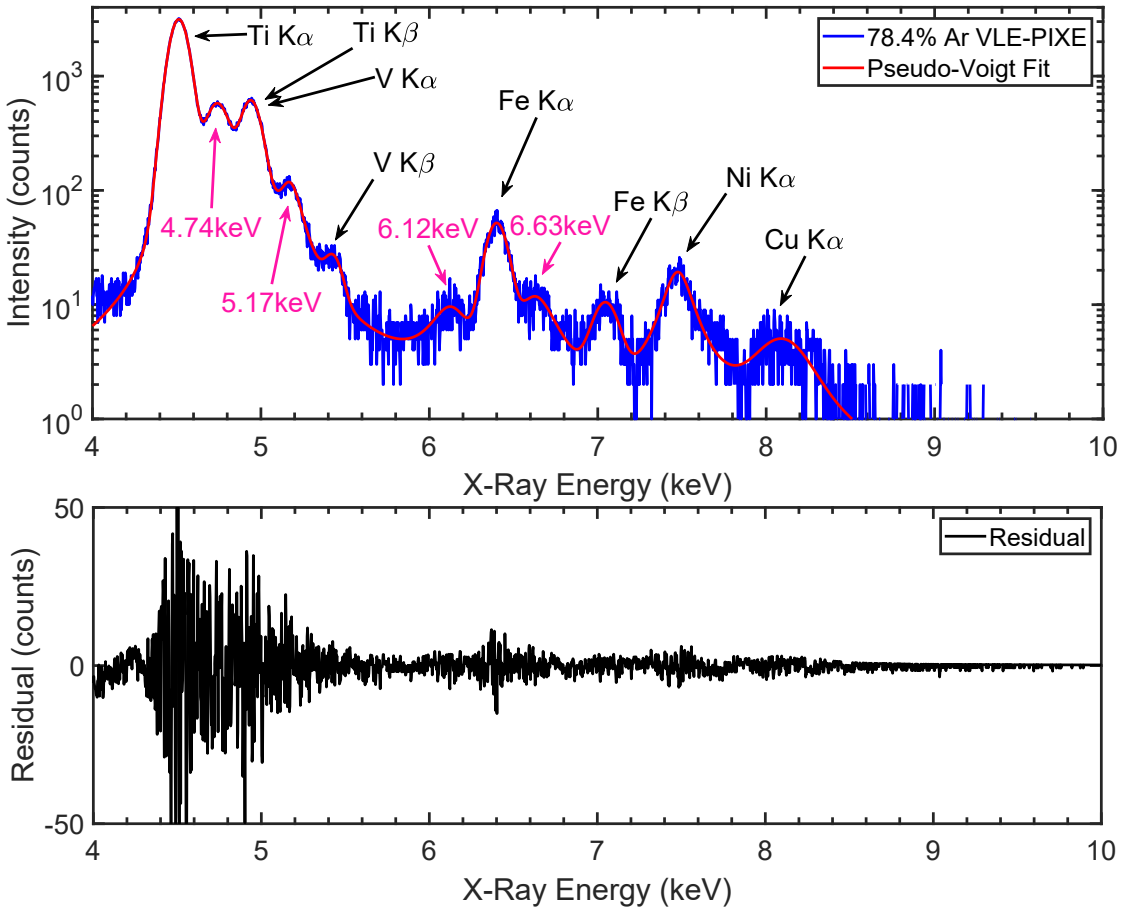

Figure 5.11: Isolated region of figure 5.9b. Unidentified peaks arising as a result of Ar interaction with the sample are labelled in magenta.

5.4 Heavy Ion VLE-PIXE Spectra

In order to determine the influence on X-Ray production of the heavy ion species alone, VLE-PIXE spectra were taken with beams where the vast majority of the beam was comprised of the dopant species N, Ar, and Xe.

5.4.1 Nitrogen VLE-PIXE Spectra

A high purity (>99%) nitrogen beam was established by pumping the FIB plasma chamber overnight. The beam composition prior to the experiment is shown in figure 5.12a where the vast majority of species in the beam are attributed to the N_2^+ ion and the N^+ ion. Trace amounts of other beam species such as hydrogen species may be present and are below the detection threshold for the current measurement.

It can be observed that a significant number of X-Rays are produced when the

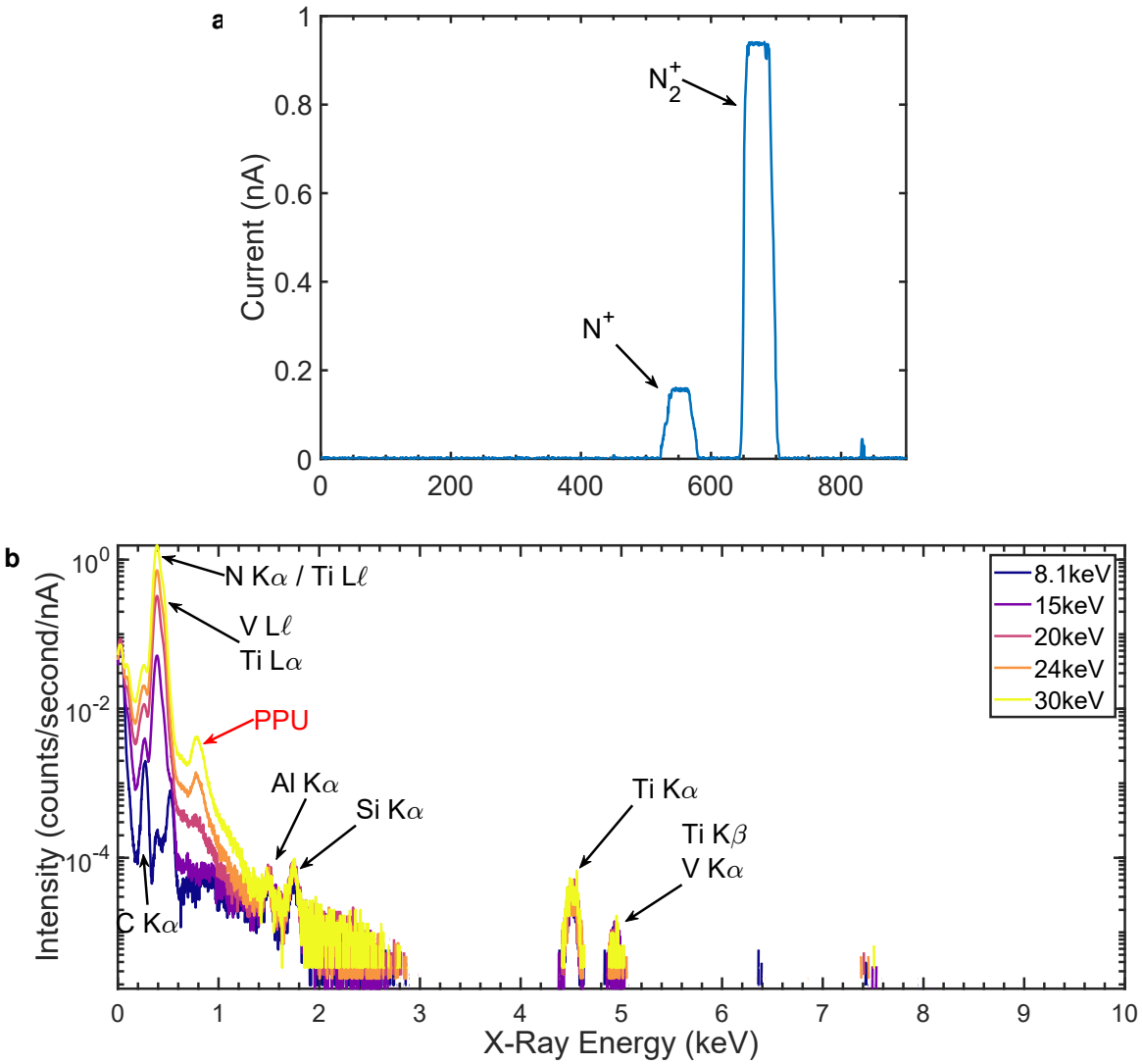

Figure 5.12: (a) Beam component current measurement of the N beam. (b) N X-Ray spectra as a function of accelerating voltage.

beam is comprised almost entirely of nitrogen. Given that these X-Rays are being produced at an energy where the Coulomb XRPCS for nitrogen ions are expected to be diminishingly small, it is quite likely that these X-Rays are being produced through quasi-molecular interactions or the trace amounts of hydrogen remaining in the beam. As Brandt and Laubert explained, due to quasi-molecular interactions between the projectile and the target atom, the cross sections for heavy ion X-Ray production will be significantly higher than for protons at such low energies [101]. These quasi-molecular interactions are investigated in section 6.2.3.

The appearance of the broad, intense peak at an energy of 0.39keV is likely attributed to molecular orbital emission originating from vacancy transfer from the N projectile ion to the target atom. This MO emission was first observed by Saris and Macdonald [138, 142], and described in detail in section 1.3.4.5. The proximity of this peak to the Ti Lℓ characteristic peak highlights the importance

of using an ion such as Xe, where no additional peaks are observed due to the primary ion. The peak shifting phenomenon described by Saris and Macdonald however could not be observed in the nitrogen VLE-PIXE spectra with changing accelerating voltage. This was due to the overlapping of the N MO emission peak with the Ti Lℓ peak, and as such, peak shifts could not be distinguished from the changing the N MO and Ti peak ratios with accelerating voltage. In addition, the electron energy shift expected by the change in distance of closest approach between 30keV and 8.1keV would be lower than the resolution of the X-Ray detector used in these experiments of 0.128keV.

Filling of a projectile vacancy with an electron from a target atom results in a vacancy in the target atom, a process originating from the formation of quasi-molecules between the projectile and the target atom. The de-excitation of this target vacancy would result in the emission of a characteristic X-Ray such as those seen in figure 5.12b. This characteristic emission occurs more efficiently than what is expected by Coulomb ionisation at such low energies and as such, can be attributed to vacancy sharing due to the quasi-molecular model. As described in section 5.2, this process is highly dependent on the Z_1/Z_2 ratio of the projectile and target atom. The only element found in the SRM 654b which N exceeds a Z_1/Z_2 ratio of 0.6 or 1, is carbon. As the only intense characteristic peak observed in figure 5.12b is the C Kα peak, this provides additional evidence that this emission is due to quasi-molecular interactions.

5.4.2 Argon VLE-PIXE Spectra

A similar experiment was performed for an Ar beam where once again, a relatively high purity beam was established as shown in figure 5.13a. Figure 5.13b displays the Ar VLE-PIXE spectra as a function of accelerating voltage. An intense peak is located at an energy of $\sim$0.22keV which is located close to the Ar Lη = 0.2217eV and Lℓ = 0.2201eV peaks. This peak is once again likely attributed to MO emission from the interaction between the projectile and the target atom as discussed for the case of the nitrogen VLE-PIXE spectrum. Some weak characteristic peaks are also observed which may be due to vacancy transfer as previously discussed.

Unlike the N VLE-PIXE spectrum, the Ar MO peak is isolated from surrounding peaks and the peak shifts associated with changing accelerating voltage could therefore be determined. Pseudo-Voigt fits to the Ar MO peak are shown in figure 5.14a, and the peak positions of the corresponding Voigt functions are given in figure 5.14b. A clear shift in peak position to higher energies can be seen as the accelerating voltage increases from 8.1 to 30keV. As the accelerating voltage

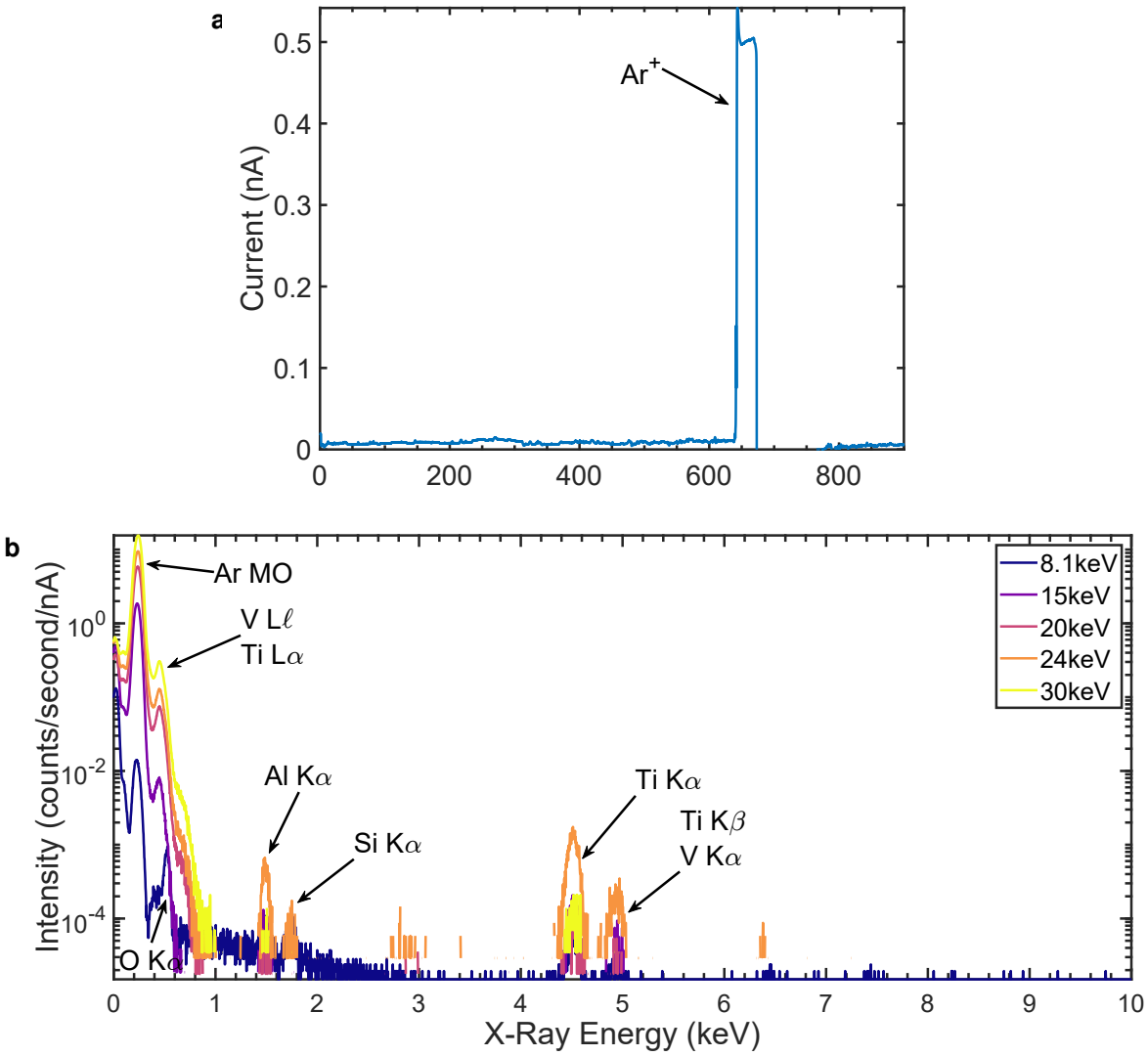

Figure 5.13: (a) Beam component current measurement of the Ar beam. (b) High purity Ar X-Ray spectra as a function of accelerating voltage.

decreases, the peak position converges towards the library peak energies of Ar Lη = 0.2217eV and Lℓ = 0.2201eV. This is expected as the distance of closest approach reaches the separated atom limit, ie. the value which is unmodified by the formation of molecular orbitals between the target and the projectile. The intensity of this peak also decreases as a function of accelerating voltage and is due to the reduced probability of vacancy transfer as the projectile and target distance of closest approach increases and the formation of quasi-molecules becomes negligible.

This peak shifting is believed to be the same behaviour observed by Saris et al. [138] and Macdonald et al. [142] who attributed this shift in energy with increasing accelerating voltage to the increase in binding energy of the 2pπ electrons, as modified by formation of molecular orbitals between the projectile and target. The peak position was demonstrated by Macdonald et al. to be dependent on the

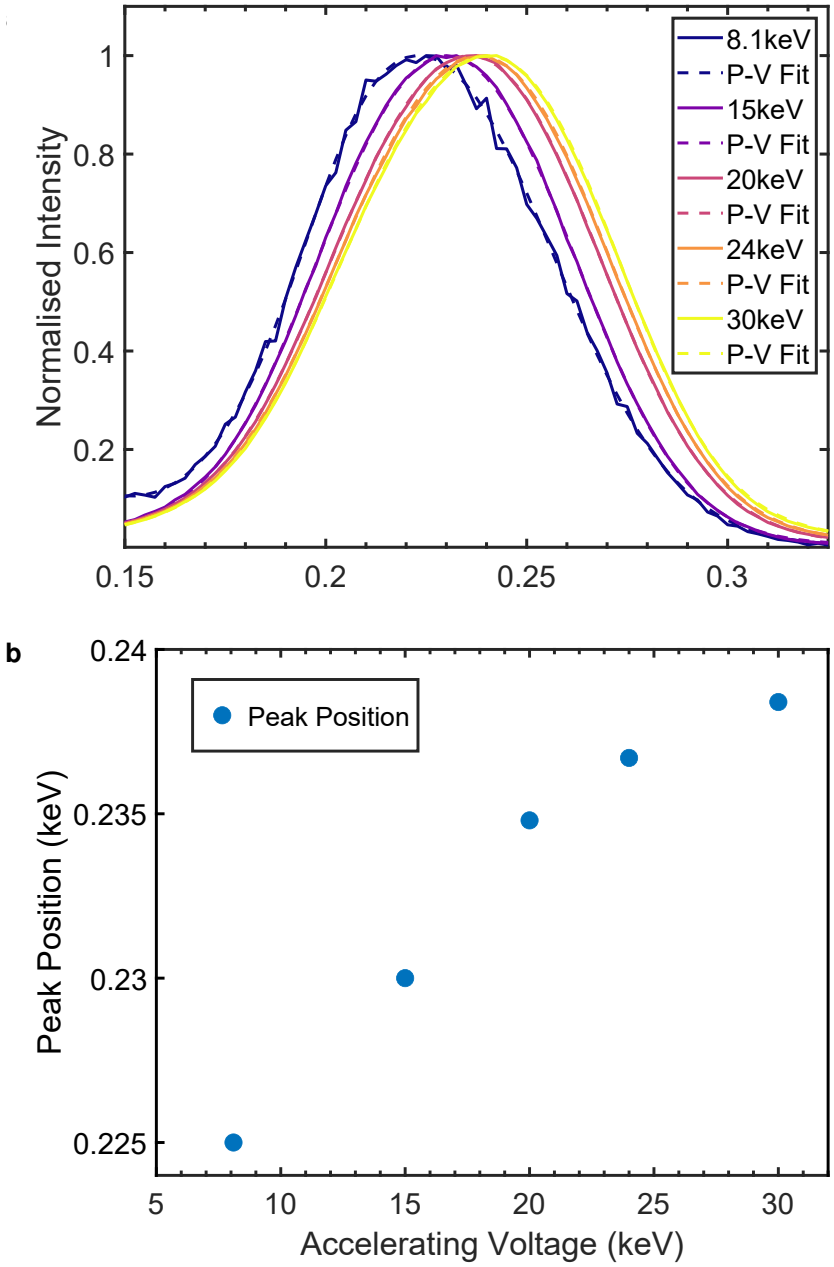

Figure 5.14: (a) Ar MO peak as a function of accelerating voltage, with pseudo-Voigt (P-V) fits displayed as dashed lines. (b) Ar MO peak positions as a function of accelerating voltage.

sample composition. This behaviour provides significant evidence that this peak is in fact due to MO emission and does not originate from characteristic X-Rays from Ar ions implanted into the sample. This also leads to the conclusion that the intense peak at around 0.22keV observed in the Ar doped beam spectrum in figure 5.8a and in the VLE-PIXE spectra as a function of Ar partial pressure in figure 5.9b are also due to MO emission. No shifts in the other spectral peaks are observed however the low intensity of these peaks makes determination of these peak positions with respect to accelerating voltage difficult.

5.4.3 Xenon VLE-PIXE Spectra

A high purity Xe beam was established using the method discussed above. The composition of this beam is shown in figure 5.15a. It should be noted that the RF power of the Xe plasma at 37W is significantly lower than the 200W used for the other species. Due to the much higher ionisation potential for the other beam species, it is likely that this Xe beam is comprised almost exclusively of Xe.

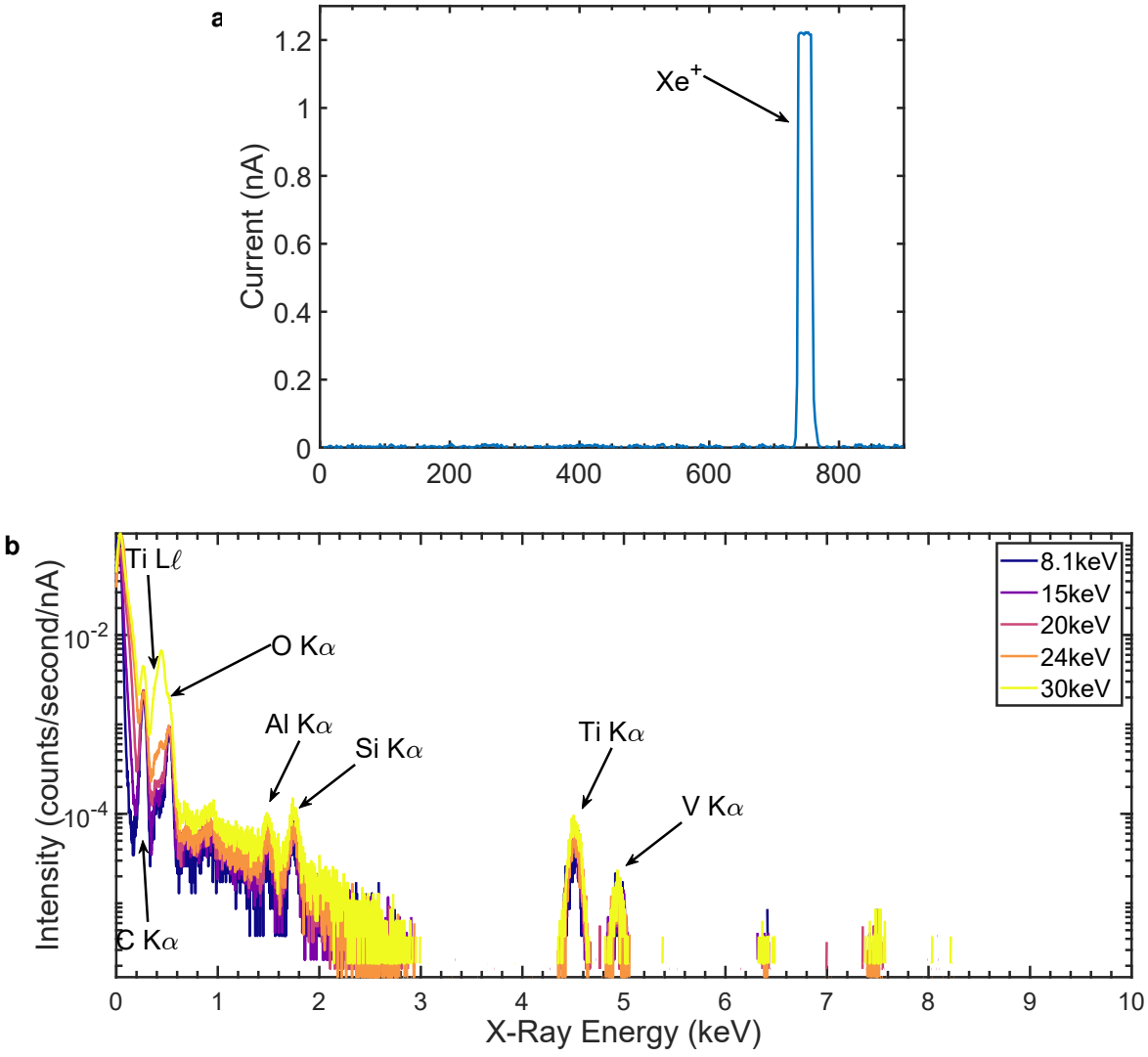

Figure 5.15: (a) Beam component current measurement of the Xe beam. (b) Pure Xe X-Ray spectra as a function of accelerating voltage.

As demonstrated in section 5.2, Xe was shown to perform well as a dopant species. The results shown in figure 5.15b demonstrates that it does so with far less influence on the underlying spectra than N or Ar due to the lack of any additional peaks as a result of electron transfer to the projectile. For this reason, Xe can be considered the optimal dopant species when compared to N or Ar. The use of Xe however will also result in greater damage to the sample due to high

sputter yield. Additionally, limitations on RF power which can be applied to the Xe plasma will limit the use of Xe as a dopant at high partial pressures of either hydrogen or Xe where higher RF powers are required for efficient ionisation of the hydrogen molecules and the formation of protons as shown in figure 2.8a.

A comparison of the >99% purity VLE-PIXE spectra for each beam species at 30keV accelerating voltage is shown in figure 5.16

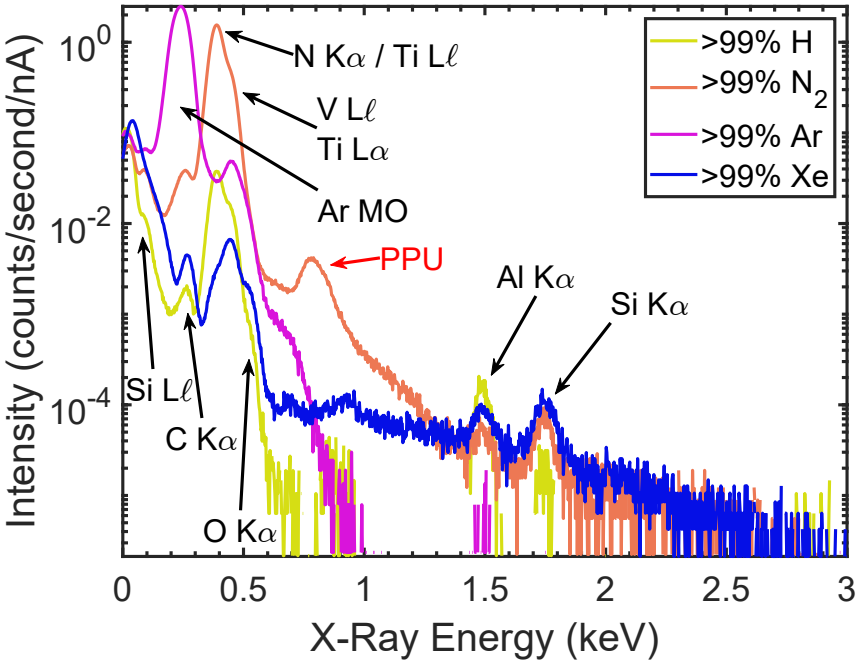

Figure 5.16: A comparison of the >99% purity VLE-PIXE spectra for each beam species at 30keV accelerating voltage.

5.5 Sum of Undoped VLE-PIXE Spectra

To determine whether the resultant doped beam spectrum is indeed greater than the spectra produced by its individual components, the most intense spectrum from the high purity hydrogen beam shown in figure 5.7a, and the most intense spectrum from the high purity Xe beam shown in figure 5.15b were added in proportion to reproduce the Xe doped hydrogen spectrum shown in figure 5.7d.

It can be clearly seen that when the individual H and Xe spectra are added together, adjusted to the proportion of each species in the beam, is significantly lower than the VLE-PIXE spectrum achieved when doping a hydrogen beam with a small percentage of Xe. This experiment confirms the result achieved in section 5.1, where the converged beams produced spectra which were greater than the sum of the separated species. The sum spectrum experiment also elimi-

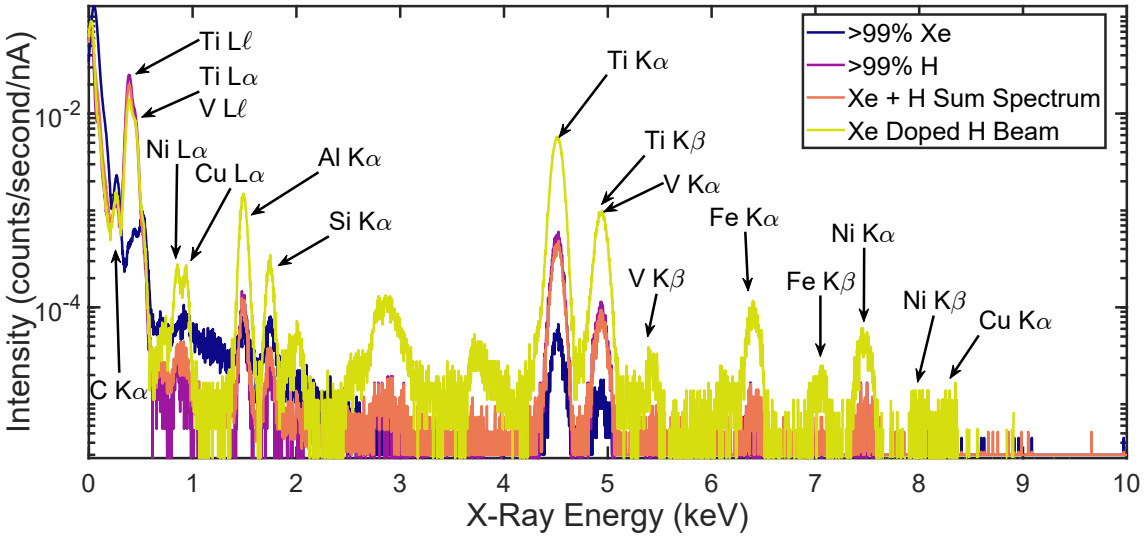

Figure 5.17: Reproduction of the Xe/H doped beam VLE-PIXE spectrum from figure 5.7a using a sum of the individual beam component spectra.

nates any additional influence from the application of the magnetic immersion field. This phenomenon is key to the high performance of the doped beam VLE-PIXE technique when compared to what is expected by PIXE performed at such low energies.

5.6 Optimised Doped Beam VLE-PIXE Parameters

Beam Configuration

- Magnetic immersion field of SEM column can be adjusted to achieve highest X-Ray signal. It was demonstrated in section 5.1 that this may be offset by ∼20% relative to the converged beam.

Dopant Species

- Xe will ideally be used as a dopant species due to lack of additional MO peaks generated by this species.
- Ar may be used in situations where high RF powers are needed as high RF power Xe plasma may cause permanent damage to plasma source.

Heavy Species Doped Hydrogen Beam

- Pump plasma chamber and FIB column overnight
- Switch to desired dopant species for a period of no less than 30 minutes

- Modify pumping cycle for a PVP delay of 10 seconds and a TMP delay of 10 seconds
- Switch to hydrogen beam. This will result in $\sim$10% dopant species with a balance of hydrogen which is optimal for trace element analysis.

Hydrogen Doped Heavy Species Beam

- Ideally a pre-mixed gas source will be used such that a beam composition of $\sim$80% heavy ion species with a balance of hydrogen species is achieved
- Alternatively, the plasma source gas delivery lines can be filled with a low pressure of hydrogen, and the heavy ion species plasma is turned on to introduce a balance of heavy ion species
- For more flexible gas mixing, an MFC can be used to control the proportion of gaseous precursor species

5.7 Conclusions

Heavy ion dopants were demonstrated to be essential for the enhanced production of X-Rays during VLE-PIXE measurements. It was also shown that the impact of both protons and a heavy ion species upon the same region of a sample produced an intensity of characteristic X-Rays greater than the sum of the individual species. The proportion of dopant species was also shown to be an important factor in considering the performance of doped beam VLE-PIXE. The addition of a small amount of dopant species to a hydrogen beam can be used for trace element analysis of a sample with reduced damage due to sputtering by the heavy ion dopant species. Adding a small amount of hydrogen to a heavy ion species was also demonstrated to generate a significant X-Ray signal and creates the potential for sample analysis during milling with a heavy ion beam.

Xe was shown to be the optimal dopant when compared to N and Ar due to the minimal contributions to the VLE-PIXE spectra by the projectile Xe ion. N and Ar dopants produced intense peaks which can be attributed to the transfer of an electron from the target atom to a projectile vacancy, the de-excitation of which can result in the emission of an X-Ray. This process is known as molecular orbital emission. The following chapter outlines an investigation into the interaction of the proton and heavy ion dopant species upon the same region of the sample, and an interpretive model is developed to help explain the doping physical mechanism.

Chapter 6

Interpretation of Doped Beam VLE-PIXE Enhancement Mechanism

Throughout this thesis, it was established that the addition of a small percentage of a heavy ion dopant species to a hydrogen ion beam is sufficient to dramatically enhance the production of X-Rays. This occurs at energies where the XRPCS are diminishingly small and PIXE characterisation is considered to be impossible. The enhancement of X-Ray production by beam doping is however not predicted by the literature and to our knowledge, has not been observed previously. As such, the physical mechanism for X-Ray enhancement is yet unknown. This section outlines an interpretation of the beam doping results achieved throughout this thesis and a physical model is suggested to help explain the resulting behaviour.

6.1 Possible Enhancement Mechanisms

The predominant mechanism for ionisation by fast, light ions is the Coulomb ionisation method described in section 1.3.4.2. Coulomb ionisation decreases rapidly at lower energies and becomes negligible for the energies utilised during VLE-PIXE. Beyond Coulomb ionisation, several additional mechanisms are described which relate to the interaction of slow, heavy ions with the target atoms and are described in section 1.3.4.5. These mechanisms alone however, do not sufficiently explain the enhancement caused when both protons and heavy ion dopant species are brought together and as such, additional interactions must be considered.

Of the various physical mechanisms outlined in section 1.3.4.5 relating to the in-

teraction of heavy ions with the sample, two mechanisms stand out which may be further enhanced by the simultaneous impact of protons and heavy ion species. These mechanisms are: the suppression of non-radiative transitions, and the electronic energy shifts relating to the formation of molecular orbitals between the target and the projectile.

6.1.1 Suppression of Non-radiative Transitions

As described in section 1.3.4.3, upon inner shell ionisation, outer shell electrons may de-excite in one of three ways:

- Through emission of an X-Ray photon
- Through transfer of a virtual photon to an adjacent electron in the same shell, leading to the emission of an Auger electron
- The transfer of a virtual photon to an electron in a higher shell, leading to the emission of a Coster-Kronig (C-K) electron.

The sum of the fluorescence yield, Auger yield and C-K yield must be equal to 1 in order to account for the fate of all the inner shell vacancies. The ratio of these yields however can change quite significantly due to the electronic configuration of the target atom with the most profound effect arising when the target atom is multiply ionised.

The multiple ionisation of a target atom results in a reduction of the Auger and C-K yields as there are less electrons present in the system for energy to be transferred to. As the Auger and C-K processes require two electrons and one vacancy, yet the emission of a characteristic X-Ray only requires one electron and one vacancy, the probability of emitting an X-Ray becomes greater than emitting an Auger electron. The end result is an increase in the X-ray fluorescence yield proportional to the number of vacancies present. This effect has been studied extensively in the literature and has been demonstrated to affect XRPCS [225, 226, 227]. Lapicki et al. described this effect as resulting in a deviation from the XRPCS calculated with the assumption of a single vacancy. This deviation was shown to be more severe at lower energies. When multiple ionisations were considered, the calculated cross sections agreed with experimental data [110]. This phenomenon demonstrates that as the energy of the incident ion decreases, the possibility of multiple ionisation increases, resulting in a higher X-Ray yield.

Multiple ionisation may occur during doped beam VLE-PIXE when the simultane-

ous impact of both a proton and heavy ion species results in the emission of more than one electron from a target atom. Additionally, if the vacancy lifetime of the target atom is sufficiently long, multiple proton impacts may occur during the life of this vacancy, possibly resulting in the removal of additional inner or outer shell electrons before de-excitation.

Miranda et al. suggested that the multiple ionisation effect can be corrected by the modification of X-Ray fluorescence yields typically published for a single vacancy [228]. Based on the X-Ray fluorescence yields tabulated by Hubbell et al. [117], the maximum enhancement in X-Ray fluorescence yield for a particular shell can be calculated when the Auger and C-K yields are equal to 0, giving a fluorescence yield of 1 ie. a 100% chance of a vacancy resulting in the emission of an X-Ray. This however suggests that the target atom remains fully stripped of electrons while it remains in the sample which is an unreasonable assumption. A fluorescence yield of 1 can however be used for the purpose of analysing the potential efficacy of this mechanism.

The literature single vacancy fluorescence yields are listed in table 6.1, alongside the maximum theoretical enhancement factors for K shell X-Ray transitions based on a fluorescence yield of 1. These values are compared to the maximum measured enhancement factors during the SRM 654b trace element analysis. The measured enhancement factors are calculated as the ratio of the pseudo-Voigt fitted peak heights for a specific transition generated by an undoped hydrogen beam compared to a Xe doped hydrogen beam. An example of this procedure is shown in figure 6.1.

Transition	Fluorescence Yield [117]	Max. Theoretical	Measured
Ti K	0.221	4.52	**9.24**
Al K	0.038	26.32	10.13
Si K	0.047	21.28	11.36
V K	0.249	4.02	**8.73**
Fe K	0.342	2.92	**6.83**
Ni K	0.414	2.42	**3.67**
Cu K	0.446	2.24	**3.71**

Table 6.1: Fluorescence yields for X-Ray transitions on the SRM 654b compared to their maximum theoretical and observed enhancement factors. Bold numbers denote measured values which exceed the maximum theoretical values.

In many cases, denoted by the bold values in table 6.1, the measured enhance-

ment factors exceed the maximum theoretical enhancement factors as determined by the fluorescence yield. This demonstrates that while the suppression of non-radiative transitions may partially explain the enhancement by beam doping, there must also be an additional mechanism responsible for the observed behaviour.

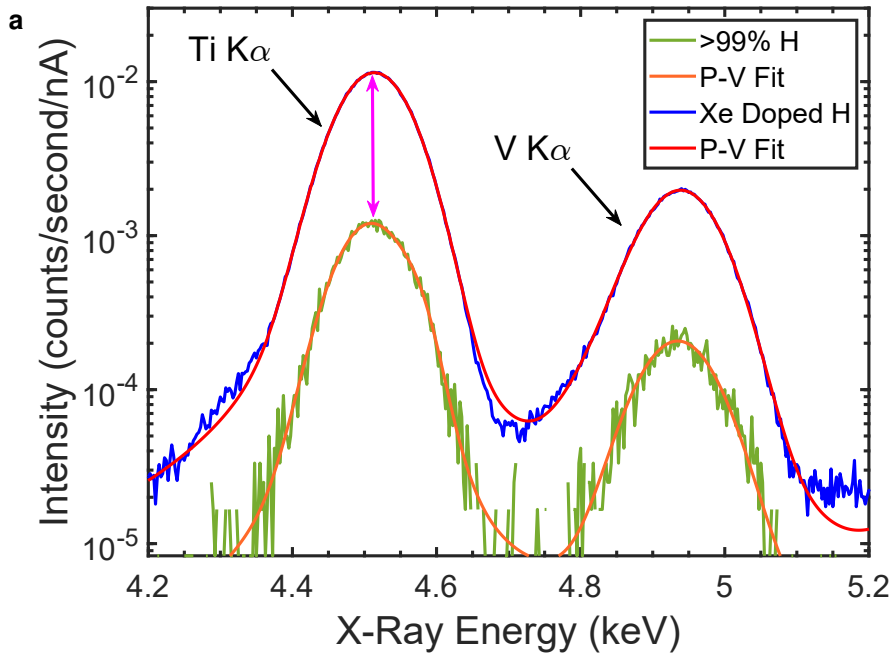

Figure 6.1: Example measurement for the calculation of enhancement factors for a doped beam relative to an undoped beam. Peak height ratio is denoted by a magenta arrow.

6.1.2 Electronic Energy Shifts

The formation of a temporary quasi-molecule and resulting shifts in the electronic energy levels of both the target and the projectile have been demonstrated in the past to result in significant increases in XRPCS. These enhanced XRPCS are attributed to mechanisms such as electron promotion and vacancy sharing as they allow ionisation at energies far below the Coulomb ionisation threshold for a slow, heavy ion [100, 96, 229]. If these mechanisms alone however were responsible for the enhanced X-Ray production, then the doped hydrogen beam would produce no greater X-Ray production than the dopant species alone. As demonstrated in section 5.5, this is not the case and the interaction of both the protons and heavy ion dopant species are required.

A possible scenario can be described as such: during the modification of the electronic energy levels during quasi-molecule formation, the heavy ion species

may modify the electronic energy levels of the target. During this period of modification, the simultaneous impact of a proton on the same atom may result in more efficient ionisation of an inner or outer-shell electron due to the modified electronic energy levels of the target atom. Due to the significant difference in velocity between the protons and heavy ion species, this may become further enhanced by the use of heavier ions. This effect will in turn also result in the suppression of non-radiative transitions due to the removal of additional electrons.

6.1.3 Vacancy Lifetime Modification

The vacancy lifetime of an atom corresponds to the time frame over which an inner-shell vacancy can exist before an outer-shell electron de-excites and fills this vacancy. As discussed previously, this de-excitation can occur radiatively or non-radiatively, with the probability of a radiative de-excitation being highly dependent on the number of outer-shell electrons. Likewise, the vacancy lifetime is also highly dependent on the number of outer-shell electrons, with a fewer number of outer-shell electrons available for de-excitation resulting in an increase in the vacancy lifetime [230]. Betz. et al. reported an order of magnitude increase in the lifetime of a K shell vacancy in multiply ionised sulfur at 1.5×10^{-14}s, compared to singly ionised sulfur at 1.5×10^{-15}s [231]. This lifetime altering phenomenon results in a change in the emission line-width, with a shorter lifetime resulting in a broader X-Ray emission peak due to the Heisenberg uncertainty principle between time and energy [232].

This increase in vacancy lifetime can result in a lingering inner-shell vacancy, during which period, an additional proton impact may result in the removal of an additional outer or inner-shell electron which may also alter the vacancy lifetime or the probability of a non-radiative transition. Such a phenomenon may result in a feedback loop of sorts which has the potential to significantly increase the production of X-Rays. This phenomenon may not be observed by protons alone due to the lack of modification of electronic energy levels leading to more efficient ionisation of target atoms, and may not be observed by heavy ions alone due to the relatively long collision times of the heavy ions relative to the vacancy lifetimes. For this reason, such a mechanism would rely on the simultaneous impact of a proton and a heavy ion species.

6.2 Calculation of Collision Parameters

The mechanisms proposed above make a number of assumptions regarding the collision between the projectile ion and the target, in particular the timings required for simultaneous impact, and the internuclear distances required to achieve sufficient shifts in electronic energy levels due to quasi-molecular formation. In order to assess the validity of these mechanisms, the kinetics of a projectile collision with an atomic target must be considered which will allow determination of a number of critical parameters relating to the proposed model such as:

- The distance of closest approach of the projectile, providing an estimate of the maximum shift in electronic energy levels based on calculations such as those provided in figure 1.25 as a function of inter-nuclear distance.
- Collision time, the time frame over which the energy levels of the projectile and target are altered due to the formation of a quasi-molecule.
- The probability of simultaneous proton strikes upon the target during the period that the quasi-molecule is formed.
- The vacancy excited state lifetimes for the projectile which will determine whether an inner-shell vacancy of the projectile can survive until it can be transferred to the target.
- The vacancy excited state lifetimes for the target which will determine the time frame over which multiple impacts are possible, which may be modified by multiple ionisation.

6.2.1 Screened Coulomb Potential

The method used to calculate the kinetic scattering of the projectile from the target atom is a modern formulation of the screened Coulomb potential method first outlined by Everhart et al. [233]. This potential is used extensively in scattering calculations such as LEIS [234], and MO calculations [143] and can be used to calculate many of the parameters listed above.

The screened Coulomb potential (V) as a function of inter-nuclear distance between the projectile and target (r) is given as:

$$V(r) = (Z_1 Z_2 e^2/r)\Phi(r/a) \tag{6.1}$$

where Z_1 and Z_1 are the atomic numbers of the projectile and target respectively, e is the fundamental charge of an electron, and a is the screening length, over which the visible charge of the nucleus is effectively reduced by the presence of the surrounding electrons.

The first term is the Coulomb force experienced between the two nuclear charges which decays linearly as a function of distance between the projectile and target nuclei and as such extends quite some distance from nuclear centre. The second term corresponds to the electron screening function which effectively reduces the contribution from the Coulomb force at very small distances. This potential decays exponentially as a function of distance from the nucleus. Using the Molière approximation to the Thomas-Fermi screening function, the function can be calculated by [234]:

$$\Phi(r/a) = 0.35\exp(-0.3\frac{r}{a}) + 0.55\exp(-1.2\frac{r}{a}) + 0.1\exp(-6.0\frac{r}{a}) \tag{6.2}$$

where, a the Firsov screening length is calculated as:

$$a = \frac{0.4685}{\left(Z_1^{1/2} + Z_2^{1/2}\right)^{2/3}} \tag{6.3}$$

6.2.2 Impact Parameter

The first term used to describe the interaction between a projectile and a target is the impact parameter (b), which is defined as the the perpendicular distance of closest approach prior to deflection of the projectile. The impact parameter is an important concept from the perspective of the molecular orbital model of collision as it dictates how close the collision partners can approach. As such, electron transfer probability due to the MO model is a function of impact parameter [100].

θ is the scattering angle following the interaction and varies inversely to the impact parameter. A distribution of impact parameters is typically experienced by the projectile due to the random insertion of projectiles into the target. These terms are shown schematically in figure 6.2a. The variation in impact parameter as a function of scattering angle is shown in figure 6.2b.

It is convenient to calculate the impact parameter b, over the possible range of scattering angles (θ) from 0 to 180°, rather than calculating the scattering angle from an unknown range of impact parameters. The impact parameter also

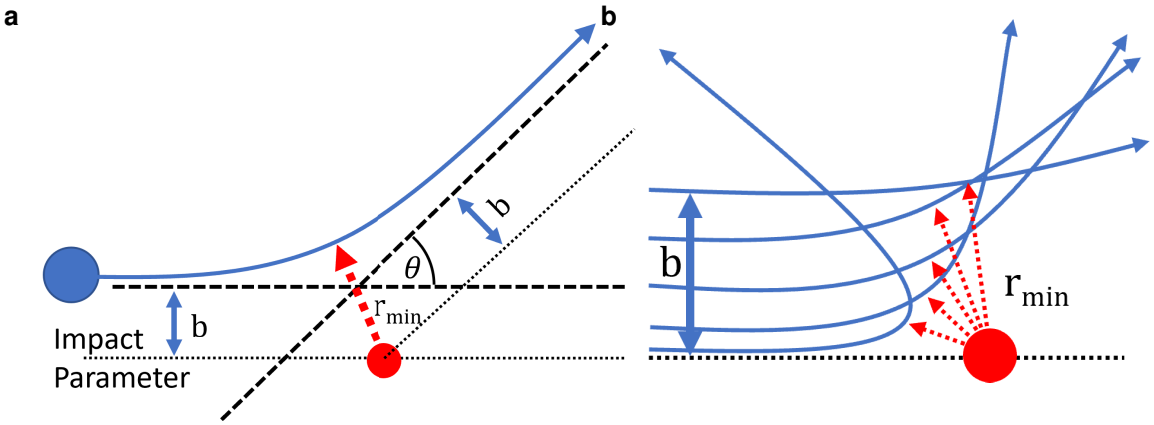

Figure 6.2: Diagram of kinetic scattering utilising a screened Coulomb potential. The projectile is marked in blue with a blue arrow denoting the trajectory. The nuclear scattering centre is marked as a red circle with distance of closest approach (r_{min}) marked as a dashed red line.

changes as a function of kinetic energy of the projectile, with a greater kinetic energy resulting in a smaller scattering angle due to greater projectile momentum. The calculation for b as a function of scattering angle is [235]:

$$b = \frac{Z_1 Z_2 k e^2}{2E_K} \sqrt{\frac{1+\cos\theta}{1-\cos\theta}} \tag{6.4}$$

where k is the Coulomb constant, and E_K is the kinetic energy of the projectile which is related to accelerating voltage by $E_K = qV$.

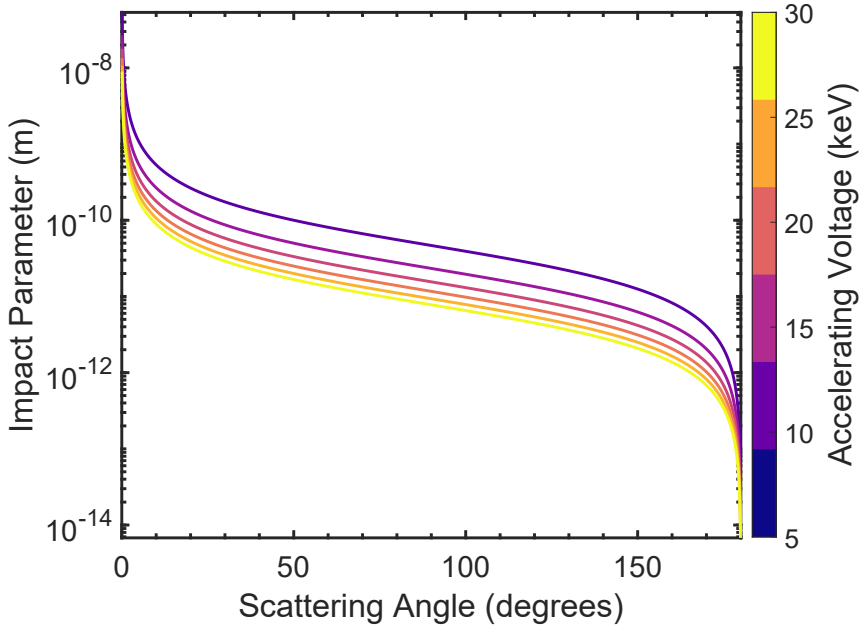

Figure 6.3: Calculated impact parameters as a function of scattering angle for the Ar $\rightarrow$ Ar system over a range of accelerating voltages.

An exemplary system of an Ar ion scattering from an Ar atomic target is used to verify the calculations, as a significant amount of information for this system is provided in the literature. The notation (projectile $\rightarrow$ target) is used to denote the projectile target scattering combination. The calculated Ar$\rightarrow$Ar impact parameter as a function of scattering angle is given in figure 6.3 for a range of energies.

6.2.3 Distance of Closest Approach

The distance of closest approach (r_{min}) is the minimum inter-nuclear distance experienced between the projectile and the target during the scattering process and is a function of impact parameter and therefore scattering angle. The distance of closest approach determines the extent to which the electronic energy levels of the projectile and target can shift as the overlap of atomic orbitals is a function of the internuclear distance between the target and projectile.

The absolute minimum distance of approach is achieved during a head-on collision between the projectile and the target, at an impact parameter of 0 and a resultant scattering angle of 180°. A scattering angle of 0 corresponds to the distance at which the projectile is unperturbed by the presence of the target and will continue on its path without deflection. In many cases, this will be a distance greater than the interatomic distance of atoms in a material and the projectile will therefore become influenced by the next nearest atomic neighbour. For simplicity, this calculation assumes an isolated atom.

The distance of closest approach (r_{min}) can be calculated from the impact parameter [235]:

$$r_{min} = \frac{b\cos(\theta/2)}{1-\sin(\theta/2)} \tag{6.5}$$

The corresponding distance of closest approach at each accelerating voltage for the Ar$\rightarrow$ Ar system is given in figure 6.4a and demonstrates the reducing distance of closest approach with both decreasing impact parameter and increasing accelerating voltage. The distance of closest approach for a 30keV Ar$\rightarrow$Ar head-on collision is calculated as 1.56$\times10^{-11}$m which is in good agreement with the value measured by Kessel and Everhart for Ar$\rightarrow$Ar of $\sim$1.5$\times10^{-11}$m [236]. For convenience, the remaining calculations will be performed for head on collisions (180°, b = 0), a commonly used technique [237], as this dictates the smallest distance of closest approach and therefore the upper bounds for electronic energy level shifts. This also reduces the collision system to one dimension.

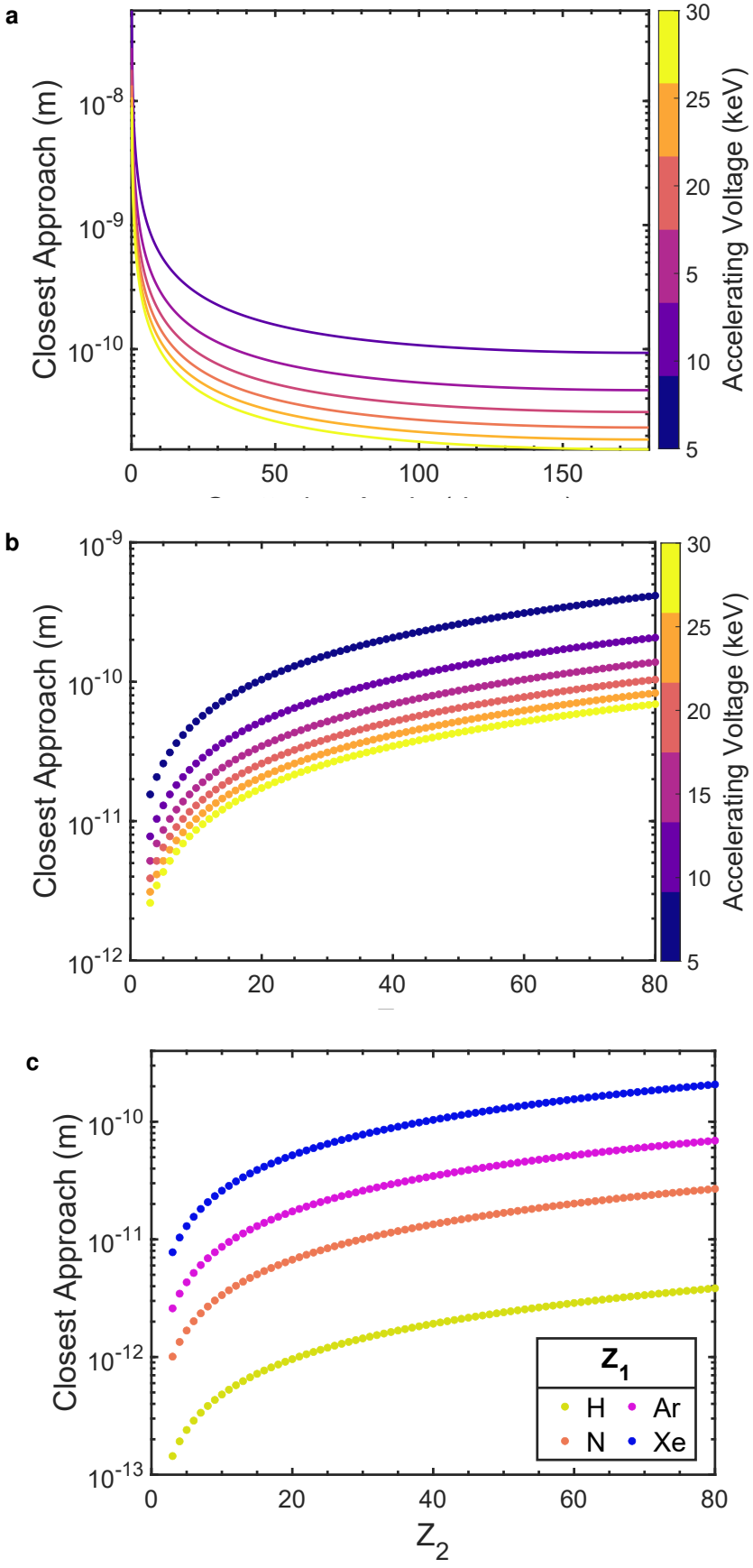

Figure 6.4: (a) Distance of closest approach as a function of scattering angle for the Ar $\rightarrow$ Ar system over a range of accelerating voltages. (b) Distance of closest approach for Ar $\rightarrow$$Z_2$ for Z_2 from 3-80 amu for a range of accelerating voltages. (c) Distance of closest approach at 30keV, 180° scattering angle for Z_1 $\rightarrow$$Z_2$

The calculation for Ar $\rightarrow$$Z_2$ for Z_2 from 3-80 amu, is shown in figure 6.4b for a range of energies at 180° scattering angle. This plot demonstrates the influence of target Z on the distance of closest approach, which increases as a function of Z_2 due to the greater nuclear charge of the target. Figure 6.4c displays the calculated distance of closest approach at 30keV, 180° scattering angle for $Z_1 \rightarrow Z_2$ with Z_1 = 1 (H), 7 (N), 18 (Ar), and 54 (Xe) and Z_2 from 3-80 amu.

The distance of closest approach for the symmetrical ion-atom scattering systems can then be compared to the calculated MO energy diagrams as a function of inter-nuclear distance, known as correlation diagrams. Correlation diagrams for the N-N, Ar-Ar, and Xe-Xe systems are shown in figures 6.5a-6.5c. Inter-nuclear distance is shown in atomic units where 1 a.u. = 5.29×10^{-11}m, the Bohr radius (a_0) of a hydrogen electron. Energy is shown in atomic units where 1 a.u. = 27.21eV, the Rydberg energy or the ground state energy of the hydrogen atom. The distances of closest approach at 30keV and 8.1keV, are marked with a dashed red line and blue line respectively to signify the range over which the electronic energy levels are modified during such collisions.

For the N $\rightarrow$ N system, the distance of closest approach at 30keV is calculated to be 2.35×10^{-12}m or 0.0444 a.u. as shown in figure 6.4c. Based on the correlation diagram in figure 6.5a, this represents a significant shift in the electronic energy levels relative to the separated atoms. The distance of closest approach for an 8.1keV, 180° collision, the lowest accelerating voltage as measured in section 5.4 is a value of 8.71×10^{-12}m or 0.16 a.u. and also represents a significant shift in electronic energy levels. The change in distance of closest approach between these two energies is very small, representing a change in the K shell binding energy of $\sim$50eV. This change is the factor attributed to the shift in peak position with accelerating voltage as described by Saris and Macdonald [138, 142] and is likely the reason why no peak shift was observed in the N spectra vs accelerating voltage as described in section 5.4.

For the Ar $\rightarrow$ Ar system, a 30keV accelerating voltage corresponds to a calculated distance of closest approach of 1.56×10^{-11}m or 0.29 a.u. For an 8.1keV, accelerating voltage, the distance of closest approach is calculated as 5.76×10^{-11}m or 1.09 a.u. From the correlation diagram shown in figure 6.5b, several level crossings can be observed up to the distance of closest approach at 30keV. These level crossings are responsible for the electron promotion model as discussed in section 1.3.4.5. This distance of closest approach also represents significant shifts in electronic energy levels for the K, L, and M shell electrons, a phenomenon which may be responsible for the enhanced X-Ray production.

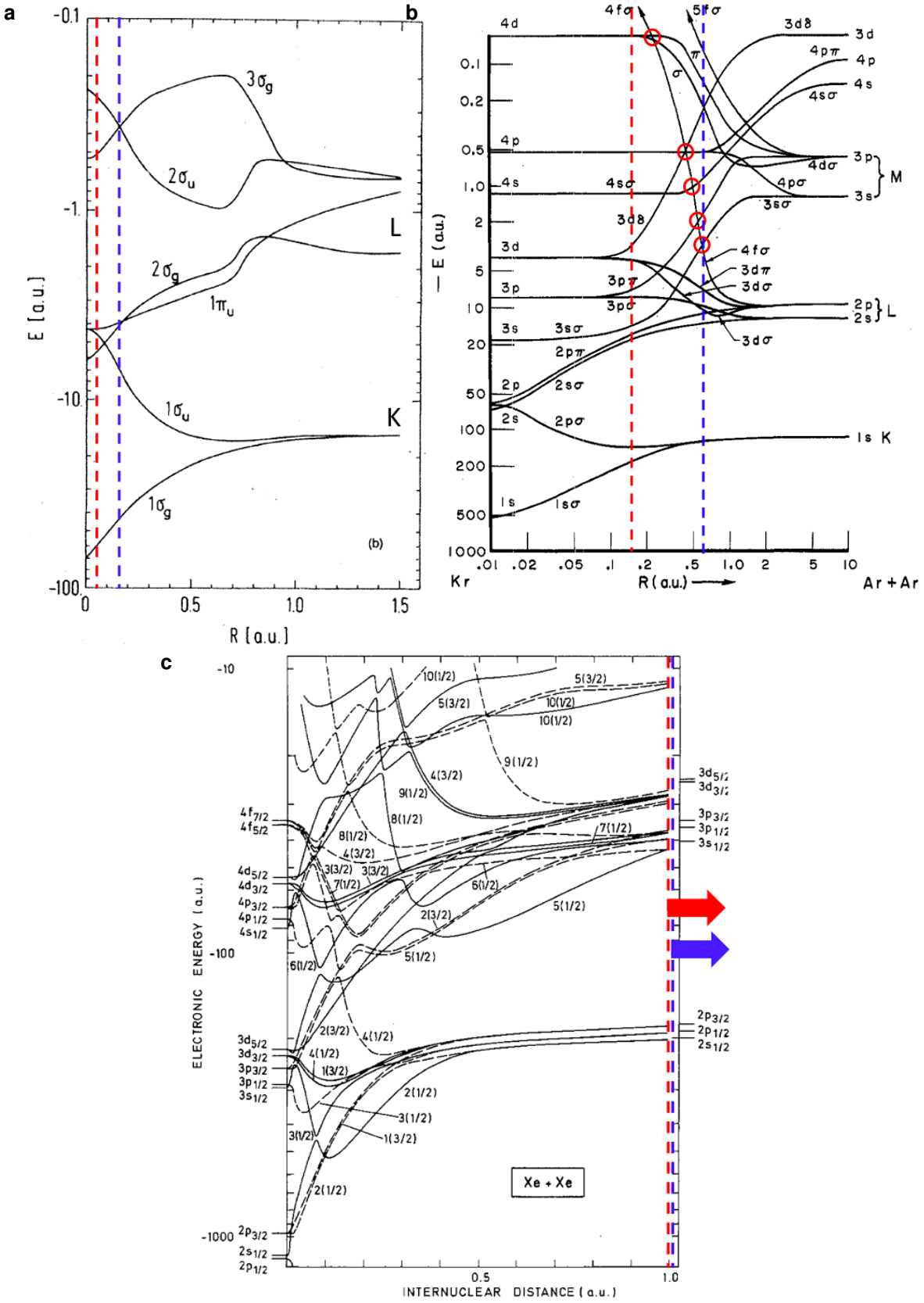

Figure 6.5: Molecular orbital correlation diagrams for the (a) N-N [238] (b) Ar-Ar [104] (c) Xe-Xe systems [239]. Distances and energy are shown in atomic units where 1 a.u. = 5.29×10^{-11}m, and 1 a.u. = 27.21eV. 30keV and 8.1keV distances of closest approach are marked with dashed red lines and blue lines respectively. The Xe-Xe diagram shows a red and blue arrow as the distances of closest approach are greater than represented by the diagram.

For the Xe $\rightarrow$ Xe system, the distance of closest approach at 30keV is calculated as 1.40$\times10^{-10}$m or 2.64 a.u. and at 8.1keV is calculated to be 5.18$\times10^{-10}$m or 9.80 a.u. The correlation diagram shown in figure 6.5c does not display the energy levels beyond 1 au and therefore the changes in electronic energy with internuclear distance could not be accurately determined. A more extensive correlation diagram could not be found in the literature however through observation of the diagram shown in figure 6.5c, it can be seen that some modification of the atomic orbital energies extends beyond the diagram shown and some change in the binding energies of the electrons can be expected.

The H $\rightarrow$ H correlation diagram is provided in appendix figure A.17 for reference, however as there are no H electronic transitions capable of producing X-Rays, the correlation diagram is not useful in this context. The calculated distances of closest approach for the different projectile-target systems are summarised in table 6.2.

	8.1keV		30keV	
System	$r_{min}(m)$	$r_{min}(a.u.)$	$r_{min}(m)$	$r_{min}(a.u.)$
H $\rightarrow$ H	1.78$\times10^{-13}$	0.003	4.80$\times10^{-14}$	0.0009
N $\rightarrow$ N	8.71$\times10^{-12}$	0.16	2.35$\times10^{-12}$	0.044
Ar $\rightarrow$ Ar	5.76$\times10^{-11}$	1.09	1.56$\times10^{-11}$	0.29
Xe $\rightarrow$ Xe	5.18$\times10^{-10}$	9.80	1.40$\times10^{-10}$	2.64

Table 6.2: Calculated distances of closest approach for the ion species used in the VLE-PIXE experiments. r_{min} = the distance of closest approach and is listed in both metres (m) and atomic units ($a.u.$)

Analysis of the correlation diagrams also provides information regarding the energy level crossings induced by the formation of molecular orbitals and can determine the possible fates of the orbital electrons on projectile approach. As can be seen from 6.5b, in the Ar-Ar system the 2s electrons are distributed into the 3dσ and the 3pσ orbitals, and the 2p electrons can be distributed as widely as the 2pπ, 2sσ, 3dπ, and the 4fσ orbitals. At the distance of closest approach at 30keV, the energy level shifts as the electrons are distributed into these orbitals is significant. At several points, the energy level of the 2p electrons crosses a higher atomic orbital, marked with red circles in figure 6.5b. Fano and Lichten stated of these level crossings:

"...the level crossing leads with high probability to the "promotion" of electrons to outer shells, as the nuclei approach. ...These transitions lead to singly or, more

often, multiply excited autoionizing states in atomic collisions. Mechanisms also exist that enhance the otherwise negligible direct ionization [129].

Such processes and the role of distance of closest approach in the collision of the target and the projectile have been discussed extensively in the literature and has been directly attributed to an increase in XRPCS [130, 131, 132]. Details of the electron promotion mechanism induced by energy level crossings in the quasi-molecular model are discussed in detail, especially for asymmetric collisions by Barat and Lichten [128]. Schiwietz et al. also demonstrated that the slow impact of $Ar^{+} \rightarrow Ar$ can result in the simultaneous ionisation of an inner and outer shell electron due to this same $4f\sigma$ mechanism [240]. This bolsters the importance of considering the non-radiative suppression mechanism for enhancing VLE-PIXE performance as discussed in section 6.1.1 and the vacancy lifetime modification mechanism as discussed in section 6.1.3, both of which are highly sensitive to multiple ionisation.

6.2.4 Collision Time

Collision time is the time frame over which the collision between the target and projectile occurs, in the region where the quasi-molecule exists between a projectile and a target atom. This is an important factor when considering the probability of a coincident proton strike on a quasi-molecule and the time frame over which a projectile or target vacancy can exist relative to the life of a quasi-molecule.

The projectile approaches a target atom at a constant velocity dictated by its accelerating voltage. The Coulomb force experienced between the projectile and the target causes the projectile to decelerate until it reaches the distance of closest approach. For a head-on collision, the velocity at the distance of closest approach will be zero and the potential energy of the system will be the accelerating voltage. During this process, the projectile transfers some energy to the target. Following collision, the projectile then retreats from the target as the potential energy acquired from the Coulomb potential is released as kinetic energy.

The energy loss due to scattering will occur continually over the course of the collision, however it can approximated that this occurs at the distance of closest approach where the Coulomb potential between the projectile and the target will be at a maximum. The average energy lost to inelastic scattering can be approximated by the total stopping power as established by Miller at al. [241], which is defined as the average amount of energy lost by the projectile per unit distance within the material. Stopping power tables for the various projectile-target sys-

tems were generated using the SRIM code, which is based on the experimental stopping power measurements by Ziegler et al. [219]. The total energy of the collision system is equal to the kinetic energy provided by the accelerating voltage plus the potential energy of the Coulomb potential. As the Coulomb potential varies as a function of internuclear distance, the kinetic energy must also change such that the following relation is satisfied due to conservation of energy:

$$E_{tot} = E_K(r) + U(r) \tag{6.6}$$

$$E_{tot} = \frac{1}{2}mv^2(r) + (Z_1 Z_2 e^2/r)\Phi(r/a) \tag{6.7}$$

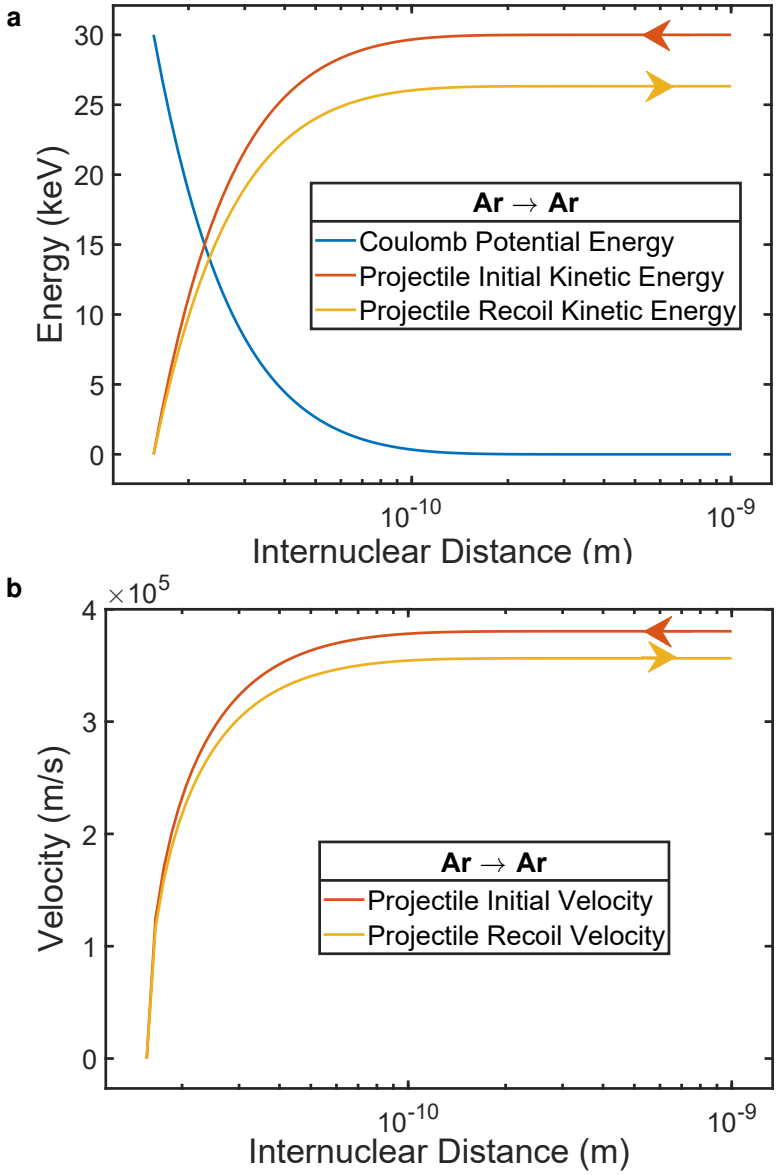

Figure 6.6: (a) Coulomb potential energy and projectile energy as a function of inter-nuclear distance for the Ar → Ar system before and after collision. (b) Velocity of projectile as a function of inter-nuclear distance before and after collision.

As the Coulomb potential energy increases, the kinetic energy of the projectile must decrease and therefore so will the projectile velocity. After scattering, at the distance of closest approach, some of the total energy has been transferred to the target and therefore has been removed from the collision system. This energy is utilised for processes such as displacement, ionisation, or excitation.

The kinetic energy and Coulomb potential of an Ar projectile as it approaches an Ar target is shown in figure 6.6a. The Coulomb potential energy increases as the projectile approaches the distance of closest approach and the kinetic energy decreases as a result of the equality shown in equation 6.7. The projectile then loses some kinetic energy to the collision between the projectile and the target at the distance of closest approach and retreats from the target as the potential energy is converted back into kinetic energy. The velocity of the particle can be calculated from the kinetic energy using the method described in section 1.3.4.2. The velocity as a function of inter-nuclear distance for the Ar $\rightarrow$ Ar system is given in figure 6.6b.

Once the velocity of the projectile over the collision distance has been established, the time taken for the collision to take place can be calculated by taking the average velocity over the collision length. The collision length (L_c) can be estimated from the sum of the atomic radii of the collision partners which in this case is the same as the projectile. The approach time, (t_a), retreat time, (t_r), and total collision time (t_{tot}) for the projectile-target pairs are shown in table 6.3. These values are only approximate and represent the slowest or longest collision time during a head-on collision.

System	$L_c(m)$	$t_a(s)$	$t_r(s)$	$t_{tot}(s)$	t_{tot} / t_p
H $\rightarrow$ H	1.06×10^{-10}	2.20×10^{-16}	2.21×10^{-16}	4.41×10^{-16}	1
N $\rightarrow$ N	1.30×10^{-10}	8.27×10^{-16}	8.49×10^{-16}	1.68×10^{-15}	7.63
Ar $\rightarrow$ Ar	3.76×10^{-10}	1.37×10^{-15}	1.46×10^{-15}	2.83×10^{-15}	12.86
Xe $\rightarrow$ Xe	4.32×10^{-10}	1.91×10^{-15}	2.27×10^{-15}	4.18×10^{-15}	19.10

Table 6.3: Calculated collision times for the ion species used in the VLE-PIXE experiments. L_c = collision length, t_a = approach time, t_r = recoil time, and t_{tot} = total collision time. t_{tot} / t_p is the ratio of the total collision time to the time of the same journey carried out by a proton.

The same calculation can then be performed with a proton impacting the same target, for example $p \rightarrow$ Ar. The approach time for the proton onto the target can then be considered and compared to the collision time of the symmetrical projectile-target pair. This allows an estimation of the potential number of proton

impacts which can occur on the sample during the period which the target and projectile atomic energy levels are modified by the formation of molecular orbitals.

The ratio of the total collision time for the symmetrical pair, compared to the approach time for the proton on the target (t_{tot} / t_p) is summarised in table 6.3. Values of up to 19.10 are calculated for the Xe-Xe system, demonstrating that up to 19.10 proton impacts can occur on the sample in the same time frame as a Xe $\rightarrow$ Xe collision. It is important however to consider that this calculation does not account for the probability of a proton striking the same atom upon the sample which would be required for the removal of an additional electron by proton impact during the time which the electronic energy levels are modified by the quasi-molecule. This effect was discussed in section 6.1.2.

6.3 Coincident Collision Monte-Carlo Simulation

As discussed previously, many of the mechanisms outlined in section 6.1 rely on the coincident impact of a proton and a heavy ion on the same region of a sample. Section 6.2 and in particular section 6.2.4 revealed that the time frame over which these collisions occur is sufficiently long that several proton impacts may occur on the sample during the presence of a quasi-molecule. What was not shown however is the probability of these coincident collisions may occur.

To resolve this, a Monte-Carlo simulation was developed in MATLAB to help calculate the probability of a simultaneous proton and heavy ion collision upon the same atom within a sample. This simulation was used to capture the random nature of particle impacts upon a sample and was necessary due to the complex nature of calculating the trajectories of multiple particles of different masses, velocities, and locations.

The simulation proceeds as such:

- The number of ions and protons emitted per second is calculated based on the beam current and the proportion of each species in the beam. Typically a 1:1 ratio of protons/heavy ions is used and a beam current of 100-200nA.
- A time step is established such that the number of ions emitted per time step is less than one. This can be thought of as the probability of an ion being emitted. Additionally, the time step is adjusted such the distance travelled per time step is smaller than the collision length of the atom to avoid the ions “teleporting” through the atom.

- The simulation iterates through time steps, adding the emission probability until it reaches a value of 1. A 25% randomness in the probability is included at each time step to achieve a semi-random emission in time whilst maintaining a constant beam current.
- When a proton or ion is emitted, it is randomly assigned an X and Y coordinate in a Gaussian distribution with width determined by a given d_{50} value to simulate an ion beam profile upon the sample.
- The protons and ions will then move through the simulation space with a velocity determined by the given accelerating voltage and as such will move a certain distance per time step.
- After a short distance, the particles will encounter a coulomb potential representing a monolayer of atoms for the projectiles to interact with. The proton and heavy ion will enter the Coulomb potential, resulting in a decrease in velocity, followed by an increase in velocity as it escapes the potential. This will include the loss of energy due to inelastic scattering. This mechanism was demonstrated in figure 6.6b.
- At each time step, the proton and heavy ion locations are compared. If both a proton and heavy ion are located within the collision length of the sample atom, they are considered to be coincidentally striking the same atom and is counted as a simultaneous proton and heavy ion interaction. This localises the proton and heavy ion in 3 dimensions.
- The number of coincident interactions is counted over period of many time steps. This value is then normalised to the beam current and simulation time to calculate a statistical value of coincidences/second/nA.

The standard parameters used for these calculations are:

- Accelerating Voltage - 30keV
- Proton/Ion Ratio - 1:1
- Beam current - 200nA
- Emission Randomness - 25%
- d_{50} - 200nm
- Time Interval - 5×10^{-17} seconds
- Time Steps - 5×10^{10}

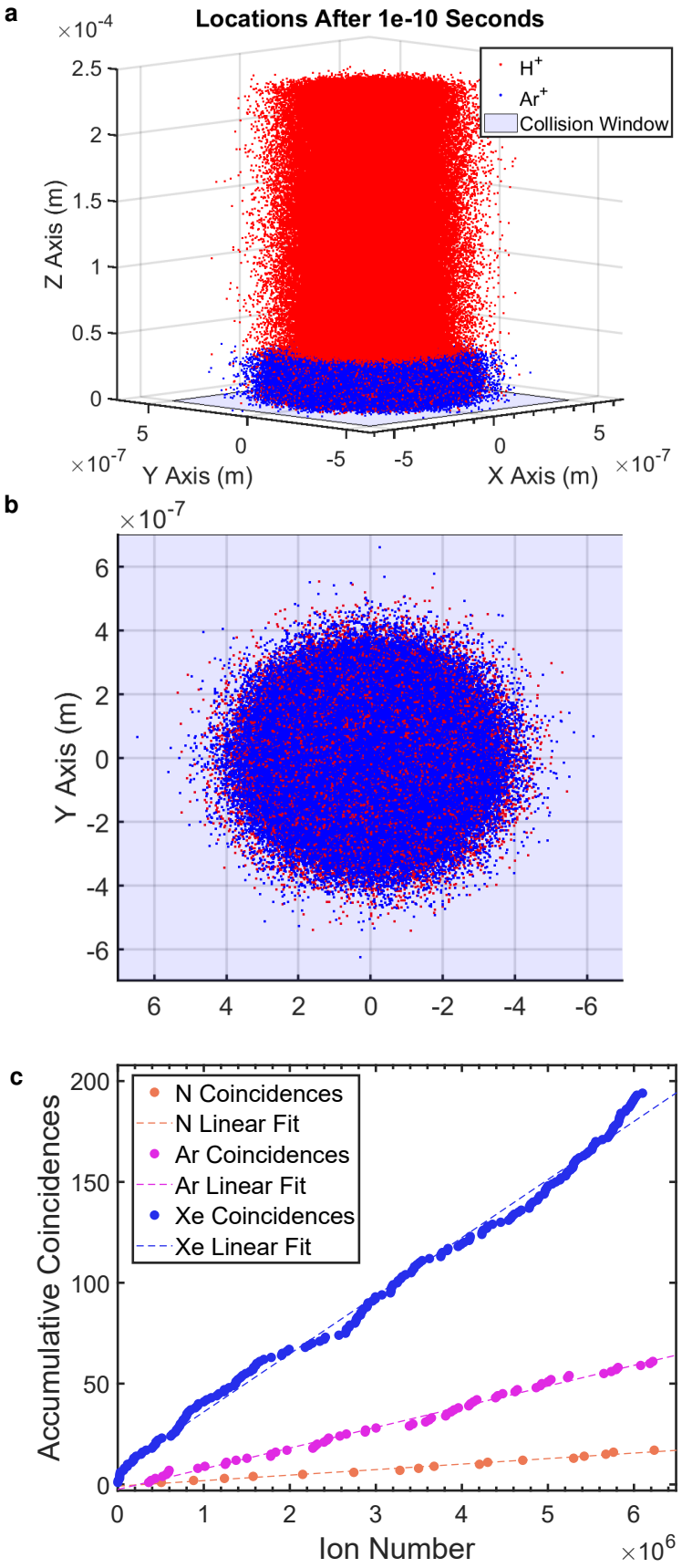

Figure 6.7: Example outputs of the Monte-Carlo simulation (a) Proton (red dots) and heavy ion (blue dots) locations after 1×10^{-10}s. The collision window is shown as a blue box. (b) X-Y plane projection of particle locations demonstrating the Gaussian distribution with a d_{50} of 200nm. (c) Example accumulative coincident events for each ion species for the number of simulated particles after 2.5×10^{-6}s.

An example output of the Monte-Carlo simulation is shown in figure 6.7a with the proton (red) and heavy ion (blue) locations shown after 1×10^{-10}s, and the collision window displayed as a blue box. The significant difference in distance travelled by the protons and heavy ions is due to the greater velocity of the protons at the same accelerating voltage. Figure 6.7c shows the number of accumulative coincident events for each ion species as a function of the ion number.

An approximate number of coincident events was established for each heavy ion species, averaged over a number of simulation runs and is outlined in table 6.4.

System	c/s/nA	$\sigma_{\bar{x}}$	n
N+H$\rightarrow$ N	13886	887	10
Ar+H$\rightarrow$ Ar	52336	4109	10
Xe+H$\rightarrow$ Xe	202252	7111	10

Table 6.4: The average number of coincidences per second, per nA of beam current. Standard error of average number of coincidences per second per nA. Number of simulation runs.

The coincident collision Monte-Carlo simulation demonstrates that a significant number of coincident proton and heavy ion strikes may occur during the course of doped beam VLE-PIXE measurements. These coincident events are key to the mechanisms outlined in section 6.1 and may result in: the more efficient ionisation of electrons by coincident proton impact while target and projectile energy levels are modified by the formation of molecular orbitals, the suppression of non-radiative transitions due to the more efficient removal of electrons responsible for Auger and C-K electron emission, and the lengthening of vacancy lifetimes due to the removal of additional outer-shell electrons which will be covered in greater detail in section 6.4.2.

This simulation is however only an approximation and a number of limitations exist such as:

- The simulation only considers a single monolayer of atoms as a sample and does not account for more complex sample interactions such as double-scattering or sub-surface collisions.
- The Coulomb potential and energy loss for the sample are only considered for the maximum, where the ion is scattered at 180°. This will represent the longest collision time and therefore the maximum number of coincident

collisions and does not consider the range of scattering angles typically experienced during scattering.

- This simulation assumes that the beam shape is perfectly Gaussian and does not properly represent realistic beam shapes which may contain a significant proportion of the beam in beam tails.
- This simulation assumes that only two particle species (protons and one heavy ion species) are present in the beam at a time and does not account for many multiple species.
- This simulation only considers the symmetric impact of a projectile atom and an identical atomic target. Every projectile and target combination would have to be calculated individually.
- The simulation does not consider vacancy lifetimes and whether long lifetimes could result in coincident collisions beyond the lifetime of the quasi-molecule. This factor discussed in section 6.4.2 would serve to increase the number of X-Rays emitted.

6.4 Vacancy Lifetimes

6.4.1 Projectile Vacancy Lifetimes

The double scattering mechanism outlined in section 1.3.4.5 relies on the presence of a vacancy in the projectile as it approaches the sample. It has been established in the literature that at low energies ($<$1MeV), vacancy sharing which arises as a result of the double-scattering mechanism is the primary inner-shell ionisation method and is responsible for the generation of a number of X-Rays at lower energies [129]. This was demonstrated for the example of Ar $\rightarrow$ Al, Si, S, Sc, Ti, and V [242], many of the elements identified in the SRM 654b.

In order for the vacancy sharing the occur, the projectile vacancy only needs to survive the time between the first collision in the double scattering process, to the distance of closest approach of the second target, a distance equal to the lattice constant of the material minus the distance of closest approach. The vacancy lifetime can be calculated from the radiative rate for the particular vacancy, values which are well known and reported in the literature. The lattice constants can also be found in the literature however due to the gaseous nature of the elements chosen, estimations based on the experimental lattice constants for solid gases

must be used. These lattice constants are quite similar to those found in the vast majority of materials and can be used as a reasonable estimate for a more general behaviour.

In order to determine whether the vacancy sharing mechanism is applicable in the system measured throughout this thesis, the calculations performed in section 6.2.4 were modified such that the collision length was equal to the lattice constant of the material minus the distance of closest approach.

The inner-shell projectile vacancy lifetimes (τ_v), lattice constants (d), lattice constant collision times (t_d) and the ratio of the vacancy lifetime to the lattice constant collision times (τ_v / t_d) for a 30keV, 180° collision are listed in table 6.5.

System	$\tau_v(s)$	$d(m)$	$t_d(s)$	τ_v / t_d
H $\rightarrow$ H	N/A	N/A	N/A	N/A
N $\rightarrow$ N	7.5$\times10^{-15}$ [243]	5.67$\times10^{-10}$ [244]	8.23$\times10^{-16}$	9.12
Ar $\rightarrow$ Ar	5.0$\times10^{-15}$ [245]	5.31$\times10^{-10}$ [246]	1.37$\times10^{-15}$	3.65
Xe $\rightarrow$ Xe	2.27$\times10^{-15}$ [247]	6.33$\times10^{-10}$ [248]	1.91$\times10^{-15}$	1.19

Table 6.5: Calculated vacancy lifetimes for the ion species used in the VLE-PIXE experiments. τ_v = vacancy lifetime, d = crystal lattice spacing, and t_d = lattice constant collision time.

It can be seen that in all the cases provided above, the collision times are shorter than than the vacancy lifetime for the given projectile. This is characterised by the ratio of the vacancy lifetime to the collision times (τ_v / τ_d) being greater than 1 for all the given projectile target pairs. This demonstrates that the projectile inner-shell vacancies can indeed survive until they reach the distance of closest approach to the target, where the vacancy can then be transferred to the target. The vacancy however may be transferred prior to the distance of closest approach which would serve to increase the ratio even further.

6.4.2 Target Vacancy Lifetime

Listed in table 6.6 are the K shell vacancy lifetimes for the elements in the SRM 654b, which only consider the presence of a single vacancy. These are known as natural vacancy lifetimes in that they are unmodified by the effect of multiple ionisation. These values are compared to approximate collision times for protons, N, Ar, and Xe on the elements listed which are found in the SRM 654b.

In most cases, the vacancy lifetimes are of a similar order or greater than the collision time for the ion species. This means that the vacancies produced will linger for some time following the collision event. This will further enhance the effect of the coincident collisions outlined in section 6.3 as the heavy ion projectile may have left the vicinity of the target atom, leaving a lingering vacancy which can survive long enough for an additional proton strike and the removal of yet another electron from the target atom prior to de-excitation. This will in turn reduce the probability of non-radiative transitions and may extend the vacancy lifetime even further due to the vacancy lifetime modification outlined in section 6.1.3

Shell	$\tau_v(s)$ [249]	$t_p(s)$	$t_N(s)$	$t_{Ar}(s)$	$t_{Xe}(s)$
Ti K	5.64×10^{-15}	$\mathbf{4.46\times10^{-16}}$	$\mathbf{1.70\times10^{-15}}$	$\mathbf{2.99\times10^{-15}}$	6.06×10^{-15}
Al K	6.21×10^{-14}	$\mathbf{4.44\times10^{-16}}$	$\mathbf{1.69\times10^{-15}}$	$\mathbf{2.94\times10^{-15}}$	$\mathbf{5.66\times10^{-15}}$
Si K	4.44×10^{-14}	$\mathbf{4.44\times10^{-16}}$	$\mathbf{1.69\times10^{-15}}$	$\mathbf{2.94\times10^{-15}}$	5.68×10^{-15}
V K	4.62×10^{-15}	$\mathbf{4.46\times10^{-16}}$	$\mathbf{1.70\times10^{-15}}$	$\mathbf{3.01\times10^{-15}}$	6.17×10^{-15}
Fe K	2.69×10^{-15}	$\mathbf{4.46\times10^{-16}}$	$\mathbf{1.70\times10^{-15}}$	3.03×10^{-15}	6.47×10^{-15}
Ni K	1.95×10^{-15}	$\mathbf{4.46\times10^{-16}}$	$\mathbf{1.71\times10^{-15}}$	3.05×10^{-15}	6.73×10^{-15}
Cu K	1.68×10^{-15}	$\mathbf{4.47\times10^{-16}}$	$\mathbf{1.71\times10^{-15}}$	3.05×10^{-15}	6.86×10^{-15}

Table 6.6: K shell vacancy lifetimes compared to approximate collision times for protons, N, Ar, and Xe on the various elements in the SRM 654b. Bold font values denote collisions which are faster than the vacancy lifetime.

Table 6.7 shows the same values as in table 6.6, expressed as the ratio of the vacancy lifetime to the collision lifetime for the various ion species. It can be seen that in the most extreme case, for the impact of protons on an Al target atom, the proton collision time is 139.86 times faster than the Al K vacancy lifetime. This means that up to 139 proton collisions may occur on the sample in the lifetime of the Al K vacancy, each of which has the possibility of removing an additional electron. Once again, this calculation does not account for the probability of a proton striking the same atom on the sample however it demonstrates the drastically enhanced probability of another proton impact occurring during the vacancy lifetime.

Transition	τ_v/t_p	τ_v/t_N	τ_v/t_{Ar}	τ_v/t_{Xe}
Ti K	**12.65**	**3.32**	**1.89**	0.93
Al K	**139.86**	**36.75**	**21.12**	**10.97**
Si K	**100.00**	**26.27**	**15.10**	**7.82**
V K	**10.36**	**2.72**	**1.53**	0.75
Fe K	**6.03**	**1.58**	0.89	0.42
Ni K	**4.37**	**1.14**	0.64	0.29
Cu K	**3.76**	0.98	0.55	0.24

Table 6.7: The ratio of K shell vacancy lifetimes to collision times for the various ion species. Bold font values denote collisions which are faster than the vacancy lifetime, ie. $\tau_v/t_I>1$.

6.4.3 Vacancy Peak Width Narrowing

The vacancy lifetimes as discussed in section 6.4.2 and outlined in table 6.6 correspond to the natural or single vacancy lifetimes. As discussed in section 6.1.3, the presence of multiple vacancies in a target atom can result in an increase in vacancy lifetime which can in turn result in a greater probability of coincident proton impact during the vacancy lifetime and the removal of additional electrons. The values listed in table 6.6 therefore correspond to the **minimum** lifetime of these vacancies. The vacancy lifetime can be determined from the Lorentzian linewidth of an X-Ray transition. As discussed in section 1.3.4.9, the shape of an X-Ray peak is determined by a Voigt function which is the convolution of a Lorentzian corresponding to the intrinsic X-Ray emission and a Gaussian corresponding to detector broadening. Careful Voigt fitting of an X-Ray peak can therefore determine the Lorentzian linewidth which can then be converted to a vacancy lifetime using the Heisenberg uncertainty principle for energy and time [250]:

$$\Delta E \Delta t \geq \hbar/2 \tag{6.8}$$

where $\hbar$ is the reduced Planck constant (6.58×10^{-16}eV·s). The vacancy lifetime can therefore be estimated by [251]:

$$\tau = \hbar/\Gamma \tag{6.9}$$

where Γ is the measured FWHM Lorentzian linewidth in eV and τ is the vacancy lifetime in seconds.

While significant effort was taken to calculate the Lorentzian width from the Voigt fit of the spectral peaks measured throughout this thesis, it was determined that the ratio of the Lorentzian width to the Gaussian width was far too large to achieve an accurate value. Such an example is given in figure 6.8 where the Lorentzian width is set to the natural linewidth of the Ti Kα X-Ray peak as given by Krause [2]. Relative to the Gaussian broadening, the Lorentzian approximates a delta function and represents a miniscule change in the Gaussian width relative to the inherent noise of the system. Should there be an increase in lifetime due to multiple ionisation, the width of the Lorentzian would only decrease further. For this reason, the effect of multiple ionisation on the vacancy lifetime could not be measured directly.

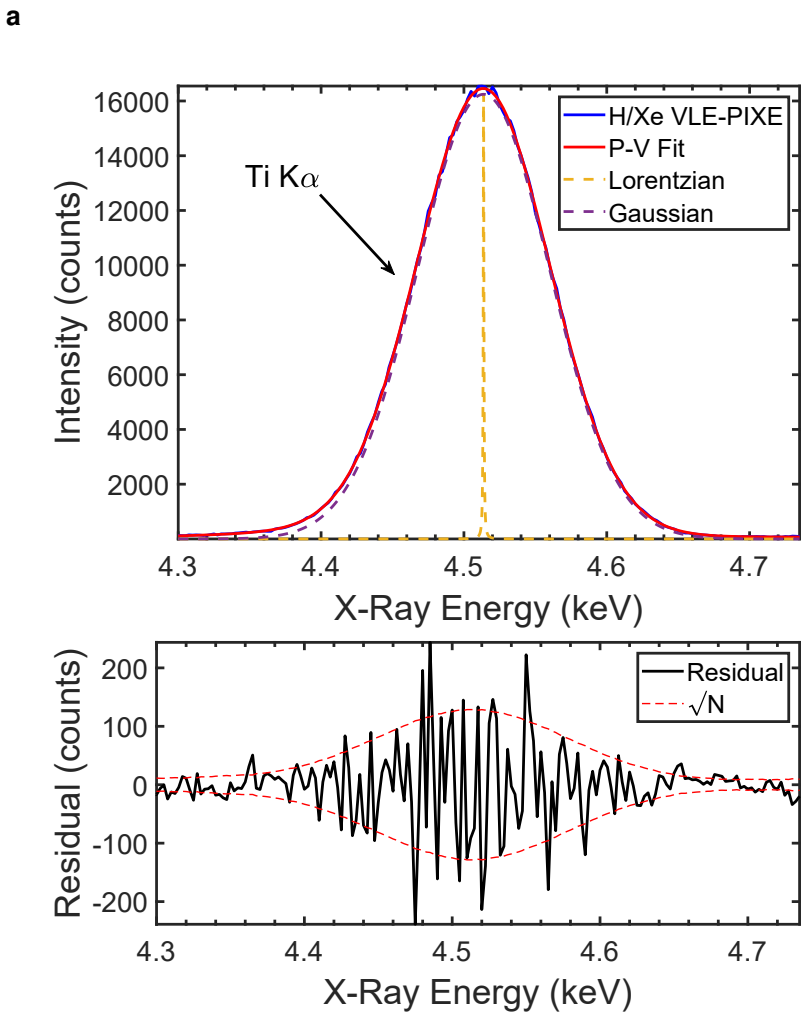

Figure 6.8: Example of the Gaussian and Lorentzian functions generated by the pseudo-Voigt fit of a Ti Kα X-Ray peak with the Lorentzian peak width fixed to the natural linewidth of the Ti Kα peak.

6.5 An Interpretive Model

Based on the analysis outlined throughout this chapter, a model is proposed which considers the full collision process of a heavy ion doped hydrogen beam upon a sample. This model includes the various mechanisms which may result in enhanced X-Ray production which are specific to the beam doping method. Where relevant, literature sources for the various mechanisms are provided. The mechanisms occurring directly as a result of beam doping are listed in bold font:

1. A slow, heavy projectile ion with an outer shell vacancy approaches the sample. The outer-shell vacancy is neutralised by an electron from the sample via any number of mechanisms (see section 1.3.3.4) [74]. An inner-shell vacancy is formed in a collision with target atom 1. This is the first interaction in the double scattering mechanism [135].

2. The projectile leaves the vicinity of the target atom 1 with an inner-shell vacancy and approaches a target atom 2. Saris et al. estimated that 10% of incident Ar ions would possess an L shell vacancy in this situation [138].

3. The projectile forms a quasi-molecule with the second target atom, leading to a modification of the projectile and target electronic energy levels. [229]

4. **During the quasi-molecule lifetime, a proton or multiple protons may impact the quasi-molecule, leading to more efficient ionisation due to the modified binding energies of the quasi-molecule electrons** [229].

5. Separation of the quasi-molecule results in inner-shell vacancy being transferred from the heavier to the lighter of the pair [141, 101]. The target also possesses multiple inner-shell vacancies due to proton impact. **The vacancy lifetimes may be extended by the presence of multiple inner and outer-shell vacancies which may result in additional proton impacts and ionisations prior to de-excitation.**

6. The de-excitation of outer shell electrons result in the emission of characteristic X-Rays from the target. **Due to the presence of multiple vacancies as a result of coincident proton impact, non-radiative Auger and C-K emissions are suppressed resulting in an increased fluorescence yield** [110].

One possible outcome of this process is outlined diagrammatically in figure 6.9 for a hypothetical collision of an Ar^+ ion on an Al sample.

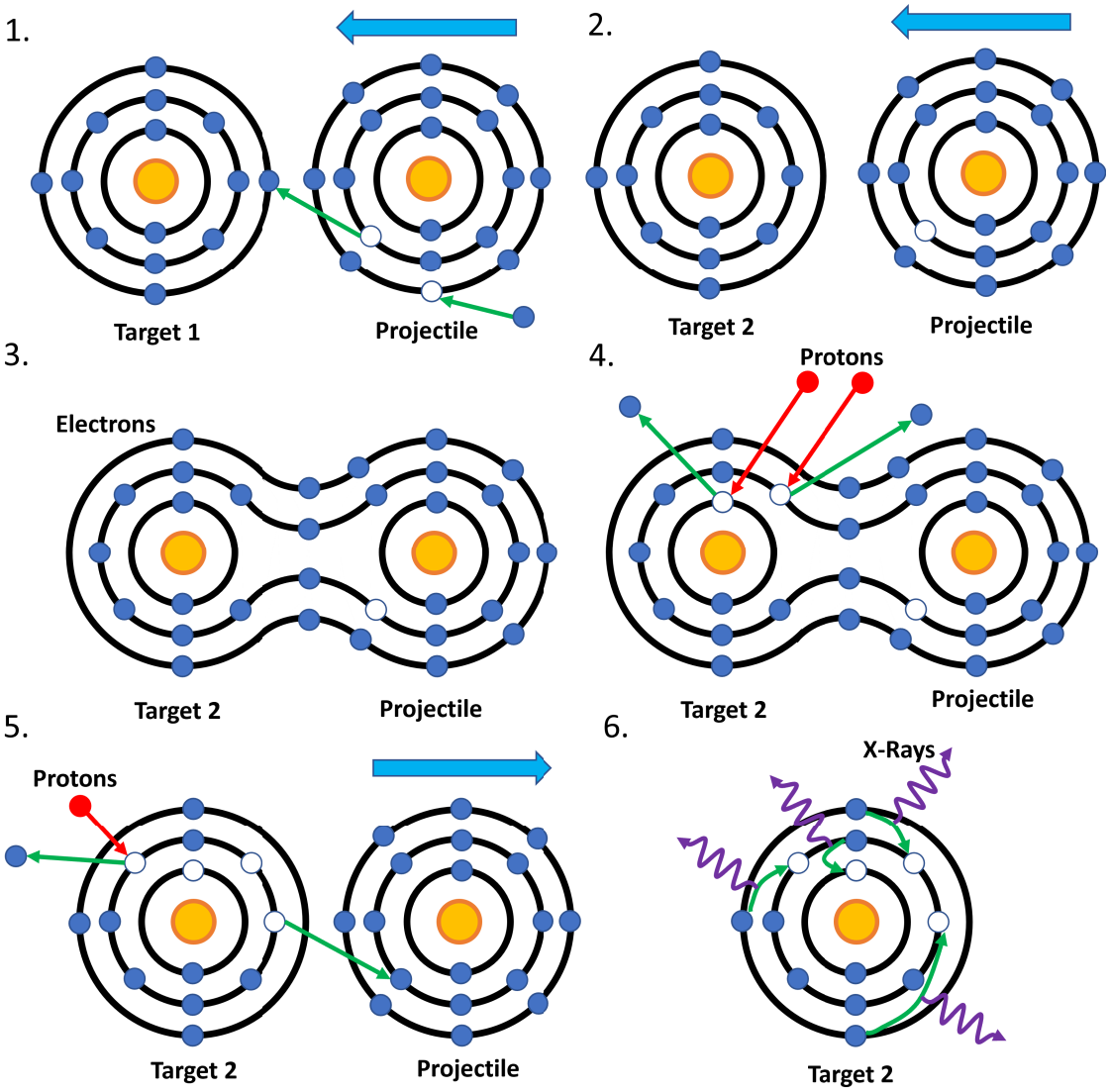

Figure 6.9: Cartoon of a possible combined enhancement model. Electrons are marked as filled blue circles with electron trajectories marked as green arrows, vacancies are marked as empty blue circles. Protons are marked as filled red circles with proton trajectories marked as red arrows. X-Rays are marked in purple and atomic nuclei in yellow. Projectile trajectories are marked with light blue arrows.

6.6 Model Limitations

Validation of the model outlined above demonstrates that under the experimental conditions used throughout the VLE-PIXE measurements, the proposed model can provide a possible explanation for the observed performance increase due to beam doping. The model however has several limitations which must be considered to provide an accurate understanding of the observed behaviour.

Symmetrical collisions were used throughout much of the validation due to the significant amount of literature information for these collisions. The most well studied collision system in the literature is the Ar $\rightarrow$ Ar system as: this was the system studied by Fano and Lichten which provided the initial findings for the quasi-molecular model [129] and sparked lasting interest in this field, Ar is a very commonly used species in many ion beam systems due to its ready availability, and Ar has a good compromise of relatively complex electronic structure as well as low mass and therefore high velocity, making it ideal for studies of the quasi-molecular model.

Extending the combined model beyond symmetrical collisions becomes increasingly complex due to the wide range of possible projectile-target combinations, and the limited experimental data available in the literature for heavy ion impacts on a variety of targets. Calculation of the MO correlation diagrams for asymmetric collisions is also a difficult task [128]. Each projectile-target combination will need to be assessed individually, with correlation calculations performed using density functional theory (DFT). The calculation of these diagrams, often performed by the variable screening method as outlined by Eichler et al. [252] are very complex, requiring quantum mechanical solutions to the interaction of the molecular orbitals formed between the target and the projectile. Such calculations are beyond the scope of this thesis, in fact, early attempts to calculate increasingly more accurate molecular orbital interactions resulted in the invention of DFT [238]. Some additional asymmetric MO correlation diagrams for the various ions are provided in appendix section A.8 for reference purposes, with r_{min} values at an energy of 30keV marked. It is assumed that the symmetric collisions may provide a good estimation of the behaviour of the model however issues may arise when highly asymmetric collision partners are used such as very heavy ions on light targets and vice versa.

Many of the assumptions and simplifications used during the model validation are outlined throughout the text when used. In particular, the distance over which the collision between a projectile and a target atom can influence the electronic

energy levels was assumed to be the sum of the atomic radii of the collision pairs. Determining the exact distance over which these particles are capable of forming molecular orbitals is once again the subject of an extensive DFT study and beyond the scope of this thesis.

While the number of coincident collisions which were calculated in section 6.3 were quite high, these values could not be translated into a number of X-Rays generated purely as a result of coincident collisions. This is due to the XRPCS only being defined for a single atomic species, particularly protons and it is unsure at this stage how exactly the presence of heavy ion dopant species will alter the XRPCS beyond that of the XRPCS for either the heavy ion or proton species individually. Given the magnitude of the observed increase in X-Ray yield with beam doping beyond the currently understood eECPSSR and analytical methods, it is likely that this task will not be trivial and won't be achieved by a simple modification of the current models, but the introduction of an extension to the current physical models to include the interaction of multiple ion species.

It is for this reason that further development of the underlying physics is required to understand how the interaction of multiple ion species with a sample results in the ejection of X-Rays. This has significant implications for quantitative doped beam VLE-PIXE, as a proper understanding of the enhancement in X-Ray yield through any number of the above effects is essential for determining an accurate method for converting a number of X-Rays to a concentration of a material on a sample. This would involve a systematic analysis of the phenomena described above to determine: if the phenomena can indeed result in an increase in X-Ray yield to the extent described throughout this chapter, whether these phenomena are separable in the sense that their impact on the X-Ray yield can be calculated individually, and whether the magnitude of the above phenomena can be converted into an enhancement of the X-Ray yield beyond what is produced by protons alone and vice versa.

6.7 Conclusions

A interpretive model was outlined which provides a possible explanation for the increased VLE-PIXE performance experienced by use of beam doping. This model takes into account a number of different mechanisms which may work together to provide an enhancement of the VLE-PIXE XRPCS beyond what is expected by the literature and beyond what can be achieved by the individual mechanisms in isolation. The basis for the proposed model is firmly grounded in the literature,

with discussion of the quasi-molecular model, the double-scattering mechanism, vacancy sharing, and electron promotion being discussed in hundreds of papers over a period of almost 6 decades.

The simultaneous impact of multiple different ion species is not commonly performed in PIXE experiments due to the complexity of the multiple ion-solid interactions confounding PIXE results. Ion beams used for PIXE are typically filtered by mass in order to achieve a single species beam. For this reason, it is likely that this phenomenon has not been observed before in the context of modifying PIXE measurements. One example was found in the literature involving PIXE, where multiple heavy ion beams as well as an MeV proton beam were directed towards the same sample for simultaneous heavy ion irradiation and PIXE/RBS analysis. There was however no discussion of any anomalous PIXE results which resemble those shown throughout this thesis and it is likely that the energy would be too high for any significant effects to be observed [253].

The behaviour demonstrated by the addition of heavy ion dopants to a hydrogen beam highlights a significant gap in the current understanding of the mechanisms resulting in ionisation by the impact of heavy ions upon a sample. Ionisation resulting from the impact of heavy ions alone is still poorly understood and the beam doping results outlined in this thesis may help shed some light on the underlying mechanisms. Hopefully the results outlined in this thesis will spark an interest in the field of doped beam VLE-PIXE, leading to an enhanced understanding of the technique and the underlying physical mechanisms.

Chapter 7

Backscattered Ion Spectroscopy with a Hydrogen FIB

As mentioned in section 3.2.4, the VLE-PIXE process generates a large number of backscattered ions from the sample which can penetrate the X-Ray detector window at energies above 24keV. These BSIs can carry information about the surface composition and structure as outlined in section 1.3.5, in particular kinetic energy losses due to scattering from the sample. Analysis can be carried out by measuring the energy of the backscattered ions following interaction with the sample. Backscattering ion spectroscopy performed at energies of less than 30keV is referred to as Low Energy Ion Scattering (LEIS). This section outlines the application of backscattering ion spectroscopy using the Hydrogen FIB.

7.1 Sample Preparation and Characterisation

Cu films were deposited on single crystal Si(100) substrates using thermal evaporation. The two thickest films were measured using atomic force microscopy (AFM) to determine the calibration factor for the quartz crystal monitor (QCM) which is used to determine the thickness of the deposited layer during the thermal evaporation procedure. The results of these thickness measurements are shown in figure 7.1a for the approximately 10nm film and 7.1b for the approximately 20nm film. The thinner samples could not be measured directly using the AFM as they could not be located using the optical microscope of the AFM. This is however not a concern as QCMs are highly accurate once calibrated using a secondary method such as the AFM described above, and are capable of measuring thin film thicknesses with an accuracy of less than an Angstrom [254]. The

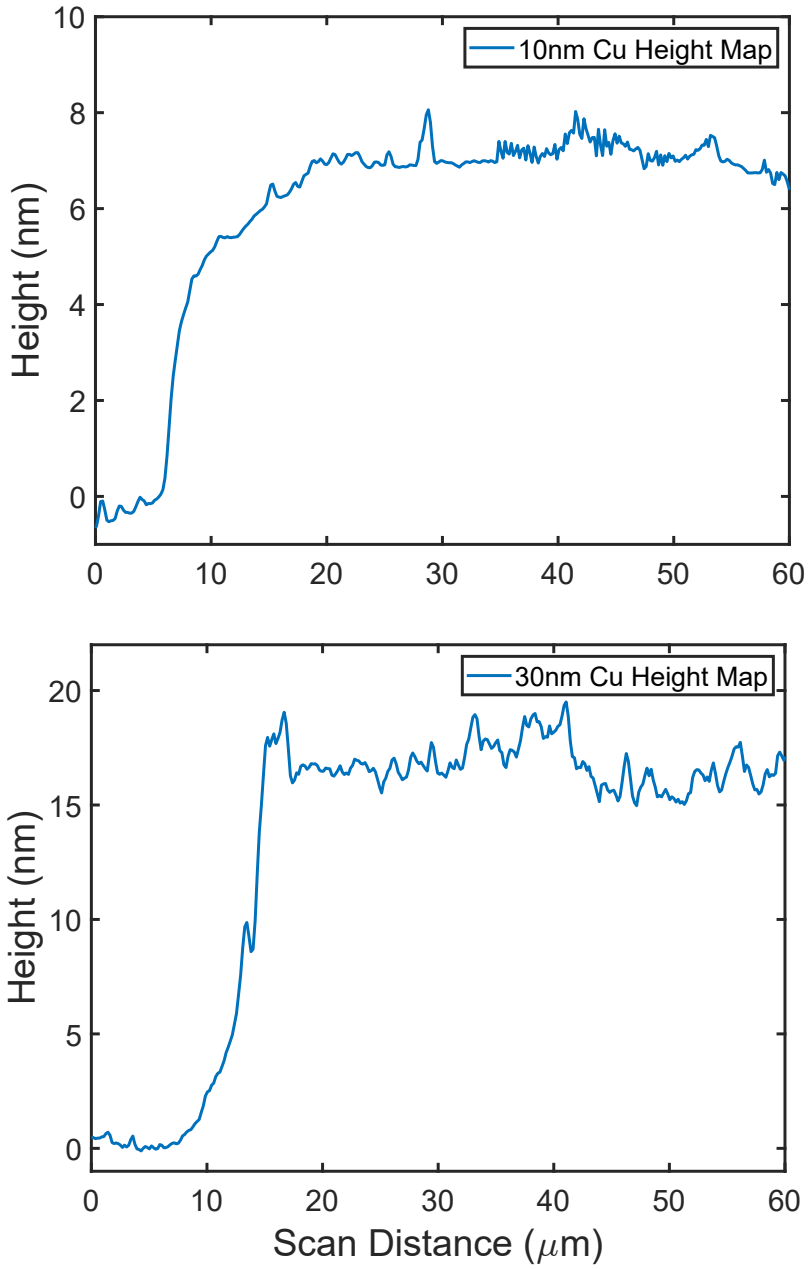

Figure 7.1: Atomic force microscope thickness measurements of an (a) 10nm and (b) 30nm thermally evaporated Cu film

result was a series of Cu films on Si with a thickness of 0.33nm, 0.7nm, 3.3nm, 6.7nm and 20nm.

The energy of the backscattered ions following interaction with the various surface atoms as a function of scattering angle can be calculated using the kinematic scattering theory outlined in section 1.3.3.2. Scattering energies for a 30keV proton beam as a function of angle are shown in figure 7.2 for the various elements is used in these experiments. These values can be used to predict the location of single scattering peaks which can otherwise be difficult to identify in LEIS spectra.

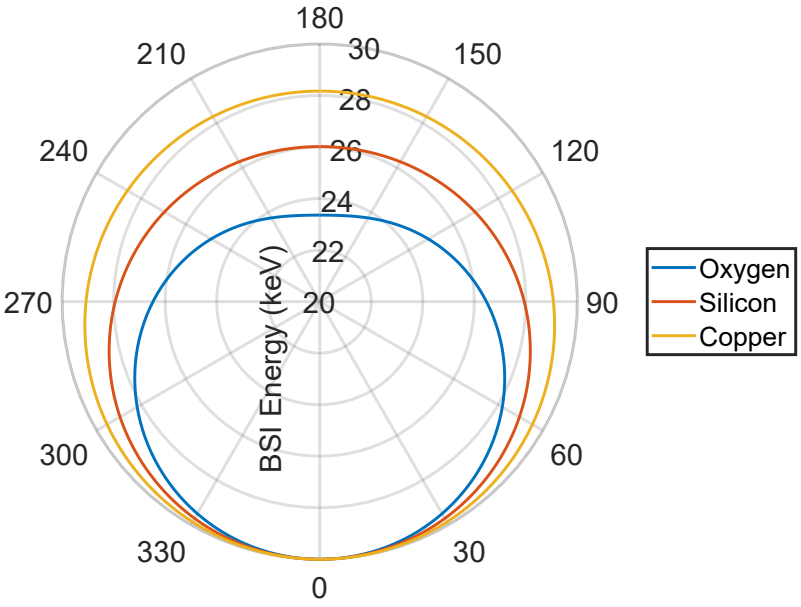

Figure 7.2: Calculated kinematic scattering vs angle for a 30keV proton beam on the elements analysed in these experiments

7.2 Cu Film Thickness Analysis With LEIS

An Oxford Ultim Extreme windowless EDS detector was used for the LEIS experiments. The windowless detector allowed protons to strike the detector surface directly, unmodified by transmission through the detector window. Following chamber pump-down, the detector was cooled for 15 minutes prior to exposure to maximise sensitivity. The maximum number of channels and a processing time of 6 was used to maximise the resolution of the collected spectra.

Due to the possibility of damage caused by direct irradiation of the detector surface, great care was taken to minimise exposure to the detector. For this reason, irradiation currents were kept to a minimum at only several pA, and exposure times were limited to 10 minutes. For all the exposures, a 20x20μm box was created using the in-built pattern generator of the microscope, set to a 10 minute mill time.

As discussed in section 1.3.4.8, when an X-Ray is incident upon and SDD detector, it will generate a number of electron hole pairs which is proportional to the energy of the X-Ray. This number of electron hole pairs will likely be different for protons and will lead to an inaccurate representation of the particle energy which must be corrected. The energy correction was determined to be a linear shift of the spectra by 13keV as determined by LEIS spectral simulations which will be discussed in the following section. The energy corrected spectra are shown in 7.3a.

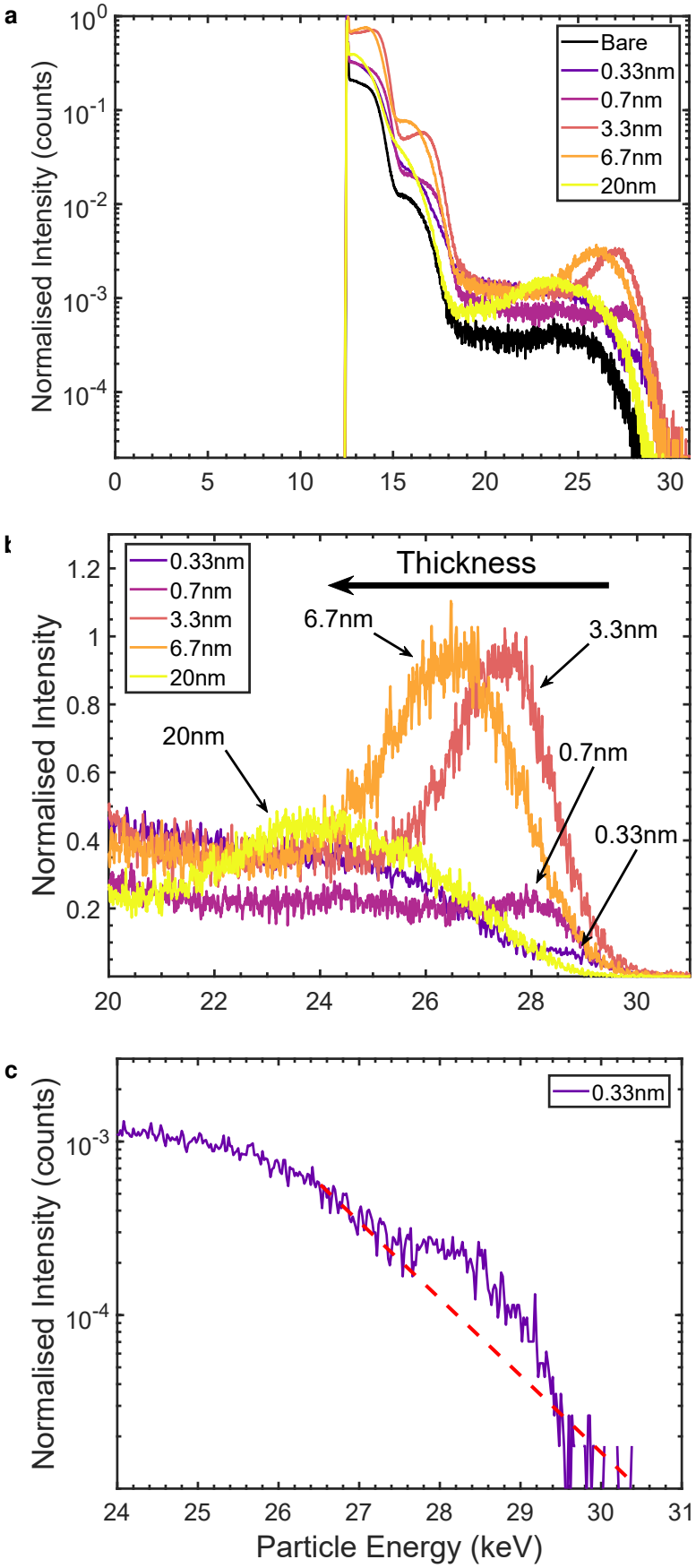

Figure 7.3: (a) Energy corrected 30keV, 10pA hydrogen LEIS spectra of the various thickness Cu films upon Si. (b) Scaled section of the energy corrected spectra showing the Cu scattering peak (c) Isolated spectra of the 0.33nm Cu film demonstrating the weak scattering peak. The red line is shown as a guide to the eye for the linear extrapolation of the bulk scattering background

The isolated region displaying the Cu scattering peaks for each film thickness are shown in figure 7.3b. The 0.33nm peak is isolated in figure 7.3c for clarity and demonstrates the presence of the very weak scattering peak even at a film thickness of less than 1nm over the irradiated region. As predicted by the theory in section 1.3.5.3, a shift towards lower energies can be seen as the film thickness increases and can thus be used to characterise the thickness of the Cu films.

Spectra of the 6.7nm Cu film were taken at accelerating voltages of 5, 10, and 20keV as shown in figure 7.4. As can be seen, at 10keV and below the Cu scattering peak at ~28keV (30keV) can no longer be resolved. For this reason, higher accelerating voltages proved to be optimal for this technique. It is theorised that this may be due to the EDS detector used for these measurements, the efficiency which may decrease with decreasing incident particle energy. In addition, the heavy particles may struggle to penetrate the thin dead layer at the surface of the detector at low energies and thus will result in a diminishing signal.

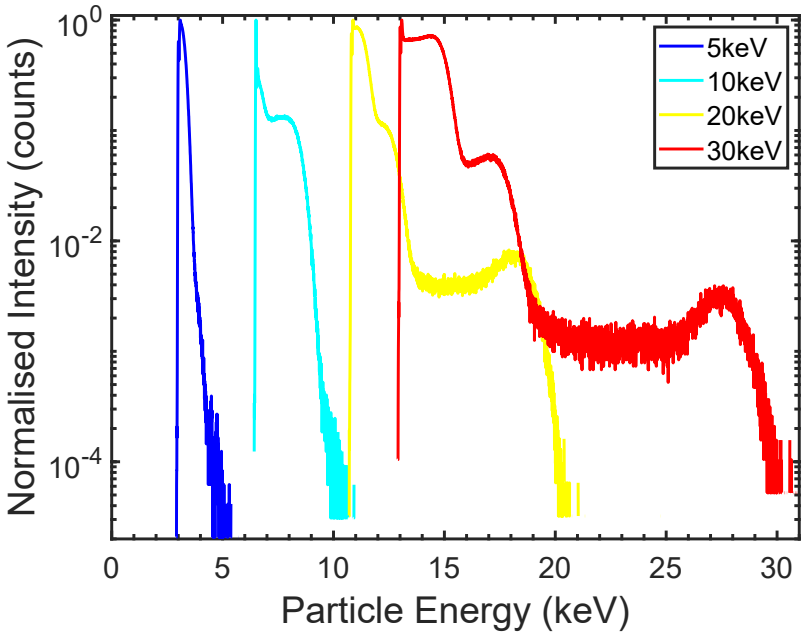

Figure 7.4: LEIS spectra of the 6.7nm Cu film on Si as a function of accelerating voltage.

7.2.1 Simulation of LEIS Spectra Using SIMNRA

To confirm the validity of the LEIS spectra taken using the hydrogen FIB, simulations of the expected spectra were performed using the SIMNRA software package, a software package dedicated to the simulation and analysis of LEIS, MEIS, RBS and NRA spectra. SIMNRA was also used to fit the experimental data and extract thickness measurements from the scattering peak [255].

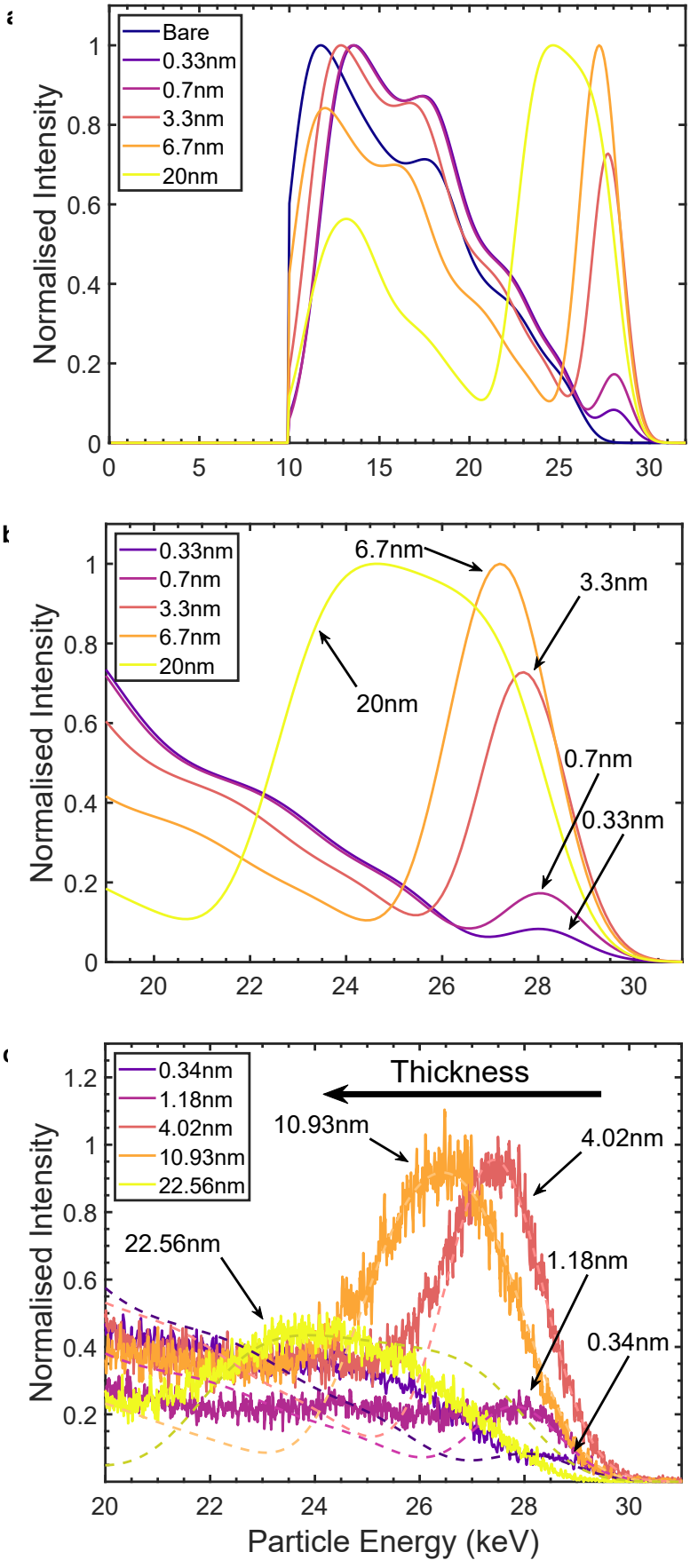

Figure 7.5: (a) Simulated LEIS spectra of the various thickness Cu films on Si. (b) Scaled region of the simulated spectra displaying the Cu scattering peak (c) LEIS spectra of Cu films with analytical fits displayed with dashed lines

Simulations were performed using a layered structure consisting of a bulk Si substrate, a 10nm native SiO_2 layer, and a Cu layer with a thickness reflecting the film thickness being analysed. The full simulated LEIS spectra of the various samples are shown in figure 7.5a and the isolated region showing the Cu scattering peaks is shown in figure 7.5b. From the simulated spectra, several spectral features can be determined which are present in both the simulated and experimental data. This includes the bulk Si scattering peak at an energy of $\sim$12keV, a feature attributed to the bulk scattering through the native SiO_2 layer at $\sim$18keV, and weak features attributed to O and Si single scattering at $\sim$23.5keV and $\sim$26keV respectively.

Utilising the SIMNRA software, theoretical fits to the experimental data can be established to determine the thickness of the Cu films, shown as dashed lines in figure 7.5c. These theoretical fits yielded a thickness of 0.34nm, 1.18nm, 4.02nm, 10.93nm, and 22.56nm. The results of these experiments are summarised in table 7.1 and are compared to the results of the AFM + QCM measurements which were outlined in section 7.1.

AFM + QCM	LEIS	% Difference
0.33nm	0.34nm	2.99
0.7nm	1.18nm	51.06
3.3nm	4.02nm	19.67
6.7nm	10.93nm	47.99
20nm	22.56nm	12.03

Table 7.1: Thickness measurements of the various copper films taken using the AFM+QCM method and LEIS.

7.2.2 Detector Damage

During the small number of LEIS experiments performed above, a noticeable decrease in the input count rate of the detector was observed under subsequent measurements with identical beam conditions. This phenomenon suggested that under the limited exposure of the backscattered ions and neutrals to the detector surface, some amount of damage was accumulating in the detector PIN junction. As such, the LEIS experiments were immediately ceased and planned future LEIS experiments were cancelled until such time that a solution could be found.

7.3 Conclusions

While a limited number of LEIS experiments could be performed to prevent permanent damage to the windowless EDS detetcor, the results of these experiments demonstrate the sensitivity of the LEIS technique as performed using the hydrogen beam. While this is not the first application of this technique to a FIB microscope, this technique has only been performed using a GFIS microscope utilising a He ion beam [170]. LEIS using a hydrogen beam in a PFIB can therefore be considered a new application of an existing technique and one which aims to expand the repertoire of the PFIB microscope.

This technique also opens the possibility for simultaneous doped beam VLE-PIXE and LEIS analysis, both of which can provide unique information about the composition of the sample. This possible technique is explored in greater detail in section 8.2.5 as well as some potential resolutions for the detector damage issue.

Chapter 8

Conclusions and Outlook

8.1 Thesis Summary

The work undertaken in this thesis has demonstrated the implementation and application of the doped beam VLE-PIXE technique on a commercial focused ion beam microscope. This technique offers trace element analysis with performance comparable to PIXE performed at much higher energies and the possibility of simultaneous FIB milling and sample analysis. This expands the availability of the PIXE technique from the relatively inaccessible particle accelerator facility to a FIB microscope which can be located in a standard laboratory facility.

Implementing a hydrogen and doped hydrogen beam on a PFIB microscope was the first and most critical step for making this technique possible. Understanding the characteristics, performance, nuances and artefacts corresponding to the hydrogen FIB were fundamental to the implementation of VLE-PIXE on this instrument and allowed validation of the VLE-PIXE technique. Particularly it allowed the elimination of spurious signals generated as the result of stray electrons, backscattered ions, or neutralised ions generated as a result of gas scattering within the FIB column and microscope chamber. Characterisation of the beam composition also demonstrated the generation of a high current of protons by the plasma FIB system, a result critical to the performance of the PIXE technique and unique to the plasma FIB as compared to previous hydrogen FIB manifestations such as the GFIS.

The role of various spurious signal sources such as stray electrons, backscattered ions and neutralised particles were investigated, and methods to eliminate such signals were outlined such as, manipulating the SEM magnetic immersion field

and FIB column lens biases. Reducing the FIB accelerating voltage to 24keV also allowed the influence of backscattered ions on the X-Ray spectrum to be limited. Ensuring a sufficient vacuum is established in the FIB column and microscope chamber prior to experiments was found to be critical to reduce the impact of secondary particles generated as a result of ion-gas collisions in the FIB column and chamber.

Trace element analysis of standard reference materials performed using a lightly Xe doped hydrogen beam allowed the validation of the performance of this technique utilising such metrics as signal to noise ratios and limits of detection. A direct comparison between an analogous technique, SEM-EDS, was performed and it was established that the sensitivity of doped VLE-PIXE was superior to EDS for almost all elements analysed due to to absence of the broad Bremsstrahlung background typical of electron X-Ray spectra. The absence of the Bremsstrahlung background also allowed the identification of several peaks using VLE-PIXE which could not be identified using EDS demonstrating a significantly increased sensitivity. The mapping capabilities of the VLE-PIXE technique were explored and were determined to be somewhat limited due to the very low signal generated by the VLE-PIXE technique. It was established that the performance of the doped beam VLE-PIXE technique was comparable to PIXE performed at much higher energies as shown by the significantly increased X-Ray production cross sections relative to a proton only beam.

Investigation of the beam doping method demonstrated that the signal produced when both protons and heavy ions are incident upon the same location on the sample was greater than the sum of the individual components. Xe was determined to be the optimum dopant species due to its relatively high performance and the absence of additional X-Ray peaks generated by the Xe projectile. The proportion of dopant species was shown to significantly increase the generation of X-Rays from the sample, reaching a maximum at $\sim$80% Ar species with a balance of hydrogen. This created the possibility for both a heavy species doped hydrogen beam as well as a hydrogen doped heavy species beam, each with unique potential applications.

Several potential physical mechanisms for the doped beam enhancement behaviour were discussed, namely the suppression of non-radiative transitions caused by the removal of additional spectator electrons in the target atom, the formation of a quasi-molecule between the target atom and the slow moving heavy projectile ion leading to modified electronic energy levels of the target and the projectile and more efficient ionisation of the target atom, and the extension of vacancy lifetimes

by the removal of multiple electrons from the target atom. A Monte-Carlo simulation was developed to estimate the probability of coincident impact of a heavy ion and a proton at the same location on the sample. It was determined that the possibility of coincident impact was high which may lead to the multiple ionisation of the target atom and resultant increase in X-Ray emission. An interpretive model was proposed which takes into account the various different mechanisms which may be responsible for the observed doped beam VLE-PIXE performance. Verification of the model using kinetic scattering calculations demonstrated that under the conditions used during the experiments performed, the proposed model has the potential to explain the increased performance observed.

The backscattered ions generated as result of the interactions of protons with the sample surface were analysed, a process known as backscattering spectroscopy or low energy ion scattering. Utilising a windowless EDS detector, energy analysis of the BSIs allowed the characterisation of the thickness of several copper films prepared by thermal evaporation on an Si substrate. The collected spectra provided a good match with simulated backscattering spectra, providing a layer thickness measurement of down to 0.34nm averaged over an area of 20 micrometres. This technique established the possibility of simultaneous doped beam VLE-PIXE measurement and backscattering ion spectroscopy.

8.2 Future Work

8.2.1 Validation of the doped beam VLE-PIXE Technique

In the future, further validation of the doped beam VLE-PIXE technique using FIB instruments other than the one which was used throughout this thesis would be highly beneficial to the validity of this technique, especially to demonstrate the reproducibility of this technique. Additionally utilising low energy decelerated particle accelerator beams will help provide further evidence of the power of very low energy PIXE analysis, as performed on well established, previously validated and purpose built PIXE systems. This would also allow the technique to be validated at higher energies to determine the performance of this phenomenon with increasing energy. This may lead to enhanced PIXE analysis in the MeV range by irradiating the sample surface with a low flux of low energy heavy ions to modify the electronic structure of the target atoms during analysis.

A more in-depth analysis into the use of doped beam PIXE utilising a wider va-

riety of heavy ion dopants for the enhancement of VLE-PIXE performance could also be carried out using multiple ion sources, each of which could be controlled independently. This is compared to the source utilised during the study performed in this thesis where limited control could be provided by the mixture of the various gas species in the source. This could also include a modification of the existing FIB hardware to allow more controlled gas mixing prior to the plasma source.

8.2.2 Endpointing and Real-Time Tomography

A potential commercial application of the doped beam VLE-PIXE technique could be a real-time elemental mapping process or an endpointing method. In section 5.3, it was demonstrated that a small amount of hydrogen could be added to a heavy ion species beam such as Ar or Xe to generate a strong VLE-PIXE signal. If this VLE-PIXE signal is monitored during the milling process on a layered sample, analysis of the change in characteristic peaks during milling could establish where one layer of a sample ends and the next begins. This technique could have significant applications in the semiconductor industry [256]. In addition, potential chemical effects induced by the mixture of the hydrogen and heavy ion species beam could provide some control over sample delayering, another critical process in semiconductor processing and failure analysis. [257] This may result in the mixture of more than two species, such as a Xe beam to induce rapid sputtering, a nitrogen beam to induce chemical effects, and a hydrogen beam to generate an analytical X-Ray signal.

Real-time elemental mapping would be a more advanced version of the endpointing technique where an X-Ray elemental map would be collected during sample milling. As demonstrated in section 3.4, X-Ray elemental mapping allows localisation of the elemental composition across a sample. As the beam scans across the sample during collection of an X-Ray map, the proportion of the heavy ion species with a greater sputtering yield than H^+, H_2^+ and H_3^+ would remove some material, such that each subsequent X-Ray map would originate from a different layer of the sample. Each map would form a “slice” of the material which when combined would establish a 3-dimensional map of the elemental composition of a material.

This technique is typically performed sequentially, where a layer of material is removed from the sample and the exposed layer is then analysed by an alternate means such as electron backscatter diffraction or EDS. This technique is known as serial sectioning tomography and is notoriously slow due to the need to re-

peatedly switch between FIB milling and sample analysis methods [8]. Utilising the VLE-PIXE method with a mixed hydrogen and heavy ion species beam, the milling and analysis steps could be combined into one and the mapping result could be captured in real-time. This has the potential to significantly increase the throughput of tomography workflows.

Potential Technique Challenges:
As the X-Ray detector will be inserted into the chamber during the milling process, due to the proximity of the detector to the sample, a significant amount of material which is sputtered from the sample will become deposited on the X-Ray detector window. This may result in a reduction of the transmission of X-Rays through the detector window, resulting in a decrease in sensitivity of X-Rays in the low energy range. As described in section 4.1.2, this may also result in the backscattered ions from the sample generating a signal upon the detector window which may contribute to the observed spectra. A possible resolution for this issue may be the addition of a replaceable screen in front of the X-Ray detector such that when the screen becomes coated in sufficient material to affect VLE-PIXE performance, it can be replaced with a new one, significantly extending the life of the detector.

Due to the high currents required in order to generate a significant X-Ray signal and the inherently lower resolution of a FIB compared to a SEM, the spatial resolution of this technique may be significantly worse than traditional serial sectioning tomography performed by a combination of a FIB and an SEM. This may however be improved over time due to generational improvements in the resolution of the PFIB instrument. For endpointing, where bulk delayering of a sample is taking place, the resolution limit may not be an issue. Due to the increased sensitivity of the doped beam VLE-PIXE, this technique may be able to detect the start of a new layer potentially sooner than other comparable analytical endpointing techniques such as secondary ion mass spectrometry (SIMS), which rely on the surface sputtering of ions for layer detection.

8.2.3 Sample Damage

While a significant investigation into the signals generated as a result of ion impact on a sample was carried out, there was not a significant focus on the damage induced in the sample by the impact of protons. While PIXE is typically considered a non-destructive technique, a significant amount of implantation, displacement, and formation of interstitials can occur which will result in a modification of the

material properties. One example of damage induced by proton irradiation at energies close to VLE-PIXE (40keV) and HE-PIXE (3MeV) demonstrated the formation of a significant number of defects [258]. A future study could involve the analysis of damage induced in the sample during the process of VLE-PIXE, using techniques such as electron backscattering diffraction (EBSD), transmission electron microscopy, and select area electron diffraction (SAED).

Doped beam VLE-PIXE will inevitably result in damage to the sample due to the high sputter yield of the relatively heavier ions. A compromise may however be identified where the X-Ray signal from a sample is still sufficient for analytical purposes, yet the sample damage is minimised due to the relatively low proportion of heavy ion species.

8.2.4 Backscattering Spectroscopy

The backscattering spectroscopy performed in chapter 7 was severely limited by the potential of damage to the windowless EDS detector. Throughout the small number of experiments performed, a noticeable decrease in the input count rate of the detector was observed under subsequent measurements with identical beam conditions and as such, the experiments were immediately ceased.

The windowless detector used in these experiments is quite expensive and damage to the detector would require replacement of the entire detector unit. This is due to the inability to replace the PIN junction which forms the detector itself. A windowless EDS detector with a field replaceable PIN detector junction would help reduce the cost of operating such a system by replacing the PIN junction once damage has reached a certain level. No such detector currently exists. In addition, the detector used for these experiments was optimised for the impact of X-Rays and as such required energy correction for accurate spectral measurements. Creating a detector which is optimised and calibrated for the impact of protons would be highly beneficial for the accuracy of the backscattering spectroscopy technique.

8.2.5 Simultaneous Backscattering Spectroscopy and Doped Beam VLE-PIXE

Using a dedicated detectors for both X-Rays and BSIs could also open the possibility for simultaneous doped beam VLE-PIXE mapping and LEIS mapping utilising the method discussed above. In such a situation, the windowed X-Ray de-

tector could be utilised to capture characteristic X-Rays from the sample whilst blocking the BSIs from reaching the detector. The windowless LEIS detector could analyse the BSI energy, providing thickness information about the surface which cannot be achieved using X-Rays alone. This is possible due to the penetration of the protons into the surface which can provide “advance” information to the user about the thickness of the upcoming layer. An ulta-thin screen could be used prior to the windowless EDS detector in order to block heavy ions whilst still allowing the transmission of protons. Such a screen could be much thinner than a typical EDS detector window as it does not need to be vacuum tight owing to the fact that the detector would typically operate without a window anyway.

This method is shown schematically in figure 8.1.

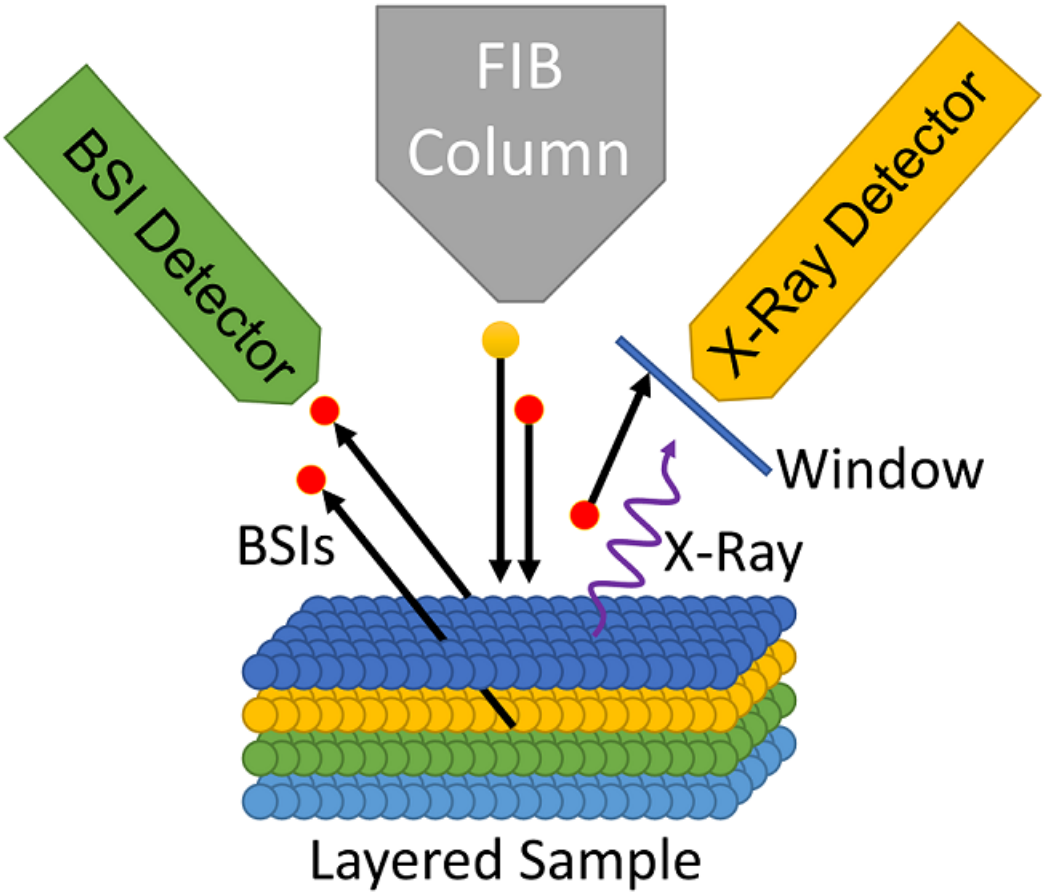

Figure 8.1: Schematic of simultaneous backscattering spectroscopy and doped beam VLE-PIXE

Appendix A

A.1 UHR Field Lorentz force

To understand how the charged particles in the FIB react to the UHR magnetic field, the Lorentz force equation can be used which describes the force applied to a moving, charged particle as it travels through an EM field [259]. The Lorentz force is calculated as:

$$\overrightarrow{F} = q(\overrightarrow{E} + v \times \overrightarrow{B}) \tag{A.1}$$

where F is the force imparted on a charged particle, q is the particle charge, E is the strength of the electric field, v is the particle velocity and B is the strength of the magnetic field. By analysing images of the particle impacts following interaction with the magnetic field of the magnetic immersion lens, it can be seen that the fields are aligned such that the magnetic field imparts a Lorentz force only in the X direction relative to the orientation of the FIB pole piece. For this reason, the force in the Y direction can be ignored. Additionally, there is no net electric field in the chamber and thus the E component can also be neglected.

When the cross product is calculated to resolve the force specifically in the X direction for equation A.1:

$$F_x = q(v_y B_z - v_z B_y) \tag{A.2}$$

It can be assumed that the vast majority of ions are positive and singly ionised [35], therefore the charge q = +1. As mentioned previously, the velocity in the y direction is negligible, and therefore v_y = 0. This simplifies equation A.2 to:

$$F_x = q(v_z B_y) = v_z B_y \tag{A.3}$$

As the Lorentz force is a product of a particle's velocity, this velocity can be calculated as a function of the particle's mass as it is accelerated through a potential such as the accelerating voltage of a focused ion beam column. This velocity can be derived from Newton's equations of motion [259]:

$$E_k = \frac{1}{2}mv^2 \tag{A.4}$$

$$q\ V_{acc} = E_k = \frac{1}{2}mv^2 \tag{A.5}$$

$$v = \sqrt{\frac{2qV_{acc}}{m}} \tag{A.6}$$

where v is the particle velocity, q is the particle charge, V_{acc} is the accelerating voltage and m is the particle mass [259]. Substituting equation A.6 into equation A.3:

$$F_x = \sqrt{\frac{2qV_{acc}}{m}} B_y \tag{A.7}$$

The work (W) done by a force (F) upon a body travelling over some displacement (d) is given by [260]:

$$W = F \cdot d \tag{A.8}$$

From equation A.3, the magnetic field produces a force in the X direction so combining and rearranging equations A.3 and A.8 gives the displacement in the x direction (d_x) imparted by the Lorentz force:

$$d_x = W / \left(\sqrt{\frac{2qV_{acc}}{m}} B_y \right) \tag{A.9}$$

A.2 Current Measuring Devices

A.2.1 Standard Faraday Cup

The current of a charged particle beam is typically measured using a device known as a Faraday cup. This device, shown in figure A.1 comprises of a deep hole drilled into a conductive stub with a small aperture covering the top of the hole. The beam is directed down the aperture which also prevents secondary electrons or ions from escaping the hole, thus collecting the entire beam current. When a charged particle from a beam impacts a surface, it creates a localised charge at the surface which is then neutralised by a positive or negative current flowing from ground. When an ammeter is placed between the device and ground, this ”compensation” current can be measured and the current of the incident charged particle beam can be determined.

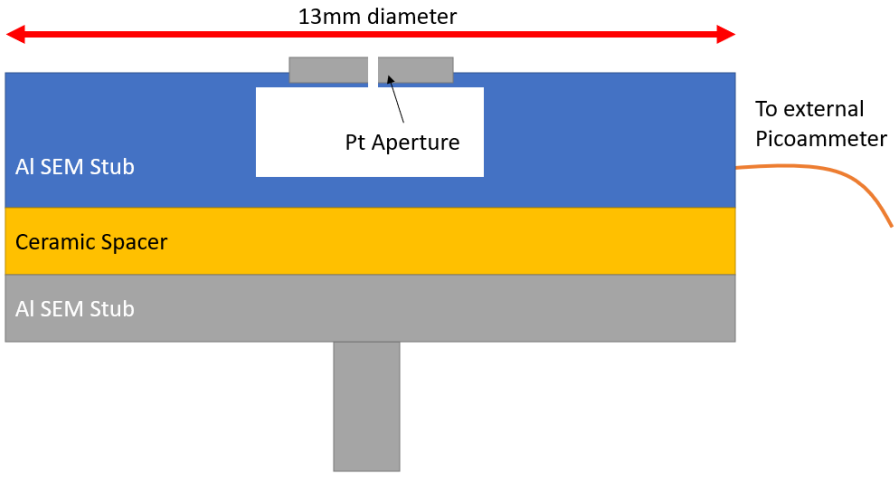

Figure A.1: A schematic of a standard Faraday cup.

The total compensation current flowing from ground through the Faraday cup can be decomposed into several components:

$$I_{total} = I_P - (I_{SE} - I_{SI+} - I'_{SE} + I'_{SI+}) \tag{A.10}$$

where I_{total} is the current measured flowing from ground, I_P is the primary beam current, I_{SE} and I_{SI+} are the secondary electrons and secondary ions emitted from the surface, and I'_{SE} and I'_{SI+} are the secondary electrons and secondary ions recollected by the same surface potential. In the case of a standard Faraday cup, due to the small aperture size, the number of secondary electrons and ions

lost from the cup are negligible and thus the number of secondary electrons and ions recollected by the cup are equal to those emitted by the cup, therefore:

$$(I_{SE} - I_{SI+} - I'_{SE} + I'_{SI+}) = 0 \tag{A.11}$$

Equation A.10 then simplifies to:

$$I_{total} = I_P \tag{A.12}$$

The current measured between the Faraday cup and ground is therefore equal to the primary beam current.

The Faraday cup shown in figure A.1 has been modified such that the current measurement is decoupled from the microscope's internal current measurement system and instead utilises an external picoammeter with a greater accuracy, ease of exporting data, and the reduced complication of systems such as the internal touch alarm which forms part of the microscope's current measurement system. This so called "standard" Faraday cup is utilised in experiments where a simple readout of the beam current is required.

A.2.2 Isolating Faraday Cup

Utilising the standard Faraday cup as discussed above, any particles hitting the top surface of the cup are also capable of producing a compensation current. For the purpose of measuring the individual beam components as outlined in section 2.2.1, this means that the standard cup is inappropriate for such a measurement and an alternate design must be used. This alternate device is called an isolating Faraday cup and is named due to the isolation of the top surface and the body of the Faraday cup.

The working principle of the isolating Faraday cup is shown in figure A.2 where the compensation current produced by the beam components hitting the top surface will flow directly to ground. Only the component which enters the aperture will be collected by the cup. Similar designs have been previously implemented for the measurement of the shape of ion beams [261].

Several design iterations were considered before settling on the double-aperture type design shown in figure A.3, resulting in the final device assembly shown in figure A.4. This design has several features which have been implemented to

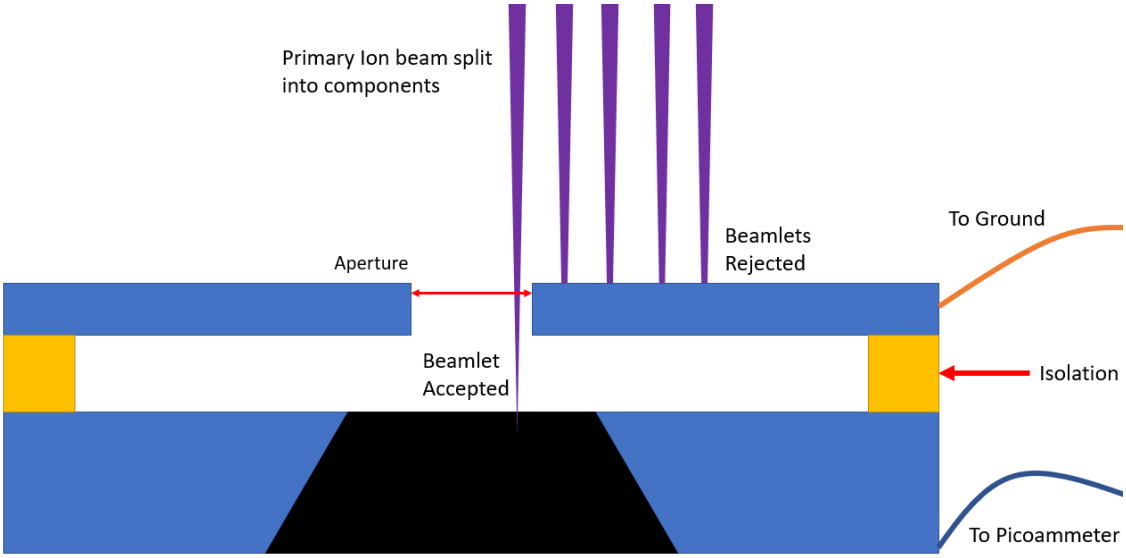

Figure A.2: The working principle of an isolating Faraday cup.

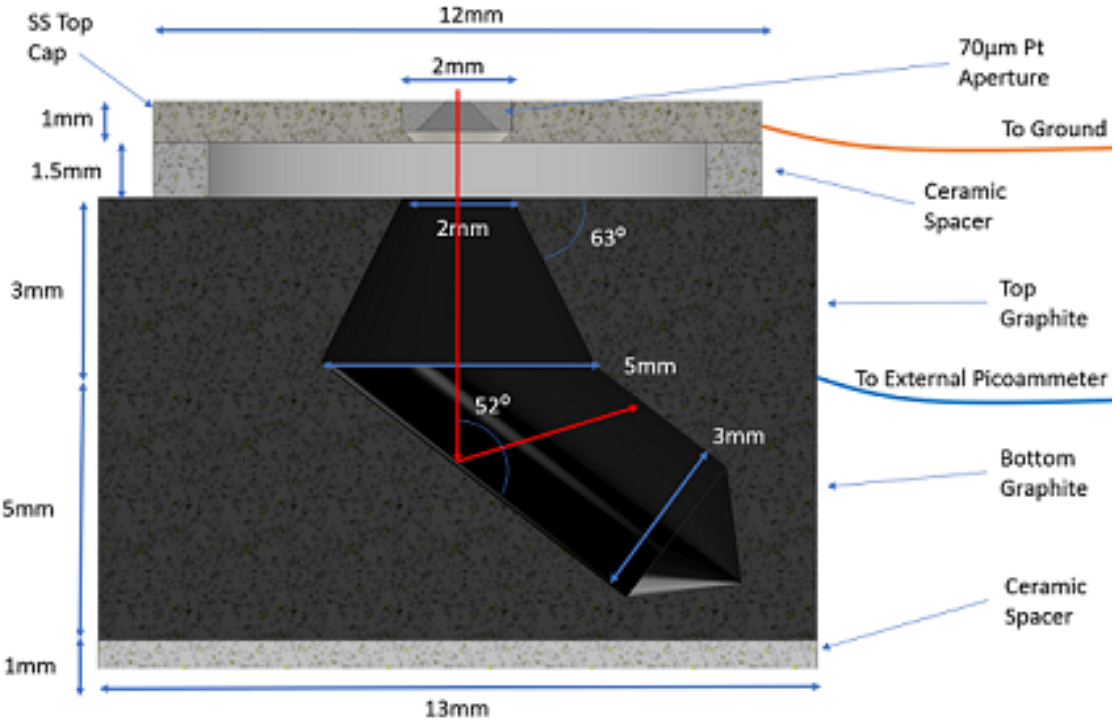

Figure A.3: Schematic drawing of the isolating Faraday cup design.

enhance the collection efficiency and accuracy of this device such as the angled ion trap in the body of the Faraday cup to direct ions towards the internal walls of the device rather than up towards the open face of the lower aperture.

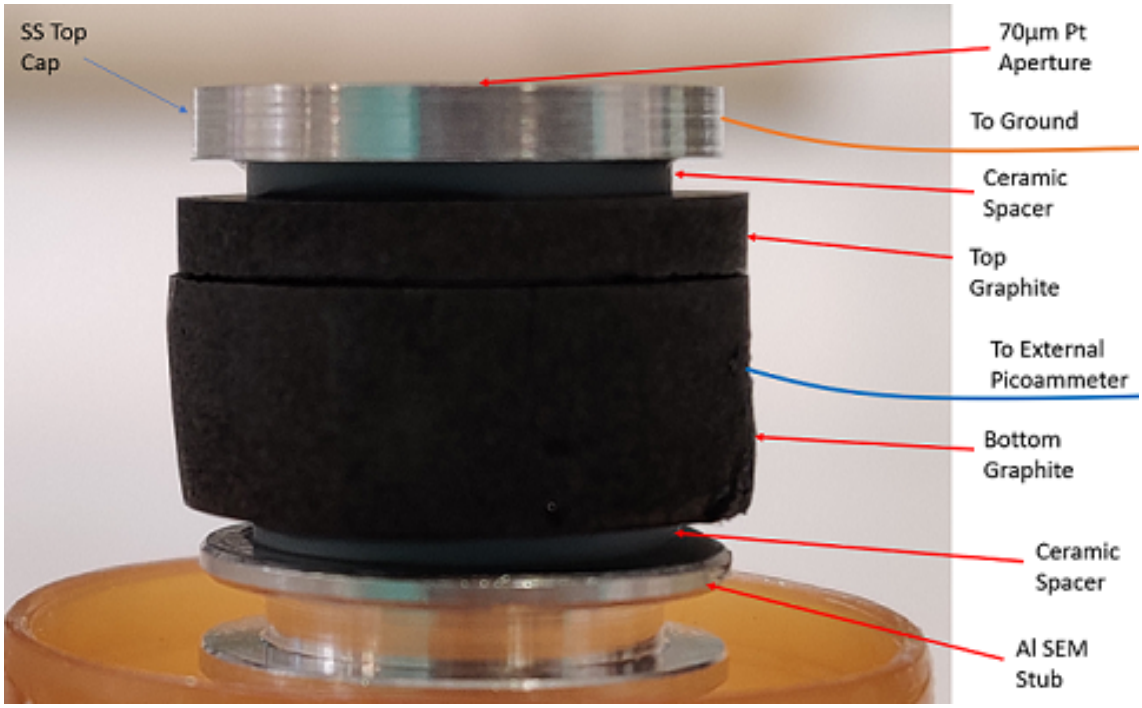

Figure A.4: The final assembly of the isolating Faraday cup device.

A.2.2.1 Isolating Faraday Cup Performance

In order to provide accurate measurements of the compensation current, the Faraday cup was connected to an external Keithley 617 electrometer via an isolated vacuum feedthrough located on the rear of the SEM chamber. The top surface of the isolating Faraday cup and aperture was grounded directly to the SEM chamber wall and affixed with Kapton tape. A schematic of the isolating Faraday cup electrical setup is shown in figure A.5.

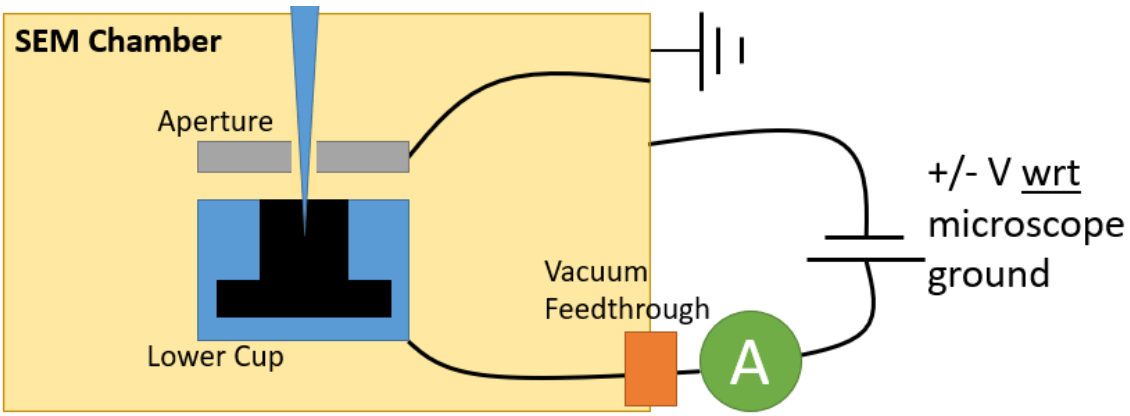

Figure A.5: A schematic of the isolating Faraday cup electrical setup.

To ensure that the beam was not hitting the inside surface of the cup, the beam was dwelled at several points inside the aperture and the current monitored to determine any current decrease resulting from collision with the side walls. The

beam was also alternately dwelled off the side of the aperture to determine the isolation efficiency of the top surface to the Faraday cup. This is demonstrated schematically in figure A.6a.

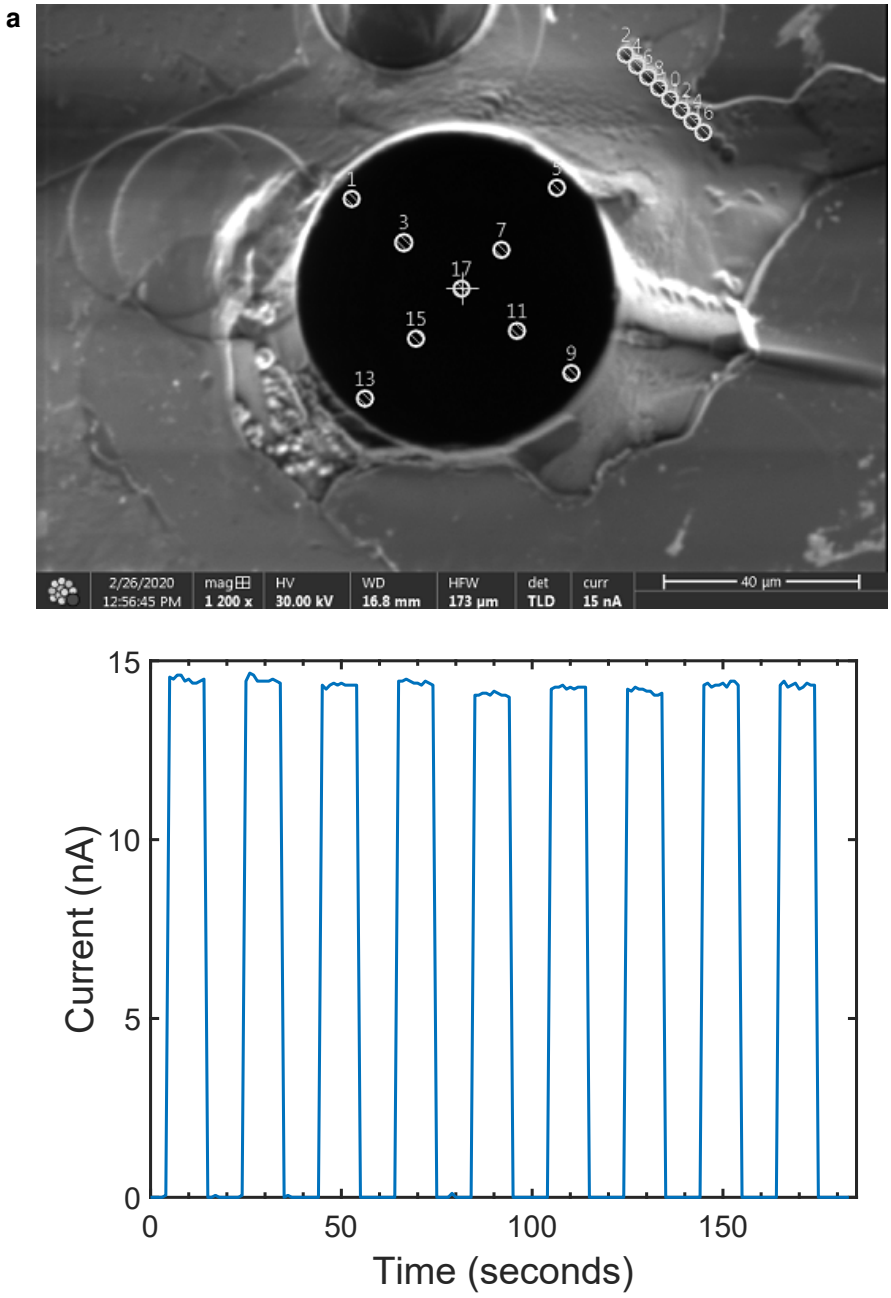

Figure A.6: Faraday cup performance verification experiments. (a) The scan pattern used to determine the side-wall collision and isolation efficiency, (b) The current measurement from the Faraday cup during the performance scan.

The results of this experiment are shown in figure A.6b where the beam does not hit the inside of the cup at any point in the scan, demonstrating that the cup can be effectively used for the desired current measurements.

A.2.3 Beam Scanning Method

In order to measure the individual components of the ion beam, the separated beam must be scanned across the face of the isolating Faraday cup. This was achieved by use of the microscope's in-built scanning pattern generator. A scan box was drawn across the aperture with a dimension in the Y-direction of less than the beam width, approximately 100nm, and with a dimension in the X-direction twice the width of the separated beam width so as to capture all the beam components.

The beam dwell time was set to the maximum permissible by the scanning software at 25ms and the scan overlap was adjusted to increase the scanning time to around 15-20 minutes per scan. Such a slow scan was necessary due to the relatively low speed of the picoammeter compared to the beam scanning and allowed the integration of multiple current values per pixel. This was especially important for low current peaks. The scanning method is shown schematically in figure A.7.

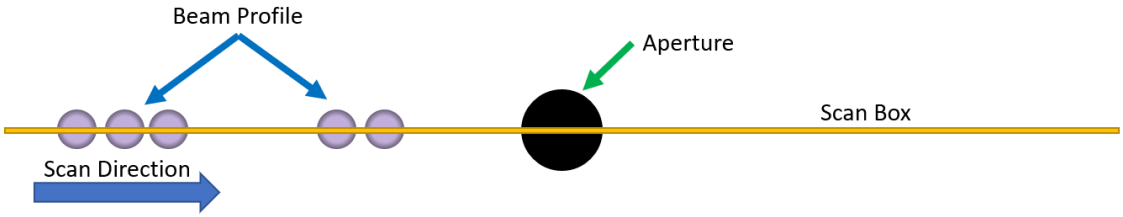

Figure A.7: Schematic of the scanning method used to acquire spectra.

An additional method was trialled where the beam remained fixed and the Faraday cup was programmatically moved in small steps below the beam. This was carried out due to concerns about the deviation of the beam separation as it passed through the varying UHR magnetic field, leading to possible mis-identification of beam component peaks. Figure A.8 shows the scan of an H^+ peak, demonstrating the difference in spectra between the stage and beam scanning methods. In the stage scanning spectrum, a significant amount of noise can be seen due to the activation and deactivation of the stage motor relay between stage movements. This noise, combined with the significantly reduced scanning step-size for the stage of 500nm compared to the beam scanning method of 10nm, and the minimum stage settling time of 1 second, rendered the stage scanning technique to be inferior compared to the beam scanning technique. Small spikes in the measured current were also observed when utilising the beam scanning method as shown in figure A.8. The source of this noise is likely attributed to improper electrical connections throughout the measurement circuit or electronic noise within the picoammeter itself. This noise did not significantly influence the measured

spectra.

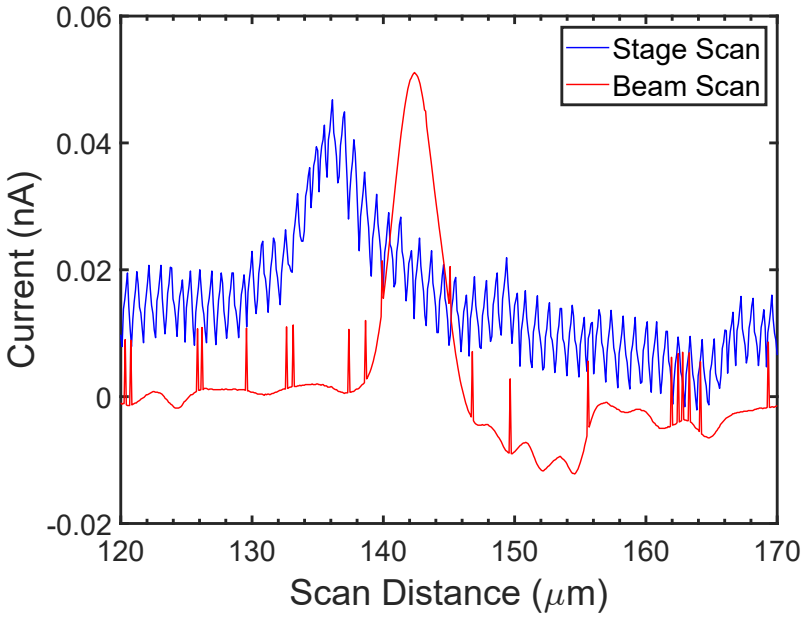

Figure A.8: Beamlet compositional current scan of an H^+ peak demonstrating the difference in the stage and beam scanning methods.

A.3 Xe Scattering Spot Burn

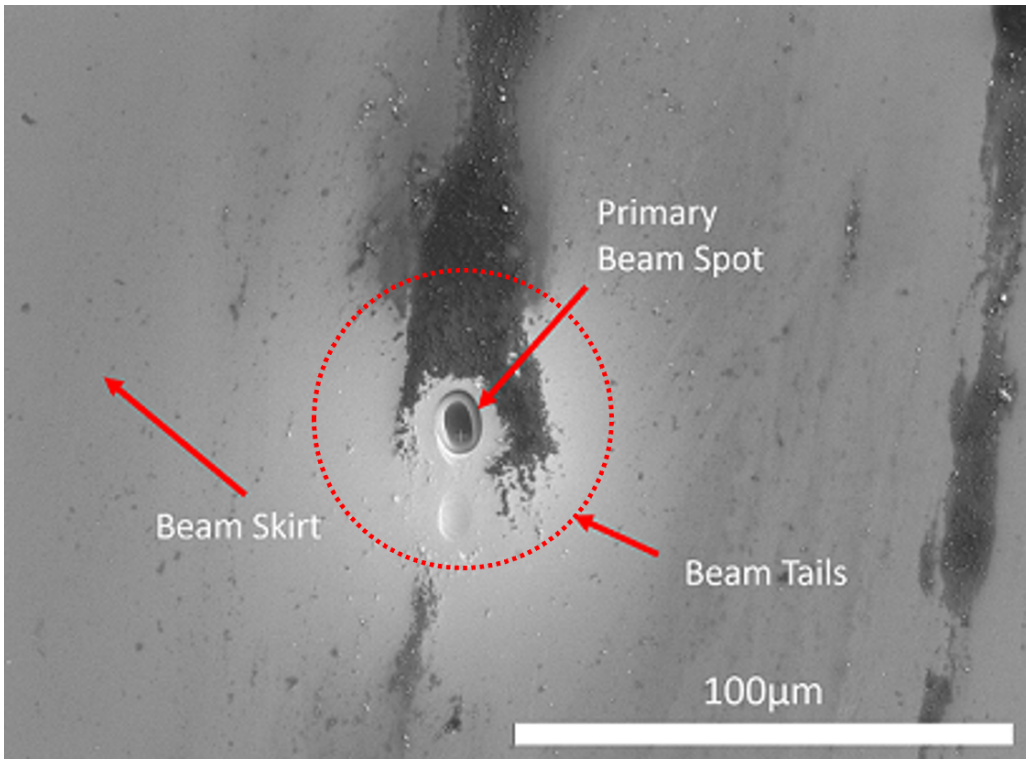

Figure A.9: Spot burn of a 2nA, 2keV Xe beam taken during chamber pump-down used to determine the size of the primary beam spot, beam tails and beam skirt.

A.4 NIST SRM EDS Characterisation

a

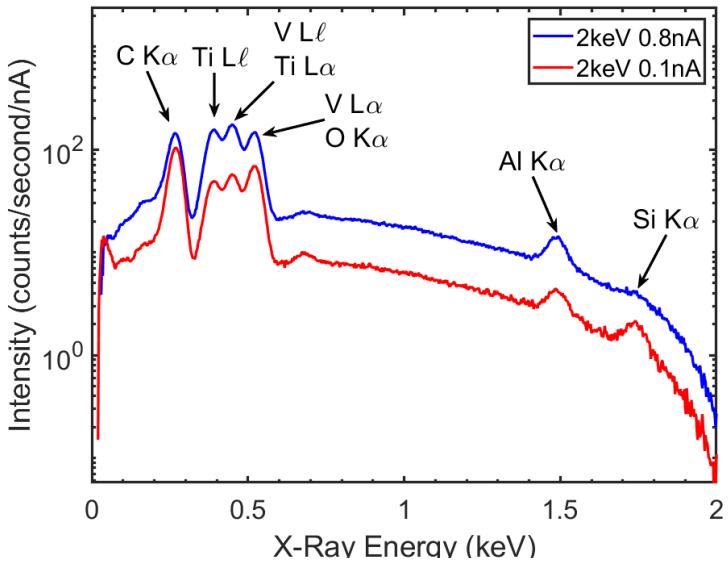

b

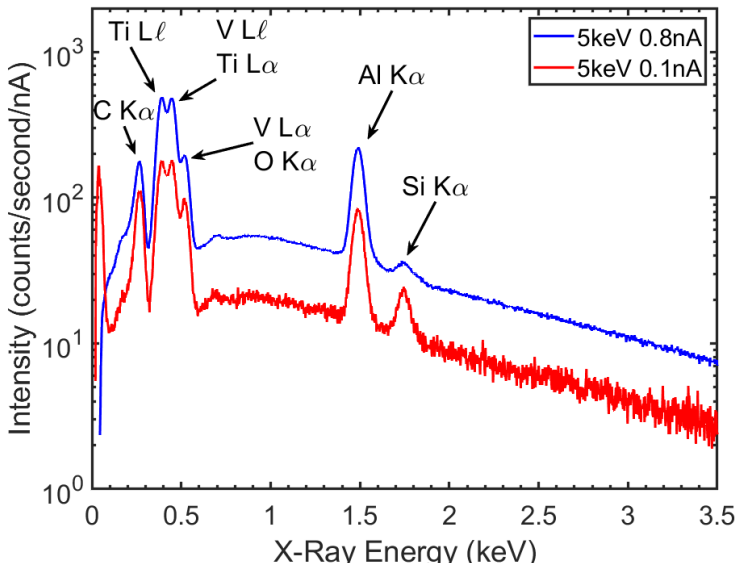

c

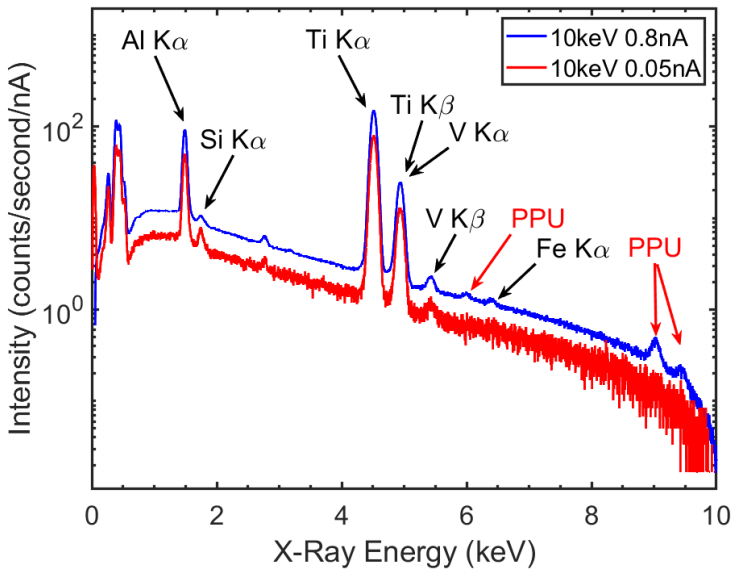

d

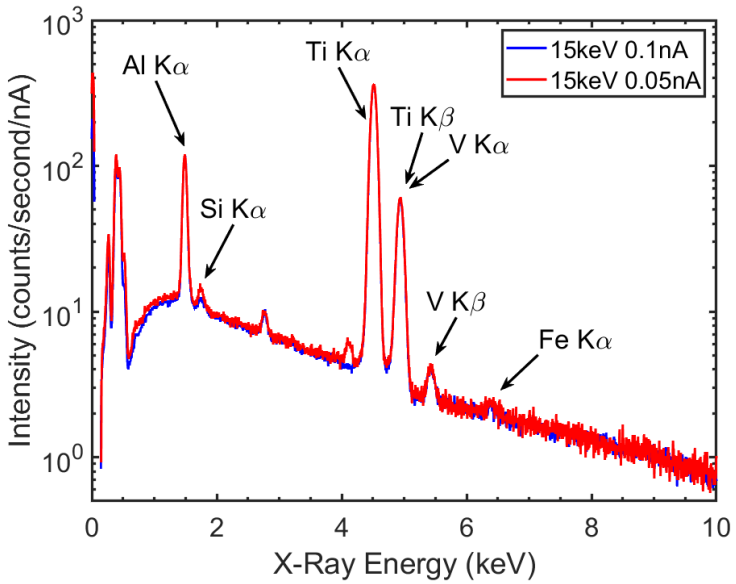
15keV 0.1nA
15keV 0.05nA
Al Kα
Si Kα
Ti Kα
Ti Kβ
V Kα
V Kβ
Fe Kα
Intensity (counts/second/nA)
X-Ray Energy (keV)

e

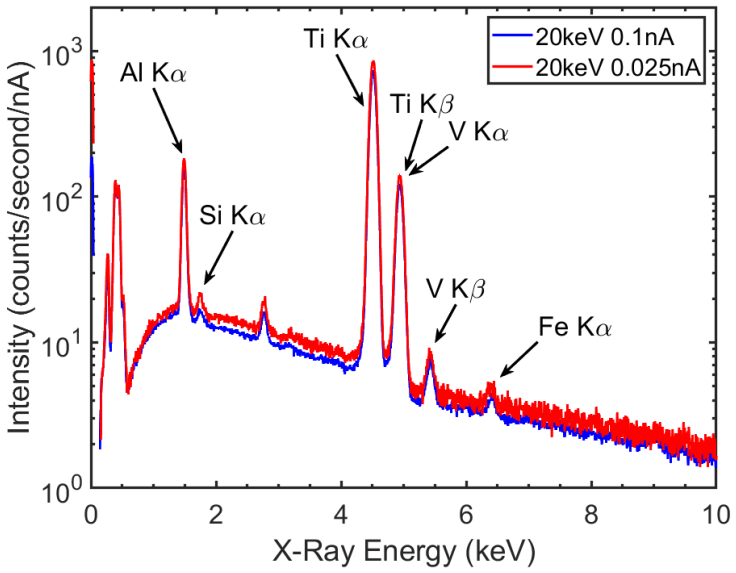
20keV 0.1nA
20keV 0.025nA
Al Kα
Si Kα
Ti Kα
Ti Kβ
V Kα
V Kβ
Fe Kα
Intensity (counts/second/nA)
X-Ray Energy (keV)

f

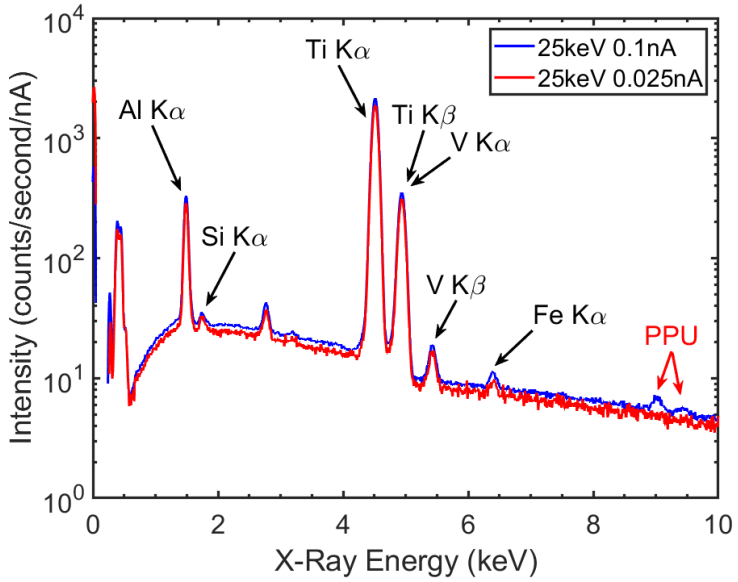
25keV 0.1nA
25keV 0.025nA
Al Kα
Si Kα
Ti Kα
Ti Kβ
V Kα
V Kβ
Fe Kα
PPU
Intensity (counts/second/nA)
X-Ray Energy (keV)

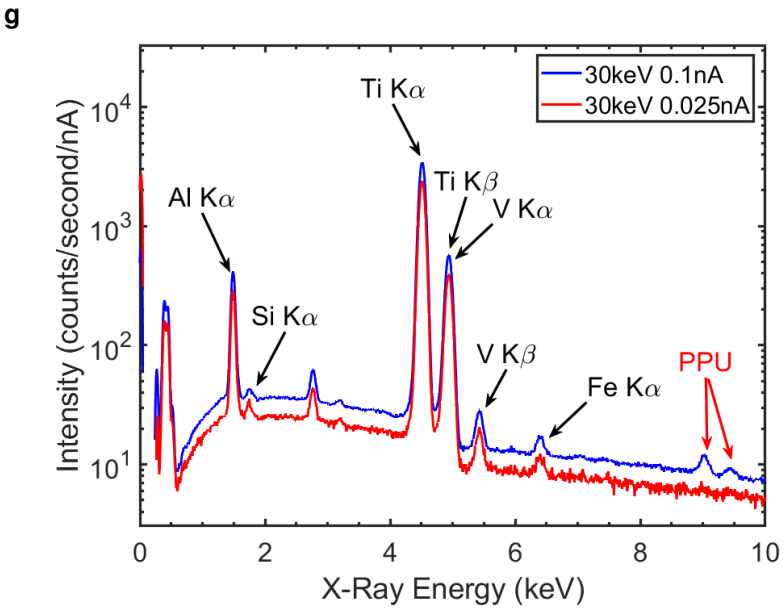

Figure A.10: EDS spectra of NIST SRM 654b (a - g) 2, 5, 10, 15, 20, 25, 30keV

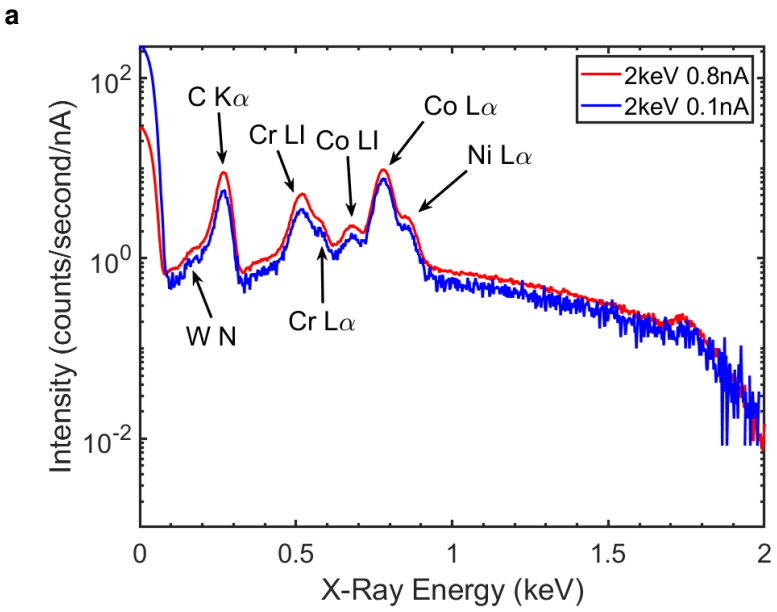

b

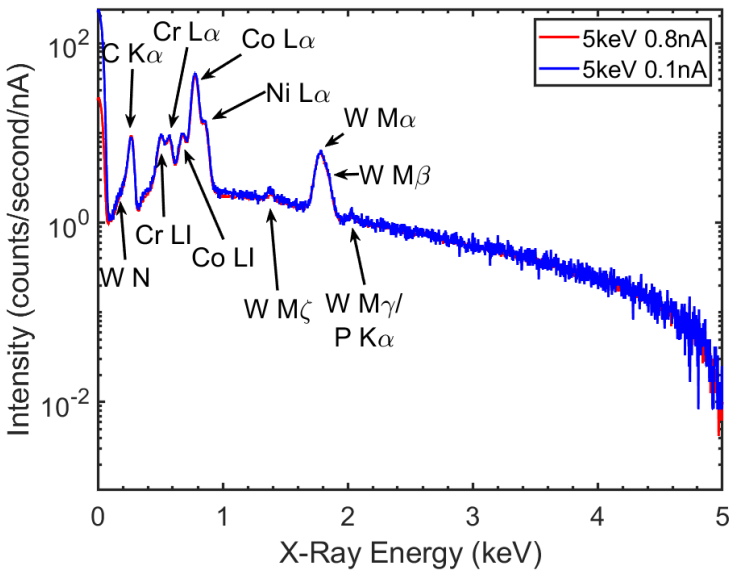
5keV 0.8nA
5keV 0.1nA
C Kα
Cr Lα
Co Lα
Ni Lα
W Mα
W Mβ
W N
Cr LI
Co LI
W Mζ
W Mγ/
P Kα
Intensity (counts/second/nA)
X-Ray Energy (keV)

c

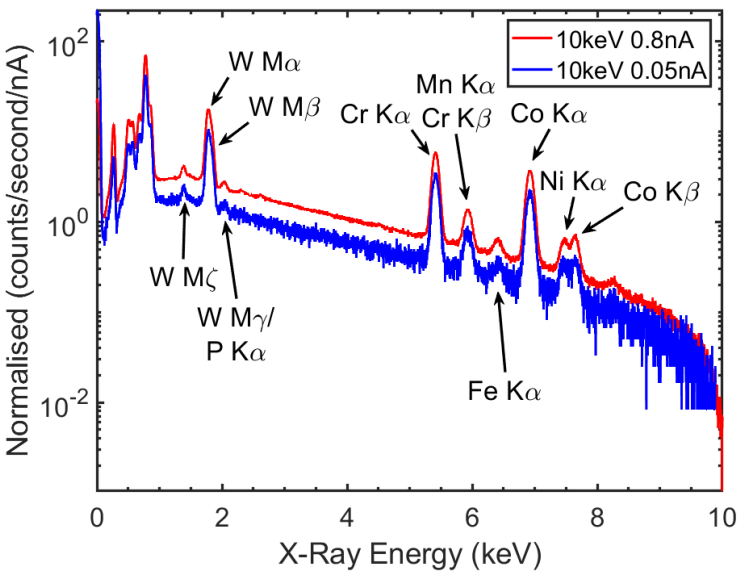
10keV 0.8nA
10keV 0.05nA
W Mα
W Mβ
Mn Kα
Cr Kα
Cr Kβ
Co Kα
Ni Kα
Co Kβ
W Mζ
W Mγ/
P Kα
Fe Kα
Normalised (counts/second/nA)
X-Ray Energy (keV)

d

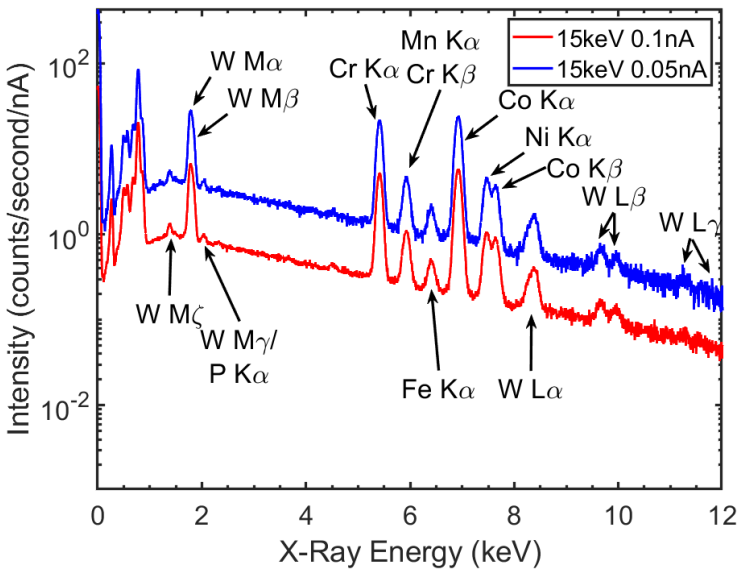
15keV 0.1nA
15keV 0.05nA
W Mα
W Mβ
Mn Kα
Cr Kα
Cr Kβ
Co Kα
Ni Kα
Co Kβ
W Lβ
W Lγ
W Mζ
W Mγ/
P Kα
Fe Kα
W Lα
Intensity (counts/second/nA)
X-Ray Energy (keV)

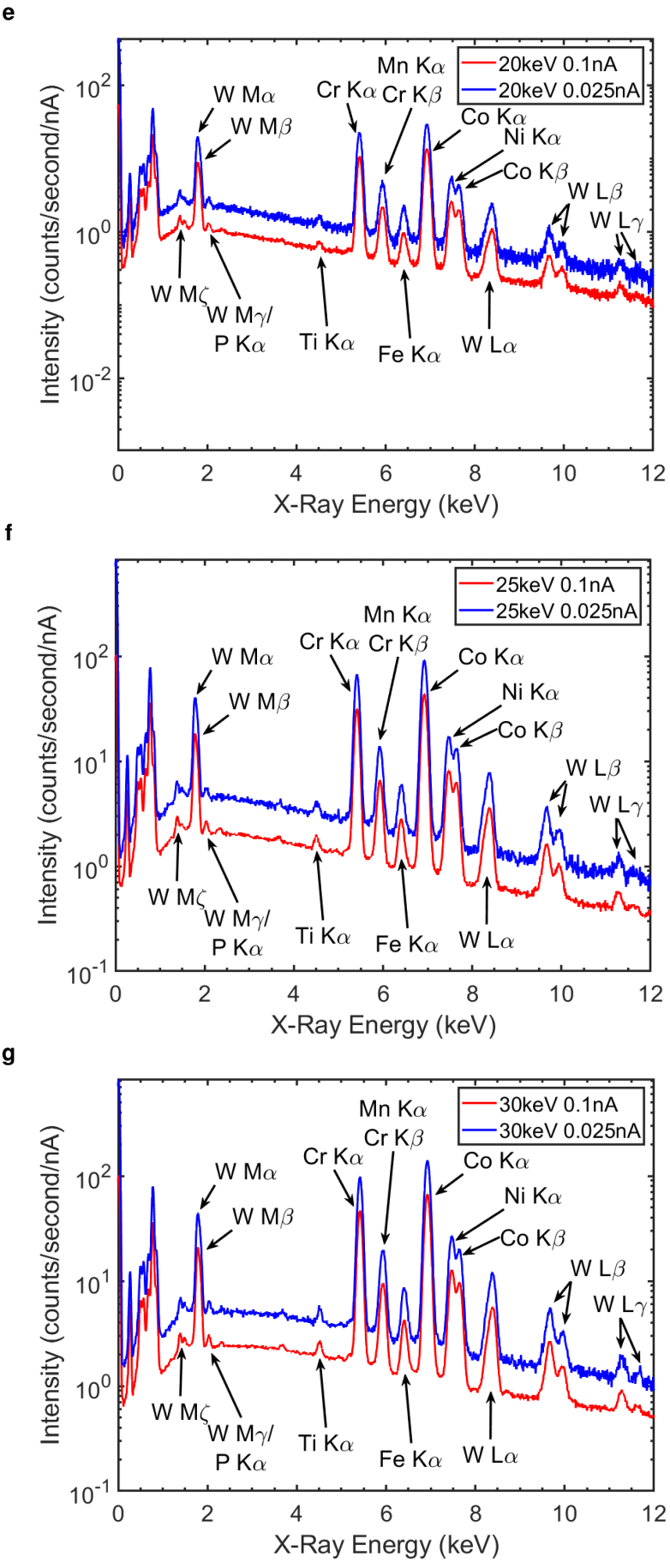

Figure A.11: EDS Spectra of NIST SRM 1242 (a - g) 2, 5, 10, 15, 20, 25, and 30keV

A.5 Beam Overlap Vs. Magnetic Field Strength

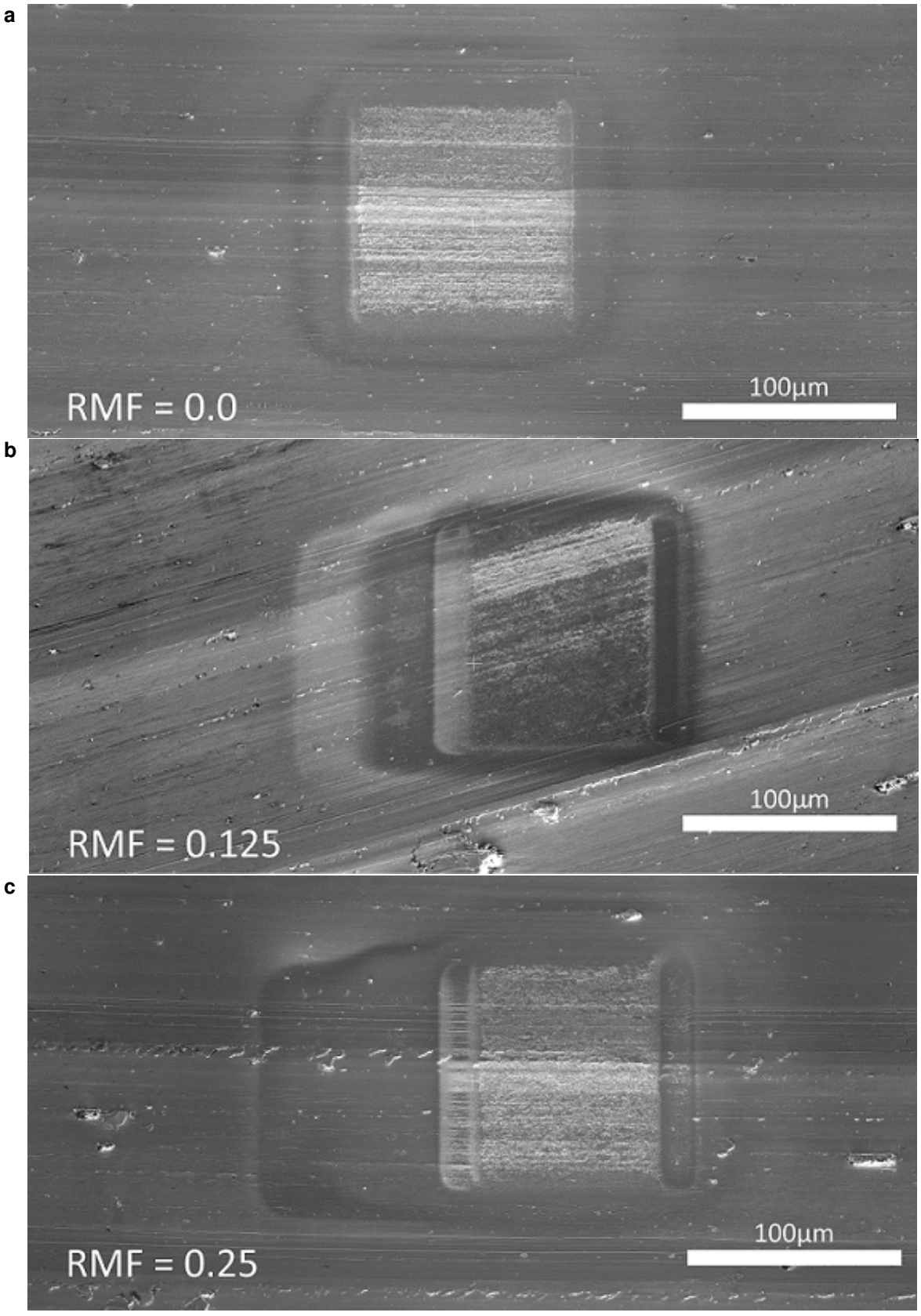

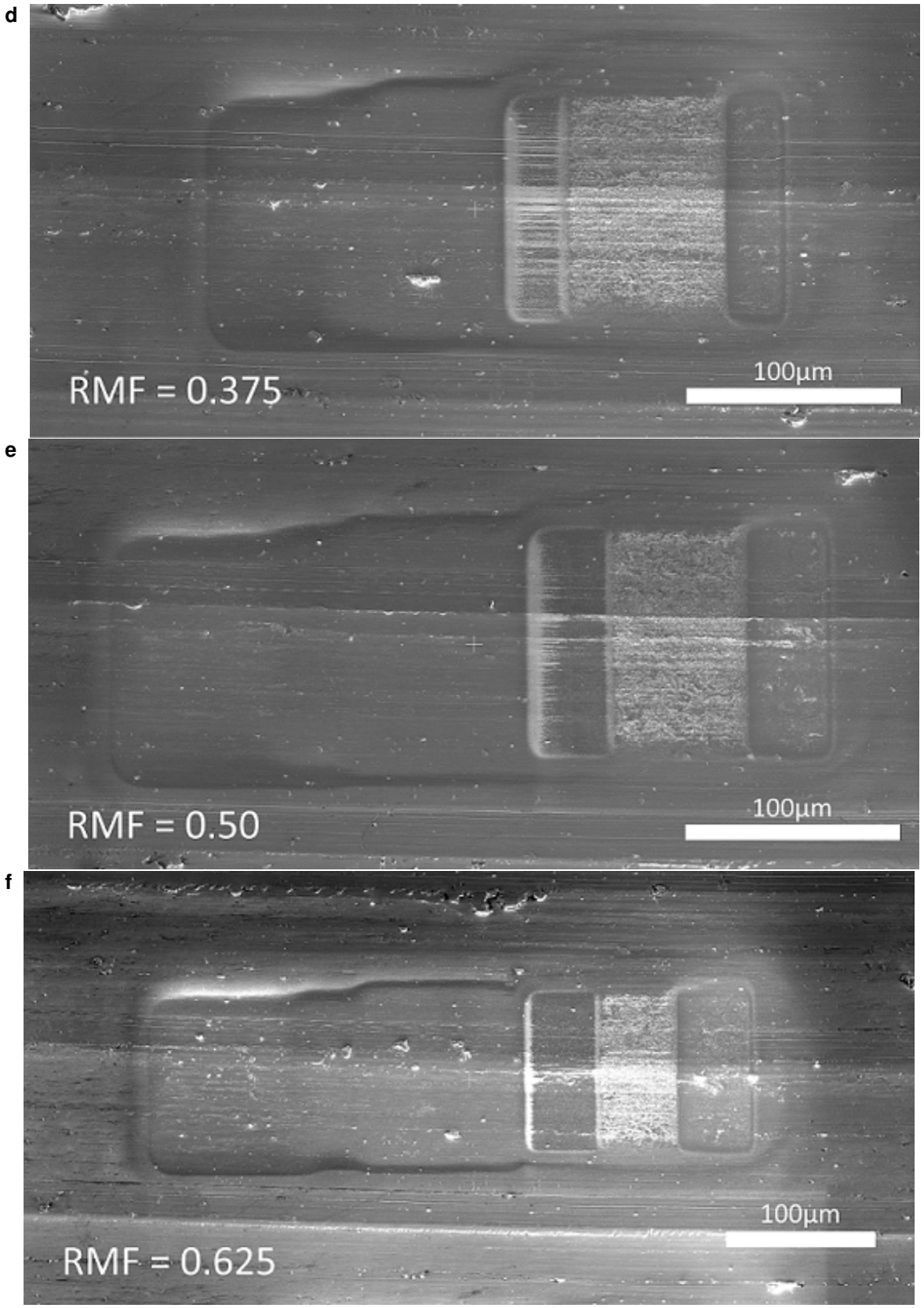
d
RMF = 0.375
100µm
e
RMF = 0.50
100µm
f
RMF = 0.625
100µm

g

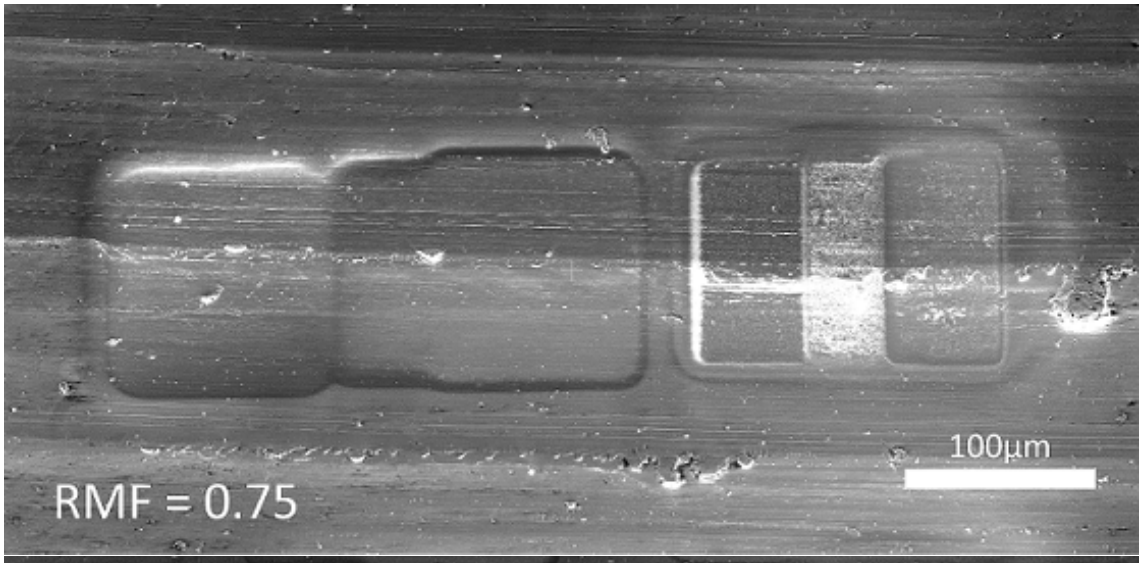

h

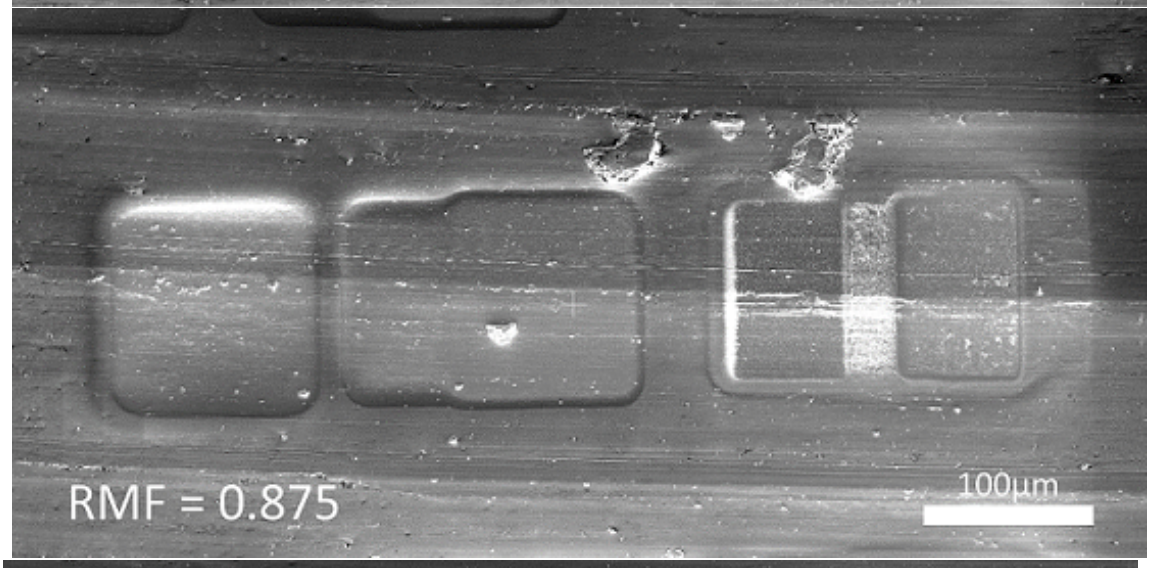

i

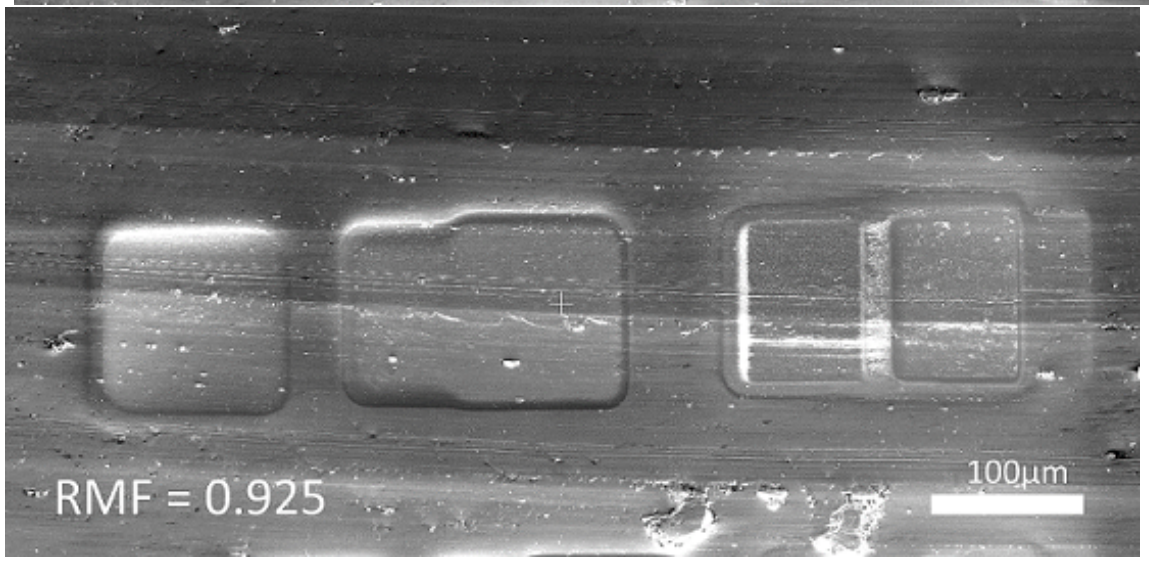

j

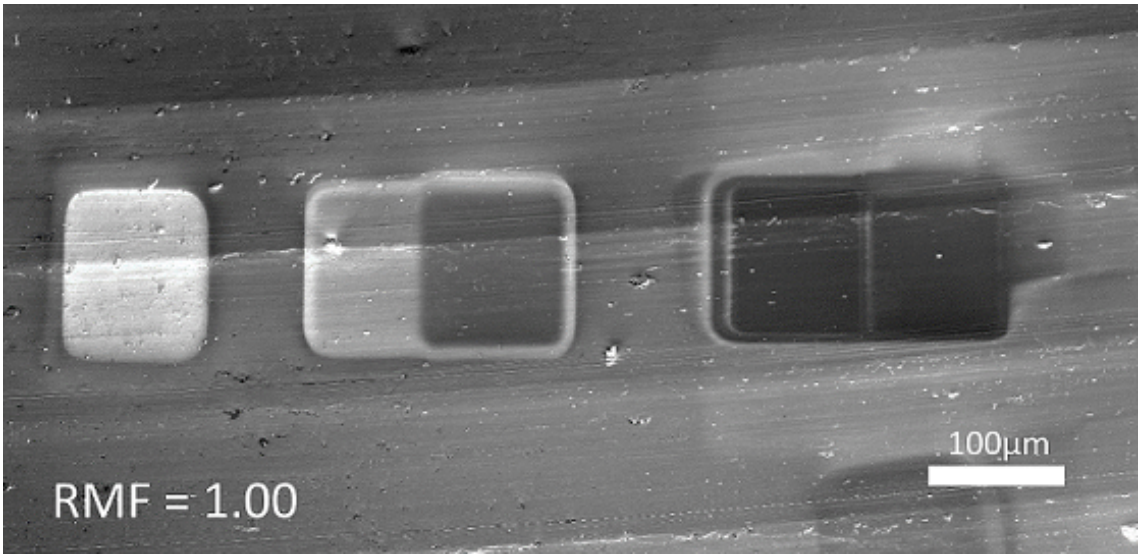

Figure A.12: (a-j) Images of irradiation spots vs relative magnetic field strength (RMF) with RMF marked on image.

A.6 Doped Beam Characterisation

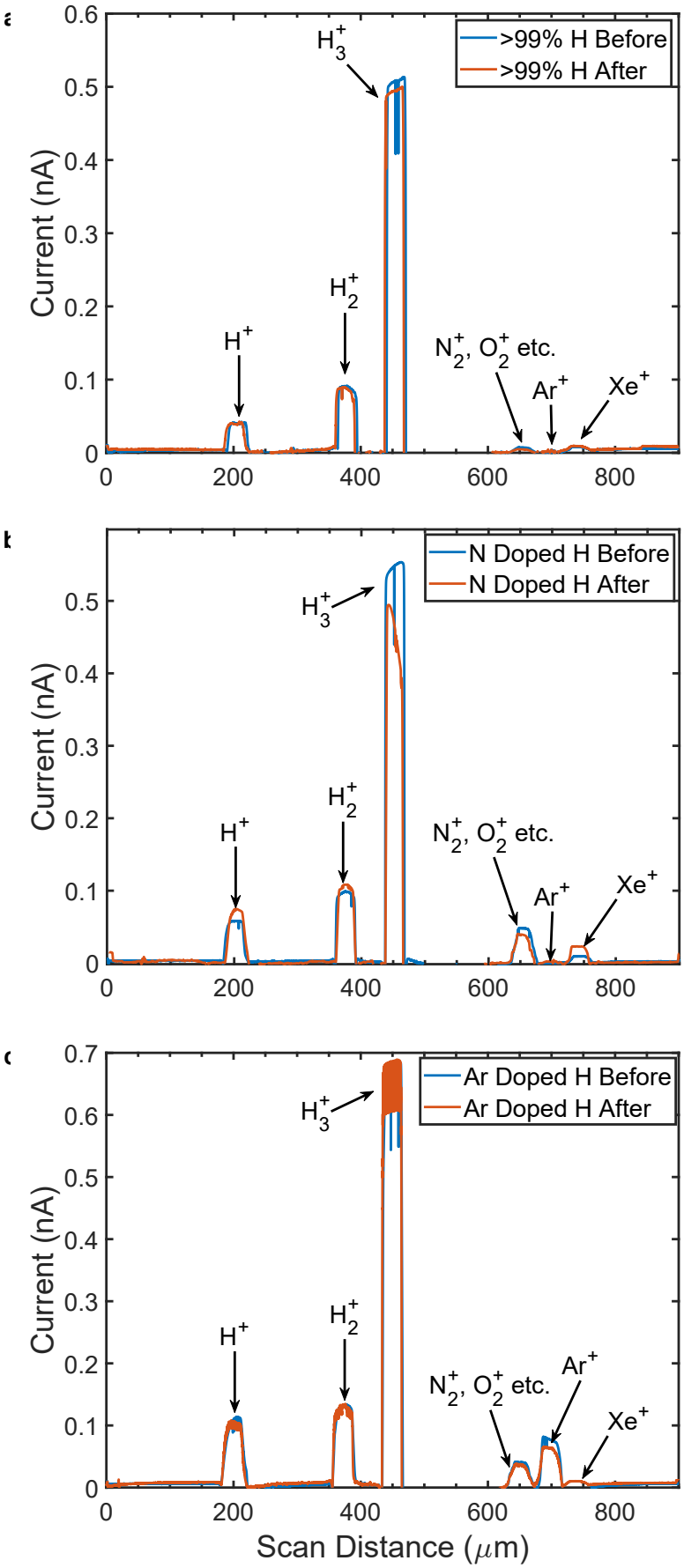

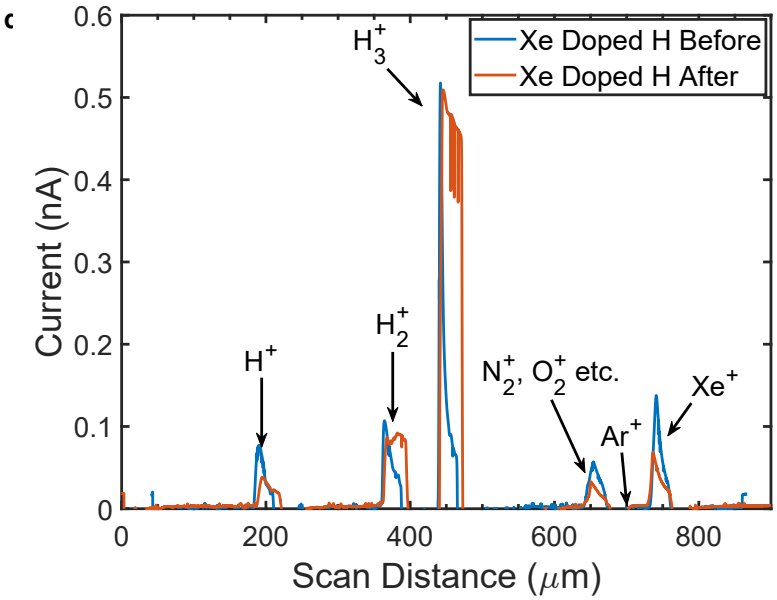

Figure A.13: Beam component currents before and after experimental exposures. (a) >99% hydrogen beam, (b) Nitrogen doped hydrogen beam, (c) Argon doped hydrogen beam, and (d) Xenon doped hydrogen beam

a

Species	Before (%)	After (%)
H^+	6.19	6.24
H_2^+	13.81	13.86
H_3^+	77.65	77.67
O_2^+, N_2^+ etc.	1.15	0.75
Ar^+	N/D	N/D
Xe^+	1.19	1.45

b

Species	Before (%)	After (%)
H^+	7.57	10.11
H_2^+	12.92	14.62
H_3^+	72.04	66.69
O_2^+, N_2^+ etc.	6.28	5.47
Ar^+	N/D	N/D
Xe^+	1.20	3.12

c

Species	Before (%)	After (%)
H^+	10.80	10.31
H_2^+	12.70	12.83
H_3^+	64.84	65.96
O_2^+, N_2^+ etc.	3.93	3.63
Ar^+	7.72	6.26
Xe^+	N/D	0.99

d

Species	Before (%)	After (%)
H^+	8.62	5.12
H_2^+	11.91	12.42
H_3^+	57.75	68.84
O_2^+, N_2^+ etc.	6.35	4.41
Ar^+	N/D	N/D
Xe^+	15.36	9.22

Figure A.14: Quantified beam component currents before and after experimental exposures (a) Clean hydrogen beam (b) Nitrogen contaminated hydrogen beam (c) Argon contaminated hydrogen beam (d) Xenon contaminated hydrogen beam

A.7 Pseudo-Voigt Peak Fits

a

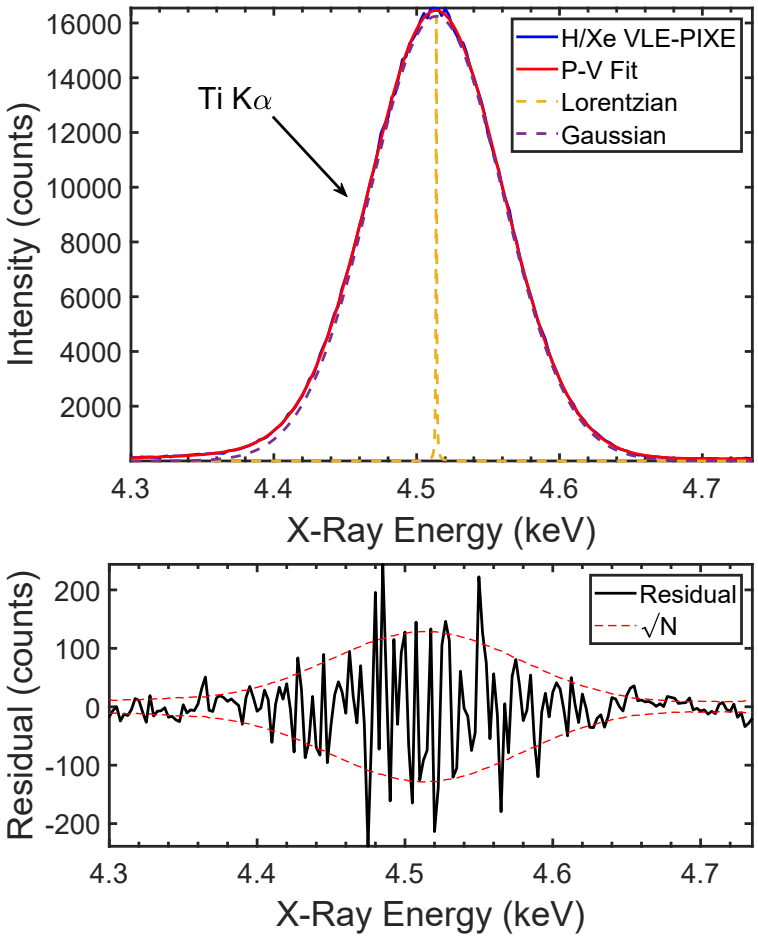

b

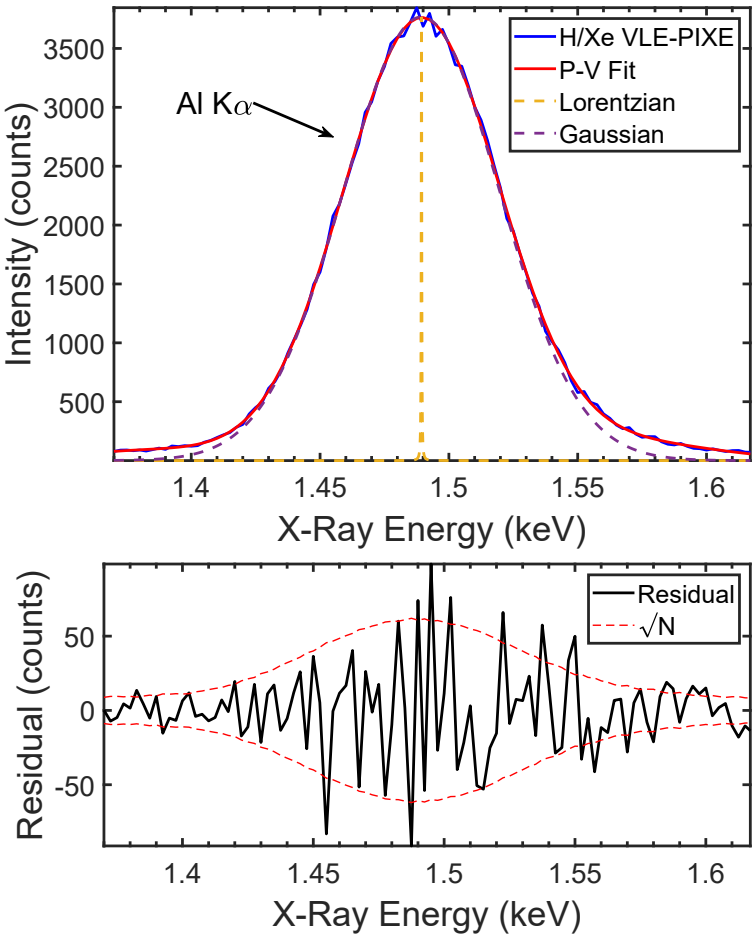
H/Xe VLE-PIXE
P-V Fit
Lorentzian
Gaussian
Al Kα
Intensity (counts)
X-Ray Energy (keV)
Residual
√N
Residual (counts)
X-Ray Energy (keV)

c

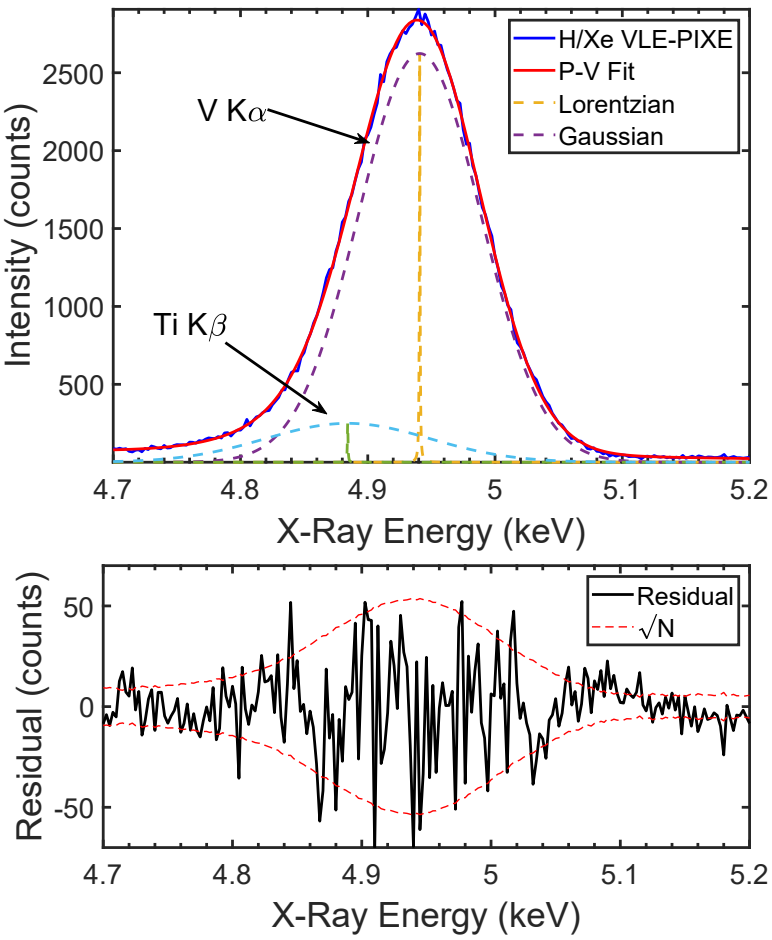
H/Xe VLE-PIXE
P-V Fit
Lorentzian
Gaussian
V Kα
Ti Kβ
Intensity (counts)
X-Ray Energy (keV)
Residual
√N
Residual (counts)
X-Ray Energy (keV)

d

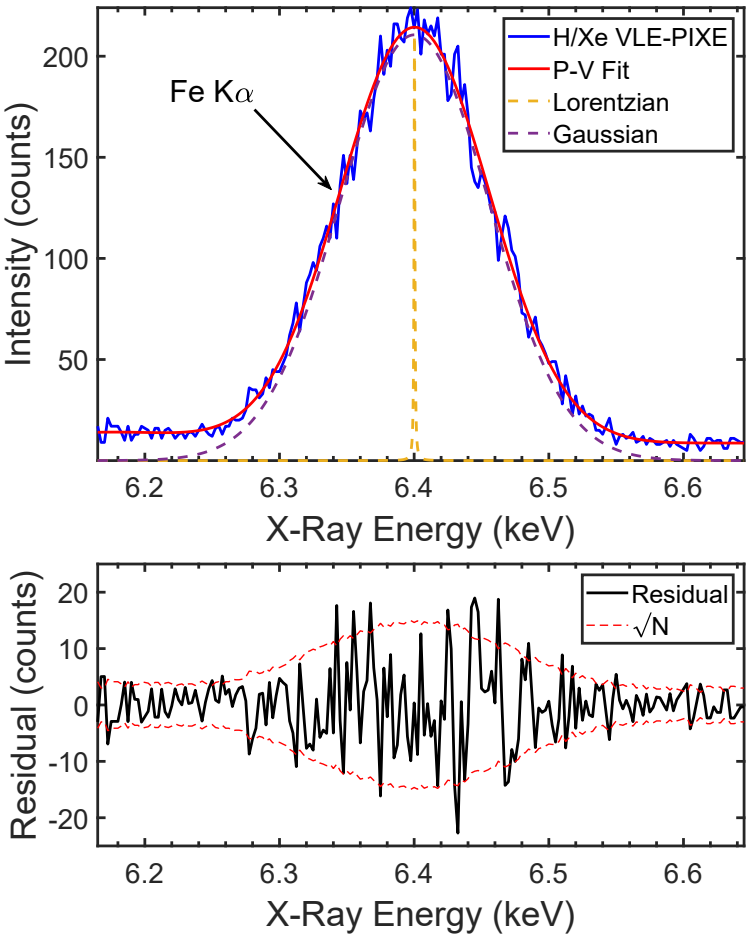
H/Xe VLE-PIXE
P-V Fit
Lorentzian
Gaussian
Fe Kα
Intensity (counts)
X-Ray Energy (keV)
Residual
√N
Residual (counts)
X-Ray Energy (keV)

e

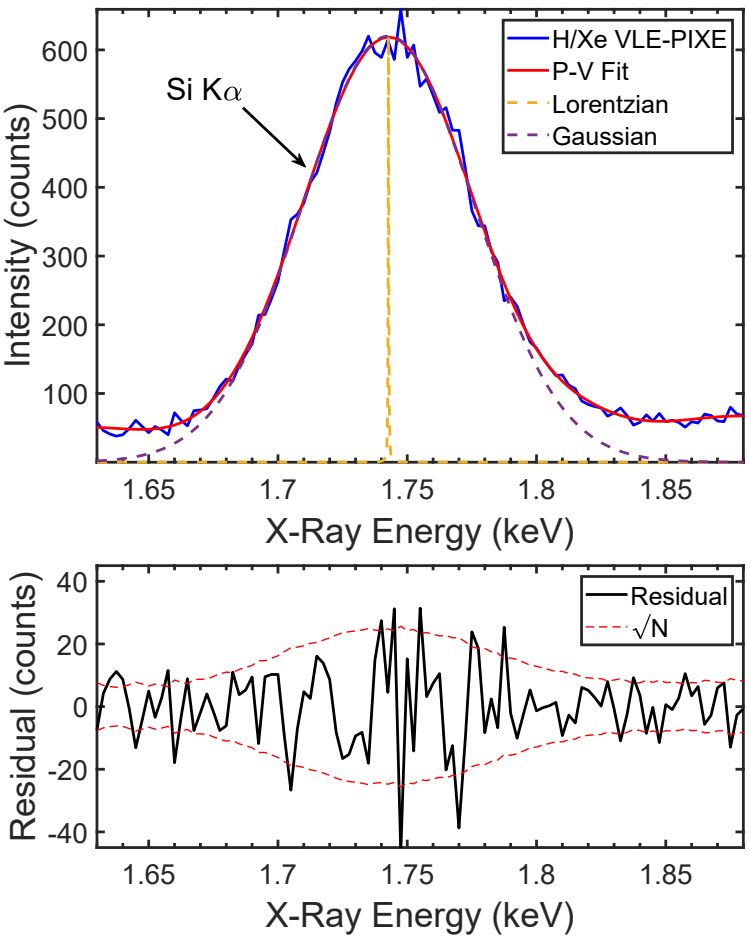
H/Xe VLE-PIXE
P-V Fit
Lorentzian
Gaussian
Si Kα
Intensity (counts)
X-Ray Energy (keV)
Residual
√N
Residual (counts)
X-Ray Energy (keV)

f

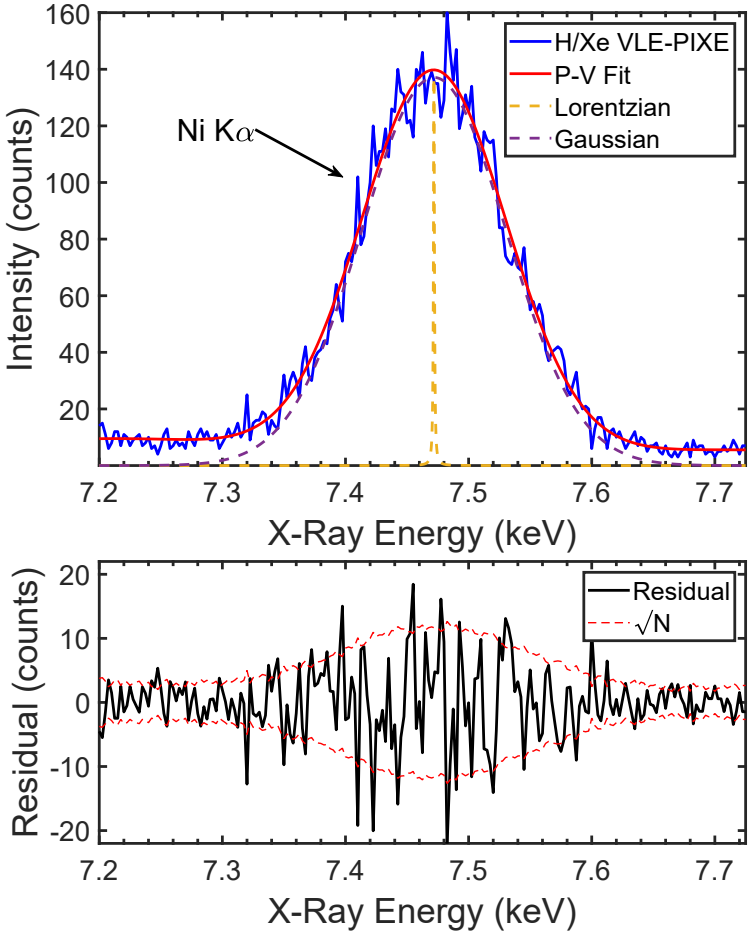
Intensity (counts)
160
140
120
100
80
60
40
20
Ni Kα
H/Xe VLE-PIXE
P-V Fit
Lorentzian
Gaussian
7.2
7.3
7.4
7.5
7.6
7.7
X-Ray Energy (keV)
Residual (counts)
20
10
0
-10
-20
Residual
√N
7.2
7.3
7.4
7.5
7.6
7.7
X-Ray Energy (keV)

g

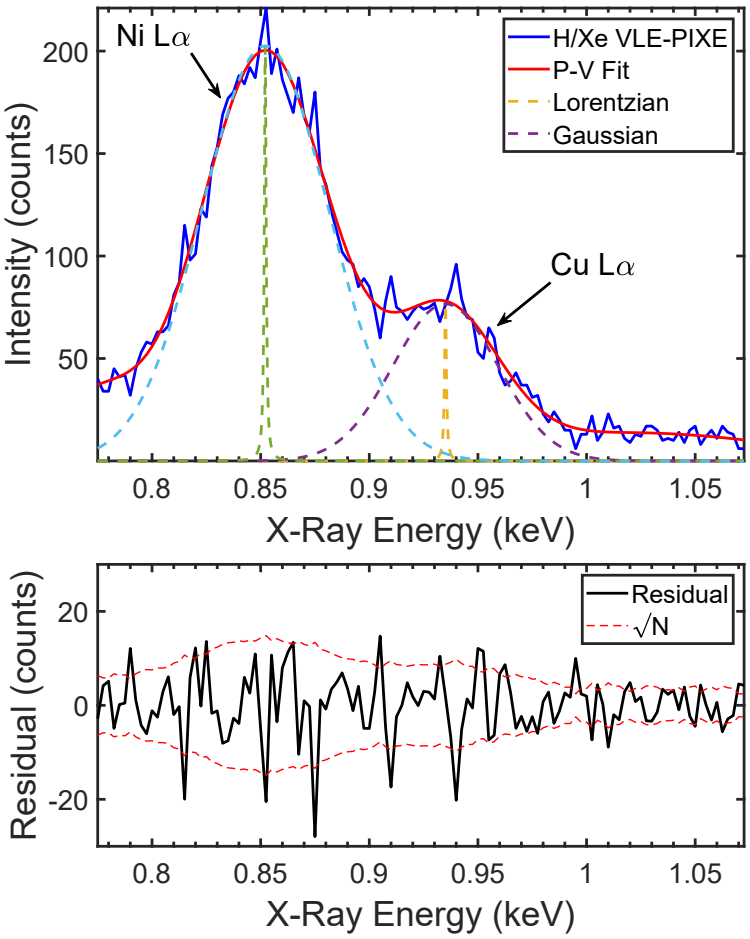

Figure A.15: Pseudo-Voigt fits for selected elements in the SRM 654b using a lightly doped H/Xe beam. The beam composition used is given in figure 4.1a. Lorentzian widths are fixed to natural linewidths as determined from [2].

a

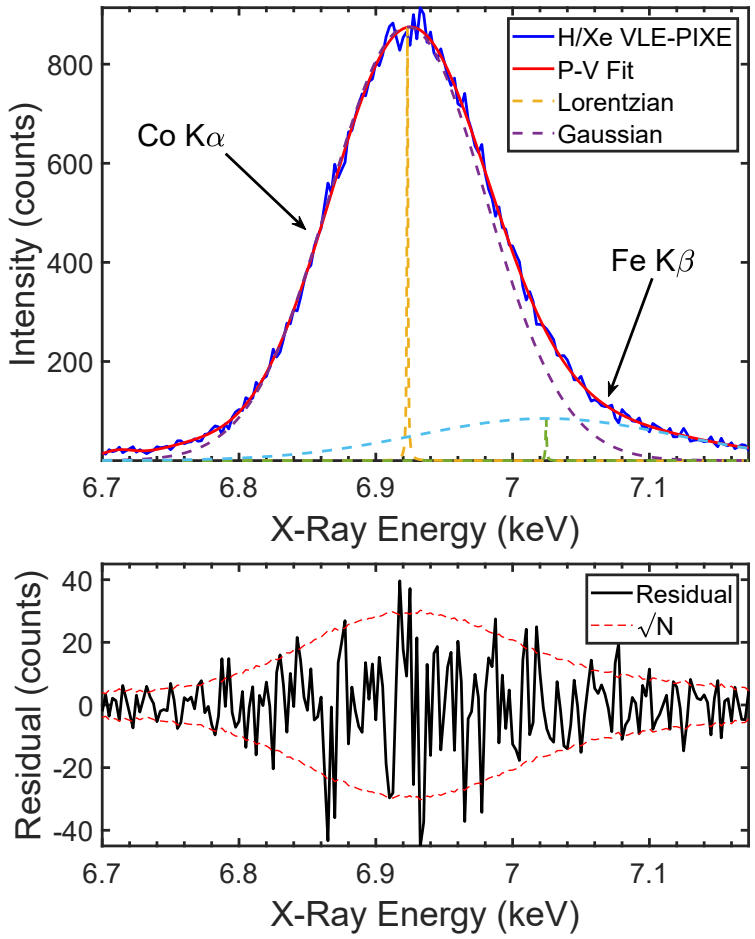
H/Xe VLE-PIXE
P-V Fit
Lorentzian
Gaussian
Co Kα
Fe Kβ
Intensity (counts)
X-Ray Energy (keV)
Residual
√N
Residual (counts)
X-Ray Energy (keV)

b

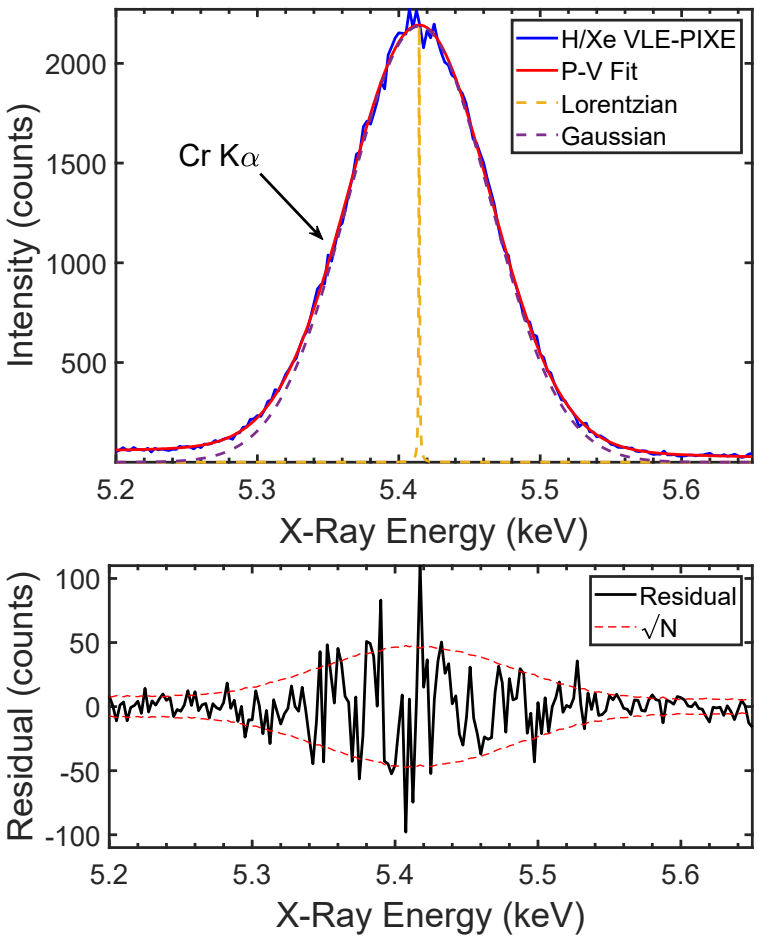
H/Xe VLE-PIXE
P-V Fit
Lorentzian
Gaussian
Cr Kα
Intensity (counts)
X-Ray Energy (keV)
Residual
√N
Residual (counts)
X-Ray Energy (keV)

c

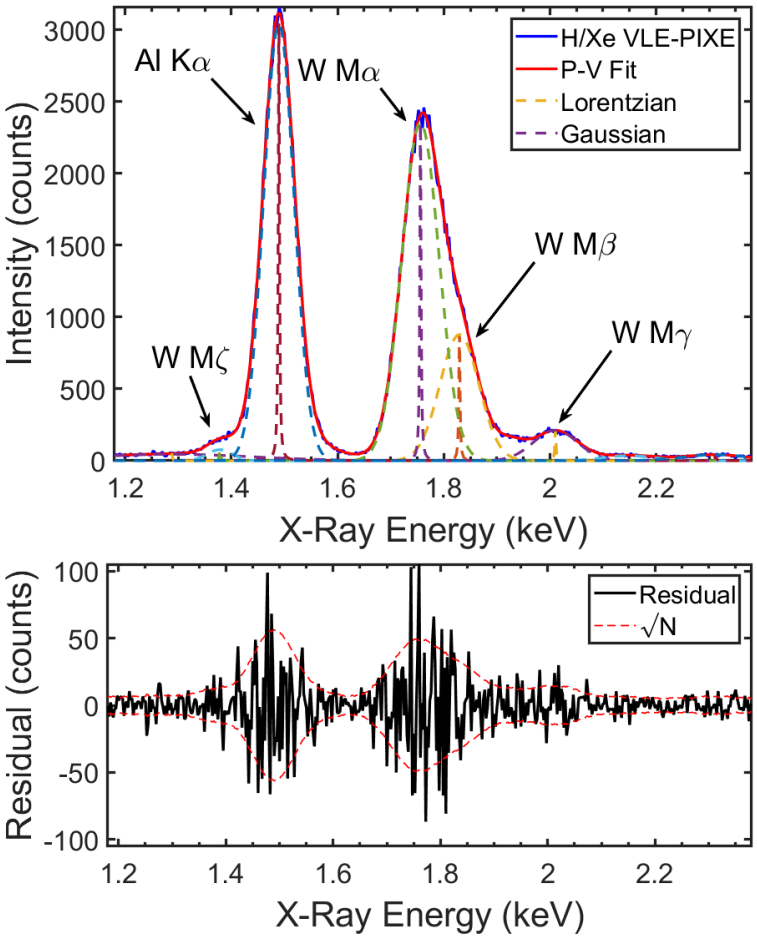
H/Xe VLE-PIXE
P-V Fit
Lorentzian
Gaussian
Al Kα
W Mα
W Mβ
W Mγ
W Mζ
Intensity (counts)
X-Ray Energy (keV)
Residual
√N
Residual (counts)
X-Ray Energy (keV)

d

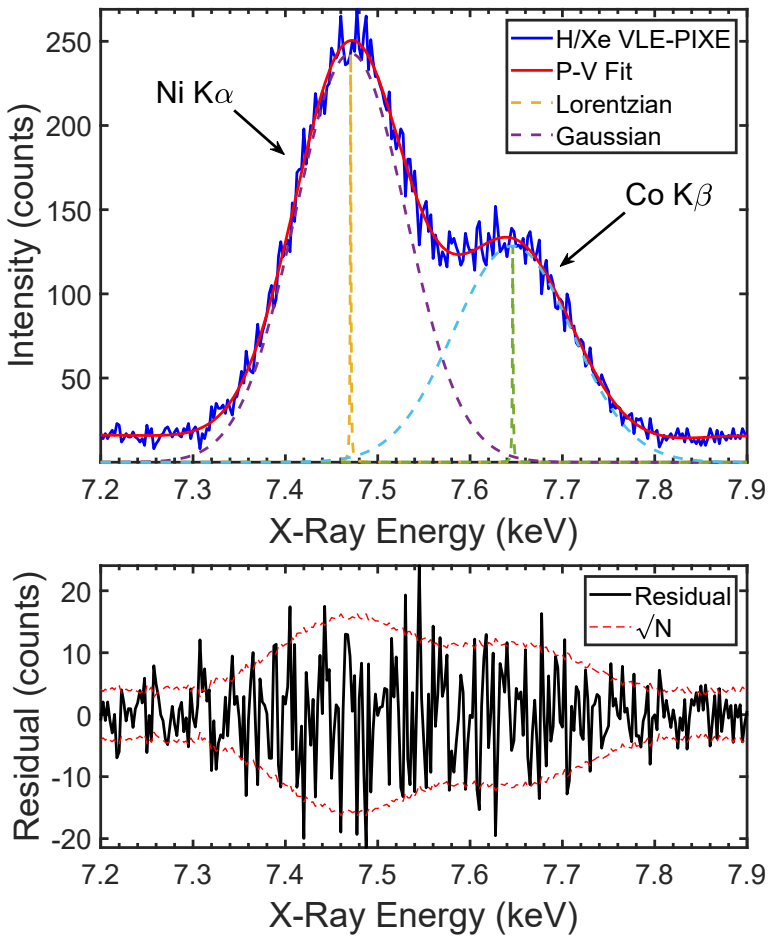
H/Xe VLE-PIXE
P-V Fit
Lorentzian
Gaussian
Ni Kα
Co Kβ
Intensity (counts)
X-Ray Energy (keV)
Residual
√N
Residual (counts)
X-Ray Energy (keV)

e

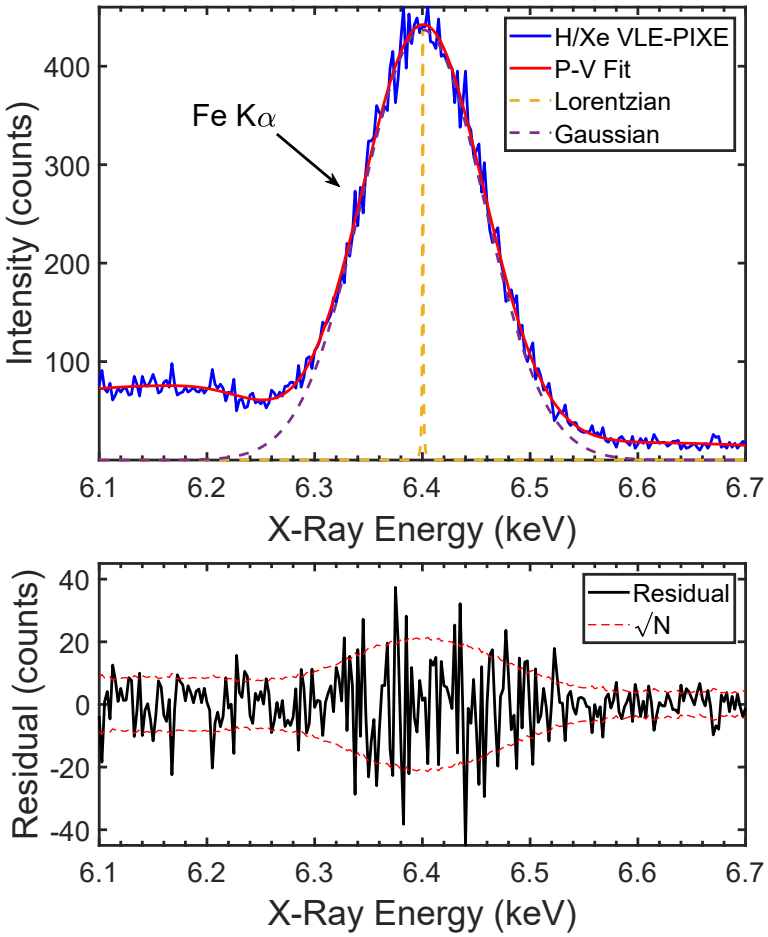
H/Xe VLE-PIXE
P-V Fit
Lorentzian
Gaussian
Fe Kα
Intensity (counts)
X-Ray Energy (keV)
Residual
√N
Residual (counts)
X-Ray Energy (keV)

f

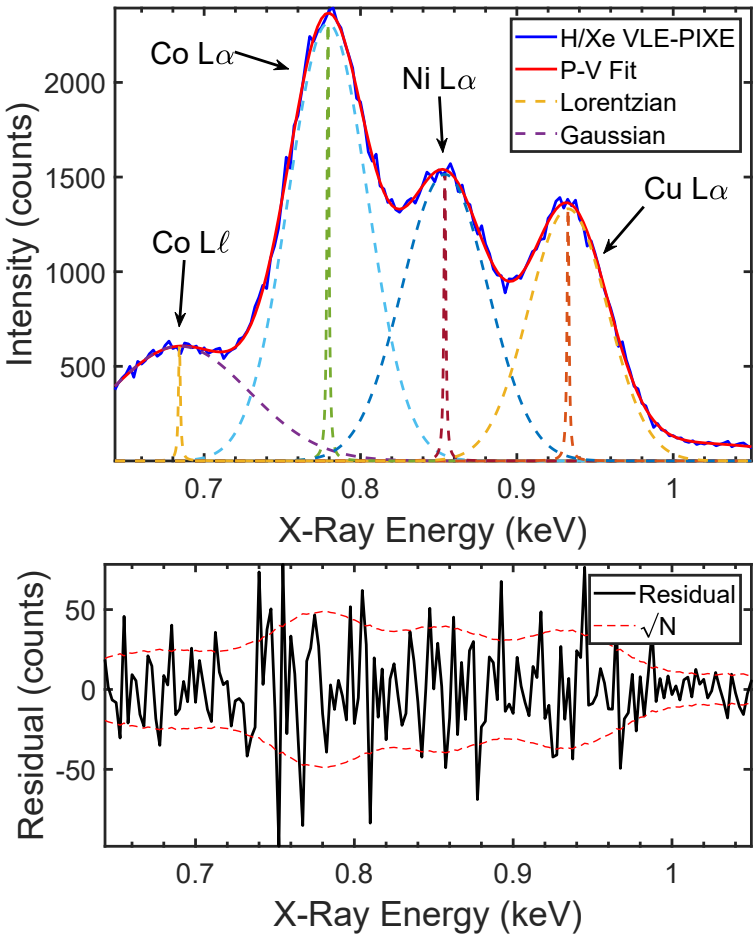

Figure A.16: Pseudo-Voigt fits for selected elements in the SRM 1242 using a lightly doped H/Xe beam. The beam composition used is given in figure 4.3a. Lorentzian widths are fixed to natural linewidths as determined from [2].

A.8 Additional MO Correlation Diagrams

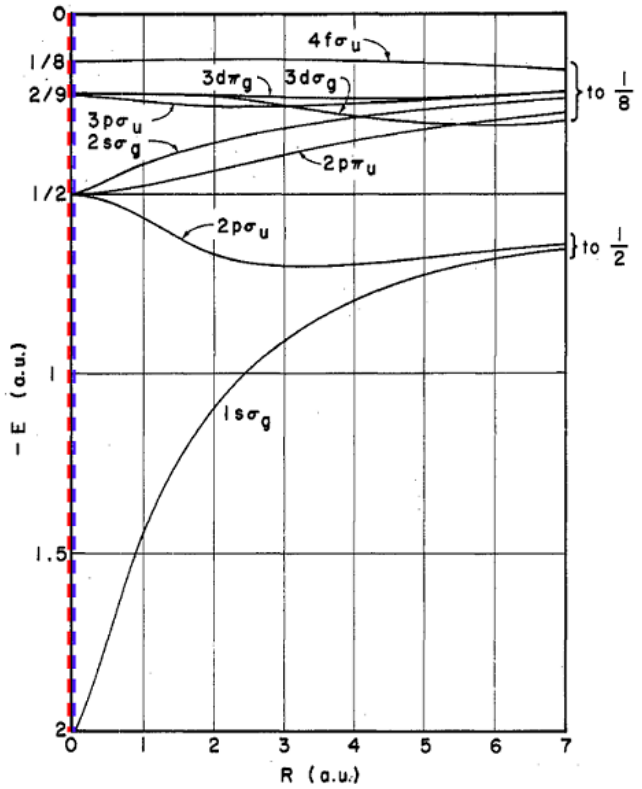

Figure A.17: H-H MO correlation diagram. 30keV and 8.1keV r_{min} are marked with dashed red lines and blue lines respectively. (From [100]).

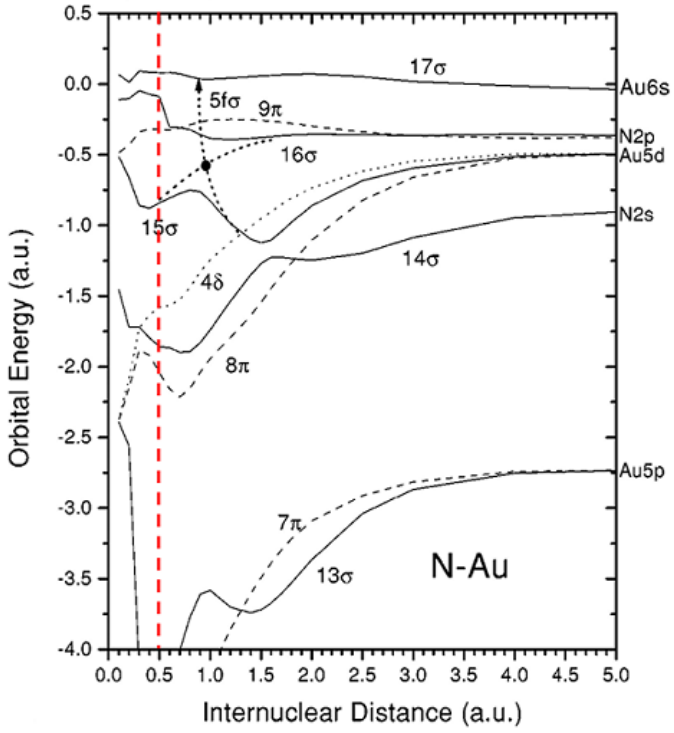

Figure A.18: Au+N MO correlation diagram with 30keV r_{min} marked with a red dashed line. (From [262])

a

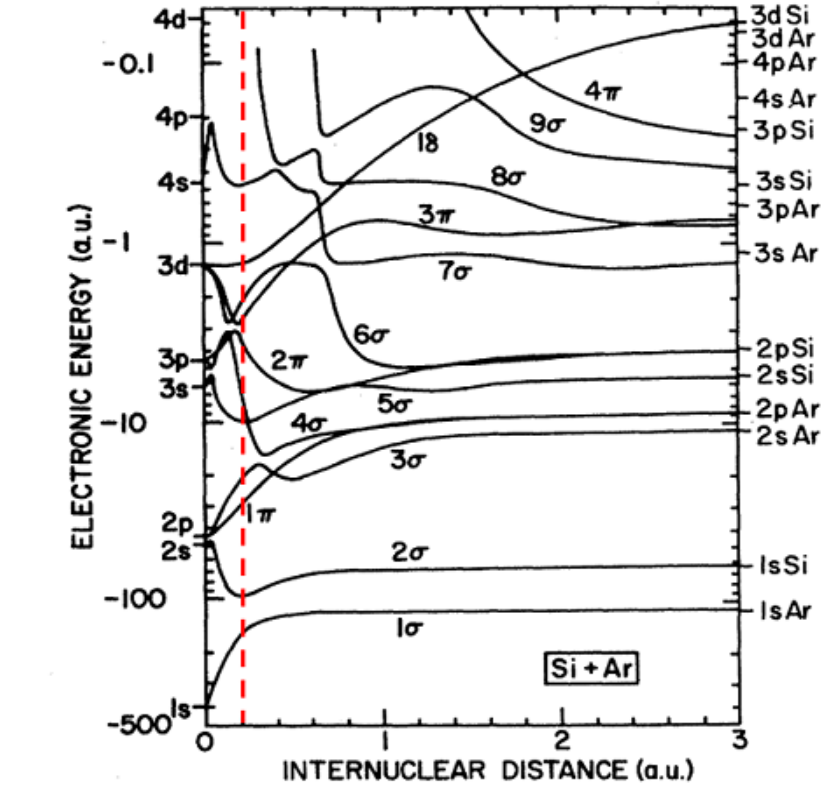
ELECTRONIC ENERGY (a.u.)
INTERNUCLEAR DISTANCE (a.u.)
Si + Ar
4d
4p
4s
3d
3p
3s
2p
2s
1s
-0.1
-1
-10
-100
-500
0
1
2
3
4π
9σ
1δ
8σ
3π
7σ
6σ
2π
5σ
4σ
3σ
1π
2σ
1σ
3d Si
3d Ar
4p Ar
4s Ar
3p Si
3s Si
3p Ar
3s Ar
2p Si
2s Si
2p Ar
2s Ar
1s Si
1s Ar

b

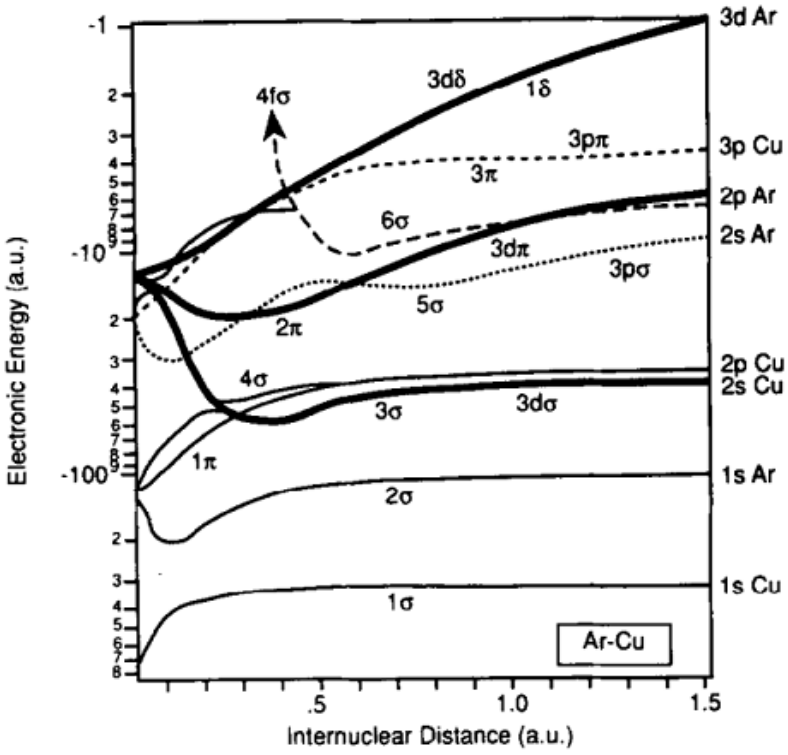
Electronic Energy (a.u.)
Internuclear Distance (a.u.)
Ar-Cu
-1
-10
-100
.5
1.0
1.5
4fσ
3dδ
1δ
3pπ
3π
6σ
3dπ
3pσ
5σ
2π
4σ
3σ
3dσ
1π
2σ
1σ
3d Ar
3p Cu
2p Ar
2s Ar
2p Cu
2s Cu
1s Ar
1s Cu

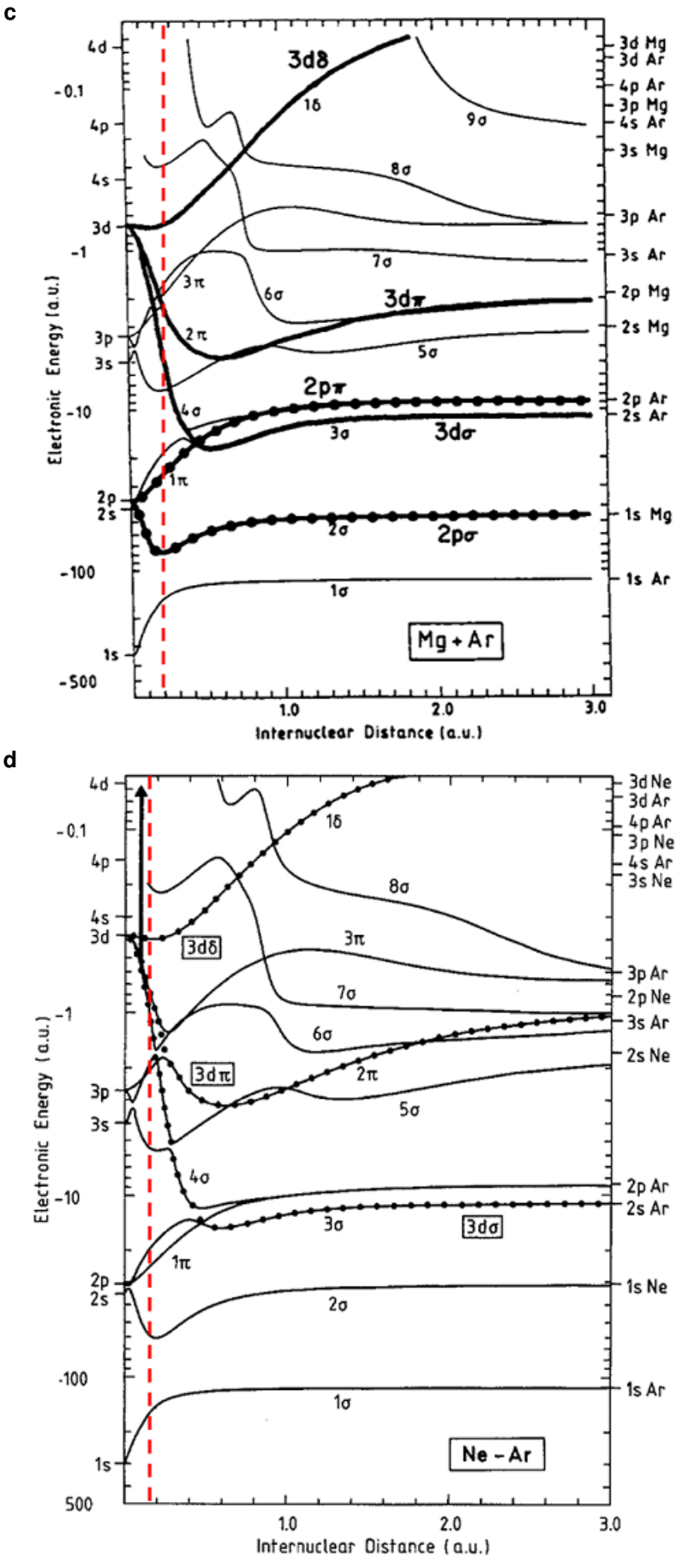

Figure A.19: Ar-Ar MO correlation diagram with 30keV r_{min} marked with a red dashed line (a) Si+Ar from [263] (b) Cu+Ar from [264] (c) Mg+Ar from [265] (d) Ne+Ar from [266].

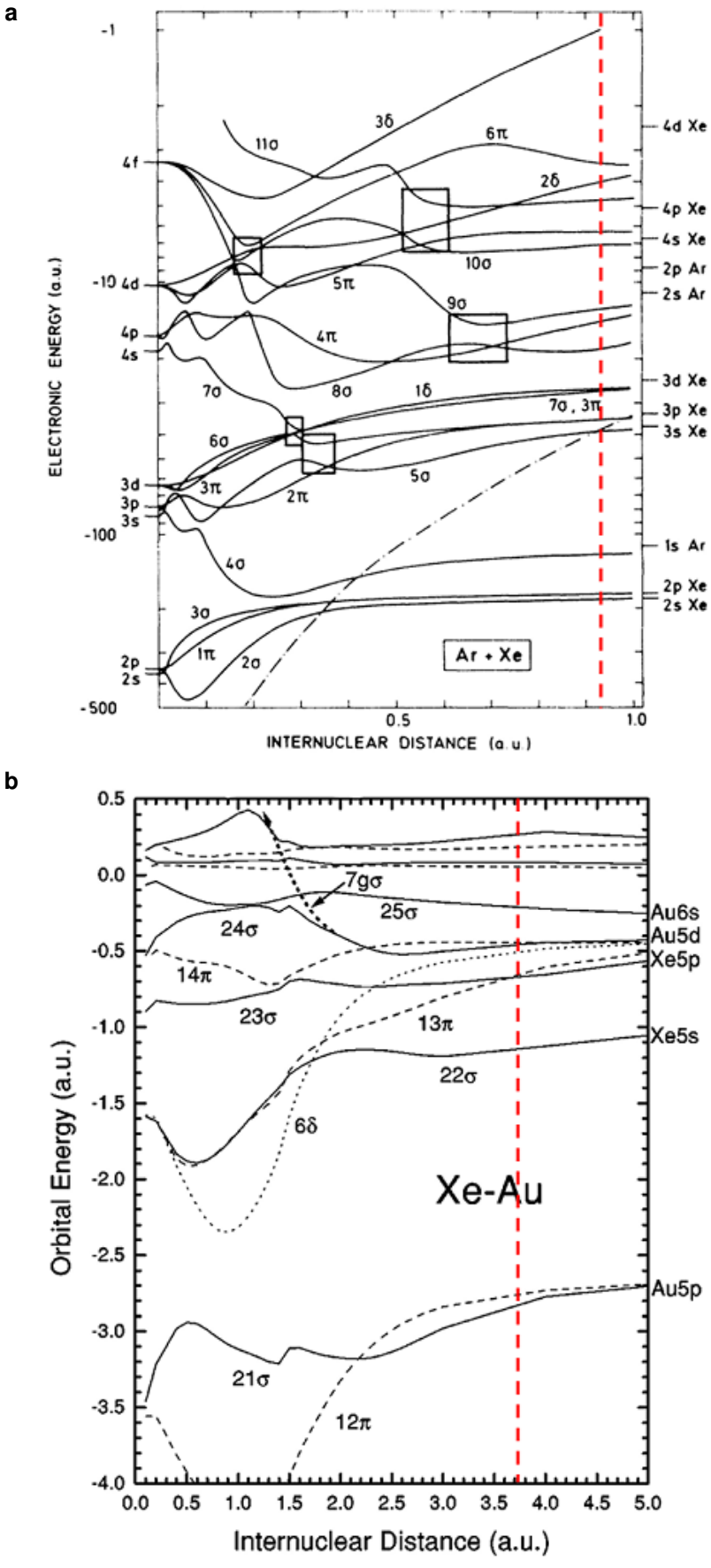

Figure A.20: Xe MO correlation diagrams with 30keV r_{min} marked with a red dashed line (a) Ar+Xe from [267], (b) Au+Xe from [262].

Bibliography

[1] Yuyan Liu, Jieli Lin, Guangming Huang, Yuanqing Guo, and Chuanxi Duan. Simple empirical analytical approximation to the Voigt profile. *JOSA B*, 18(5):666–672, 2001.

[2] Manfred Otto Krause and JH Oliver. Natural widths of atomic k and l levels, k α x-ray lines and several kll auger lines. *Journal of Physical and Chemical Reference Data*, 8(2):329–338, 1979.

[3] McLean P Echlin, Marcus Straw, Steven Randolph, Jorge Filevich, and Tresa M Pollock. The TriBeam system: Femtosecond laser ablation in situ SEM. *Materials Characterization*, 100:1–12, 2015.

[4] Yongqi Fu and Kok Ann Bryan Ngoi. Focused ion beam direct fabrication of micro-optical elements: features compared with laser beam and electron beam direct writing, 2004.

[5] Lucille A Giannuzzi et al. *Introduction to focused ion beams: instrumentation, theory, techniques and practice*. Springer Science & Business Media, 2004.

[6] Lucille A Giannuzzi and Frederick A Stevie. A review of focused ion beam milling techniques for TEM specimen preparation. *Micron*, 30(3):197–204, 1999.

[7] Richard Young, C Rue, S Randolph, C Chandler, G Franz, R Schampers, A Klumpp, and L Kwakman. A comparison of xenon plasma FIB technology with conventional gallium LMIS FIB: imaging, milling, and gas-assisted applications. *Microscopy and Microanalysis*, 17(S2):652–653, 2011.

[8] TL Burnett, R Kelley, B Winiarski, L Contreras, M Daly, A Gholinia, MG Burke, and PJ Withers. Large volume serial section tomography by Xe Plasma FIB dual beam microscopy. *Ultramicroscopy*, 161:119–129, 2016.

[9] Naohiro Shimizu and SR Hart. Applications of the ion microprobe to geochemistry and cosmochemistry. *Annual Review of Earth and Planetary Sciences*, 10(1):483–526, 1982.

[10] Sarah Witman. Ten things you might not know about particle accelerators. *Symmetry Magazine (Department of Energy*, 2014.

[11] Waldemar Scharf. *Particle accelerators and their uses*. CRC Press, 1986.

[12] R Curtis Bird and James Stanislaus Williams. *Ion beams for materials analysis*. Elsevier, 1990.

[13] Sven AE Johansson and Thomas B Johansson. Analytical application of particle induced X-ray emission. *Nuclear Instruments and Methods*, 137(3):473–516, 1976.

[14] CG Ryan. Quantitative trace element imaging using PIXE and the nuclear microprobe. *International Journal of Imaging Systems and Technology*, 11(4):219–230, 2000.

[15] AJ dAlfonso, B Freitag, D Klenov, and LJ Allen. Atomic-resolution chemical mapping using energy-dispersive x-ray spectroscopy. *Physical Review B*, 81(10):100101, 2010.

[16] Dale Newbury, Nicholas Ritchie, Michael Mengason, and Keana Scott. SEM/EDS Trace Analysis: Limits Imposed by Fluorescence of the Detector. *Microscopy and Microanalysis*, 23(S1):1026–1027, 2017.

[17] K Ishii and S Morita. Theoretical estimation of PIXE detection limits. *Nuclear Instruments and Methods in Physics Research Section B: Beam Interactions with Materials and Atoms*, 34(2):209–216, 1988.

[18] A Denker, J Opitz Coutureau, M Griesser, R Denk, and H Winter. Non-destructive analysis of coins using high-energy PIXE. *Nuclear Instruments and Methods in Physics Research Section B: Beam Interactions with Materials and Atoms*, 226(1-2):163–171, 2004.

[19] Chris Jacobsen. Soft x-ray microscopy. *Trends in cell biology*, 9(2):44–47, 1999.

[20] Javier Miranda. Low energy PIXE: advantages, drawbacks, and applications. *Nuclear Instruments and Methods in Physics Research Section B: Beam Interactions with Materials and Atoms*, 118(1-4):346–351, 1996.

[21] J Miranda. Low energy PIXE revisited: is it still alive? *Revista Mexicana de Física*, 56(1):82–84, 2010.

[22] David C Joy, Harry M Meyer, Mehdi Bolorizadeh, Yinghong Lin, and Dale Newbury. On the Production of X-rays by Low Energy Ion Beams. *Scanning: The Journal of Scanning Microscopies*, 29(1):1–4, 2007.

[23] Jürgen H Gross. *Mass spectrometry: a textbook*. Springer Science & Business Media, 2006.

[24] LW Swanson. Use of the liquid metal ion source for focused beam applications. *Applied surface science*, 76:80–88, 1994.

[25] PD Prewett and DK Jefferies. Characteristics of a gallium liquid metal field emission ion source. *Journal of Physics D: Applied Physics*, 13(9):1747, 1980.

[26] RG Forbest. Understanding how the liquid-metal ion source works. *Vacuum*, 48(1):85–97, 1997.

[27] John Morgan, John Notte, Raymond Hill, and Bill Ward. An introduction to the helium ion microscope. *Microscopy today*, 14(4):24–31, 2006.

[28] Gregor Hlawacek, Vasilisa Veligura, Raoul van Gastel, and Bene Poelsema. Helium ion microscopy. *Journal of Vacuum Science & Technology B, Nanotechnology and Microelectronics: Materials, Processing, Measurement, and Phenomena*, 32(2):020801, 2014.

[29] Hironori Moritani, Radovan Urban, Mark Salomons, Robert Wolkow, and Jason Pitters. Hydrogen Ion Beams from Nanostructured Gas Field Ion Sources. *Microscopy and Microanalysis*, 22(S3):612–613, 2016.

[30] Hironori Moritani, Radovan Urban, Kyle Nova, Mark Salomons, Robert Wolkow, and Jason Pitters. Selective production of hydrogen ion species at atomically designed nanotips. *Ultramicroscopy*, 186:42–48, 2018.

[31] Shinichi Matsubara, Hiroyasu Shichi, Yoshimi Kawanami, and Tomihiro Hashizume. Novel Scanning Ion Microscope with H3+ Gas Field Ionization Source. *Microscopy and Microanalysis*, 22(S3):614–615, 2016.

[32] John A Notte, Lou Farkas, Raymond Hill, and Bill Ward. An Introduction to Helium Ion Microscopy and its Nanotechnology Applications. *NanoScience and Technology Institute*, 2006.

[33] R Hill and FHM Faridur Rahman. Advances in helium ion microscopy. *Nuclear Instruments and Methods in Physics Research Section A: Accelerators, Spectrometers, Detectors and Associated Equipment*, 645(1):96–101, 2011.

[34] Alexander Piel. *Plasma physics: an introduction to laboratory, space, and fusion plasmas*. Springer, 2017.

[35] NS Smith, WP Skoczylas, SM Kellogg, DE Kinion, PP Tesch, O Sutherland, Ane Aanesland, and RW Boswell. High brightness inductively coupled plasma source for high current focused ion beam applications. *Journal of Vacuum Science & Technology B: Microelectronics and Nanometer Structures Processing, Measurement, and Phenomena*, 24(6):2902–2906, 2006.

[36] Noel Smith, Clive D Chandler, Mark Utlaut, Paul P Tesch, and Dave Tuggle. Multi-source plasma focused ion beam system, December 13 2011. US Patent 8,076,650.

[37] Anthony Graupera and Charles Otis. Inductively-coupled plasma ion source for use with a focused ion beam column with selectable ions, September 2 2014. US Patent 8,822,913.

[38] AA Pupyshev and VT Surikov. Application of negative ions in inductively coupled plasma-mass spectrometry. *Spectrochimica Acta Part B: Atomic Spectroscopy*, 59(7):1021–1031, 2004.

[39] JP Boeuf, GJM Hagelaar, P Sarrailh, G Fubiani, and N Kohen. Model of an inductively coupled negative ion source: II. Application to an ITER type source. *Plasma Sources Science and Technology*, 20(1):015002, 2011.

[40] Lucien Bex. Review of latest developments of ions sources. In *EPAC 92-Third European Particle Accelerator Conference*, pages 252–256, 1992.

[41] Ragnar Hellborg and Harry J Whitlow. *The Electrostatic Accelerator*. 2053-2571. Morgan and Claypool Publishers, 2019.

[42] Ardenne Manfred Von. Arrangement for glow discharge tubes, March 11 1958. US Patent 2,826,709.

[43] C Lejeune. Theoretical and experimental study of the duoplasmatron ion source: Part I: Model of the duoplasmatron discharge. *Nuclear Instruments and Methods*, 116(3):417–428, 1974.

[44] DJ Chivers. Freeman ion source: an overview. *Review of scientific instruments*, 63(4):2501–2506, 1992.

[45] DC Faircloth. Negative Ion Sources: Magnetron and Penning. *arXiv preprint arXiv:1404.0944*, 2014.

[46] Joshua L Rovey, Brandon P Ruzic, and Thomas J Houlahan. Simple Penning ion source for laboratory research and development applications. *Review of Scientific Instruments*, 78(10):106101, 2007.

[47] Tatsuya Kuzumi and Motoi Wada. Development of a miniaturized duoplasmatron ion source. *Review of Scientific Instruments*, 91(1):013505, 2020.

[48] VG Dudnikov. Review of high brightness ion sources for microlithography. *Review of scientific instruments*, 67(3):915–920, 1996.

[49] Nicolae C Podaru and Dirk JW Mous. Recent developments and upgrades in ion source technology and ion beam systems at HVE. *Nuclear Instruments and Methods in Physics Research Section B: Beam Interactions with Materials and Atoms*, 371:137–141, 2016.

[50] Boris Sharkov and Richard Scrivens. Laser ion sources. *IEEE Transactions on plasma science*, 33(6):1778–1785, 2005.

[51] D Doria, A Lorusso, F Belloni, V Nassisi, L Torrisi, and S Gammino. A study of the parameters of particles ejected from a laser plasma. *Laser and Particle Beams*, 22(4):461–467, 2004.

[52] David N Jamieson, William IL Lawrie, Simon G Robson, Alexander M Jakob, Brett C Johnson, and Jeffrey C McCallum. Deterministic doping. *Materials Science in Semiconductor Processing*, 62:23–30, 2017.

[53] MS Bronsgeest, JE Barth, LW Swanson, and P Kruit. Probe current, probe size, and the practical brightness for probe forming systems. *Journal of Vacuum Science & Technology B: Microelectronics and Nanometer Structures Processing, Measurement, and Phenomena*, 26(3):949–955, 2008.

[54] Tomáš Radlička and Bohumila Lencová. Coulomb interactions in Ga LMIS. *Ultramicroscopy*, 108(5):445–454, 2008.

[55] W Knauer. Boersch effect in electron-optical instruments. *Journal of Vacuum Science and Technology*, 16(6):1676–1679, 1979.

[56] Q Ji, X Jiang, T-J King, K-N Leung, K Standiford, and SB Wilde. Improvement in brightness of multicusp-plasma ion source. *Journal of Vacuum*

Science & Technology B: Microelectronics and Nanometer Structures Processing, Measurement, and Phenomena, 20(6):2717–2720, 2002.

[57] Jacques Gierak. Focused ion beam technology and ultimate applications. *Semiconductor science and technology*, 24(4):043001, 2009.

[58] Larry B Stotts. *Free Space Optical Systems Engineering: Design and Analysis*. John Wiley & Sons, 2017.

[59] JE Barth and P Kruit. Addition of different contributions to the charged particle probe size. *Optik (Stuttgart)*, 101(3):101–109, 1996.

[60] Frank Machalett and Paul Seidel. Focused Ion Beams and Some Selected Applications. *digital Encyclopedia of Applied Physics*, pages 1–39, 2003.

[61] K-U Riemann. The Bohm criterion and sheath formation. *Journal of Physics D: Applied Physics*, 24(4):493, 1991.

[62] Jacques Gierak, Paul Mazarov, Lars Bruchhaus, Ralf Jede, and Lothar Bischoff. Review of electrohydrodynamical ion sources and their applications to focused ion beam technology. *Journal of Vacuum Science & Technology B, Nanotechnology and Microelectronics: Materials, Processing, Measurement, and Phenomena*, 36(6):06J101, 2018.

[63] Hiroyasu Shichi, Shinichi Matsubara, and Tomihiro Hashizume. Comparison of Characteristics of Neon, Argon, and Krypton Ion Emissions from Gas Field Ionization Source with Single Atom Tip. *Microscopy and Microanalysis*, 23(S1):274–275, 2017.

[64] BW Ward, John A Notte, and NP Economou. Helium ion microscope: A new tool for nanoscale microscopy and metrology. *Journal of Vacuum Science & Technology B: Microelectronics and Nanometer Structures Processing, Measurement, and Phenomena*, 24(6):2871–2874, 2006.

[65] JF Ziegler. The electronic and nuclear stopping of energetic ions. *Applied Physics Letters*, 31(8):544–546, 1977.

[66] JF Ziegler and GJ Iafrate. The stopping of energetic ions in solids. *Radiation Effects*, 46(3-4):199–219, 1980.

[67] RJ Beuhler and L Friedman. A model of secondary electron yields from atomic and polyatomic ion impacts on copper and tungsten surfaces based upon stopping-power calculations. *Journal of Applied Physics*, 48(9):3928–3936, 1977.

[68] Kai Nordlund, Dage Sundholm, Pekka Pyykkö, Daniel Martinez Zambrano, and Flyura Djurabekova. Nuclear stopping power of antiprotons. *Physical Review A*, 96(4):042717, 2017.

[69] WD Wilson, LG Haggmark, and JP Biersack. Calculations of nuclear stopping, ranges, and straggling in the low-energy region. *Physical Review B*, 15(5):2458, 1977.

[70] Abdullah Atef Shukri, Fabien Bruneval, and Lucia Reining. Ab initio electronic stopping power of protons in bulk materials. *Physical Review B*, 93(3):035128, 2016.

[71] HH Brongersmal and PM Mu. Analysis of the outermost atomic layer of a surface by low-energy ion scattering. *Surface Science*, 35:393–412, 1973.

[72] M Mayer. Rutherford backscattering spectrometry (RBS). In *Workshop on Nuclear Data for Science and Technology: Materials Analysis*, volume 34, 2003.

[73] SR Kasi, H Kang, CS Sass, and JW Rabalais. Inelastic processes in low-energy ion-surface collisions. *Surface Science Reports*, 10(1-2):1–104, 1989.

[74] Raúl A Baragiola. Principles and applications of ion-induced auger electron emission from solids. *Radiation Effects*, 61(1-2):47–72, 1982.

[75] GH Kinchin and RS Pease. The displacement of atoms in solids by radiation. *Reports on progress in physics*, 18(1):1, 1955.

[76] SJ Pearton, CB Vartuli, JC Zolper, C Yuan, and RA Stall. Ion implantation doping and isolation of GaN. *Applied physics letters*, 67(10):1435–1437, 1995.

[77] Peter David Townsend, PJ Chandler, and L Zhang. *Optical effects of ion implantation*, volume 13. Cambridge University Press, 2006.

[78] W Ensinger. Modification of mechanical and chemical surface properties of metals by plasma immersion ion implantation. *Surface and Coatings Technology*, 100:341–352, 1998.

[79] Bernd Schmidt and Klaus Wetzig. *Ion beams in materials processing and analysis*. Springer Science & Business Media, 2012.

[80] K Cho, WR Allen, TG Finstad, WK Chu, J Liu, and JJ Wortman. Channeling effect for low energy ion implantation in Si. *Nuclear Instruments and Methods in Physics Research B*, 7:265–272, 1985.

[81] Gregor Hlawacek, Vasilisa Veligura, Stefan Lorbek, Tijs F Mocking, Antony George, Raoul van Gastel, Harold JW Zandvliet, and Bene Poelsema. Imaging ultra thin layers with helium ion microscopy: Utilizing the channeling contrast mechanism. *Beilstein journal of nanotechnology*, 3(1):507–512, 2012.

[82] C Yang, NP-O Larsson, E Swietlicki, KG Malmqvist, DN Jamieson, and CG Ryan. Imaging with ionoluminescence (IL) in a nuclear microprobe. *Nuclear Instruments and Methods in Physics Research Section B: Beam Interactions with Materials and Atoms*, 77(1-4):188–194, 1993.

[83] JP Biersack. Computer simulations of sputtering. *Nuclear Instruments and Methods in Physics Research Section B: Beam Interactions with Materials and Atoms*, 27(1):21–36, 1987.

[84] Philip JW Moll. Focused ion beam microstructuring of quantum matter. *Annual Review of Condensed Matter Physics*, 9:147–162, 2018.

[85] Masaaki Sugiyama and Genichi Sigesato. A review of focused ion beam technology and its applications in transmission electron microscopy. *Microscopy*, 53(5):527–536, 2004.

[86] Werner Wesch and Elke Wendler. *Ion Beam Modification of Solids*, volume 61. Springer, 2016.

[87] HS Cheng, ZQ Zhang, HN Xia, JC Jiang, and FJ Yang. Non-destructive analysis and appraisal of ancient Chinese porcelain by PIXE. *Nuclear Instruments and Methods in Physics Research Section B: Beam Interactions with Materials and Atoms*, 190(1-4):488–491, 2002.

[88] Giuseppe Pappalardo, E Costa, C Marchetta, L Pappalardo, FP Romano, A Zucchiatti, P Prati, PA Mandò, A Migliori, L Palombo, et al. Non-destructive characterization of Della Robbia sculptures at the Bargello museum in Florence by the combined use of PIXE and XRF portable systems. *Journal of Cultural Heritage*, 5(2):183–188, 2004.

[89] HS Cheng, ZQ Zhang, B Zhang, and FJ Yang. Non-destructive analysis and identification of jade by PIXE. *Nuclear Instruments and Methods in*

Physics Research Section B: Beam Interactions with Materials and Atoms, 219:30–34, 2004.

[90] David B Williams and C Barry Carter. The transmission electron microscope. In *Transmission electron microscopy*, pages 3–17. Springer, 1996.

[91] SJB Reed. Wavelength dispersive spectrometry: a review. *X-Ray spectrometry in electron beam instruments*, pages 221–238, 1995.

[92] Keizo Ishii. PIXE and its applications to elemental analysis. *Quantum Beam Science*, 3(2):12, 2019.

[93] R Jenkins, R Manne, R Robin, and C Senemaud. Nomenclature, symbols, units and their usage in spectrochemical analysis-VIII. Nomenclature system for X-ray spectroscopy (Recommendations 1991). *Pure and applied chemistry*, 63(5):735–746, 1991.

[94] Jens Lindhard, Allan H So, et al. Relativistic theory of stopping for heavy ions. *Physical Review A*, 53(4):2443, 1996.

[95] Werner Brandt and Grzegorz Lapicki. Energy-loss effect in inner-shell Coulomb ionization by heavy charged particles. *Physical Review A*, 23(4):1717, 1981.

[96] JD Garcia, RJ Fortner, and TM Kavanagh. Inner-shell vacancy production in ion-atom collisions. *Reviews of Modern Physics*, 45(2):111, 1973.

[97] E Görlich. The effective nuclear charges and the softness of the atomic cores. *Zeitschrift für Physikalische Chemie*, 271(1):169–174, 1990.

[98] Henry Gwyn Jeffreys Moseley. XCIII. The high-frequency spectra of the elements. *The London, Edinburgh, and Dublin Philosophical Magazine and Journal of Science*, 26(156):1024–1034, 1913.

[99] ˇZ ˇSmit and G Lapicki. Energy loss in the ECPSSR theory and its calculation with exact integration limits. *Journal of Physics B: Atomic, Molecular and Optical Physics*, 47(5):055203, 2014.

[100] William Lichten. Molecular orbital model of atomic collisions. *The Journal of Physical Chemistry*, 84(17):2102–2116, 1980.

[101] Werner Brandt and Roman Laubert. Pauli excitation of atoms in collision. *Physical Review Letters*, 24(19):1037, 1970.

[102] Grzegorz Lapicki and William Losonsky. Coulomb deflection in ion-atom collisions. *Physical Review A*, 20(2):481, 1979.

[103] George Basbas, Werner Brandt, and RH Ritchie. Perturbed-stationary-state theory of atomic inner-shell ionization by heavy charged particles. *Physical Review A*, 7(6):1971, 1973.

[104] R Anholt. Theoretical investigation of electronic relativistic effects on K-vacancy production by charged particles. *Physical Review A*, 17(3):976, 1978.

[105] Werner Brandt and Grzegorz Lapicki. L-shell Coulomb ionization by heavy charged particles. *Physical Review A*, 20(2):465, 1979.

[106] John L Campbell, Theodore L Hopman, John A Maxwell, and Zdenek Nejedly. The Guelph PIXE software package III: alternative proton database. *Nuclear Instruments and Methods in Physics Research Section B: Beam Interactions with Materials and Atoms*, 170(1-2):193–204, 2000.

[107] CG Ryan, E Van Achterbergh, CJ Yeats, SL Drieberg, G Mark, BM McInnes, TinTin Win, G Cripps, and GF Suter. Quantitative, high sensitivity, high resolution, nuclear microprobe imaging of fluids, melts and minerals. *Nuclear Instruments and Methods in Physics Research Section B: Beam Interactions with Materials and Atoms*, 188(1-4):18–27, 2002.

[108] Gregory Lapicki. The status of theoretical K-shell ionization cross sections by protons. *X-Ray Spectrometry: An International Journal*, 34(4):269–278, 2005.

[109] Gregory Lapicki, GAV Ramana Murty, GJ Naga Raju, B Seetharami Reddy, S Bhuloka Reddy, and V Vijayan. Effects of multiple ionization and intrashell coupling in L-subshell ionization by heavy ions. *Physical Review A*, 70(6):062718, 2004.

[110] Gregory Lapicki, R Mehta, Jerome L Duggan, PM Kocur, JL Price, and Floyd Del McDaniel. Multiple outer-shell ionization effect in inner-shell X-ray production by light ions. *Physical Review A*, 34(5):3813, 1986.

[111] Gregory Lapicki. The status of theoretical L-subshell ionization cross sections for protons. *Nuclear Instruments and Methods in Physics Research Section B: Beam Interactions with Materials and Atoms*, 189(1-4):8–20, 2002.

[112] Byung-Ho Choi. Hartree-Slater calculation of the cross section for L-shell ionization of argon by simple heavy charged particles. *Physical Review A*, 11(6):2004, 1975.

[113] M Msimanga, CA Pineda Vargas, and M Madhuku. K-shell X-ray production cross sections in Ti by 0.3–1.0 MeV/u 12C and 28Si ions for heavy ion PIXE. *Nuclear Instruments and Methods in Physics Research Section B: Beam Interactions with Materials and Atoms*, 380:90–93, 2016.

[114] M Lugo Licona, J Miranda, and C Romo Kröger. L-shell X-ray production cross section measured by heavy ion impact on selected rare earth elements. *Journal of radioanalytical and nuclear chemistry*, 262(2):391–401, 2004.

[115] MC Masekane, SJ Moloi, M Madhuku, and M Msimanga. Measurement of 12Cq+ and 35Clq+ ion induced X-ray production cross sections in V, Zr and Sn metal oxide films at 0.1 MeV/u-1.0 MeV/u energies. *Radiation Physics and Chemistry*, 176:109083, 2020.

[116] José Emilio Prieto, Alessandro Zucchiatti, Patricia Galán, and Pilar Prieto. Cross sections of X-ray production induced by C and Si ions with energies up to 1 MeV/u on Ti, Fe, Zn, Nb, Ru and Ta. *Nuclear Instruments and Methods in Physics Research Section B: Beam Interactions with Materials and Atoms*, 406:167–172, 2017.

[117] JH Hubbell, PN Trehan, Nirmal Singh, B Chand, D Mehta, ML Garg, RR Garg, Surinder Singh, and S Puri. A review, bibliography, and tabulation of K, L, and higher atomic shell x-ray fluorescence yields. *Journal of Physical and Chemical Reference Data*, 23(2):339–364, 1994.

[118] Norman Allen Dyson and Norman Allen Dyson. *X-rays in Atomic and Nuclear Physics*. Cambridge University Press, 2005.

[119] VP Petukhov, EA Romanovskii, H Kerkow, and G Kreysch. Proton-induced L-shell ionization cross-sections of elements with 28 Z2 79 for projectile energies between 70 and 500 keV. *physica status solidi (a)*, 60(1):79–83, 1980.

[120] H Paul. An analytical cross-section formula for K X-ray production by protons. *Nuclear Instruments and Methods in Physics Research Section B: Beam Interactions with Materials and Atoms*, 3(1-3):5–10, 1984.

[121] CH Sow, I Orlic, KK Loh, and SM Tang. New parameters for the calculation of L subshell ionization cross sections. *Nuclear Instruments and Methods in Physics Research Section B: Beam Interactions with Materials and Atoms*, 75(1-4):58–62, 1993.

[122] M Pajek, M Jaskóła, T Czyżewski, L Głowacka, D Banaś, J Braziewicz, W Kretschmer, G Lapicki, and D Trautmann. M-shell X-ray production cross sections for PIXE applications. *Nuclear Instruments and Methods in Physics Research Section B: Beam Interactions with Materials and Atoms*, 150(1-4):33–39, 1999.

[123] Rainer Siegele, David D Cohen, and Nick Dytlewski. The ANSTO high energy heavy ion microprobe. *Nuclear Instruments and Methods in Physics Research Section B: Beam Interactions with Materials and Atoms*, 158(1-4):31–38, 1999.

[124] RC Der, RJ Fortner, TM Kavanagh, and JM Khan. Production of Carbon K X Rays by Heavy-Ion Bombardment. *Physical Review A*, 4(2):556, 1971.

[125] Uwe Wille and Rainer Hippler. Mechanisms of inner-shell vacancy production in slow ion-atom collisions. *Physics Reports*, 132(3-4):129–260, 1986.

[126] Wikimedia Commons. Molecular orbital diagram of water, 2015.

[127] Ulrich Muller. *Inorganic structural chemistry*, volume 25. John Wiley & Sons, 2007.

[128] M Barat and Wm Lichten. Extension of the electron-promotion model to asymmetric atomic collisions. *Physical Review A*, 6(1):211, 1972.

[129] U Fano and W Lichten. Interpretation of Ar+-Ar collisions at 50 keV. *Physical Review Letters*, 14(16):627, 1965.

[130] George M Thomson. Trajectory and charge dependence of L x-ray fluorescence following Ar++ Ar collisions. *Physical Review A*, 25(2):816, 1982.

[131] R Shanker, R Bilau, R Hippler, U Wille, and HO Lutz. Impact parameter dependence of Ar L-shell excitation in slow Ar-Ar collisions. *Journal of Physics B: Atomic and Molecular Physics*, 14(6):997, 1981.

[132] PH Woerlee, RJ Fortner, and FW Saris. Charge-state dependence of inner-shell vacancy production in heavy ion-atom collisions with atomic number larger than 10. *Journal of Physics B: Atomic and Molecular Physics*, 14(17):3173, 1981.

[133] John B Boffard, RO Jung, Chun C Lin, and AE Wendt. Optical emission measurements of electron energy distributions in low-pressure argon inductively coupled plasmas. *Plasma Sources Science and Technology*, 19(6):065001, 2010.

[134] James H Scofield. Radiative decay rates of vacancies in the K and L shells. *Physical Review*, 179(1):9, 1969.

[135] Joseph Macek, JA Cairns, and JS Briggs. Double-Scattering Mechanism to Account for the Si K-X-Ray Yields Observed during Argon-Ion Bombardment of Silicon. *Physical Review Letters*, 28(20):1298, 1972.

[136] LC Feldman, PJ Silverman, and RJ Fortner. Lifetime studies of Ar-2p-vacancies travelling through solids. *Nuclear Instruments and Methods*, 132:29–33, 1976.

[137] Ch Heitz, J Cailleret, and G Lagarde. Importance of projectile inner-shell vacancies in X-ray analysis using MeV Ar beams. *Nuclear Instruments and Methods in Physics Research Section B: Beam Interactions with Materials and Atoms*, 15(1-6):598–601, 1986.

[138] FW Saris, WF Van der Weg, H Tawara, and Roman Laubert. Radiative transitions between quasimolecular levels during energetic atom-atom collisions. *Physical Review Letters*, 28(12):717, 1972.

[139] W Heiland and E Taglauer. Low energy ion scattering: Elastic and inelastic effects. *Nuclear Instruments and Methods*, 132:535–545, 1976.

[140] Wolfram Research. LatticeData, Wolfram Language function, 2007.

[141] WE Meyerhof. K-vacancy sharing in near-symmetric heavy-ion collisions. *Physical Review Letters*, 31(22):1341, 1973.

[142] James R Macdonald and Matt D Brown. Noncharacteristic X-Ray Bands Produced in Targets of C, Al, Si, and Solid Ar by Argon Ions at keV Energies. *Physical Review Letters*, 29(1):4, 1972.

[143] James R Macdonald, Matt D Brown, and Tang Chiao. Observation of a K X-Ray band emitted by the transient CC system formed at keV energies. *Physical Review Letters*, 30(11):471, 1973.

[144] M Uda, O Benka, K Fuwa, K Maeda, and Y Sasa. Chemical effects in PIXE spectra. *Nuclear Instruments and Methods in Physics Research Section B: Beam Interactions with Materials and Atoms*, 22(1-3):5–12, 1987.

[145] Hem Raj Verma. *Atomic and nuclear analytical methods*. Springer, 2007.

[146] Terrence Jach, John A Small, and Dale E Newbury. Improving energy stability in the National Institute of Standards and Technology Microcalorimeter X-ray detector. *Powder diffraction*, 20(2):134–136, 2005.

[147] Terrence Jach, Nicholas Ritchie, Joel Ullom, and James A Beall. Quantitative analysis with the transition edge sensor microcalorimeter X-ray detector. *Powder diffraction*, 22(2):138–141, 2007.

[148] Keizo Ishii and Susumu Morita. Continuous backgrounds in PIXE. *International Journal of PIXE*, 1(01):1–29, 1990.

[149] Yoshiko Moriya, Yasuro Ato, and Sohji Miyagawa. Sensitivity in light element analysis by 2 MeV and 150 keV proton and photon induced X-rays. *Nuclear Instruments and Methods*, 150(3):523–528, 1978.

[150] SA Corrêa, E Pitthan, MV Moro, and D Primetzhofer. A multipurpose set-up using keV ions for nuclear reaction analysis, high-resolution backscattering spectrometry, low-energy PIXE and in-situ irradiation experiments. *Nuclear Instruments and Methods in Physics Research Section B: Beam Interactions with Materials and Atoms*, 478:104–110, 2020.

[151] Wataru Kada, Atsuya Kishi, Masato Sueyasu, Fuminobu Sato, Yushi Kato, and Toshiyuki Iida. Development of a low-energy PIXE analysis system based on an ion implanter. *Nuclear Instruments and Methods in Physics Research Section B: Beam Interactions with Materials and Atoms*, 318:51–54, 2014.

[152] Milo Boirot. Implementation of low-energy PIXE at the new scattering chamber of the 350 kV implanter, 2019.

[153] M Soueidan, M Roumié, and B Nsouli. PIXE detection limit for aluminium thin film deposited on Si-based matrix. *Nuclear Instruments and Methods in Physics Research Section B: Beam Interactions with Materials and Atoms*, 406:71–74, 2017.

[154] SJC do Carmo, FIGM Borges, AMF Trindade, and CAN Conde. K X-ray production cross sections in aluminium for 15, 20 and 25 keV protons. *Nuclear Instruments and Methods in Physics Research Section B: Beam Interactions with Materials and Atoms*, 293:16–20, 2012.

[155] Werner Nakel. The elementary process of bremsstrahlung. *Physics reports*, 243(6):317–353, 1994.

[156] Keizo Ishii. High energy limit of atomic bremsstrahlung. *Nuclear Instruments and Methods in Physics Research Section B: Beam Interactions with Materials and Atoms*, 99(1-4):163–165, 1995.

[157] Emilio Gatti and Pavel Rehak. Review of semiconductor drift detectors. *Nuclear Instruments and Methods in Physics Research Section A: Accelerators, Spectrometers, Detectors and Associated Equipment*, 541(1-2):47–60, 2005.

[158] M Kavčič. Improved detection limits in PIXE analysis employing wavelength dispersive X-ray spectroscopy. *Nuclear Instruments and Methods in Physics Research Section B: Beam Interactions with Materials and Atoms*, 268(22):3438–3442, 2010.

[159] MA Reis, LC Alves, NP Barradas, PC Chaves, B Nunes, A Taborda, KP Surendran, A Wu, PM Vilarinho, and E Alves. High Resolution and Differential PIXE combined with RBS, EBS and AFM analysis of magnesium titanate (MgTiO3) multilayer structures. *Nuclear Instruments and Methods in Physics Research Section B: Beam Interactions with Materials and Atoms*, 268(11-12):1980–1985, 2010.

[160] L Strüder, P Lechner, and P Leutenegger. Silicon drift detector–the key to new experiments. *The Science of Nature*, 85(11):539–543, 1998.

[161] A Niculae, P Lechner, H Soltau, G Lutz, L Strüder, C Fiorini, and A Longoni. Optimized readout methods of silicon drift detectors for high-resolution X-ray spectroscopy. *Nuclear Instruments and Methods in Physics Research Section A: Accelerators, Spectrometers, Detectors and Associated Equipment*, 568(1):336–342, 2006.

[162] Tara Nylese and Jens Rafaelsen. Improvements in SDD efficiency–from X-ray counts to data. *Microscopy Today*, 25(2):46–53, 2017.

[163] Pierre Hovington, Vladimir Timoshevskii, Simon Burgess, Hendrix Demers, Peter Statham, Raynald Gauvin, and Karim Zaghib. Can we detect Li KX-ray in lithium compounds using energy dispersive spectroscopy? *Scanning*, 38(6):571–578, 2016.

[164] Oxford Instruments. Silicon Drift Detectors Explained. 2012.

[165] Archer Hoyt. The shape of an x-ray line. *Physical Review*, 40(4):477, 1932.

[166] HR Zulliger and DW Aitken. Fano factor fact and fallacy. *IEEE Transactions on Nuclear Science*, 17(3):187–195, 1970.

[167] Burton L Henke and Kazuo Taniguchi. Quantitative low-energy x-ray spectroscopy (50–100-å region). *Journal of Applied Physics*, 47(3):1027–1037, 1976.

[168] GK Wertheim, MA Butler, KW West, , and DNE Buchanan. Determination of the gaussian and lorentzian content of experimental line shapes. *Review of Scientific Instruments*, 45(11):1369–1371, 1974.

[169] David A Armbruster and Terry Pry. Limit of blank, limit of detection and limit of quantitation. *The clinical biochemist reviews*, 29(Suppl 1):S49, 2008.

[170] Nico Klingner, René Heller, Gregor Hlawacek, Johannes von Borany, John Notte, Jason Huang, and Stefan Facsko. Nanometer scale elemental analysis in the helium ion microscope using time of flight spectrometry. *Ultramicroscopy*, 162:91–97, 2016.

[171] N Klingner, J Vogt, and D Spemann. Optimizing the Rutherford Backscattering Spectrometry setup in a nuclear microprobe. *Nuclear Instruments and Methods in Physics Research Section B: Beam Interactions with Materials and Atoms*, 306:44–48, 2013.

[172] Horst Niehus, Werner Heiland, and Edmund Taglauer. Low-energy ion scattering at surfaces. *Surface Science Reports*, 17(4-5):213–303, 1993.

[173] Cody V Cushman, Philipp Brüner, Julia Zakel, George H Major, Barry M Lunt, Nicholas J Smith, Thomas Grehl, and Matthew R Linford. Low energy ion scattering (LEIS). A practical introduction to its theory, instrumentation, and applications. *Analytical Methods*, 8(17):3419–3439, 2016.

[174] Gorelick Sergey, Korneev Denis, Handley Ava, Gervinskas Gediminas, Oorschot Viola, Pocock Roger, et al. Oxygen plasma focused ion beam scanning electron microscopy for biological samples. *BioRxiv*, page 457820, 2018.

[175] KH Bai, SJ You, Hong-Young Chang, and HS Uhm. Plasma parameters analysis of various mixed gas inductively coupled plasmas. *Physics of Plasmas*, 9(6):2831–2838, 2002.

[176] Katsushige Tsuno, Nobuo Handa, and Sunao Matsumoto. Immersion lenses for low-voltage SEM and LEEM. In *Electron-Beam Sources and Charged-Particle Optics*, volume 2522, pages 243–252. International Society for Optics and Photonics, 1995.

[177] BL Thiel, M Toth, RPM Schroemges, JJ Scholtz, G Van Veen, and WR Knowles. Two-stage gas amplifier for ultrahigh resolution low vacuum scanning electron microscopy. *Review of scientific instruments*, 77(3):033705, 2006.

[178] EW Lemmon, MO McLinden, DG Friend, P Linstrom, and W Mallard. NIST chemistry webbook. *NIST standard reference database*, 1(69):20899, 2011.

[179] Alfred O Nier. A mass-spectrographic study of the isotopes of Hg, Xe, Kr, Be, I, As, and Cs. *Physical Review*, 52(9):933, 1937.

[180] Thierry Czerwiec, F Greer, and DB Graves. Nitrogen dissociation in a low pressure cylindrical ICP discharge studied by actinometry and mass spectrometry. *Journal of Physics D: Applied Physics*, 38(24):4278, 2005.

[181] Mark W Kiehlbauch and David B Graves. Inductively coupled plasmas in oxygen: Modeling and experiment. *Journal of Vacuum Science & Technology A: Vacuum, Surfaces, and Films*, 21(3):660–670, 2003.

[182] Denis Pick, Matthias Leiterer, and Jürgen W Einax. Reduction of polyatomic interferences in biological material using dynamic reaction cell ICP-MS. *Microchemical Journal*, 95(2):315–319, 2010.

[183] Osamu Fukumasa, R Italani, and S Saeki. Numerical simulation of hydrogen ion species in the steady-state plasma of a low-pressure ion source. *Journal of Physics D: Applied Physics*, 18(12):2433, 1985.

[184] HM Sullivan. Vacuum pumping equipment and systems. *Review of Scientific Instruments*, 19(1):1–15, 1948.

[185] RA Smith. The capture of electrons by positive ions from neutral gas atoms. In *Mathematical Proceedings of the Cambridge Philosophical Society*, volume 30, pages 514–519. Cambridge University Press, 1934.

[186] FB Yousif, J Geddes, and HB Gilbody. Charge states of heavy-ion beams in hydrogen. *Journal of Physics D: Applied Physics*, 20(8):998, 1987.

[187] Gennadi N Ogurtsov. Energy spectra of electrons ejected in ion-atom collisions. *Reviews of Modern Physics*, 44(1):1, 1972.

[188] Carl A Frische. Ionization and scattering accompanying positive ion impact in gases. *Physical Review*, 43(3):160, 1933.

[189] Nick FW Thissen, RHJ Vervuurt, JJL Mulders, JW Weber, WMM Kessels, and AA Bol. The effect of residual gas scattering on Ga ion beam patterning of graphene. *Applied Physics Letters*, 107(21):213101, 2015.

[190] Masanori Komuro. Radii broadening due to molecular collision in focused ion beams. *Applied physics letters*, 52(1):75–77, 1988.

[191] M Rommel, G Spoldi, V Yanev, S Beuer, B Amon, J Jambreck, S Petersen, AJ Bauer, and L Frey. Comprehensive study of focused ion beam induced lateral damage in silicon by scanning probe microscopy techniques. *Journal of Vacuum Science & Technology B, Nanotechnology and Microelectronics: Materials, Processing, Measurement, and Phenomena*, 28(3):595–607, 2010.

[192] Tohru Ishitani, Yoshimi Kawanami, and Shoji Shukuri. Focused-ion-beam broadening due to collisions with residual gas atoms. *Japanese journal of applied physics*, 26(10R):1777, 1987.

[193] Scott A Wight. Experimental data and model simulations of beam spread in the environmental scanning electron microscope. *Scanning*, 23(5):320–327, 2001.

[194] Lucille A Giannuzzi. Particle-induced x-ray analysis using focused ion beams. *Scanning*, 27(4):165–169, 2005.

[195] A Pillay and M Peisach. Production of charge-induced X-rays during PIXE studies using light and heavy ion-beams. *Journal of radioanalytical and nuclear chemistry*, 200(1):53–74, 1995.

[196] Tom Wirtz, Olivier De Castro, Jean-Nicolas Audinot, and Patrick Philipp. Imaging and analytics on the helium ion microscope. *Annual Review of Analytical Chemistry*, 12:523–543, 2019.

[197] W Eckstein, H Verbeek, and S Datz. Backscattering of keV molecular hydrogen ions from Au surfaces. *Applied Physics Letters*, 27(10):527–528, 1975.

[198] Robert E Alvarez. Signal to noise ratio of energy selective x-ray photon counting systems with pileup. *Medical physics*, 41(11):111909, 2014.

[199] Peter Lechner, Stefan Eckbauer, Robert Hartmann, Susanne Krisch, Dieter Hauff, Rainer Richter, Heike Soltau, Lothar Strüder, Carlo Fiorini, Emilio Gatti, et al. Silicon drift detectors for high resolution room temperature X-ray spectroscopy. *Nuclear Instruments and Methods in Physics Research*

Section A: Accelerators, Spectrometers, Detectors and Associated Equipment, 377(2-3):346–351, 1996.

[200] Barrie Glyn Lowe and Robert Anthony Sareen. *Semiconductor X-Ray Detectors*. CRC Press, 2019.

[201] Jorge Trincavelli, Silvina Limandri, and Rita Bonetto. Standardless quantification methods in electron probe microanalysis. *Spectrochimica Acta Part B: Atomic Spectroscopy*, 101:76–85, 2014.

[202] Michael H Loretto. *Electron beam analysis of materials*. Springer Science & Business Media, 2012.

[203] Xavier Llovet, Cedric J Powell, Francesc Salvat, and Aleksander Jablonski. Cross sections for inner-shell ionization by electron impact. *Journal of Physical and Chemical Reference Data*, 43(1):013102, 2014.

[204] David D Cohen. K and L shell X-ray cross sections for use in PIXE analysis systems. *Nuclear Instruments and Methods in Physics Research Section B: Beam Interactions with Materials and Atoms*, 49(1-4):1–9, 1990.

[205] Usama M El Ghawi, Beni M Bahal, and Salem K Al Arbi. Possibility of using a low-energy proton beam for particle-induced X-ray emission microanalysis. *Radiation research*, 131(3):243–248, 1992.

[206] Jean-Louis Pouchou. Standardless x-ray analysis of bulk specimens. *Microchimica Acta*, 114(1):33–52, 1994.

[207] WJ Teesdale, JA Maxwell, A Perujo, JL Campbell, L Van der Zwan, and TE Jackman. Limits of detection and quantitation in PIXE analysis of thick targets. *Nuclear Instruments and Methods in Physics Research Section B: Beam Interactions with Materials and Atoms*, 35(1):57–66, 1988.

[208] M Khaliquzzaman, ST Lam, DM Sheppard, and LG Stephens Newsham. Dependence of X-ray yields on different parameters for light element matrices in thick target PIXE and use of standards for calibration in such analysis. *Nuclear Instruments and Methods in Physics Research*, 216(3):481–488, 1983.

[209] JL Campbell, JA Maxwell, WJ Teesdale, J-X Wang, and LJ Cabri. Micro-PIXE as a complement to electron probe microanalysis in mineralogy. *Nuclear Instruments and Methods in Physics Research Section B: Beam Interactions with Materials and Atoms*, 44(3):347–356, 1990.

[210] CG Ryan, DR Cousens, SH Sie, WL Griffin, GF Suter, and E Clayton. Quantitative pixe microanalysis of geological matemal using the CSIRO proton microprobe. *Nuclear Instruments and Methods in Physics Research Section B: Beam Interactions with Materials and Atoms*, 47(1):55–71, 1990.

[211] Alessandro Borghi, Roberto Cossio, and C Mazzoli. A mineralogical application of micro-PIXE technique: Yttrium zoning in garnet from metamorphic rocks and its petrologic meaning. *Nuclear Instruments and Methods in Physics Research Section B: Beam Interactions with Materials and Atoms*, 189(1-4):412–417, 2002.

[212] B Nsouli, M Roumié, K Zahraman, JP Thomas, and M Nasreddine. On the phosphorus characterization in thin SiO2 (P, B) CVD layer deposited onto a silicon substrate by PIXE. *Nuclear Instruments and Methods in Physics Research Section B: Beam Interactions with Materials and Atoms*, 192(3):311–317, 2002.

[213] K Zahraman, B Nsouli, M Roumié, JP Thomas, and S Danel. On the optimization of the PIXE technique for thickness uniformity control of ultra-thin chromium layers deposited onto large surface quartz substrate. *Nuclear Instruments and Methods in Physics Research Section B: Beam Interactions with Materials and Atoms*, 249(1-2):447–450, 2006.

[214] H Paul and J Sacher. Fitted empirical reference cross sections for K-shell ionization by protons. *Atomic Data and Nuclear Data Tables*, 42(1):105–156, 1989.

[215] Maria Grazia Pia, Georg Weidenspointner, Mauro Augelli, Lina Quintieri, Paolo Saracco, Manju Sudhakar, and Andreas Zoglauer. PIXE simulation with Geant4. *IEEE transactions on nuclear science*, 56(6):3614–3649, 2009.

[216] Javier Miranda and Gregory Lapicki. Experimental cross sections for L-shell x-ray production and ionization by protons. *Atomic data and nuclear data tables*, 100(3):651–780, 2014.

[217] L Rodrıguez Fernández, J Miranda, JL Ruvalcaba Sil, E Segundo, and A Oliver. Measurement of M-shell X-ray production induced by protons of 0.3–0.7 MeV on W, Au, Pb, Bi, Th and U. *Nuclear Instruments and Methods in Physics Research Section B: Beam Interactions with Materials and Atoms*, 189(1-4):27–32, 2002.

[218] J H Hubbell and S M Seltzer. Tables of x-ray mass attenuation coefficients and mass energy-absorption coefficients 1 keV to 20 meV for elements z = 1 to 92 and 48 additional substances of dosimetric interest. 5 1995.

[219] James F Ziegler and Jochen P Biersack. The stopping and range of ions in matter. In *Treatise on heavy-ion science*, pages 93–129. Springer, 1985.

[220] Peter Duncumb, Ian R Barkshire, and Peter J Statham. Improved x-ray spectrum simulation for electron microprobe analysis. *Microscopy and Microanalysis*, 7(4):341–355, 2001.

[221] DM Schlosser, P Lechner, G Lutz, A Niculae, H Soltau, L Strüder, R Eckhardt, K Hermenau, G Schaller, F Schopper, et al. Expanding the detection efficiency of silicon drift detectors. *Nuclear Instruments and Methods in Physics Research Section A: Accelerators, Spectrometers, Detectors and Associated Equipment*, 624(2):270–276, 2010.

[222] FW Saris. Cross sections for ar l-shell x-ray emission in collisions of he+, c+, n+, o+, al+, cl+, ti+, fe+, cu+ on ar. *Physica*, 52(2):290–298, 1971.

[223] M Msimanga, CA Pineda-Vargas, and M Madhuku. L-shell x-ray production cross sections in metal oxide thin films due to 12c, 16o and 28si ion beams at mev sims energies. *Nuclear Instruments and Methods in Physics Research Section B: Beam Interactions with Materials and Atoms*, 440:186–190, 2019.

[224] EO Ejeh, TT Hlatshwayo, M Madhuku, M Legodi, and M Msimanga. Measurement of l-shell x-ray production cross sections in 89y, 158gd and 209bi due to 0.3 mev/u–1.0 mev/u 12c ions. *Applied Radiation and Isotopes*, 177:109930, 2021.

[225] FP Larkins. Dependence of fluorescence yield on atomic configuration. *Journal of Physics B: Atomic and Molecular Physics*, 4(5):L29, 1971.

[226] O Benka. The influence of multiple ionization upon fluorescence yield. *Nuclear Instruments and Methods in Physics Research Section B: Beam Interactions with Materials and Atoms*, 4(2):279–282, 1984.

[227] LH Toburen and FP Larkins. Effects of Multiple Ionization on the Fluorescence Yield of Carbon. *Physical Review A*, 6(6):2035, 1972.

[228] J Miranda, OG de Lucio, EB Téllez, and JN Martınez. Multiple ionization effects on total L-shell X-ray production cross sections by proton impact. *Radiation Physics and Chemistry*, 69(4):257–263, 2004.

[229] Rev Anholt. X rays from quasimolecules. *Reviews of modern physics*, 57(4):995, 1985.

[230] AS Schlachter, MM Sant'Anna, AM Covington, A Aguilar, MF Gharaibeh, ED Emmons, SWJ Scully, RA Phaneuf, G Hinojosa, I Álvarez, et al. Lifetime of a k-shell vacancy in atomic carbon created by 1s 2p photoexcitation of c+. *Journal of Physics B: Atomic, Molecular and Optical Physics*, 37(5):L103, 2004.

[231] H-D Betz, F Bell, H Panke, G Kalkoffen, M Welz, and D Evers. New technique for the measurement of lifetimes of heavy-ion inner-shell vacancies. *Physical Review Letters*, 33(14):807, 1974.

[232] K Hämäläinen, DP Siddons, JB Hastings, and LE Berman. Elimination of the inner-shell lifetime broadening in x-ray-absorption spectroscopy. *Physical review letters*, 67(20):2850, 1991.

[233] Edgar Everhart, Gerald Stone, and RJ Carbone. Classical calculation of differential cross section for scattering from a Coulomb potential with exponential screening. *Physical Review*, 99(4):1287, 1955.

[234] Wataru Takeuchi. Evaluation of screening length corrections for interaction potentials in impact-collision ion scattering spectroscopy. *Nuclear Instruments and Methods in Physics Research Section B: Beam Interactions with Materials and Atoms*, 313:33–39, 2013.

[235] Carl Rod Nave. Hyperphysics, 2021.

[236] Quentin C Kessel and Edgar Everhart. Coincidence Measurements of Large-Angle Ar+-on-Ar Collisions. *Physical Review*, 146(1):16, 1966.

[237] R Frekers, H Schulze, W-H Schulte, and B Cleff. Threshold behaviour of L-shell ionisation in slow symmetric ion-atom collisions with 32 Z 54. *Journal of Physics B: Atomic and Molecular Physics*, 19(18):2907, 1986.

[238] A Toepfer, EKU Gross, and RM Dreizler. Thomas-Fermi approach to diatomic systems. II. Correlation diagrams for NN and Ne-Ne. *Physical Review A*, 20(5):1808, 1979.

[239] P Kaufmann and U Wille. Relativistic effects in the variable-screening model. *Zeitschrift für Physik A Atoms and Nuclei*, 279(3):259–270, 1976.

[240] G Schiwietz, B Skogvall, J Tanis, and D Schneider. Investigation of simultaneous inner-and outer-shell ionization and Auger-electron emission in slow

Ar++ Ar collisions at intermediate impact parameters. *Physical Review A*, 38(11):5552, 1988.

[241] MS Miller and JW Boring. Total inelastic energy loss by heavy ions stopped in a gas. *Physical Review A*, 9(6):2421, 1974.

[242] M Nekab, A Pape, and Ch Heitz. A study of the ionization of Al, Si, S, Sc, Ti and V by Ar ions in the energy range 1–5 MeV. *Nuclear Instruments and Methods in Physics Research Section B: Beam Interactions with Materials and Atoms*, 85(1-4):123–127, 1994.

[243] JD Garcia, RJ Fortner, HC Werner, D Schneider, N Stolterfoht, and D Ridders. Quasimolecular inner-shell charge-transfer cross sections for light projectiles in solids. *Physical Review A*, 22(5):1884, 1980.

[244] E Yu Tonkov and EG Ponyatovsky. *Phase transformations of elements under high pressure*. CRC press, 2018.

[245] Sam J Cipolla and Plark Mildebrath. Vacancy-Transfer Cross Sections and L-Vacancy Lifetimes for Low-Energy Collisions of Ar++ with Mg, Al, and Si. *IEEE Transactions on Nuclear Science*, 30(2):999–1001, 1983.

[246] Philipp Haas, Fabien Tran, and Peter Blaha. Calculation of the lattice constant of solids with semilocal functionals. *Physical Review B*, 79(8):085104, 2009.

[247] DL Walters and Ch P Bhalla. Nonrelativistic Auger Rates, X-Ray Rates, and Fluorescence Yields for the 2 p Shell. *Physical Review A*, 4(6):2164, 1971.

[248] PR Granfors, AT Macrander, and RO Simmons. Crystalline xenon: Lattice parameters, thermal expansion, thermal vacancies, and equation of state. *Physical Review B*, 24(8):4753, 1981.

[249] James H Scofield. Exchange corrections of K X-ray emission rates. *Physical Review A*, 9(3):1041, 1974.

[250] Stephen Croft, Andrew D Nicholson, Robert Dennis McElroy, and Tyler Guzzardo. On the relationship between the natural line width and lifetime of x-ray transitions. Technical report, Oak Ridge National Lab.(ORNL), Oak Ridge, TN (United States), 2015.

[251] BG Gokhale, SN Shukla, and Raman Nath Srivastava. Precise measurement of the widths of some l x-ray lines of tungsten. *Physical Review A*, 28(2):858, 1983.

[252] Jörg Eichler and Uwe Wille. Variable-screening model for the quasimolecular treatment of ion-atom collisions. *Physical Review A*, 11(6):1973, 1975.

[253] I Bizyukov and K Krieger. Dual beam experiment for simultaneous irradiation of surfaces with ion species of gaseous and solid-state elements. *Review of scientific instruments*, 77(4):043501, 2006.

[254] E Benes. Improved quartz crystal microbalance technique. *Journal of Applied Physics*, 56(3):608–626, 1984.

[255] Matej Mayer. SIMNRA, a simulation program for the analysis of NRA, RBS and ERDA. In *AIP conference proceedings*, volume 475, pages 541–544. American Institute of Physics, 1999.

[256] D Zudhistira, V Viswanathan, V Narang, JM Chin, S Sharang, K Novotny, and J Vincen Oboňa. Precision Xe plasma FIB delayering for physical failure analysis of sub-20 nm microprocessor devices. In *ISTFA 2017*, pages 574–579. ASM International, 2017.

[257] Roger Alvis, Trevan Landin, Chad Rue, Peter Carleson, Oleg Sidorov, Andrew Erickson, Sean Zumwalt, Sinjin Dixon Warren, Wan-Yi Liu, Shih-Hsin Chang, et al. Plasma FIB DualBeam Delayering for Atomic Force NanoProbing of 14 nm FinFET Devices in an SRAM Array. In *ISTFA 2015*, pages 388–400. ASM International, 2015.

[258] I Ipatova, Robert W Harrison, PT Wady, SM Shubeita, Dmitry Terentyev, Stephen E Donnelly, and Enrique Jimenez Melero. Structural defect accumulation in tungsten and tungsten-5wt.% tantalum under incremental proton damage. *Journal of Nuclear Materials*, 501:329–335, 2018.

[259] David Halliday, Robert Resnick, and Jearl Walker. *Fundamentals of physics*. John Wiley & Sons, 2013.

[260] Debora M Katz. *Physics for Scientists and Engineers: Foundations and Connections*, volume 1. Nelson Education, 2015.

[261] CE Sosolik, AC Lavery, EB Dahl, and BH Cooper. A technique for accurate measurements of ion beam current density using a Faraday cup. *Review of Scientific Instruments*, 71(9):3326–3330, 2000.

[262] Jan Lörinčík, Zdeněk ˇSroubek, Hannes Eder, Friedrich Aumayr, and Hannspeter Winter. Kinetic electron emission from clean polycrystalline gold induced by impact of slow C+, N+, O+, Ne+, Xe+, and Au+ ions. *Physical Review B*, 62(23):16116, 2000.

[263] D Schneider, G Nolte, U Wille, and N Stolterfoht. Total cross sections for L-shell Auger-electron production and vacancy production in slow Si-Ar collisions. *Physical Review A*, 28(1):161, 1983.

[264] Sam J Cipolla and Kennedy J Reed. Molecular orbital analysis of L X-ray cross sections measured for slow Ar-Cu collisions. *Nuclear Instruments and Methods in Physics Research Section B: Beam Interactions with Materials and Atoms*, 79(1-4):203–205, 1993.

[265] Yi-ming Xiong and Sam J Cipolla. Coupled state calculations of vacancy transfer probabilities from 2p and 3d rotational coupling in Ar-Mg collisions. *Nuclear Instruments and Methods in Physics Research Section B: Beam Interactions with Materials and Atoms*, 24:237–239, 1987.

[266] R Shanker, R Hippler, U Wille, R Bilau, and HO Lutz. 3dσ excitation in slow Ne-Ar collisions. *Zeitschrift für Physik A Atoms and Nuclei*, 313(4):281–288, 1983.

[267] J Eichler, U Wille, B Fastrup, and K Taulbjerg. Systematic investigation of diabatic correlations. *Physical Review A*, 14(2):707, 1976.